Wave-structure interactions of a submerged elastic plate for wave energy conversion.

Gatien Polly

Université Paris Cité

ESPCI PARIS

THÈSE DE DOCTORAT
D'UNIVERSITÉ PARIS CITÉ

Spécialité : Physique

École doctorale nº564: Physique en Île-de-France

réalisée au

Laboratoires de Physique et Mécanique des Milieux Hétérogènes, et Matière et Systèmes Complexes

sous la direction de **Ramiro GODOY-DIANA et Benjamin THIRIA**

présentée par

Gatien Polly

pour obtenir le grade de :
DOCTEUR D'UNIVERSITÉ PARIS CITÉ

Sujet de la thèse :

Interactions vague-structure d'une plaque flexible immergée pour la conversion de l'énergie des vagues

Wave-structure interactions of a submerged elastic plate for wave energy conversion

Présentée et soutenue publiquement le 9 novembre 2023

devant le jury composé de :

Dr.	**Malin Göteman**	**Upsalla University**	**Rapportrice**
Dr.	**David Fabre**	**Université Paul Sabatier**	**Rapporteur**
Dr.	**Claudia Brunner**	**Max Planck Institute**	**Examinatrice**
Pr.	**Michel Benoit**	**EDF R&D LNHE** **Lab. d'Hydraulique Saint-Venant**	**Examinateur**
Pr.	**Benjamin Thiria**	**Université de Paris**	**Directeur**
Pr.	**Ramiro Godoy-Diana**	**ESPCI**	**Directeur**
Dr.	**Gaële Perret**	**Université Le Havre Normandie**	**Membre invitée**
Dr.	**Alexis Mérigaud**	**ESPCI**	**Membre invité**

Mot clés

Interaction vague-structure, théorie de la houle linéaire, bassin à houle à petite échelle, réflexion et transmission, jet.

Résumé

L'interaction vague-structure est un domaine riche et aux intérêts applicatifs cruciaux tels que la protection côtière ou la production d'électricité par conversion d'énergie des vagues. Cette thèse s'inscrit dans ce contexte et s'intéresse au cas spécifique d'une plaque élastique submergée, maintenue à son bord d'attaque, et excitée par des vagues. Ce dispositif, qui est envisagé comme un potentiel convertisseur d'énergie des vagues, a été longuement étudiée dans le cas d'un écoulement uniforme ou pour un fluide au repos. En revanche, l'effet de l'excitation, par des vagues, d'une plaque élastique submergée reste mal connu.
Pour pallier à ce manque, cette thèse a pour but de décrire l'interaction entre une plaque élastique submergée, tenue à son bord d'attaque et des vagues. Pour ce faire, un premier travail théorique est menée en s'appuyant sur la théorie de la houle linéaire. Le but de cette approche est d'obtenir une première compréhension du système, c'est-à-dire de formaliser le problème physique et d'obtenir des informations sur la réponse des plaques excitées par les vagues. Pour cela, la réflection et la transmission des vagues sont évaluées et mises en perspective grâce à l'observation des déplacements de la plaque. De cette étude, il ressort que les plaques élastiques possèdent des motifs de résonnance complexes, qui varient en fonction de la profondeur, longueur ou rigidité des plaques.
Cette approche théorique linéaire, limitée au cas idéal de petites amplitudes de vagues et des petits déplacements de la plaque, est enrichie par une étude expérimentale de l'interaction plaque-vagues. Une des originalités de cette thèse réside dans les dimensions du dispositif expérimental. Le bassin utilisé mesure 2 mètres par 50 centimètres et est beaucoup plus petit que pour la majorité des travaux d'interaction vague-structure. Cette petite taille permet d'utiliser des méthodes expérimentales différentes et d'obtenir des informations supplémentaires. Ainsi, la hauteur du champ de vagues peut être estimée en tout point par imagerie Schlieren, ce qui permet la mesure de coefficients de réflexion et de transmission. Les champs de vitesse du fluide peuvent être évalués par Vélocimétrie par Image de Particules. Plusieurs faits marquant ressortent de ces mesures. Tout d'abord, à petites amplitudes de vagues, les fréquences des pics de réflexions mesurés expérimentalement coincident avec les prévisions numériques de pics dits "larges". Ensuite, en comparant la réflexion engendrée par des plaques flexibles avec le cas d'une plaque rigide de même dimension, il apparaît que les réflexions sont dues à la flexibilité. Finalement, à grandes amplitudes de vagues, un jet est créé par la plaque. Le jet pourrait être responsable d'un changement de position moyenne de la plaque, pour la plaque la moins rigide, entraînant une dissipation totale de l'énergie des vagues.

Key words

Wave-structure interaction, linear wave theory, small scale wave tank, reflection and transmission, jet.

Abstract

Wave-structure interaction is a rich field with crucial application interests, such as coastal protection or electricity production through wave energy conversion. This thesis is part of that context and focuses on the specific case of a submerged elastic plate, attached at its leading edge, and forced by water waves. This device, considered as a potential wave energy converter, has been extensively studied for uniform flows or in a still fluid. However, the effect of wave-induced forcing on a submerged elastic plate remains little studied.

To address this gap, the purpose of this thesis is to describe the interaction between a submerged elastic plate, held at its leading edge, and a monochromatic surface wave field. For that purpose, an initial theoretical work is carried out based on linear wave theory. The objective of this approach is to gain a preliminary understanding of the system, namely, to formalize the physical problem and obtain information about the plate response to wave excitation. Thus, waves reflection and transmission are evaluated and contextualized through the plate's displacements observation. From this study, the elastic plates exhibit complex resonance patterns that vary based on the submergence depth, length, and rigidity of the plates.

This linear theoretical approach, limited to the ideal case of small wave amplitudes and small plate displacements, is complemented by an experimental study of plate-wave interaction. An original aspects of the thesis lies in the dimensions of the experimental setup. The utilized wave tank measures 2 meters by 50 centimeters, and is considerably smaller than the experimental facilities used in the majority of wave-structure interaction studies. This reduced size allows for the use of different experimental methods and the acquisition of additional information. Consequently, the wave field height measurements can be performed on the whole surface of the tank, using Schlieren imaging, leading to a robust estimation of wave reflection and transmission coefficient. Additionally, the fluid velocity field in the bulk can be assessed using Particle Image Velocimetry.

Several notable points emerge from those measurements. First, at small wave amplitudes, experimentally measured reflection peaks coincide with numerical predictions of so-called "wide" peaks. Furthermore, by comparing the reflection generated by flexible plates to the case of a rigid plate of the same dimensions, it becomes apparent that the reflections are due to flexibility. Finally, at large wave amplitudes, a jet is generated by the plate. This jet, could be responsible for a change in the average position of the plate, leading to total wave energy dissipation for the least rigid plate.

List of Symbols

Roman letters

A	Incoming wave amplitude
a	Plate half-length
b	Plate width
b_t	Tank width
B', b'	Wave-maker amplitude of motion
c_g	Wave group velocity
c_φ	Phase velocity
d	Plate submergence depth
E	Plate Young's modulus
f	Wave frequency
f_n	Plate deformation modes
f_0	Plate natural frequency in the air
$f_{0\mathrm{ma}}$	Plate natural frequency in water
f_c	Resonance peak central frequency
F_p	Pressure force
g	Gravity
h	Bottom depth
I	Plate second moment of inertia
k	Wave vector
K_r	Reflection coefficient in energy
K_t	Transmission coefficient in energy
K_{rc}	Resonance peak central value
L	Plate length
l	Plate thickness
n_g	Optical index of glass
n_w	Optical index of water
n_pc	Polycarbonate optical index
P_w	Wave power
P_j	Jet power
R_n	Reflected waves amplitude
r	Ratio stiffness VS plate density
t	Time
TWA	Target Wave Amplitude
T_n	Transmitted waves amplitude
U	Flow speed
u	Checkerboard deformation
w	Plate displacement
w_mean	Plate mean position
w_ref	Plate reference position
x	Horizontal coordinate
z	Vertical coordinate

Greek letters

α	Jet angle
$\mathbf{\Gamma}$	Plate internal damping coefficient
Δ_i	Plate tip mean displacement
η	Free surface elevation
Ξ, ξ	Plate displacement from its mean position
ξ_n	Plate deformation modes amplitudes
$\hat{\xi}$	Plate normalized motion amplitude
λ	Wavelength
μ'	Plate added mass
ν	Wave internal dissipation
ρ_p	Plate density
ρ	Water density
σ_n	Wave-vector over the plate
$\mathbf{\Phi}$, ϕ	Flow potential
ω	Radial frequency

Remerciements

La soutenance de ma thèse a été une belle occasion de réunir toutes les personnes qui me sont chères. J'avais préparé pour cette occasion un discours pour les remercier de vive voix. Cette partie remerciement du manuscrit est simplement une retranscription de ce discours afin de garder une trace écrite de cette belle journée du 9 novembre 2023 qui a conclue trois années de thèse riches en émotions, en rencontres et en abnégation.

Thank you.
First of all, I would like to thank the members of the jury for accepting to review my work and and doing it so carefully. Now, I would like to switch back to French to thank the people I've worked with during those nice three years.
Pour commencer je souhaiterais remercier Ramiro et Benjamin de m'avoir accepté dans l'équipe Biomim. En sortie d'étude, je cherchais un espace de liberté pour explorer un sujet précis et y concentrer mes efforts, voir un peu ce que je pouvais faire en me concentrant sur un même sujet pendant longtemps. Tout au long de ma thèse, vous avez montré de la confiance à pousser les sujets que j'explorais ce que j'ai grandement apprécié. Je souhaitais ensuite remercier spécifiquement Alexis qui a été un membre essentiel de l'équipe pour faire ce projet. Au quotidien, tes compétences techniques et ainsi que l'intérêt que tu as montré pour le problème ont enrichi ma thèse, tant en termes d'idées pratiques que de prise de recul sur les phénomènes que j'observais.
Ensuite, il y a évidemment toute l'équipe Biomim qui a eu un impact fort sur ce travail ne serait-ce que parce que j'étais content d'aller au laboratoire tous les jours. Tristan et Baptiste, je vous mets un peu dans le même panier, on a commencé ensemble, et passé beaucoup de temps tous les trois notamment pendant un beau voyage en Grèce. Le temps que vous êtes capables de prendre pour aider les gens et votre rigueur de tous les jours m'a beaucoup appris et a participé au fait que je devienne docteur.

Vincent, on a commencé la thèse ensemble mais surtout j'ai l'impression qu'on l'a fini ensemble, au mois d'août à écouter de la musique alors qu'il commençait à faire nuit. Tu as été un soutien précieux pour ne pas se sentir seul et de pouvoir rigoler et se plaindre avec quelqu'un qui vivait la même chose au même moment. Désolé de t'avoir abandonné 1 mois avant la fin de ta rédaction pour partir en vacances.
Il y a aussi les gens qui étaient là avant. Enfin les gens, Roméo que j'ai regardé rédiger et qui a laissé un grand vide dans l'équipe en terminant sa thèse. Et les gens qui sont encore là pour les prochaines années, Gauthier, Camille et Diane, je suis heureux d'avoir pu partager votre quotidien et vous avoir au laboratoire a rendu le mien plus sympathique. Particulièrment, merci à toi Diane pour ton aide en fin de thèse et ton beau travail sur les manips de PIV qui a enrichi le mien.
Ce qui a rendu cette période plus sympathique, c'est aussi tous les gens du laboratoire qui y font régner une atmosphère de bienveillance et de bonne humeur. Les doctorants avec qui on a partagé des aventures et un cluster COVID. En particulier, merci à Chloé, Baptiste, Manon, Samantha, bon anniversaire, Renaud l'Ironman, Antoine, Gauthier, Juan, pour leur investissement pour faire vivre la vie de labo, à toute la team CROUS pour leur bonne humeur, leur ponctualité et pour tous ces repas partagés.
Je voudrais aussi remercier les chercheureuse du laboratoire qui sont toujours disponibles et qui font du PMMH un merveilleux lieu de recherche. A titre d'exemple, cette semaine j'ai demandé à Laurent, Etienne et Damien qui trainaient dans le couloir de venir assister à une de mes répétitions et ils ont tous dit oui avec le sourire pour prendre 2h de leur temps pour m'aider. Je voudrais remercier les ingénieurs de l'atelier qui se sont toujours rendu disponibles pour nous aider et particulièrement Amaury qui j'espère fait bonne usage du tablier du secret santa.
Finalement, passage obligé, de tous les remerciements, je souhaiterais remercier Fred et Claudette qui font un travail formidable pour l'organisation du laboratoire. Vous nous accueillez toujours avec beaucoup de bonne humeur et nous rendez la vie tellement facile alors que le CNRS semble faire beaucoup de choses pour vous la compliquer.
Cela fait un moment que je parle, donc je vais remercier brièvement une première fois, mes amis, ma famille et Alice qui sont tous là aujourd'hui pour leur soutiens et leur amour. Et je vais libérer tout le monde pour commencer ce buffet et déboucher le champagne. Je reprendrais la parole après quelques coupes pour continuer.

Bon maintenant beaucoup d'entre vous vont découvrir que j'aime beaucoup les discours, prenez rapidement une coupe ou de quoi manger parce que ça va être long. J'ai déjà parlé un moment tout à l'heure pour remercier les gens avec qui j'ai travaillé directement et qui m'ont

énormément apportés au cours de ces trois ans. Mais faire cette thèse n'aurait pas été un aussi bon moment si je n'avais pas été plus globalement, très bien entouré. Comme j'ai dit tout à l'heure, je suis arrivé en thèse, fatigué d'être assis en amphi, passif à réviser pour des exams et avec l'envie de laisser libre cours à ma curiosité, pour voir un peu ce que je pouvais faire si on me laissait un peu de temps à chercher un problème. Quand je regarde ce que j'ai fait pendant ces trois ans je suis fier du travail que j'ai accompli. J'ai appris énormément de choses et surtout j'ai l'impression d'avoir fait parmi les choses les plus dures que je n'ai jamais réalisées. Le fait d'avoir fait preuve d'abnégation pour résoudre des problèmes et surmonter des périodes de doutes où on se réveille au milieu de la nuit en se disant que ça ne marchera jamais et réussir à la fin à trouver des solutions ça en vaut largement la chandelle.

Mais réussir à faire cela ça nécessite d'avoir environnement qui est là pour vous soutenir et vous aérer l'esprit. Et cet environnement, je dois dire que je suis chanceux de l'avoir ce qui m'assure une bonne humeur quasi quotidienne. On a peu d'occasion dans la vie d'avoir en face de soi la plupart des personnes qui nous sont chères pour leur dire à quel point elles participent à rendre la vie meilleure et nous aident, juste par le fait de les cotoyer, à accomplir de belles choses. Donc je tenais à prendre le temps de remercier toutes les personnes dont je suis proche car la réussite de cette thèse c'est aussi un peu la vôtre. En commençant par les plus récents, les PUCistes, que je vois plutôt régulièrement ces deux dernières années et avec qui j'ai pu découvrir ce beau sport qu'est le triathlon. C'est aussi un environnement accueillant de gens différents mais tous accueillant et toujours ravis de partager des bons moments jusqu'à aller explorer la Bourgogne pour m'accompagner dans mon boycott du triathlon de Paris, merci beaucoup ça me touche que vous soyez là.

J'ai ensuite 3 groupes d'amis qui me servent de piliers. Par ordre inversement chronologique :

Les 5/2 (tu vois Eve-Line c'est pour ça qu'avoir un nom de groupe c'est important c'est nul de dire ça dans un discours). Eve-Line, Léna, Ugo, Joël, William, Miléna, Tanel, grâce à Joël, j'ai déjà eu l'occasion de dire très récemment tout le bien que je pense de vous. Mais ça ne fait pas trop mal de se répéter. Vous faites tous et toutes des choses extraordinnaires et votre approche de la vie m'apporte énormément. Je voudrais aussi remercier particulièrement Léna et Eve-Line avec qui nous avons pu partager des expériences de thèse m'a permis de mettre en perspéctive ce que je faisais.

Les Narvalos ensuite. Dinh Phi, Iona, Manon, Thibaut, Hector, Tanel (pour le gens qui se poserait la question, c'est le même Tanel que tout à l'heure). Vous m'apportez aussi toujours énormément. Notamment la course à pied et par extension le triathlon me vient de vous et des première courses que l'on a faites ensemble jusqu'à la tradition des ekidens.

Les princes du kebabs un nom qui comme on l'entend maintenant revient de loin puisqu'on

se connait depuis plus de 20 ans et le CE2/CM1 avec Florence. Comme vous êtes des grands de CM1 quand moi j'étais un petit de CE2, vous avez toujours eu un coup d'avance sur moi. Vous regardez m'a guidé tout au long de mes études et m'a permis notamment en prépa de gagner énormément de temps. Je vous dois beaucoup pour ça et nos franches rigolades sur des choses qui ont eu lieu il y a plus de 10 ans ont quelque chose de rassurants qui apportent à ma vie une sensation de stabilité. Il y a 1000 personnes que je voudrais remercier individuellement, Marlone, Thibaut, Baptiste, Gabriel merci d'être là dans ma vie. Cette thèse, même si je n'aime pas trop ce statut étudiant, car j'ai tout de même eu l'impression de travailler, c'est aussi l'aboutissement de mes études. Et des études longues puisque j'ai maintenant 28 ans. Et tout au long de ces études j'ai pu compter sur le soutien inconditionnel de toute ma famille qui a tout déployé pour me faciliter la vie. Plus particulièrement, je voudrais remercier Dadou et Mamé, qui m'ont gardé et pendant la plupart des vacances scolaires et qui m'ont transmis des valeurs fortes de goût du travail et de réussite qui m'ont servi de moteur tout au long de mon parcours scolaire. Je voulais aussi remercier Arthur, mon frère, tu es d'une maturité impressionante et malgré le fait que je sois le plus vieux j'apprends beaucoup à ton contact. Te savoir dans ma vie a quelque chose de rassurant et m'apporte de la sérénité, un peu à la manière des Princes du Kebabs, celle d'une relation que le temps n'atteint pas et qui durera pour toujours. Finalement, il y a mes parents. Papa Maman il est très clair que je n'aurais jamais été dans cette salle devant tout ce monde sans votre investissement quotidien. Vous m'avez toujours poussé et surtout accompagné à aller chercher la réussite par les études. Et cette thèse n'aurait jamais vu le jour si vous n'aviez pas pris le temps de m'accompagner dans chacun de mes choix. Cette thèse à ce titre c'est un peu la votre aussi. Et si moi j'ai eu le droit à des applaudissements tout à l'heure je pense que vous les méritez aussi et j'aimerais donc qu'on applaudisse maintenant mes parents. Quand j'ai pensé ces remerciements, je ne savais pas trop où parler de toi. Dans le travail, car finalement, tes conseils, tes schémas, tes réflexions ont directement enrichis ce travail. Dans les amis, car tu es surement ma meilleure amie, celle avec qui je rigole de tout et peut parler de tout. Dans la famille, car c'est bien ce que tu es maintenant après un peu plus de six ans de relations, une membre de ma famille. Je voulais donc parler de toi partout au long de ce discours mais finalement je me suis dit que non, ta place était bien à la fin pour conclure ces remerciements en tant que personne la plus importante de ma vie. Alice, ta présence au quotidien m'illumine, et comme nous nous le sommes dit après que j'ai rendu mon manuscrit, il n'était plus évident de trouver par quel mot se désigner chacun. Nous en sommes venus à coéquipier et coéquipière qui traduit pour ma part bien le fait que tu es là pour franchir n'importe quel obstacle devant nous. Pour reprendre les mots que tu m'as dit un jour, ce n'ai pas une demande mais juste une déclaration, j'ai hâte de te rejoindre à Chicago.

Résumé long en français

Introduction

L'interaction vague-structure est un domaine à la physique riche et aux applications nombreuses que ce soit pour la production d'électricité à faible émission de carbone ou pour la protection des côtes face à l'érosion. La récupération d'énergie des vagues présente de nombreux challenges causés par des conditions en mer (eaux salés, tempête...) et la concurrence d'autres énergies marines comme l'éolien offshore. De ce fait, de nombreux designs de convertisseurs d'énergie des vagues on vu le jour. Cependant, aucun n'est parvenu à s'imposer comme une solution industrielle durable à ce jour.

Parmi les designs envisagés, des convertisseurs basés sur l'oscillation de plaques flexibles pourraient offrir des perspectives intéressantes, de part, notamment, leur survavibilité. Dans ce cas, pourtant particulier, plusieurs utilisations des plaques flexibles sont envisagées. Par exemple, dans le cas du "Wave Carpet", une plaque flexible est placée submergée et attachée en plusieurs points au sol par des systèmes extracteurs d'énergie, qui permettent de produire de l'électricité à partir du mouvement de la plaque.

Dans ce contexte, cette thèse s'intéresse à l'interaction entre des vagues et une plaque élastique submergée. Dans toute cette étude, les plaques sont maintenues à leur bord d'attaque et laissées libre au bord de fuite, similairement à un drapeau. Le cas d'un drapeau dans un écoulement a été largement étudié, cependant son forçage par les vagues est encore peu renseigné et un des objectifs de ce travail est de palier à ce manque.

Ce travail peut être décomposé en deux parties. Dans la première, une description théorique de l'interaction entre des vagues et une plaque flexible submergée est présentée. Dans la seconde, l'interaction est étudiée expérimentalement. Contrairement à la plupart des études expériementales pour le développement de convertisseurs d'énergie des vagues, cette thèse se concentre sur un bassin de petite taille (de l'ordre de 2 m de long). Ce choix, qui représente

un certains challenge expérimental, permet d'utiliser des méthodes expérimentales spécifiques aux petites échelles (imagerie Schlieren, vélocimétrie par image de particule...) pour avoir des informations supplémentaires sur l'interaction vague-plaque.

Théorie de la houle linéaire

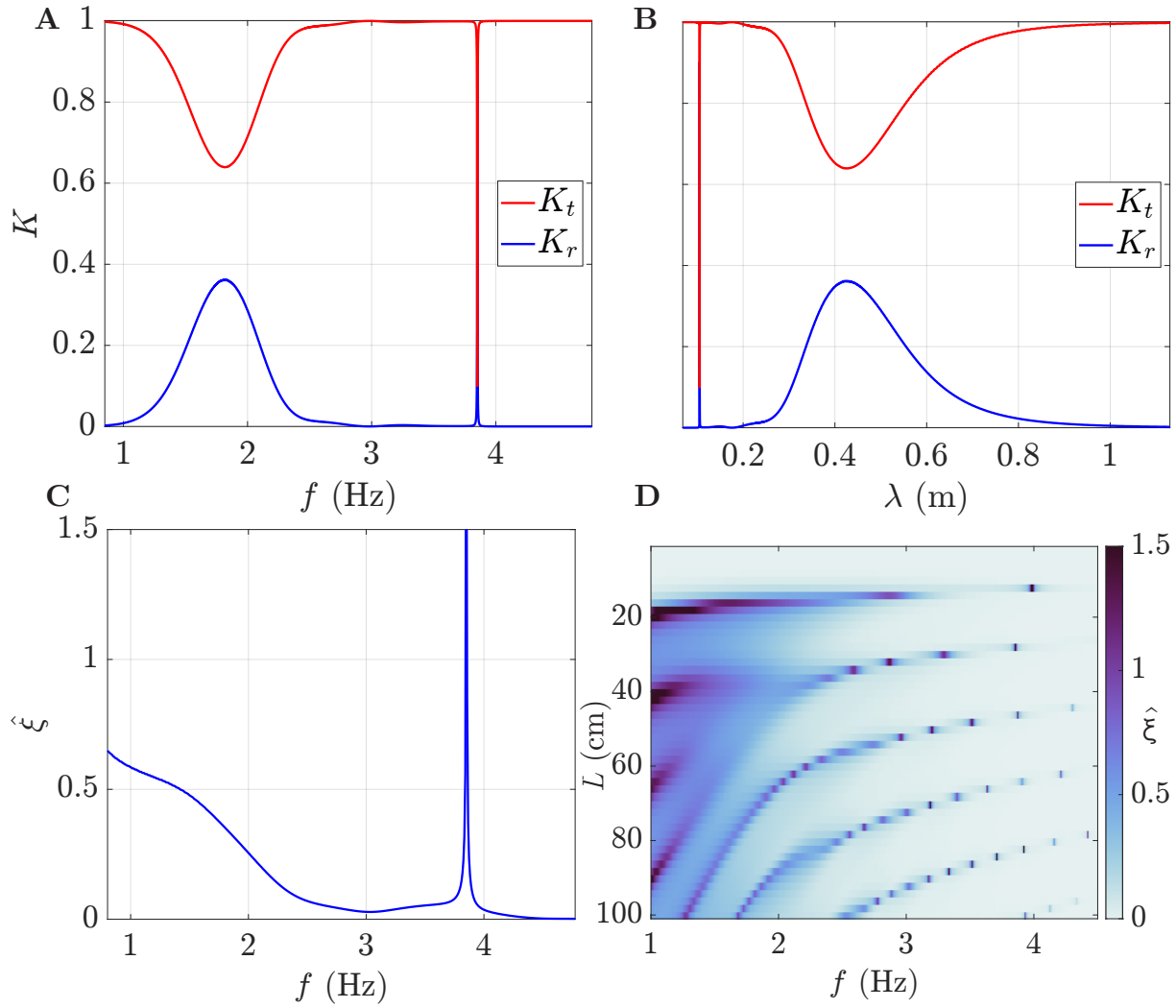

Figure 1: **A** Coefficients de réflexion et de transmission, K_r and K_t, en fonction de la fréquence des vagues, f. **B** Coefficients de réflexion et de transmission, K_r and K_t, en fonction de la longueur d'onde des vagues incidentes, λ. **C** Amplitude du mouvement de la plaque normalisée par l'amplitude de la vague incidente, $\hat{\xi}$, en fonction de la fréquence des vagues. **D** Diagramme longueur de plaque, L, fréquence, f, montrant l'amplitude du mouvement de la plaque normalisée par l'amplitude de la vague incidente, $\hat{\xi}$.

Pour ce faire, la théorie de la houle linéaire est utilisée. De manière synthétique, cette approche consiste à déterminer le potentiel, $\mathbf{\Phi}$, dans un domaine de fluide à deux dimensions. $\mathbf{\Phi}$ est défini comme :

$$\mathbf{u} = \boldsymbol{\nabla}\mathbf{\Phi},$$

et du fait de l'incompressibilité du liquide, $\mathbf{\Phi}$ est solution de l'équation de Laplace :

$$\Delta\mathbf{\Phi} = 0.$$

L'expression de $\mathbf{\Phi}$ dans le cadre spécifique du problème d'une plaque flexible attachée à son bord d'attaque est ensuite calculée en utilisant les conditions aux limites à la surface libre et sur les bords.
Le calcul de $\mathbf{\Phi}$ permet de déterminer l'amplitude des vagues réfléchies et transmises par la plaque subermergée, ainsi que le mouvement de la plaque. De ces calculs, les coefficients de réflexion et transmission, K_r et K_t, sont déterminés. Ils quantifient la part d'énergie transmise ou réfléchie par la plaque et permettent de caractériser l'interaction plaque-vague.
Afin d'illustrer les différents comportements observés, K_r et K_t sont calculés pour une plaque avec les propriétés indiquées en Table 1 et une profondeur d'eau de 10 cm: Figure 1 **A** **B**

Profondeur de la plaque	Longueur, L	Epaisseur	Largeur	Densité	Rigidité
5 cm	28 cm	1 m	10 cm	1200 kg.m^{-3}	8.10^{-2} N.m^2

Table 1: Propriétés de la plaque.

présentent les résultats de ces calculs pour différentes fréquences de vagues et longueurs d'onde respectivement. Il apparaît deux pics de réflexion. Un large qui se trouve entre 1 et 2.5 Hz (ou 0.2 et 0.8 m) et un pointu à 3.8 Hz. Ces deux pics illustrent les différentes types réflexion observées en variant les paramètres de simulation. Ces études paramétriques montrent que les deux sortes de pics sont de natures différentes.
Cette différence de nature transparaît clairement en regardant l'amplitude du mouvement de la plaque. Figure 1 **C** montre l'amplitude de mouvement de la plaque normalisée par l'amplitude de la vague incidente, $\hat{\xi}$ en fonction de la fréquence des vagues. A la fréquence du pic dit pointu, une claire résonance de la plaque apparaît, $\hat{\xi}$ augmente sensiblement. L'effet sur l'amplitude de la plaque est moins visible au niveau du pic large.
Finalement, des études paramétriques sont menées et soulignent la complexité de l'interaction. A titre d'illustration, Figure 1 **D** présente un diagramme montrant $\hat{\xi}$ pour différentes valeurs de longueur de plaque. Pour des plaques de moins de 20 cm, la plaque ne bouge pas. Cependant, pour des plaques plus longues, des motifs plus complexes sont observés. Cette

complexité est également soulignée par le fait que les paramètres exacts influençant les pics de réflexion ne sont pas clairs.

Méthodes et résultats expérimentaux

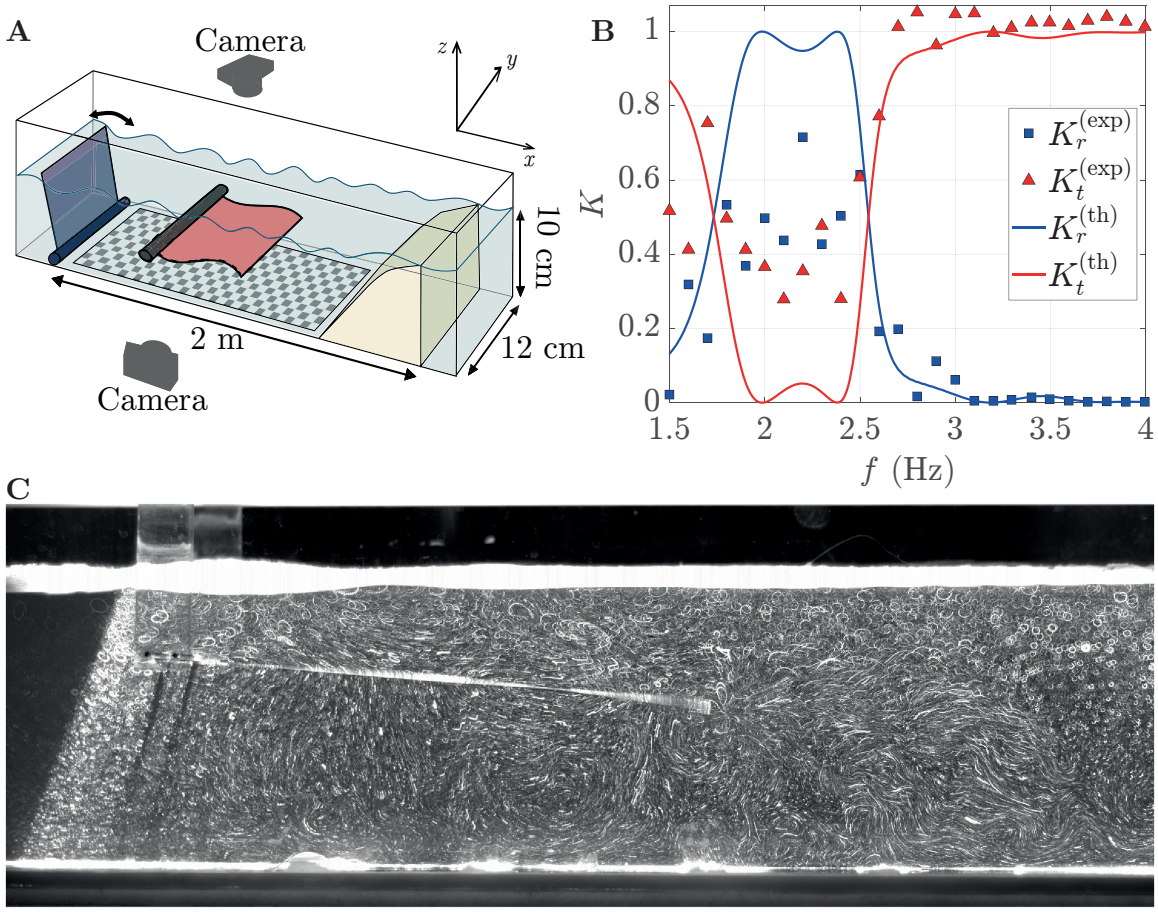

Figure 2: **A** Schéma du dispositif expérimental. **B** Coefficients de réflexion et de transmission expérimentaux (carré bleus et triangles rouges respectivement) et théoriques (lignes bleues et rouges) en fonction de la fréquence des vagues incidentes. Ces données sont obtenues pour une plaque en polycarbonate de 28 cm de long, d'épaisseur 0.75 mm et à une profondeur de 3 cm. **C** Image obtenue avec la vue de côté du canal après avoir placé des particules dans l'eau et montrant la trajectoire des particules. La plaque utilisée ici a une longueur de 19 cm, une épaisseur de 0.75 mm et est placée à une profondeur de 3 cm. Les vagues ont une fréquence de 3 Hz et les vagues une amplitude de l'ordre de 5 mm.

La seconde partie de cette thèse est consacrée à l'étude expérimentale de l'interaction vague-plaque. Pour cela, le dispositif expérimental schématisé Figure 2 **A** est utilisé. Les vagues sont produites en utilisant un batteur à clapet, représenté à gauche du schéma. Son oscilla-

tion produit des vagues qui se propagent ensuite le long du bassin. La plaque, schématisée en rouge, est placée au centre du bassin à une profondeur choisie sous la surface libre. Finalement, une plage, en beige sur la figure, est placée au bout du canal pour limiter la réflexion des vagues sur le mur au bout du bassin. Ces différents éléments permettent le forçage par des vagues d'une plaque flexible submergée. Le choix du matériau est crucial pour la conception des plaques. En effet, afin de rester relativement horizontale, la plaque doit avoir une densité proche de celle de l'eau et être suffisament rigide pour compenser les écarts de densité. Dans cette thèse, des plaques en polycarbonate ou en polypropylène sont utilisées.
Dans ce dispositif, les mesures sont faites en filmant avec des caméras. La première, située au dessus du bassin, permet de reconstruire le champ de vague dans le canal par imagerie Schlieren [Wildeman, 2018]. Cette reconstruction permet de déterminer l'amplitude des l'ondes incidentes, transmises ou réfléchies en fittant la hauteur déformation de la surface libre. La mesure de ces amplitudes permet de calculer les coefficients de transmission et réflexion.
La seconde caméra, placée sur le côté du bassin, a deux utilisations, suivre la déformation de la plaque ou observer l'écoulement en ajoutant des particules dans l'eau.
Figure 2 **B** montre les coefficients de réflexion et de transmission en fonction de la fréquence des vagues pour une plaque en polycarbonate de 28 cm de long, d'épaisseur 0.75 mm et à une profondeur de 3 cm. Les vagues incidentes ont une amplitude de l'ordre de 1 mm. Expérimentalement une claire réflection peut être observée entre 1.5 et 2.7 Hz. Cette zone de réflexion est bien prédite par le modèle théorique, cependant les valeurs de maximum de réflexion sont surestimée. Plusieurs facteurs peuvent expliquer cette différence, le fait que la plaque soit de largeur finie, sa position à l'équilibre qui n'est pas parfaitement horizontale ou la présence de non-linéarités. Similairement au modèle théorique, la réflexion est induite par une complexe interaction vague-structure et les facteurs exacts responsables de la réflexion des vagues ne sont pas clairs. Cependant, contrairement au modèle théorique, le dispositif expérimental permet de tester le cas d'une plaque rigide. Pour des plaques de même dimensions, aucune réflexion n'est observée dans ce cas. Cette observation met en évidence que c'est le mouvement de la plaque qui permet la réflexion.
De ces mesures de réflexion et transmission, il vient également que les plaques flexibles dissipent l'énergie des vagues. En effet, si l'énergie des vagues est conservée lors de l'interaction avec un objet, $K_r + K_t$ doit être égal à 1. Or, pour les plus basses fréquences, cette condition n'est pas toujours vérifiée. Afin d'examiner les causes de cette dissipation, des particules sont placées dans l'eau pour observer l'écoulement autour des plaques flexibles. Un exemple de résultat est présenté Figure 2 **C**. Cette image présente la trajectoire des particules observées à l'aide de la vue de côté du bassin. Dans un champ de vague sans objet, les trajectoires

des particules doivent être circulaires. Cependant, sur la Figure 2 **C**, les trajectoires au bout de la plaque sont plutôt droites, ce qui correspond à la création d'un jet en bout de plaque. Ce jet découle de processus non-linéaires qui sont de bons candidats pour expliquer la dissipation d'énergie des vagues. Cependant, un bilan d'énergie dans le jet montre que les pertes engendrées par sa création ne peuvent expliquer les dissipations observées. Ce jet a malgré tout des propriétés intéressantes puisque son orientation provoque des changement de position moyenne de la plaque. Dans le cas de la plaque la plus flexible en polypropylne, le changement de position est tel que le bout de la plaque peut atteindre la surface libre ce qui a pour effet d'amortir complètement les vagues.
Pour proposer des pistes pour fermer le bilan d'énergie, les particules sont suivies en regardant dans le plan xy. De ces films, il ressort une augmentation importante de la vitesse des particules entre les murs et la plaque ce qui pourrait engendrer de la dissipation supplémentaire.

Conclusion

Cette étude a donc mis en évidence une grande variété de phénomènes complexes et ouvre la voie à de nombreux travaux. Tout d'abord, la détermination exacte des causes de réflexion reste un problème ouvert qui semble riche. De plus, l'implémentation théorique de la production de vortex au bord de fuite de la plaque pourrait être un dévelopement intéressant dans l'optique d'évaluer correctement les dissipations des vagues par la plaque. Des mesures à plus grandes échelles pourraient également être utilisées pour valider les résultats expérimentaux présentés ici.

Table of contents

Chapter 1
Introduction

Figure 1.1: "La Vague", oil painting from 1869 by Gustave Courbet, exposed in the Musée d'art moderne André Malraux in Le Havre, France.

1.1 Wave energy potential

Gustave Courbet's painting "La Vague", ("The Wave"), depicts a seascape where ocean waves crash against a rocky shore. Here, the artist aims at transcribing the power of ocean waves. An aim which is brilliantly achieved by combining the visual effects of menacing clouds, shadows that emphasize the wave steepness, and the vulnerability of boats in the foreground. Wave power, that is forcefully sensible in this painting, represents a hazard for coastal areas. As waves break on the coast, they participate to erosion. Coastal towns and facilities must therefore protect themselves against the slow damages inflicted by sea waves. Protection is all the more crucial during storms, which can otherwise lead to significant floods. However, the relentless back-and-forth motion of the waves also offers opportunities for electricity production, what could be a blessing for human societies, facing climate change and trying to find low carbon energy sources.

1.1.1 Wave Energy Converters

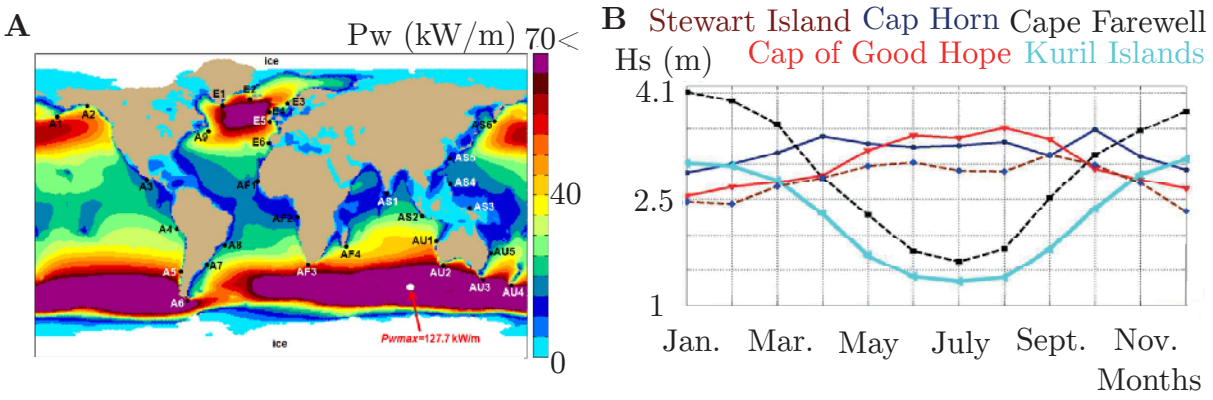

Figure 1.2: **A** World map wave of power density, Pw, from [Rusu and Onea, 2017]. **B** Monthly-averaged significant wave-hieght (Hs) variations for five locations, also from [Rusu and Onea, 2017]

The potential of ocean waves as an electricity source is undeniable. Worldwide wave-based electricity production potential is estimated at 32 000 TWh per year. As a comparison, it is more than the global electricity consumption in 2019, that was estimated at 23 921 TWh by the U.S. Energy Information Administration (EIA) ([Sheng, 2019], [Mork et al., 2010], EIA [2019]). As highlighted in a 2014 report by SIOcean [2014] (Strategic Initiative for Ocean Energy), wave power plants could represent a larger market than offshore wind turbines by

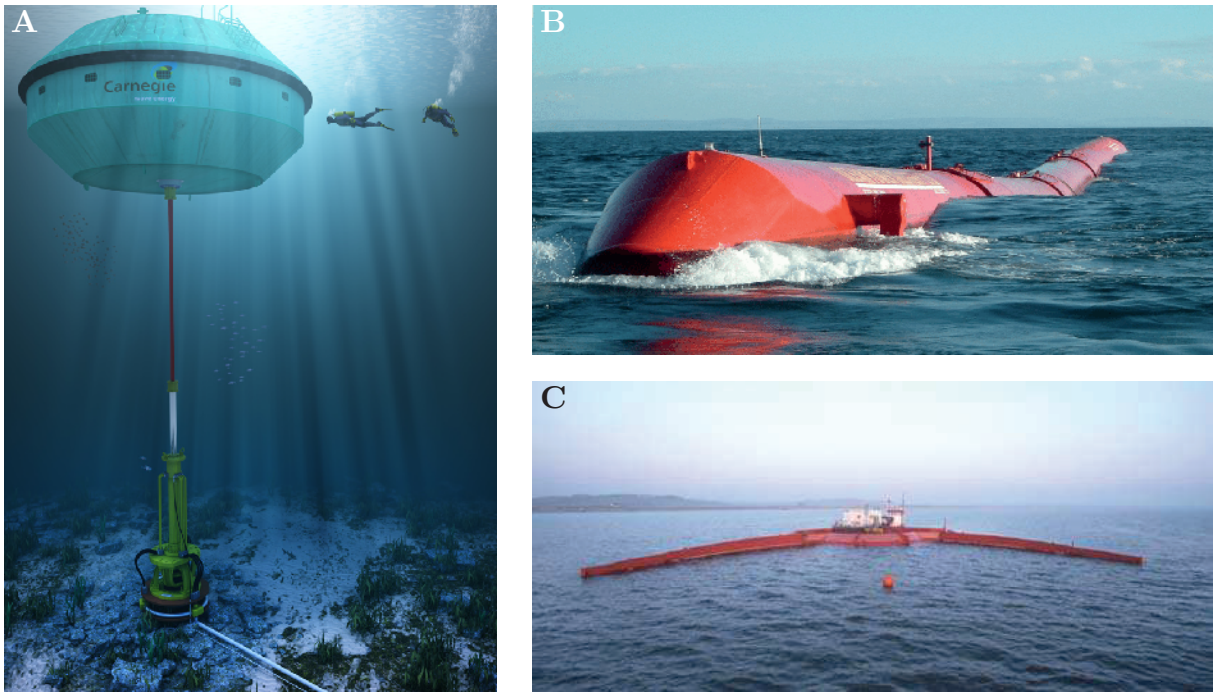

Figure 1.3: **A** Artist view of the CETO 3 device, from [wikipedia.org, 2023]. **B** Picture of the Pelamis device, from Mercier [2019]. **C** Picture showing the Dragon Wave Energy Converter.[Tedd et al., 2006].

2050. Indeed, harnessing wave energy offers multiple advantages compared to wind or even solar energy. Wave energy does not suffer from day/night intermittency. Furthermore, it shows a relatively high energy density, meaning that significant amount of energy could be extracted from relatively small plants [Lehmann et al., 2017]. However, as shown in Figure 1.2 **A**, wave power distribution heavily depends on the geographical location. Therefore, the development of wave energy converters (WEC) is particularly attractive for countries located between 40 and 60 degrees latitude, both North and South. Southern latitudes hold an advantage due to reduced seasonal variations, as depicted in Figure 1.3 **B**.

Different types of systems can be distinguished in order to harness wave energy. There are different classifications for WECs, but one way to get a good overview of existing systems could be to consider: point absorbers, attenuators, pressure-driven, terminators WECs, as stated by Rusu and Onea [2017] and Collins et al. [2021]. Point absorber systems are the most intuitive. Typically, they involve buoys anchored to the seabed that oscillate with the waves. A power take-off system, then, converts this motion into electricity. One of the most advanced point absorber systems is the CETO developed by Carnegie, illustrated in Figure 1.3 **A**.

Attenuator devices are among the most iconic wave energy systems, with Pelamis receiving significant media attention during its development between 2004 and 2014. Attenuator sys-

tems operate similarly to point absorbers, utilizing the vertical motion created by waves to generate electricity. However, unlike point absorbers, they are spatially extended. They are positioned perpendicular to the waves, as shown in Figure 1.3 **B**, and absorb wave energy over tens of meters.

Terminator systems face the waves and feature more innovative designs, exploiting alternative methods to harness wave energy. For example, some systems, called overtopping devices, use artificial beaches to amplify wave amplitudes, causing them to break and allowing the capture of slightly elevated water in a reservoir. The reservoir can be emptied and directed toward a turbine. The Wave Dragon system is based on such a principle, as shown in Figure 1.3 **C**. It utilizes arms to channel waves towards the beach, where a reservoir is located. Oscillating water column devices are also terminators systems and consist in cavities placed on the water surface. The passage of waves compress and expand the air volume within the cavity, causing pressure changes that drive a turbine as air enters and exits the cavity. Those systems are often located along coastlines where the wave direction is relatively constant due to refraction and to let the infrastructure and power conversion system built on-shore.

Pressure differential systems are based on pressure variations created by the waves. As the waves propagate in the sea, they induce pressure changes due to water elevation and flow speed. Induced pressure gradients will create a force on the objects, causing them to move. Object motion can, then, be exploited to produce electricity. For many pressure differential Wave Energy Converters (WECs), pressure differences are used to activate flexible membranes (see [Babarit et al., 2017] for instance).

Finally, in addition to the previous categories, WECs relying on the lift force, created by the relative speed between the structure and the wave flow, are under development. The LiftWEC project is an example of such a WEC. It is based on a turbine producing electricity by rotation. In the LiftWEC system, a rotor is set in motion thanks to foils, placed so that a lift force is created by the wave flow. No WEC concept based on lift has yet reached an industrial level yet but they could offer interesting performance according to Folley and Lamont-Kane [2021] or Lamont-Kane et al. [2021].

This wide variety of wave energy converter types is unfortunately explained by the inability to establish a clear efficient design. As underlined by Roche et al. [2019], WEC development is facing a huge challenge, as industrial constraints impose to be cost-effective at an early development stage, what is in contradiction with the very nature of this technology development, which requires costly experimental campaigns, in wave-tanks or at sea. In addition, wave energy suffers from the comparison with other marine energies as offshore wind. An idea to overcome this problem is to build combined plants, extracting electricity from both offshore wind and waves [Kalogeri et al., 2017].

1.1.2 Flexible WEC designs

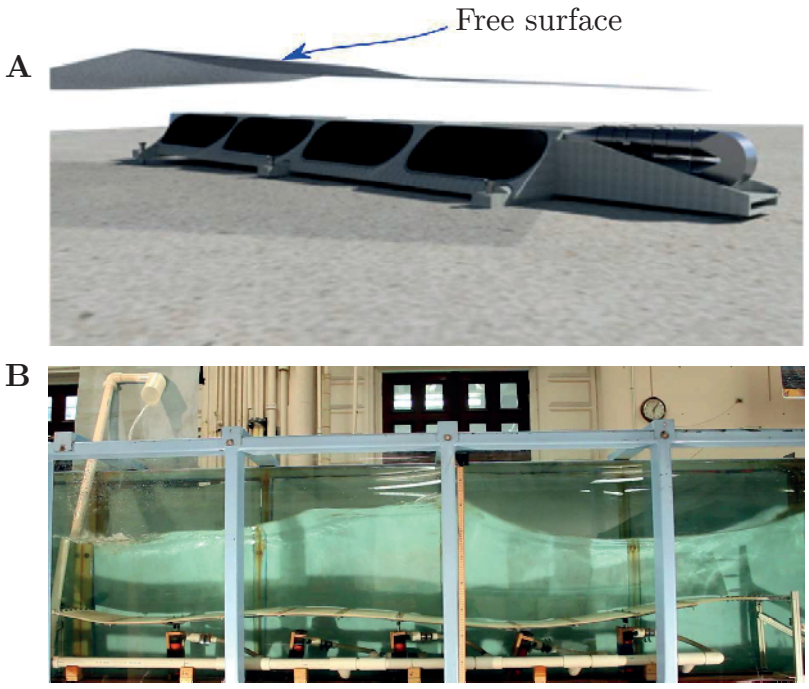

Figure 1.4: **A** View of the Bombora Wave Power by Algie et al. [2017]. Elastic plates are represented as a darker area on the structure. They are placed between the air cavity and a concrete structure placed on sea bottom in gray. The free surface is represented as a blue sheet. **B** Picture taken by Lehmann et al. [2013] conducting experiment with the wave carpet. The Carpet is hinged at the bottom of the tank.

The previous section highlights the wide variety of existing WECs. However, effective industrial solutions are still to be found or are under development. From observations in nature, plants such as kelp contribute to wave attenuation in coastal areas and can withstand high storm forces. Using flexible objects as efficient wave attenuators could be a route to wave-based electricity generation [Luhar et al., 2017] [Nové-Josserand et al., 2019].
In practice, using flexible structures already offers interesting perspectives for the development of new efficient WEC designs. As underlined by Renzi et al. [2021], flexible WECs observe a fast development thanks to progress in material science. For instance, using electro-active polymers or piezo-electric materials would be appropriate to convert the mechanical deformation into electric power.
Collins et al. [2021] show that numerous flexible WECs are based on converting the motion of elastic plates into electricity. Elastic plates are mainly used in two different configurations.

In pneumatic cells, the elastic plate is located at the interface between water and an air-filled cavity. Under the effect of waves, the plate oscillates and pumps the air in the cavity, creating an air flow. The induced air flow is then utilized to produce electricity. The Bombora mWave represented in Figure 1.4 **A**, is a typical example of a pneumatic cell WEC.
Wave-induced plate motion can also be used directly to produce electricity. The WEC category utilizing this concept is called the "Tethered Carpet" by Collins et al. [2021]. Two prototypes are listed in their work, the CalWave Wave Carpet and the Lilypad. The LilyPad is constituted of two parallel plates, one at the surface and the other submerged below the first one. It works as an attenuator, and electricity is produced thanks to the relative motion of the two plates, using piston-like Power Take Off systems.
The CalWave Wave Carpet is, more simply, composed of a single plate hinged to the seafloor. Due to pressure differences along its length, the plate oscillates and electricity can be generated from that motion. Electricity is produced in a similar way as for the LilyPad, with piston-like Power Take Off systems placed between the carpet and the sea floor.
In summary, elastic plates could form the core principle of efficient, innovative WEC concepts. They are at the center of this thesis.

1.2 Thesis description

1.2.1 Thesis purpose

This thesis is set in the context of wave energy harvesting and focuses on studying the behavior of an elastic plate under wave forcing. More precisely, this work aims at characterizing the behavior of a horizontal elastic plate clamped at only one edge. In contrast to the CalWave Wave Carpet, which is clamped at both edges, the down wave edge remains free in this thesis. Similar systems are already used to harvest river flow energy ([Allen and Smits, 2001], [Taylor et al., 2001]). However, considering their potential application as a WEC is a more recent project. Shoele [2023] modeled a piezo-electric plate clamped at one edge to be a potential hybrid flow and wave energy harvester.
One of the original features of this thesis, from a wave-structure interaction point of view concerns the size of the experimental set-up developed. Most of the experimental investigations dealing with wave energy are performed in relatively large facilities (see [Ning et al., 2016], [Ning et al., 2019] or [Orer and Ozdamar, 2007] for instance). One of the purposes of this thesis is to show that interesting characterizations can also be performed at smaller scales even though technical difficulties may arise, which will be thoroughly discussed.
In addition, working with an elastic plate clamped at one edge allows this work to be at

the frontier of wave-structure and fluid-structure interaction. Indeed, from a more academic perspective, this thesis revisits a classic fluid-structure interaction problem. Elastic plates clamped at one edge in a flow are the subject of an abundant literature (see [Shelley and Zhang, 2011] for instance). Most of the previous studies have been either performed in a still fluid or in a uniform, constant flow. This work finally consists in changing the forcing by investigating the effect of waves on the elastic plate. Working at the frontier between those two communities is an opportunity to enrich this thesis, by combining the different approaches to address a scientific question. In the end, a variety of rich and complex phenomena arise from this combination.

1.2.2 Thesis outline

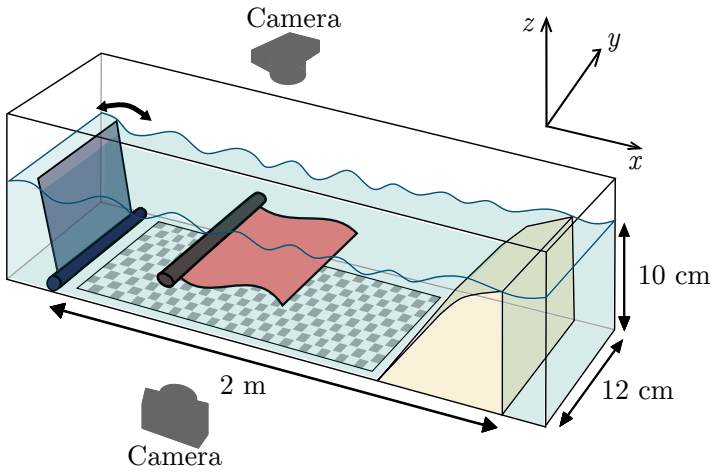

Figure 1.5: Sketch of the experimental set up. On the left, the flap-type wave-maker used to generate waves is pictured. The plate is placed at the tank center. Its up-wave edge is clamped. A parabolic beach is placed at tank end to break waves. Data is extracted by filming from the top and the side of the tank.

The main theoretical tools to understand the wave-plate interaction, and a more precise literature review on existing work, are given in Chapter 2. First, a description of water waves is given. Then, their interaction with objects in general is described. Finally, a description of elastic plates and their interaction with waves is presented.
From that work, it appears that linear wave theory is an efficient and well-established tool utilized to characterize objects interaction with waves. Consequently, in order to get a first view on the plate behavior in a wave field, Chapter 3 proposes a two dimensional linear model of a clamped at one edge submerged elastic plate under wave forcing. In this Chapter,

reflection and transmission coefficients are computed together with the plate motion response for various parameters, showing a wide variety of complex behaviors.

Chapter 2 also highlights that few experimental works are dedicated to the study of elastic plates in a wave field. Chapter 4 describes the experimental set-up designed to address this shortcoming and the different experimental methods used. As sketched in Figure 1.5, the tank used is 2 m long and 12 cm wide. Taking advantage of the set-up small size, specific experimental methods can be deployed. Data is extracted by filming from the top and the side of the tank. The top view enables free surface deformation reconstruction by using Schlieren imaging (see [Wildeman, 2018]). The side view is utilized to, either, follow plate motion or to perform flow field reconstruction by Particle Image Velocimetry (PIV) (see [Raffel et al., 1998] for instance), depending on the experiment.

Chapter 5 presents the results obtained, first, for small amplitude waves, and, second, for higher amplitudes. Similarly to computations from Chapter 2, reflection and transmission coefficients are measured together with the plate motion response. Those measurements show that the plate flexibility can induce significant wave reflection. However, calculating the wave energy balance shows that elastic plates are also able to remove energy from the waves. To investigate dissipation mechanisms, PIV experiments are performed, and reveal the presence of a jet at the plate tip and complex three dimensional flows.

Chapter 2

Submerged elastic plate in a wave field

This Chapter gives more technical details and notions on concepts that will be used in Chapters 3, 4 and 5. First, Section 2.1 focuses on water waves and their interaction with structures in general. Then, in Section 2.2, elastic plates are described and their behavior in a still fluid or a uniform flow is investigated. Finally, the more specific problem of submerged plates in a wave field is discussed.

2.1 Generalities on wave structure interaction

2.1.1 Linear wave theory

The simplest mathematical theory to describe the evolution of freely propagating waves was proposed by Airy [1845] and consists of a linear model of wave motion. Despite its simplicity, this model remains accurate and is still widely used, particularly for numerical simulation or predicting the behavior of energy converters.

The following development can be found in most of the books dealing with water waves (see Mei et al. [2005] or Holthuijsen [2010] for instance). As shown in Figure 2.1, it is considered that water occupies a domain between the seabed at $z = -h$ and the free surface at $z = 0$. The fluid perturbation is assumed to be monochromatic, plane waves propagating in the x direction only. Focusing on only one propagation direction allows to consider the problem in the xz-plan and invariant along y. The free surface deformation is denoted as η, its wavelength as λ, and its angular frequency as ω. The classical equations of fluid mechanics describe the velocity field, $\mathbf{u}$, throughout the domain. Given the velocities and the pressures observed, the fluid is considered incompressible, implying that its mass density, ρ, is constant in time and space. Therefore:

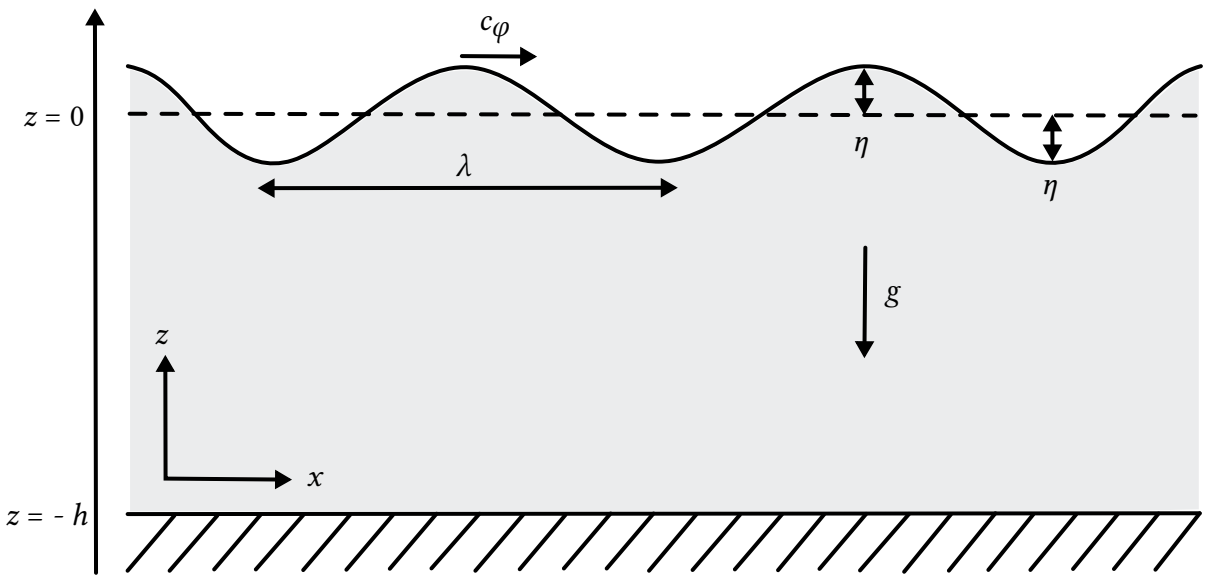

Figure 2.1: Schematic view of the two-dimensional linear problem. z stands for depth, x for location in the wave propagation direction, η for the free surface elevation. Bottom depth is located at $z = -h$. λ is wave wavelength, c_φ represents wave phase velocity and indicates wave propagation direction. Water is represented in gray and air in white.

$$\boldsymbol{\nabla}.\mathbf{u} = 0. \tag{2.1.1}$$

The fluid is assumed irrotational across the whole domain. As stated in Mei et al. [2005], if vorticity is zero at time 0, there can be no creation of vorticity. Considering a fluid initially at rest and subsequently subjected to waves, the wave flow is thus non-rotational. The equation governing the evolution of the velocity field $\mathbf{u}$, in time and space, is the Navier-Stokes equation:

$$\rho(\partial_t \mathbf{u} + (\mathbf{u} \cdot \boldsymbol{\nabla})\mathbf{u}) = -\boldsymbol{\nabla} P + \rho \mathbf{g} + \nu \Delta \mathbf{u}. \tag{2.1.2}$$

Here, ρ is the fluid mass density, t is time, P is pressure within the fluid, $\mathbf{g}$ is gravity, and ν is the kinematic viscosity of water which is, approximately, 10^{-6} m^2.s^{-1}.
The characteristic speed of waves, c_φ, with a wavelength of $\lambda = 1$ m, is approximately 1 m/s. Consequently, the Reynolds number for this flow is:

$$Re = \frac{c_\varphi \lambda}{\nu} = 10^5. \tag{2.1.3}$$

The last term in the Navier-Stokes equation (2.1.2) can thus be neglected, and the fluid can be treated as ideal.

The scalar potential, $\mathbf{\Phi}$, associated with the velocity field, $\mathbf{u}$, is then introduced to simplify the mathematical description of waves. By definition:

$$\mathbf{u} = \boldsymbol{\nabla}\mathbf{\Phi}. \tag{2.1.4}$$

The Laplace equation, describing the flow in terms of the potential throughout the domain is obtained by injecting this expression into (2.1.1), yielding:

$$\boxed{\Delta\mathbf{\Phi} = 0}. \tag{2.1.5}$$

From the Navier-Stokes equation (2.1.2), the Bernoulli's equation is derived by integrating with respect to space:

$$\boxed{-\frac{P}{\rho} = gz + \partial_t\mathbf{\Phi} + \frac{1}{2}|\boldsymbol{\nabla}\mathbf{\Phi}|^2}. \tag{2.1.6}$$

Note that the integration introduces a spatial constant, which is incorporated into the potential, $\mathbf{\Phi}$.

Boundary Conditions

Solving this problem also requires knowing the kinematic and dynamic boundary conditions at the bottom and surface. At the bottom, $z = -h$, the no-flow condition gives, for a flat bottom:

$$\boxed{\partial_z\mathbf{\Phi} = 0 \quad (z = -h)}. \tag{2.1.7}$$

Then, at the free surface for $z = \eta$, the kinematic condition is obtained by noting that the fluid velocity is the same as that of the interface at the surface. Hence:

$$\mathbf{u} \cdot \mathbf{n} = \mathbf{V} \cdot \mathbf{n} \text{ for } z = \eta. \tag{2.1.8}$$

Here, $\mathbf{n}$ is a unit normal vector to the surface, and $\mathbf{V}$ is the interface velocity. An expression of $\mathbf{n}$ in Cartesian coordinates is needed to express the left-hand side of the equation. For this purpose, it is observed that the two tangent vectors to the surface can be written as follows:

$$\mathbf{t}_1 = \cos(\partial_x\eta)\mathbf{e}_x - \sin(\partial_x\eta)\mathbf{e}_z \quad ; \quad \mathbf{t}_2 = \cos(\partial_y\eta)\mathbf{e}_y - \sin(\partial_y\eta)\mathbf{e}_z. \tag{2.1.9}$$

Here, $\mathbf{t}_1$ and $\mathbf{t}_2$ are two tangent vectors to the surface. Approximating for small angles:

$$\mathbf{t}_1 = \mathbf{e}_x - \partial_x\eta\mathbf{e}_z \quad ; \quad \mathbf{t}_2 = \mathbf{e}_y - \partial_y\eta\mathbf{e}_z. \tag{2.1.10}$$

Finally, $\mathbf{n}$ is expressed as the vector product of these vectors, yielding:

$$\mathbf{n} = -\partial_x \eta \mathbf{e}_x - \partial_y \eta \mathbf{e}_y + \mathbf{e}_z. \tag{2.1.11}$$

Thus:

$$\mathbf{u} \cdot \mathbf{n} = \partial_z \Phi - \partial_x \Phi \partial_x \eta - \partial_y \Phi \partial_y \eta. \tag{2.1.12}$$

Furthermore, assuming vertical fluid displacements:

$$\mathbf{V} \cdot \mathbf{n} = \partial_t \eta. \tag{2.1.13}$$

Hence, the kinematic boundary condition at the surface is:

$$\boxed{\partial_t \eta + \partial_x \Phi \partial_x \eta + \partial_y \Phi \partial_y \eta = \partial_z \Phi. \quad (z = \eta)} \tag{2.1.14}$$

Finally, the dynamic condition at the free surface is obtained by applying Bernoulli's equation (2.1.6) at the surface:

$$\boxed{\frac{P_0}{\rho} = g\eta + \partial_t \Phi + \frac{1}{2}|\nabla \Phi|^2 \quad (z = \eta)}. \tag{2.1.15}$$

Pressure P_0 corresponds to atmospheric forcing. By combining the kinematic and dynamic conditions at the surface, an equation involving Φ and $\mathbf{u}$ is obtained by considering constant atmospheric pressure at the interface:

$$\partial_t^2 \Phi + g \partial_z \Phi + \partial_t \mathbf{u}^2 + \frac{1}{2}(\mathbf{u} \cdot \nabla)\mathbf{u}^2 = 0, \text{ at } z = \eta. \tag{2.1.16}$$

This equation clearly separates linear terms from non-linear terms. Although all the equations previously written are clearly non-linear, their linearization results in physically interesting and sufficiently accurate results for a rich wave description. The physical parameter quantifying the non-linearities is the wave steepness, $\epsilon = kA$, with k being the wave vector magnitude and A the wave amplitude. A development to order 0 in steepness gives Airy's model, which consists of the linearized equations together with the linearized boundary conditions:

$$\Delta \Phi = 0 \ \forall x, z, t, \tag{2.1.17}$$

$$\partial_z \Phi = 0 \text{ at } z = -h \text{ and } \forall x, t, \tag{2.1.18}$$

$$\partial_t \eta = \partial_z \Phi \text{ at } z = 0 \text{ and } \forall x, t, \tag{2.1.19}$$

$$\partial_t \Phi + g\eta = -\frac{P_0}{\rho} \text{ at } z = 0 \text{ and } \forall x, t. \tag{2.1.20}$$

This system of four equations allows the determination of numerous wave properties. For monochromatic waves, η is given by:

$$\eta = A\cos(\omega t - kx + \varphi), \tag{2.1.21}$$

where A is the wave amplitude, ω is the wave angular frequency, and φ represents a phase. Considering harmonic and steady state motion complex notations are utilized from here to ease calculation. Complex wave amplitude $\underline{\eta}$ is defined as:

$$\underline{\eta} = \underline{A}.\exp(ikx), \tag{2.1.22}$$

and is related to η by:

$$\eta = \mathrm{Re}(\underline{\eta} e^{-i\omega t}). \tag{2.1.23}$$

In the following, all underscored quantities correspond to complex amplitude, assuming harmonic motion. Physical, real quantities are obtained through equations analogous to Equation (2.1.23).

Potential expression over a constant depth

The expression of complex potential amplitude, $\underline{\phi}(x, z)$, can be determined thanks to separation of variables and considering harmonic forcing. Separation of variables is a method used, notably, to solve heat diffusion or the Melde's experiment problems, see [Sanz et al.] for example. $\underline{\phi}(x, z)$ can be written:

$$\underline{\phi}(x, z) = \underline{F}(x)\underline{G}(z). \tag{2.1.24}$$

By injecting the latter expression in Equation (2.1.5), it is obtained that:

$$\frac{\underline{F}''}{\underline{F}}(x) = -\frac{\underline{G}''}{\underline{G}}(z), \tag{2.1.25}$$

where superscript $'$ stands for the derivative. Written in that form, a function of x ($\underline{F}''/\underline{F}$) is equal to a function of z ($\underline{G}''/\underline{G}$). It implies that both those functions are constants of x and z:

$$\frac{\underline{F}''}{\underline{F}}(x) = -\frac{\underline{G}''}{\underline{G}}(z) = -\underline{k}^2, \tag{2.1.26}$$

where $\underline{k}$ is a constant of x and z, which will be found to be the wave wavenumber. From here F and G are differential equation solutions:

$$\underline{F}'' + \underline{k}^2\underline{F} = 0 \text{ and } \underline{G}'' - \underline{k}^2\underline{G} = 0, \tag{2.1.27}$$

and the complex potential can be written:

$$\underline{\phi} = (\underline{A}_0 \exp(i\underline{k}x) + \underline{B}_0 \exp(-i\underline{k}x))(\underline{C}_0 \cosh(\underline{k}(z+h)) + \underline{D}_0 \sinh(\underline{k}(z+h))), \tag{2.1.28}$$

with $\underline{A}_0$, $\underline{B}_0$, $\underline{C}_0$ and $\underline{D}_0$ being constants. $\underline{D}_0$ can be determined using the no penetration condition on the bottom, Equation (2.1.18). It is obtained that either $\underline{D}_0$ or $\underline{k}$ must be equal to 0. Since $\underline{k} = 0$ does not corresponds to a propagative wave this solution is physically excluded and $\underline{\phi}$ is written:

$$\underline{\phi} = (\underline{A}_1 \exp(i\underline{k}x) + \underline{B}_1 \exp(-i\underline{k}x)) \cosh(\underline{k}(z+h)), \tag{2.1.29}$$

with $\underline{A}_1$ and $\underline{B}_1$ equal to $\underline{A}_0\underline{C}_0$ and $\underline{B}_0\underline{C}_0$, respectively. The term of complex amplitude $\underline{B}_1$ corresponds to waves propagating respectively forward and backward. In the case considered here, a single wave propagating along forward in the x direction implies $\underline{B}_1 = 0$. However, in many wave-structure interaction cases, reflected waves have to be considered and consequently, amplitude of waves propagating will be different than 0. $\underline{\phi}$ is finally reduced to:

$$\underline{\phi} = \underline{A}_1 \cosh(\underline{k}(z+h)) \exp(i\underline{k}x). \tag{2.1.30}$$

$\underline{A}_1$ expression can be determined from Equation (2.1.20). In the absence of forcing on the free surface, as wind for instance, atmospheric pressure, P_0, is a constant. For the sake of simplicity, it is taken equal to 0. Injecting potential expression from Equation (2.1.30), in Equation (2.1.20) with $P_0 = 0$ gives:

$$\underline{A}_1 = -\frac{ig\underline{A}}{\omega \cosh(\underline{k}h)}. \tag{2.1.31}$$

Consequently, in the case of a single wave propagating forward in the x direction:

$$\boxed{\underline{\phi} = -\frac{ig\underline{A}}{\omega}\frac{\cosh(\underline{k}(z+h))}{\cosh(\underline{k}h)}\exp(i\underline{k}x)}, \tag{2.1.32}$$

The case of a variable depth can also be treated but is less standard and will be of no use in this thesis, see the work by Keller [1958] for instance.
In general, pressure in the fluid can be decomposed into a hydrostatic, $-\rho gz$ and a part which originates from the flow velocity. This second part is called dynamic pressure. Using the linearized Bernoulli's Equation in the whole domain, complex dynamic pressure expression, $\underline{p}$, is given by:

$$\underline{p} = i\omega\rho\underline{\phi}. \tag{2.1.33}$$

It illustrates that wave dynamic pressure is in opposite phase, with respect to the potential.

Gravity wave dispersion relation

The dispersion relation, relating k and ω, can be obtained by injecting the expressions for $\underline{\eta}$ and $\underline{\phi}$ into Equation (2.1.19), resulting in the simplification of exponential terms:

$$-\underline{A}i\omega = -\frac{i\underline{A}g}{\omega}\underline{k}\tanh(\underline{k}h). \tag{2.1.34}$$

Thus, the dispersion relation for waves in the general case of finite depth is:

$$\boxed{\omega^2 = g\underline{k}\tanh(\underline{k}h)}. \tag{2.1.35}$$

Equation 2.1.35 admits one real solution and an infinity of imaginary ones. The real value of $\underline{k}$ corresponds to the propagative mode while imaginary values of $\underline{k}$ represent to non-propagative evanescent modes. Those non-propagative modes appear near an obstacle for instance. In the rest of this thesis k refers to the wavenumber associated to the propagative mode and $\underline{k}$ to both propagative and evanescent modes.
In general, the potential has to be expressed as a sum of the propagative and the evanescent waves, so that:

$$\underline{\phi} = \sum_{n\in\mathbb{N}} \underline{\phi}_n(x,z), \tag{2.1.36}$$

with $(\phi_n)_{n\in\mathbb{N}}$ the spatial part of the potential associated with the n^{th} mode.
The gravity wave dispersion relation can be simplified under the hypothesis of deep or shallow

water. For deep water, $kh \gg 1$, leading to:

$$\omega = \sqrt{gk}. \tag{2.1.37}$$

The other limit, $kh \ll 1$, corresponding to shallow water, gives:

$$\omega = k\sqrt{gh}. \tag{2.1.38}$$

Gravity waves are non-dispersive in the shallow water limit and dispersive in the deep water limit.

Wave group and phase velocity

From the dispersion relation, the phase velocity and group velocity of the waves, denoted as c_φ and c_g respectively, can be derived:

$$c_\varphi = \sqrt{\frac{g}{k}\tanh(kh)}, \tag{2.1.39}$$

$$c_g = \frac{1}{2}c_\varphi\left(1 + kh\frac{1-\tanh^2(kh)}{\tanh(kh)}\right). \tag{2.1.40}$$

Hence, the phase velocity and group velocity differ for water waves. Those expressions can be simplified based on whether assumptions of deep or shallow water assumption is valid, as indicated below:

	Deep water	Shallow water
ω	$\sqrt{gk}$	$k\sqrt{gh}$
c_φ	$\sqrt{\frac{g}{k}}$	$\sqrt{gh}$
c_g	$\frac{c_\phi}{2}$	$\sqrt{gh}$

Thus, the quantities in deep water involve the wave vector, k, while in shallow water, the characteristic length is the depth, h. The different regimes are illustrated in Figure 2.2 **A**. Wavelength is presented as a function of wave frequency, f, over a 1 cm or 10 cm depth bottom (in red and black respectively) and is compared with predicted wavelength for the restricted case of shallow water and deep water. For $h = 1$ cm, both complete dispersion relation and shallow water approximation give the same results. For $h = 10$ cm, λ_{th}, the wavelength given by the general dispersion relation, is close to wavelength calculated within the shallow water wave approximation, λ_{sw} ,at small frequencies. For frequencies larger than 2.5 Hz, deep water approximation is accurate over a 10 cm bottom. Note that increasing

water depth would lead λ_{th} to follow λ_{dw}, wavelength given in the deep approximation for lower frequencies.

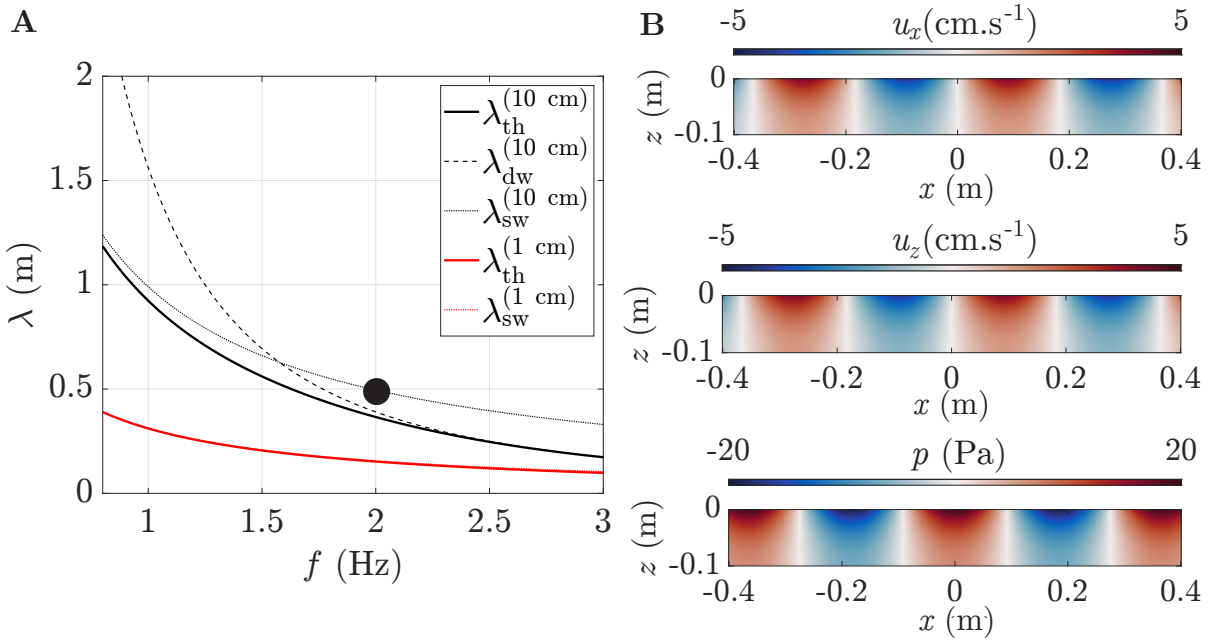

Figure 2.2: **A** Wavelength, λ, as a function of wave frequency, f, for a 1 or 10 cm bottom depth, h. Wavelength given by complete dispersion relation, λ_{th}, is represented in plain line and approximated versions in shallow, λ_{sw}, and deep water, λ_{dw}, are shown with dotted and dashed lines respectively. Superscripts indicate bottom depth used for the calculation. **B** Maps of the $x-z$ plan showing values of u_x, u_x and p at t=0 for 2 Hz waves of 2 mm amplitude, A over a 10 cm depth.

Velocity fields and fluid particle trajectories in waves

Fluid particle trajectories can be obtained from the potential, ϕ, as indicated in Holthuijsen [2010], since by definition:

$$\underline{u}_x = \partial_x \underline{\phi} \text{ and } \underline{u}_z = \partial_z \underline{\phi}. \tag{2.1.41}$$

Here, $\underline{u}_i$ represents the component along axis i of the velocity field. Thus:

$$\underline{u}_x = \frac{g\underline{A}k}{\omega}\frac{\cosh(k(z+h))}{\cosh(kh)}\exp(ikx), \tag{2.1.42}$$

$$\underline{u}_z = -\frac{ig\underline{A}k}{\omega}\frac{\sinh(k(z+h))}{\cosh(kh)}\exp(ikx). \tag{2.1.43}$$

Substituting the wave vector k with its expression given by the dispersion relation:

$$\underline{u_x} = \underline{A}\omega\frac{\cosh(k(z+h))}{\sinh(kh)}\exp(ikx) \text{ and } \underline{u_z} = -i\underline{A}\omega\frac{\sinh(k(z+h))}{\sinh(kh)}\exp(ikx). \tag{2.1.44}$$

Hence, the x-wise velocity is maximum at wave crests and troughs, while the z-wise reaches its maximum value along z for $\eta = 0$.

Figure 2.2 **B** shows the velocity fields in the x and z direction for a 2 mm waves amplitude, 2 Hz wave frequency and $h = 10$ cm. It appears clearly that u_x and u_z are in opposite phase. The dynamic pressure, p, is in phase with u_x. The fact that u_x is different from 0 close to $-h$ illustrates the intermediate depth regime case.

Particle trajectories can be calculated from those expressions, the velocity term along each axis is integrated with respect to time, considering x and z as constants, equal to $\bar{x}$ and $\bar{z}$ respectively. This assumption reflects the fact that particles remain close to these coordinates. It is obtained that:

$$\underline{\delta x} = i\underline{A}\frac{\cosh(k(\bar{z}+h))}{\sinh(kh)}\exp(ik\bar{x}) \ ; \ \underline{\delta z} = \underline{A}\frac{\sinh(k(\bar{z}+h))}{\sinh(kh)}\exp(ik\bar{x}). \tag{2.1.45}$$

$\underline{\delta x}$ and $\underline{\delta z}$ are the coordinates of fluid particles. Under these conditions, $\underline{\delta x}$ and $\underline{\delta z}$ are in phase opposition and correspond to the coordinates of particles following elliptical trajectories with half-major axes:

$$a_x = A\frac{\cosh(k(\bar{z}+h))}{\sinh(kh)} \ ; \ a_z = A\frac{\sinh(k(\bar{z}+h))}{\sinh(kh)}, \tag{2.1.46}$$

where a_x and a_z denote the half-major axes along x and z respectively. In deep water, those expressions become:

$$a_x = A\exp(-kz) \ ; \ a_z = A\exp(-kz), \tag{2.1.47}$$

and particle trajectories are circular.

Particles trajectories have been observed by Gray and Greated [1988] conducting Particle Image Velocimetry (PIV), experiments but a striking illustration of particles trajectories can be found in *An Album of Fluid Motion*, Chapter 7. Figure 2.3 shows two pictures from this book. Figure 2.3 **A** shows particle trajectories for propagative waves, which, from Equation 2.1.45 are ellipses. Interestingly, in the specific case of standing waves, *i.e.* waves of same amplitudes propagating in opposite directions, the particle motions change drastically as illustrated in Figure 2.3 **B**.

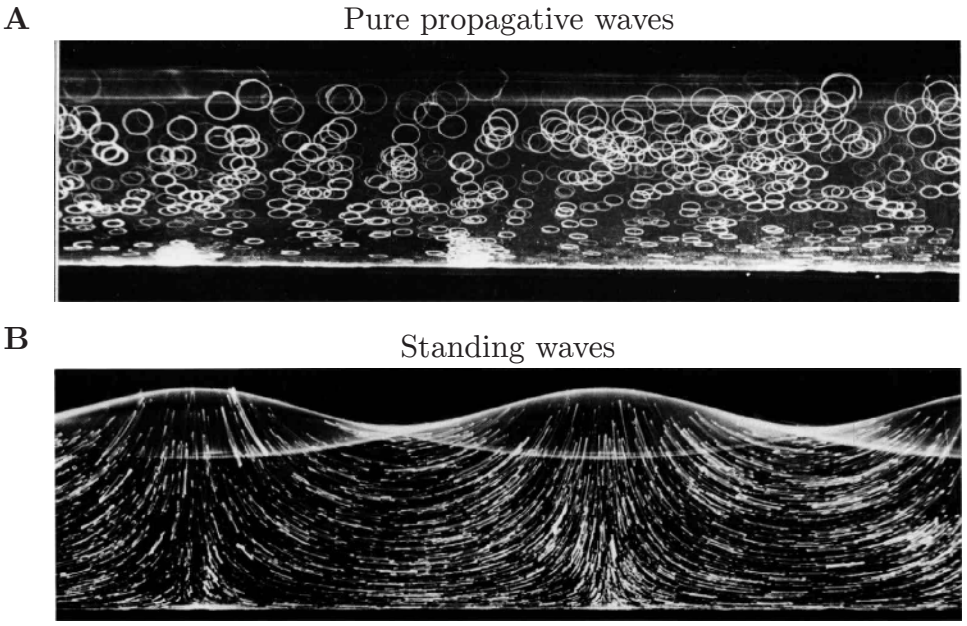

Figure 2.3: Pictures from An Album of Fluid Motion Chapter 7. **A** Particle trajectories in propagative waves. **B** Particle trajectories in standing waves.

Wave energy density

The wave energy density can also be estimated using linear theory. Energy transported by a water wave takes two forms. Potential energy, as fluid particle heights can be higher than the mean free surface level, or kinetic energy as fluid particles are moving.
By integrating the fluid particles kinetic energy density and potential energy density (respectively E_{wk} and E_{wp}) can be obtained:

$$E_{wp} = E_{wk} = \frac{1}{4}\rho g A^2. \tag{2.1.48}$$

Finally, the total wave energy density, E_w, is given by the sum of those two densities:

$$E_w = \frac{1}{2}\rho g A^2. \tag{2.1.49}$$

E_w is a key quantity as it allows to determine the energy available for wave energy converters. In addition, the mean wave power, P_w, corresponding to the energy incoming upon an object of width, b, can be obtained from the wave energy density. Indeed, since wave energy travels at group speed, c_g, P_w for an object of width b can be expressed as:

$$P_w = c_g b E_w = \frac{1}{2}\rho g A^2 c_g b. \tag{2.1.50}$$

2.1.2 Wave structure interaction

Modeling the interactions between waves and elastic membranes also requires understanding how objects and waves interact, which is the subject of this subsection.

Diffracted and radiated potentials

An object in the waves will produce three main effects: diffraction, radiation, and dissipation. Diffraction, similar to optics, is due to the interaction of a wave with an object of size close to its wavelength. Radiation is caused by the movement of the object in the wave field; the oscillating object itself creates waves that propagate on the surface. Finally, there can be various causes of dissipation, including viscous dissipation due to water movement over the object, the generation of turbulence, or the absorption of energy by the object, as in wave energy converters. Under the assumption of small flow perturbation and small body motion, linear potential flow theory remains valid. The problem linearity allows the decompostion of the flow potential, Φ, into the sum of a diffracted flow potential, Φ_D, and a radiated flow potential, Φ_R ([Mei et al., 2005][Linton and McIver, 2001]):

$$\Phi = \Phi_D + \Phi_R, \tag{2.1.51}$$

with

$$\Phi_D = \Phi_I + \Phi_S, \tag{2.1.52}$$

where Φ_I is the potential associated with the incident wave and given by potential theory, and Φ_S is the potential created by diffraction. And:

$$\Phi_R = \sum_\alpha f_\alpha \Phi_\alpha, \tag{2.1.53}$$

Here, f_α is the amplitude of the oscillation modes of the object, and Φ_α is the radiated potential associated with each mode.

Forces on a body in a wave field

In all fluid-structure interactions, waves exert forces onto the solid. Forces exerted by the object on the fluid are due to pressure differences on its surface. Pressure difference originates from two different physical causes, depth variation and velocity field variation. Depth variation leads pressure to vary according to the first law of hydrodynamic. Depth contribution

to difference in pressure is generally referred as static pressure, p_s. It can be expressed as:

$$p_s = -\rho g z \tag{2.1.54}$$

Static pressure leads to a hydrostatic force on the object written:

$$\mathbf{F_s} = -\rho g \int_S z.\mathbf{n} \mathrm{d}S, \tag{2.1.55}$$

where $\mathbf{n}$ is a normal vector to the surface and S is the surface of the object. In opposition to static pressure, dynamic pressure is caused by the fluid velocity. Dynamic pressure in the fluid is related to the potential through Bernoulli's relation (2.1.6) and p is the dynamic pressure. After linearization, it is written:

$$p = -\rho \partial_t \mathbf{\Phi}. \tag{2.1.56}$$

The force, $\mathbf{F}$, exerted by the waves on the object is the sum of the pressure forces over its entire surface. Thus:

$$\mathbf{F} = \int_S p.\mathbf{n} \ \mathrm{d}S, \tag{2.1.57}$$

Therefore, according to linear theory, in the complex space:

$$\underline{\mathbf{F_p}} = -i\rho\omega \int_S \underline{\phi} \ \mathrm{d}S, \tag{2.1.58}$$

and as $\mathbf{\Phi}$ decomposes into a radiated wave and a diffracted wave:

$$\underline{\mathbf{F_p}} = -i\rho\omega(\int_S \underline{\phi}_D.\mathbf{n}, \mathrm{d}S + \sum_\alpha f_\alpha \int_S \underline{\phi}_\alpha.\mathbf{n}.\mathrm{d}S). \tag{2.1.59}$$

Added mass and radiation damping

The first term of Equation (2.1.59) corresponds to the direct excitation of the object by the waves, while the second is the fluid's reaction to the movement of the object (see [Mei et al., 2005] Section 8.3.2 for instance). It is possible to show that the second term decomposes into two forces common in fluid-structure interactions: one proportional to acceleration - added mass - and the other proportional to the object's velocity - radiation damping. Added mass accounts for a change in the object inertia. Radiation damping corresponds to an additional damping due to wave creation. The object spends some of its potential and kinetic energy radiating waves.

Reflection and transmission coefficients, K_r and K_t

Generally, to characterize the object effect on the waves, in two dimensions or in a wave channel, one looks at reflected and transmitted waves. Reflection and transmission are measured using coefficients based either on amplitude or energy. In an idealized 2D case those coefficients are defined using the incident, $\underline{A}_i$, reflected, $\underline{A}_r$, and transmitted $\underline{A}_t$ wave amplitude. Reflection and transmission coefficients with respect to amplitude, k_r and k_t are simply defined as follow:

$$k_r = \frac{\underline{A}_r}{\underline{A}_i} \text{ and } k_t = \frac{\underline{A}_t}{\underline{A}_i}. \tag{2.1.60}$$

To obtain reflection and transmission coefficients with respect to energy, K_r and K_t, one can consider the power of the incident, reflected and transmitted waves respectively P_{wi}, P_{wr} and P_{wt}. K_r and K_t can then be defined as:

$$K_r = \frac{P_{wr}}{P_{wi}} \text{ and } K_t = \frac{P_{wt}}{P_{wi}}. \tag{2.1.61}$$

Powers can expressed as a function a wave amplitudes using Equation (2.1.50). It results that:

$$K_r = \left(\frac{A_r}{A_i}\right)^2 \text{ and } K_t = \left(\frac{A_t}{A_i}\right)^2. \tag{2.1.62}$$

If the object does not dissipate or extract wave energy, K_r and K_t are related through energy conservation so that:

$$K_r + K_t = 1. \tag{2.1.63}$$

For the rest of the manuscript, the wave-structure interaction will be analyzed primarily with consideration to the energy budget. Thus, only K_r and K_t will be considered.

Solving linear wave theory problems

The equations presented in this section can be solved, and offer good predictions for small-amplitude wave-structure interactions [Linton and McIver, 2001]. The main idea is to solve the Laplace Equation (2.1.5) in the fluid domain using boundary conditions specific to the object.

In some cases, such as a stepped bottom or a 2D elastic plate equations can be solved semi-analytically. To do so different methods, thoroughly explained by Linton and McIver [2001], can be used. A possible method, which is used in Chapter 3, consists in decomposing the potential onto a basis of function, depending on one variable of space uniquely. In Chapter 3,

the spatial part of potential $\underline{\phi}$ as:

$$\underline{\phi} = \sum_{n=0}^{\infty} (\underline{A}_n \exp(i\underline{k}_n x) + \underline{B}_n \exp(-i\underline{k}_n x)) Z_n(z), \tag{2.1.64}$$

with $(Z_n(z))_{n\in\mathbb{N}}$ a base function depending on z, $(\underline{A}_n)_{n\in\mathbb{N}}$ and $(\underline{B}_n)_{n\in\mathbb{N}}$ modes amplitude of propagative and counter-propagating waves respectively and k_n the angular frequency associated to the mode n. There, $(\underline{A}_n)_{n\in\mathbb{N}}$ and $(\underline{B}_n)_{n\in\mathbb{N}}$ generally become the problem unknowns and are found using boundary conditions projected on the different modes, using $(Z_n)_{n\in\mathbb{N}}$ orthogonality.
In addition, numerical solutions can be searched directly when the problem is too complex to be solved semi-analytically. Different methods that can be used are thoroughly described in Göteman et al. [2022].

2.1.3 Considering non-linearities

Linear wave theory is based on the linearization of the free-surface boundary condition and Bernoulli's equation with respect to wave steepness. When wave steepness increases, non-linear terms have to be included, so that predictions remain accurate.

A large variety of non-linear phenomena

A wide variety of non-linear phenomena can be observed when increasing wave steepness. One of the first effects to arise is Stokes drift. While gravity waves travels without global fluid displacement according to linear theory, fluid particles follow circular trajectories. However, one can show than an increase in wave steepness creates a mean flow in the direction [Andrews and McIntyre, 1978]. It leads to particle trajectories to become helicoidal. It is particularly crucial in small tank experiments, as mean flow leads to complex recirculation patterns in all the tank due to the tank finite size.
On the other side, one of the most extreme non-linear phenomenon is wave breaking. It consists in a violent decrease in wave amplitude caused by wave steepness increase. Typically, it is observed when waves travel over a decreasing bottom depth such as a beach for instance, and leads to surfing waves and rollers. Breaking waves can also be generated directly in a wave tank using to high wave-maker amplitudes.
Between linear wave theory and wave breaking, a large variety of waves can be observed offering a beautiful playground for physicists and mathematicians. For instance, Robbe-Saule et al. [2021] shows the different waves that can be observed when producing waves with a granular media collapse to investigate tsunami formation. Rogue waves can also be

caused by waves non-linearities. They consists in particularly steep and high waves localized spatially and temporally. It is a rare natural phenomenon that appear as "water walls" for ships that encounters them. Their nature makes them particularly difficult to observe, see [Slunyaev et al., 2023] for instance.
An other example of non-linear waves that can be observed in nature is solitary waves, which are waves packets that travel incredibly far with almost no dissipation. Tidal bores, waves that propagate along rivers against the current, are typical examples of solitary waves caused by tides. A physical origin of solitary waves in deep water lies in the fact that wave steepness allows to counteract wave dispersion that should normally disperse the wave packet, see [Mei et al., 2005] Chapter 13 for instance.

Non-linearities in wave-structure interaction

Non-linearity may also occurs at the interface between the wave induced flow and a submerged object. For instance, Stiassnie et al. [1984] experimentally measured the reflection and transmission of a vertical plate and compared their measurements to linear theory. Energy dissipation is observed and is attributed to vortex shedding at the plate edge. In the same spirit, Ting and Kim [1994] observe the difference between linear theory and experiments. Using Particle Image Velocimetry (PIV), they map the flow velocity field and observed vortex formation at the edge of the object. Vortex formation is a non-linear phenomenon that can be induced by the objects edges where large velocities are predicted by linear theory [Knott and Mackley, 1980]. In addition, object motion can lead to vortex creation. Hence, more discrepancy from linear theory could be expected for strongly moving objects. Finally, vortex creation in the fluid does not only generates vortices but also creates a force that opposes object motion, drag force. For high Reynolds numbers, which is mostly the case in water gravity wave, drag force is proportional to the square of the relative velocity between the object and the flow. It is by essence a non-linear effect, since it is not proportional to the relative velocity.

Morison's law

Different attempts to include the effect of drag in simulation have been made. One of the most classical tool ones has been proposed by Morison et al. [1950]. It consists in the addition of a quadratic force that is written:

$$\mathbf{F_d} = -\frac{1}{2}\rho C_d S|\boldsymbol{\xi} - \mathbf{u_i}|(\boldsymbol{\xi} - \mathbf{u_i}), \tag{2.1.65}$$

with $\boldsymbol{\xi}$ object amplitude, $\mathbf{u_i}$ the velocity field associated to the incident potential, ϕ_I, *i.e.* flow velocity as if there was no object. S is a surface characteristic of the object and C_d a drag coefficient. The main difficulty being to calibrate C_d the drag coefficient associated to Morison's formula. In addition, Morison formula has been found to be inaccurate in some situations. For instance, Cummins and Dias [2017] explore a new formulation for drag force in diffraction dominated wave-structure interaction where Morison's formula is not accurate.

Solving non-linear wave-structure interaction problems

Most non-linear wave-structure interaction problems have to be solved numerically. Keys to tackle such problem are also described by Göteman et al. [2022] or Davidson and Costello [2020], the main approach being to use Computational Fluid Dynamics software. In those problems, the modelling choices can have a significant impact, as shown by Ransley et al. [2020], who compare different models with experimental data.

2.2 Behavior of an elastic plate in a flow

Section 2.1 focused on generalities on wave-structure interaction. This section is more focused on the subject of this manuscript, plate behavior in a flow.

2.2.1 Euler-Bernouilli beam theory

Before examining the flow effect onto a plate, it seems primordial to describe plate behavior. The Euler-Bernoulli beam theory proposes a theoretical description neglecting effects in the y direction and assuming small amplitudes. It is a well known problem that is clearly presented by Antier [2021]. The clamped plate edge is located in $x = -a$, with a the half-length of the plate, to remain consistent with Chapter 3. The equation governing the palte vertical deflection, $\Xi(x,t)$, of the plate states that for all x along the plate:

$$EI\partial_x^4\Xi(x,t) + \rho_p S\partial_t^2\Xi(x,t) = F_{\text{ext}}. \tag{2.2.1}$$

Here, E is the Young's modulus of the plate, I is its moment of inertia, S is its cross-section area, and F_{ext} is the external forcing on the plate. Typically, in a flow, the external forcing can be caused by dynamic pressure. Equation (2.2.1) shows that two terms rule the plate motion, the first one corresponding to the plate stiffness and the second to the plate inertia. I, is the moment of inertia of the plate cross-section. For a rectangular plate, it can be expressed as:

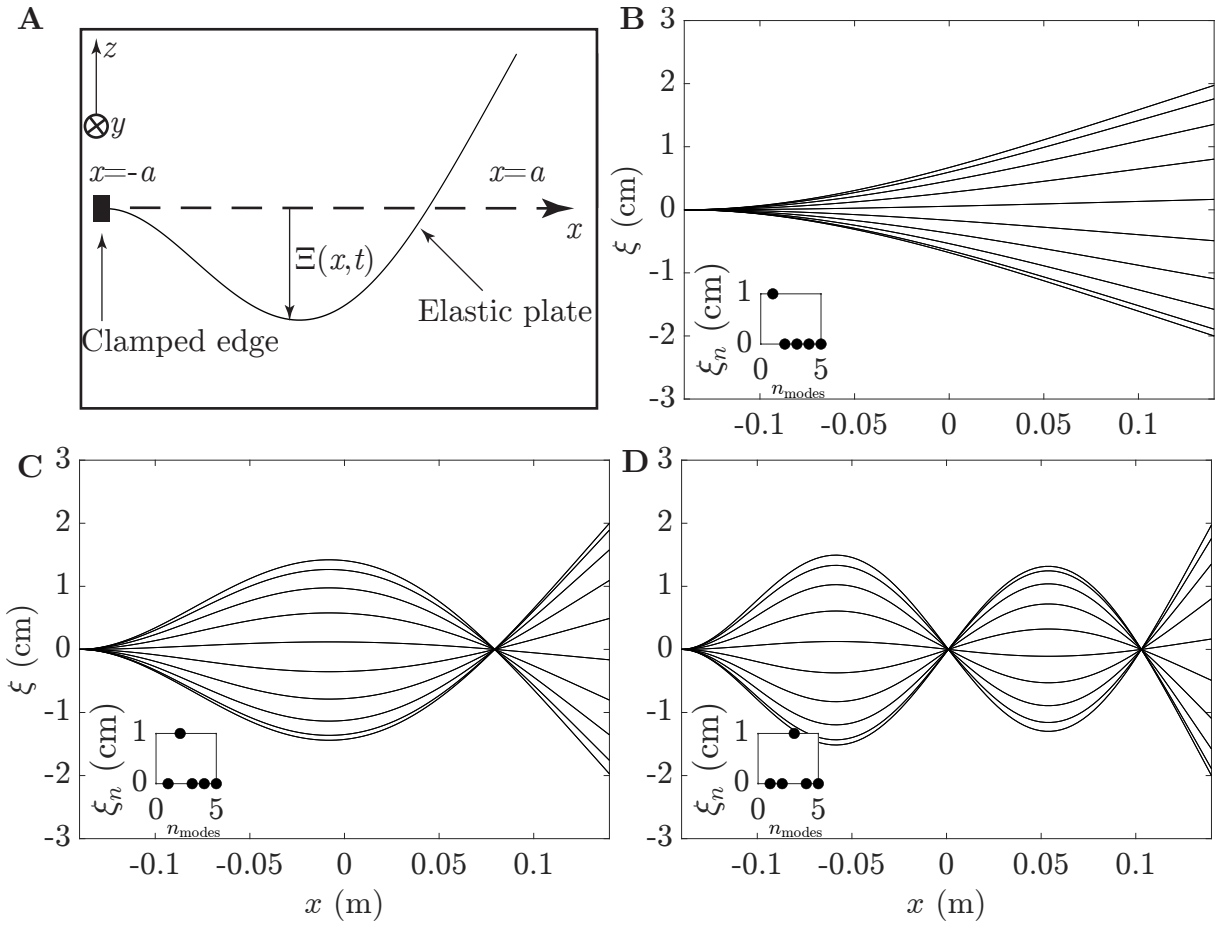

Figure 2.4: **A** Scheme of the cantilevered elastic plate. **B** Plate oscillations over a period for the first mode. **C** Plate oscillations over a period for the second mode. **D** Plate oscillations over a period for the first mode. Inserts show amplitude distribution among the different modes.

$$I = \int_{-l/2}^{l/2} \int_{-b/2}^{b/2} z^2 \mathrm{d}y\mathrm{d}z, \tag{2.2.2}$$

considering that the plate has a width b and a thickness l. It leads to:

$$I = \frac{l^3 b}{12}. \tag{2.2.3}$$

If the excitation is harmonic, as it will be the case for a plate in a wave field, Ξ and Φ can be expressed as:

$$\begin{cases} \Xi(x,t) = \mathrm{Re}\{\underline{\xi}(x)\exp(-\mathrm{i}\omega t)\} \\ \Phi(x,z,t) = \mathrm{Re}\{\underline{\phi}(x,z)\exp(-\mathrm{i}\omega t)\} \\ F_{\mathrm{ext}} = \mathrm{Re}\{\underline{f}_{\mathrm{ext}}\exp(-\mathrm{i}\omega t)\} \end{cases} \tag{2.2.4}$$

The equation (2.2.1) then becomes:

$$EI\partial_x^4\underline{\xi}(x) - \omega^2\rho_p S\underline{\xi}(x) = \underline{f}_{\text{ext}} \tag{2.2.5}$$

For a symmetric membrane with the origin at its center, a solution in the form below is seeked:

$$\underline{\xi} = C_1\cos(k_l(x+a)) + C_2\sin(k_l(x+a)) + C_3\cosh(k_l(x+a)) + C_4\sinh(k_l(x+a)),\ \forall\, x \in [-a, a], \tag{2.2.6}$$

with C_1, C_2, C_3 and C_4 being constants. Boundary conditions on the plate are given by:

$$\underline{\xi}(-a) = 0 \tag{2.2.7}$$

$$\underline{\xi}'(-a) = 0 \tag{2.2.8}$$

$$\underline{\xi}''(a) = 0 \tag{2.2.9}$$

$$\underline{\xi}'''(a) = 0 \tag{2.2.10}$$

The no-movement conditions at the fixation point give:

$$C_1 = -C_3 \text{ and } C_2 = -C_3. \tag{2.2.11}$$

The following matrix equation is obtained:

$$\begin{pmatrix} -\cos(2k_la) - \text{ch}(2k_la) & -\sin(2k_la) - \text{sh}(2ka) \\ \sin(2k_la) - \text{sh}(2k_la) & -\cos(2k_la) - \text{ch}(2k_la) \end{pmatrix} \begin{pmatrix} C_1 \\ C_2 \end{pmatrix} = \begin{pmatrix} 0 \\ 0 \end{pmatrix} \tag{2.2.12}$$

This requires the determinant of the square matrix to be zero (otherwise, $C_1 = C_2 = 0$):

$$1 + \cos(2k_la)\text{ch}(2k_la) = 0. \tag{2.2.13}$$

The numerical resolution of this equation yields quantized values of k_l that correspond to the eigenmodes of the clamped beam, only real values of k_l are considered here. These k_l values are related to the natural frequencies, ω_l, by:

$$k_l^4 = \frac{\rho_p S}{EI}\omega_l^2. \tag{2.2.14}$$

Finally, C_1 and C_2 are related by:

$$C_2 = \gamma C_1, \tag{2.2.15}$$

with γ given by:

$$\gamma = -\frac{\cos(2k_l a) + \mathrm{ch}(2k_l a)}{\sin(2k_l a) + \mathrm{sh}(2k_l a)}. \tag{2.2.16}$$

C_1 is a constant, as the amplitudes of the modes relative to each other are what matter. Therefore, C_1 is taken as 1. The modes are expressed as:

$$f_l(x) = \cos(k_l(x+a)) - \mathrm{ch}(k_l(x+a)) + \gamma(\sin(k_l(x+a)) - \mathrm{sh}(k_l(x+a))) \tag{2.2.17}$$

A representation of the plate envelope for the first three modes is given in Figures 2.4 **B**, **C** and **D**.

Note that internal effects in the plate or external forces dependent on plate motion would change Equation (2.2.1), and consequently the plate modes. Such changes occur, typically, if internal dissipation is added to the plate model (see [Van Horssen and Zarubinskaya, 2003] or [Renzi, 2016] for instance).

In practice, when forced at a given frequency, different from the plate natural frequency, different modes exist in the plate. In the absence of non-linear effects, the plate deflection can be written as a superposition of modes contributions:

$$\xi(x) = \sum_n \xi_n f_n(x), \tag{2.2.18}$$

$(\xi_n)_{n\in\mathbb{N}}$ being the n^{th} mode amplitude. Figure 2.5 shows the plate deflection, ξ, over one wave period for different mode combinations. Figure 2.5 **A**, **B** and **C** illustrate the effect of different distributions of modes 1 and 2. It appears that, when modes 1 and 2 have the same amplitude, a node is located at the plate end. As mode 2 amplitude increases, this node moves closer to the plate clamped edge. Figure 2.5 **D** is another example, which illustrates the wide variety of shapes that can be obtained combining all the modes.

2.2.2 Elastic plates oscillations in a still fluid

Plate oscillations are of high interest in the case of locomotion either of fishes or for eventual boats. More generally, elastc plates exhibit rich and intriguing physics when couple with a fluid. This section first focuses on elastic plates in a still flow. First, vortex formation can be observed at the plate edges as observed by Lai and Platzer [1999]. Vortex formation

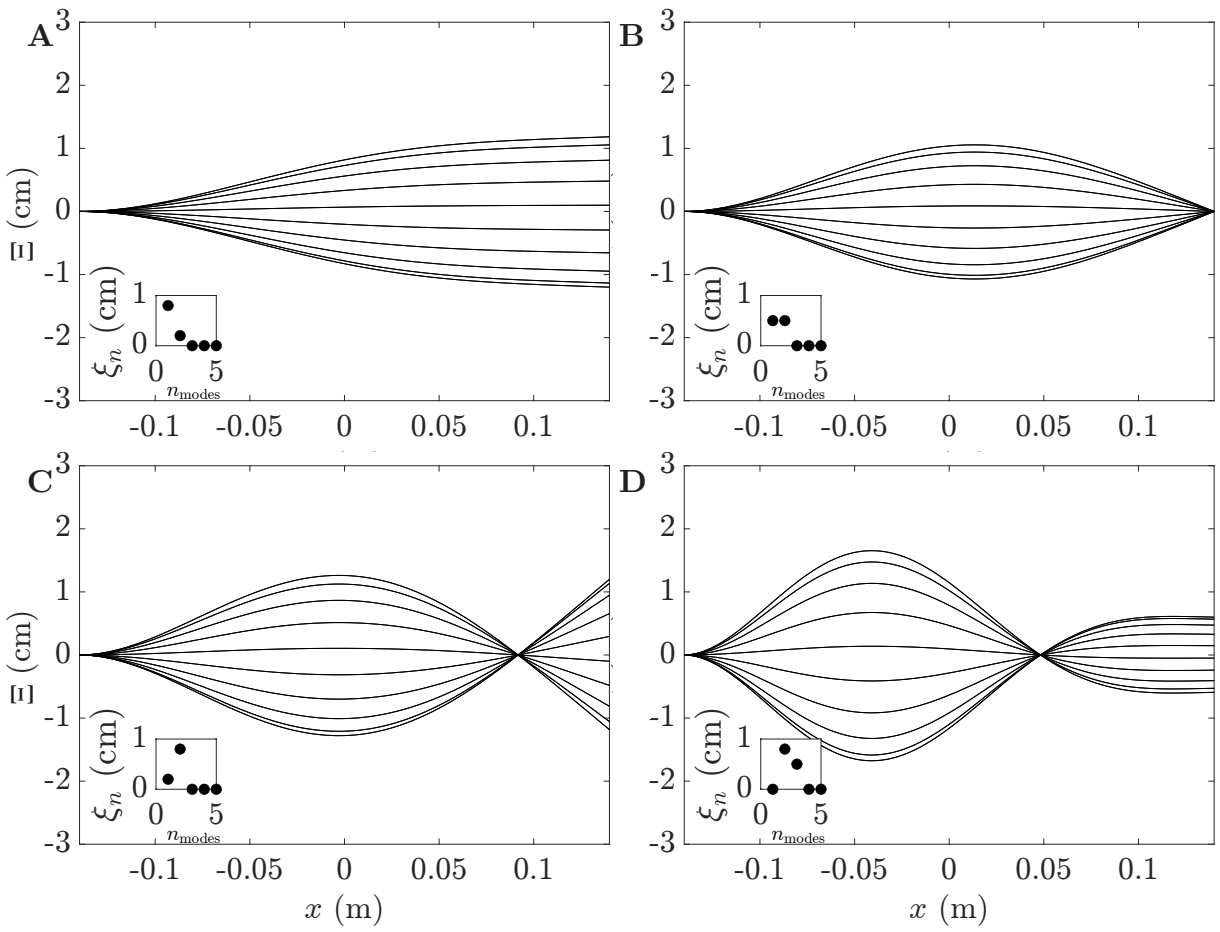

Figure 2.5: **A** Plate oscillations over a period for ξ_1=0.8 cm and ξ_2=0.2 cm. **B** Plate oscillations over a period for ξ_1=0.5 cm and ξ_2=0.5 cm. **C** Plate oscillations over a period for ξ_1=0.2 cm and ξ_2=0.8 cm. **D** Plate oscillations over a period for ξ_2=0.8 cm and ξ_3=0.5 cm.

results in the creation of a jet. Jet can result in thrust creation as it has been shown by Shinde and Arakeri [2018]. In addition, they conducted PIV experiment in the xz plan. They observed vortices formation also in that plan associated with field showing reverse Bénard–von Kármán vortex street. As illustrated in Figure 2.6, a Bénard–von Kármán street corresponds to repeating vortices ejected from to the plate tip. The difference between a reverse Bénard–von Kármán vortex street and a reverse Bénard–von Kármán lies in vortices orientation. To investigate propulsion further, Vandenberghe et al. [2004] and Vandenberghe et al. [2006] observed vortex formation over a heaving rigid plate which can rotate around its center. They show that such a system can start to rotate due to vortex creation. In addition, Raspa et al. [2014] show PIV experiments performed in a plan transverse to the plate also exhibiting vortex creation. Two phenomena arise from those studies. Since elastic plates are moving objects in a flow, their motion is associated with vortex generation and drag. In addition, the plate motion can induce thrust and possibly be used as propellers.

Added mass of a flexible plate

Plate motion in a fluid is also associated with added mass. In addition to added mass caused by wave radiation in Section 2.1, a force proportional to object acceleration can exist even far from the free surface. It corresponds to the force needed by the plate to move the fluid that surrounds it. Added mass caused by fluid displacement has been estimated by Payne [1981]. It is obtained that the plate added mass, μ, can be expressed as:

$$\mu = \frac{\frac{\pi}{4}\rho L^2 b}{[1 + (\frac{L}{b})^n]^{1/n}}, \tag{2.2.19}$$

with L being the plate length ($L = 2a$) and n a natural number, the value of which depends on the plate geometry. This relation is fitted to correspond to experimental observations that states that $\mu = \frac{\pi}{4}\rho L^2 b$ if $b \gg L$ and $\mu = \frac{\pi}{4}\rho L b^2$ if $L \gg b$.
The result given in [Payne, 1981] is valid for a simple unattached plate. In the case of a cantilevered plate, Piñeirua et al. [2015] proposed a slightly different expression for added mass per unit of area, μ', homogeneous to a mass per unit of length, based on plate amplitude and width:

$$\mu' = \frac{\frac{\pi}{4}\rho b \zeta_0}{[1 + (\frac{A_0}{b})^n]^{1/n}}, \tag{2.2.20}$$

with ζ_0 being the initial displacement at the plate tip. In that case, n is found to be equal to 5.
In practice, added mass changes plate natural frequencies that can be written as:

$$\omega_l = \sqrt{\frac{EI}{\rho_p S + \mu'} k_l^2} \tag{2.2.21}$$

2.2.3 Elastic plates in a uniform velocity flow

In the presence of a uniform flow plate behavior can change drastically. To illustrate those changes, Godoy-Diana et al. [2009] studied experimentally the vortices produced by a pitching foil in a uniform flow. It appears that changing plate amplitude and Strouhal number allows to observe a wide variety of different wakes. The wake downstream an elastic plate appears in a beautiful way in the work of Zhang et al. [2000], where an elastic plate is placed a uniform flow. The plate is not forced manually, but starts to oscillate due to the flow (see Figure 2.6). Elastic plates in a uniform velocity flow have been widely studied due to their omnipresence for diverse applications. Only some context is given in this Section and readers interested for more detail can refer to reviews by Shelley and Zhang [2011] or Godoy-Diana and Thiria

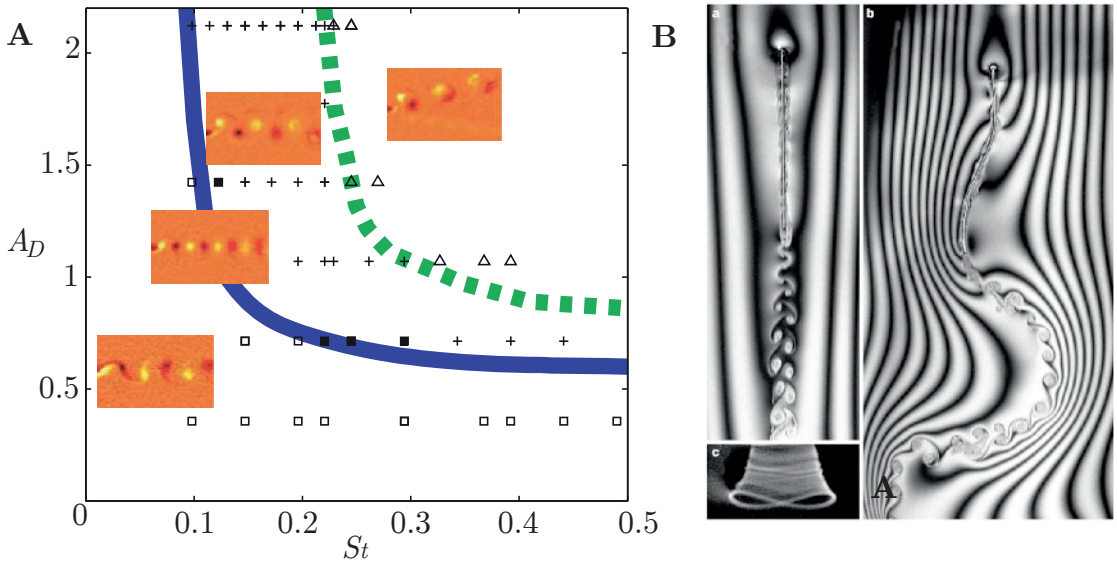

Figure 2.6: **A** Figure by Godoy-Diana et al. [2009]. Forcing amplitude-Strouahl diagram illustrating the wide variety of wakes that can be observed in the wake of a flapping foil. **B** Figure by Zhang et al. [2000]. Visualization of an elastic plate wake using interference patterns under a sodium lamp.

[2018]. For instance, interests in such a an elastic plate in a uniform flow can lie in the understanding of flags behavior. Taneda [1968] studied experimentally the development of waves on a flag in a wind tunnel. More recent works allow to obtain a deeper understanding of this wide problem. For example, Michelin et al. [2008] developed models to take vortices emissions into account.

Elastic plates are also studied as potential bioinspired propulsion devices. Beal et al. [2006] showed that a dead fish could propel itself due to flow induced oscillations. The link between passive fish propulsion and elastic plates lies in fish models that consist in approximating the fish as a plate of variable section profile (see [Lighthill, 1969] or [Piñeirua et al., 2017] for instance). In a more controlled environment, Paraz et al. [2016] study experimentally the thrust created by a clamped elastic plate and effectively measured the thrust produced. D'Adamo et al. [2022] look at the flow created by a heaving plate, showing vortices creation and mean flow creation at the plate tip.

Studying elastic plates in a uniform flow is also of interest for the energy harvesting, in a river for instance. Based on the fact that an elastic plate clamped at one edge oscillates due to flow forcing, Allen and Smits [2001] and Taylor et al. [2001] suggest that electricity could be produced from those oscillations.

2.3 Submerged plates in a wave field

The wave-plate problem has been studied both for coastal protection and wave energy harvesting. Plates can be used in different configurations, vertical, horizontal while floating at the free-surface or horizontal and submerged. In those different configurations, rigid or elastic plates are used. The interest in flexibility lies in the fact that flexibility would offer a better survivability to the device or could be used to generate electricity [Mérigaud et al., 2021].
The case of vertical plates has been studied both theoretically and experimentally. For instance, Dean [1945] computes theoretical reflection and transmission coefficients in deep water and Dick and Brebner [1968] confirme Dean's results experimentally. Nové-Josserand et al. [2019] or Mérigaud et al. [2021], inspired by algae dynamics in sea waves, investigate the impact of flexibility on such a structure.
Horizontal plates at the free-surface are of particular interest to model the sea ice. Their interaction with water waves has also been investigated using experimental and theoretical approaches (see [Meylan and Peter, 2009], [Kohout and Meylan, 2008] or Domino et al. [2018] for instance).
The rest of this section focuses on horizontal submerged plates.

2.3.1 Rigid submerged plate in a wave field

Submerged horizontal rigid plates have been considered before elastic plates for coastal protection. Theoretically, Burke [1964] calculated reflection and transmission coefficients for water waves in deep water using the Wiener-Hopf technique. Patarapanich [1984] extend the calculation of reflection and transmission coefficients calculations to wider cases utilizing the finite-element method.
Those first theoretical results were obtained in the case of linear wave theory. However, a submerged rigid plate also offers a wide variety of fascinating non-linear phenomena. Grue [1992] shows experimentally that second order waves modes can appear due to plate wave interaction. Boulier and Belorgey [1994] and Poupardin et al. [2012] conduct Particle Image Velocimetry in such a system and observed vortex creation at the plate tip, leading to the apparition of a mean flow. Pinon et al. [2017] confirm those results numerically. The apparition of a mean flow due to wave-plate interaction has even been considered as a pumping mechanism, Carmigniani et al. [2017].

2.3.2 Submerged elastic plate in a wave field

The study of submerged elastic plates in a wave field is an extension of stheir rigid counterparts. The interest in the addition of flexibility lies in the possible improvement of the object to survive a storm and the ability to produce electricity utilizing plate motion.

Submerged elastic plate for wave energy harvesting and coastal protection

The idea of using horizontal submerged elastic plates as wave barriers originates from Cho and Kim [1998], who proposed analytical solutions to the problem by mode decomposition and by solving the radiation and diffraction problems separately. This solution is compared with numerical and experimental studies confirming the results obtained using linear theory. Alam [2012] suggested to convert the plate motion into electricity, based on the observation that muddy seafloors are efficient to damp waves. The Wave-Carpet, a Wave Energy Converter made of a flexible plate hinged to the seafloor where electricity is produced by the plate oscillation through power take-off pistons, is directly inspired from this idea. The Wave Carpet potential has been investigated numerically and experimentally by Desmars et al. [2018], Asaeian et al. [2020] or Lehmann et al. [2013]. Achour et al. [2020] investigated the same system in the presence of both waves and current. Alternatives Wave Carpet designs have also been investigated. Renzi [2016] suggests using piezoelectric material instead of pistons to produce electricity. Similarly, Shoele [2023] investigated the efficiency of a submerged elastic plate made of piezoelectric material but only clamped at one edge in order to create an hybrid wave-current converter. In addition to linear wave theory, vortex emission is taken into account in the model. This interesting concept is close to the system studied in this thesis at the difference that no piezoelectric device will be used here.
Finally, note that wave-plate interactions have been studied in many more complex configurations such as with a plate close to a wall [Gayathri et al., 2020] [Guo et al., 2020] [Mohapatra and Guedes Soares, 2020] [Zheng et al., 2021] or superimposed with other flexible plates [Mohapatra and Sahoo, 2014] [Mohapatra and Soares, 2019] [Behera, 2021].

Wave driven propulsion by a submerged elastic plate

At the exception of the recent work of Shoele [2023], submerged elastic plates for wave energy harvesting and coastal protection were limited to plates clamped at both edges. However, looking at a submerged elastic plates in a wave field offers other perspectives as they could be used as propulsion devices. As underlined by Rozhdestvensky and Ryzhov [2003], Section 7.1.1, the use of wave-activated flapping wings could allow to increase ship propulsion.

Such a system has also been investigated numerically by Belibassakis et al. [2021] and Filippas et al. [2020]. Kumar and Shin [2019] consider adding an elastic plate to such a system to enhance thrust propulsion. An open question emerges from those study: can a submerged elastic plate alone generate propulsion? A partial answer to this question will be given in Chapter 5, Section 5.3.
In the end, the interaction between submerged elastic plates and waves has been mostly studied numerically or theoretically. This thesis aims at addressing this rich problem from a dual perspective, both numerical and experimental.

2.4 Conclusion

This Chapter, by exposing the useful notions to understand elastic plate-wave interaction, highlighted a multitude of beautiful physical phenomena which can arise from the interaction of a flow with a plate. Firstly, linear wave theory gives keys to apprehend wave-structure interactions for small amplitudes waves. Some insights on the influence of non-linearities has also been described. Secondly, the plate behavior in a flow has also been discussed. All those elements can be assembled in order to give a specific description of a submerged elastic plate in a wave field. It is the subject of the next chapter, which focuses on examining the predicted submerged elastic plate behavior in a wave field within the framework of linear wave theory.

Chapter 3

Two dimensional linear theory of the interaction between water waves and a submerged elastic plate

As stated in Chapter 2, linear wave theory is a long-establish tool to describe wave-object interaction. This Chapter consists in utilizing linear theory to describe the plate behavior. Previous works have been interested in studying the interaction between an elastic plate and waves using linear theory. However, most of them considered a plate clamped at both edges, or under the effect of a mean flow. The procedure followed here is very similar to the one developed by Hassan et al. [2009], Renzi [2016] or Zheng et al. [2021] to study elastic plates clamped at both edges, but the boundary conditions on the plate are changed to fit to the present problem.

3.1 Two dimensional model

3.1.1 Problem definition

As mentioned in Chapter 2, wave linear theory is restricted to small waves amplitudes. Similarly, the plate motion should be limited to small oscillations. It means that the plate motion is assumed to be restricted to infinitesimal vertical deformations. That way, the plate is considered submerged at $z = -d$ at over all its length. As stated in Hassan et al. [2009], contrary to most wave-structure interaction, the problem can be solved without a decomposition of the potential as the sum of a diffracted flow and radiated flow. Laplace's equation (2.1.5) is solved for the whole problem directly.

With those assumptions, the fluid domain can be decomposed into four zones, independent of the plate motion and of the free surface deformation. As depicted in Figure 3.1, zone 1 ($x \in [-\infty; -a]$) corresponds to the up-wave region, where the incident wave and the reflected

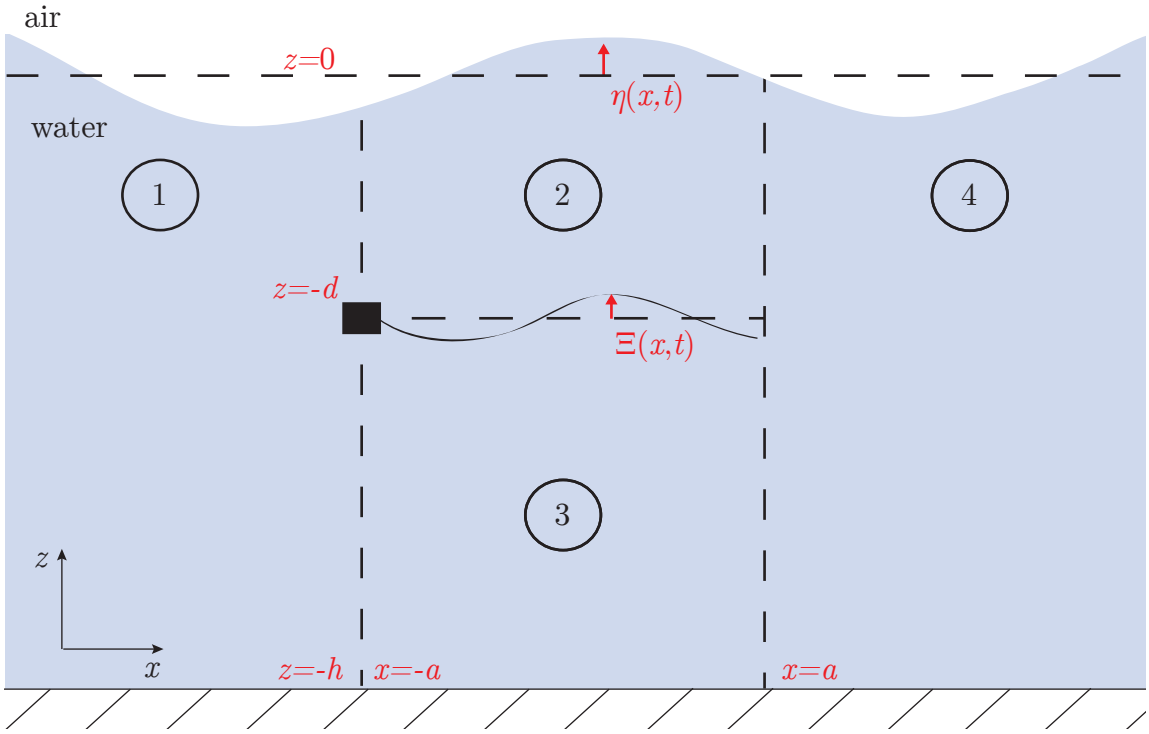

Figure 3.1: Schematic of the 2D linear problem. z stands for depth, η for the free surface elevation, Ξ is the plate vertical displacement and a is the half the plate length. The plate is submerged at depth $z = -d$ and extends from $x = -a$ to $x = a$. The water depth is constant at $z = -h$.

wave propagate. Zone 2 ($x \in [-a; a]$ and $z \in [-d; -0]$) and 3 ($x \in [-a; a]$ and $z \in [-h; -d]$) correspond, respectively, to the regions above and below the plate. Finally, zone 4 ($x \in [a; \infty]$) corresponds to the down-wave region. In the four zones, Laplace's equation has to be solved using appropriate boundary conditions. At the free surface (over the upper limit of zones 1, 2 and 4), the free surface boundary condition (3.1.1) holds, written as:

$$g\partial_z\Phi + \partial_t^2\Phi = 0, \text{ for } z = 0 \text{ and } \forall x, \tag{3.1.1}$$

as presented in Chapter 2. On the bottom, a no-flow condition is applied:

$$\partial_z\Phi = 0, \text{ for } z = -h \text{ and } \forall x. \tag{3.1.2}$$

Finally, a no-flow condition is also applied between zones 2 and 3, on the plate. The latter condition states that the vertical velocity of the plate must be equal to the fluid vertical velocity at $z = -d$ which, in terms of potential yields:

$$\partial_z\Phi = \partial_t\Xi, \text{ for } z = -d \text{ and } x \in [-a; a]. \tag{3.1.3}$$

Now, assuming harmonic forcing, and using the problem linearity, Φ and Ξ can be separated into the product of a function of space and a harmonic function of time:

$$\Phi(x,z,t) = \mathrm{Re}\left\{\underline{\phi}(x,z)e^{-i\omega t}\right\} \text{ and } \Xi(x,-d,t) = \mathrm{Re}\left\{\underline{\xi}(x)e^{-i\omega t}\right\}, \tag{3.1.4}$$

ω being the angular frequency of the incident wave and $\underline{\phi}(x,z)$ and $\underline{\xi}(x)$ are complex-valued functions, depending on space only. From Equations (3.1.1), (3.1.3) and (3.1.2), the complex potential function satisfies the following set of conditions:

$$\begin{cases} g\partial_z\underline{\phi} + \partial_t^2\underline{\phi} = 0, \text{ for } z = 0 \text{ and } \forall x, \\ \partial_z\underline{\phi} = 0, \text{ for } z = -h \text{ and } \forall x, \\ \partial_z\underline{\phi} = -i\omega\underline{\xi}, \text{ for } z = -d \text{ and } x \in [-a;a]. \end{cases} \tag{3.1.5}$$

For the remainder of this section, the potential in each zone will be noted as $\underline{\phi}_j$, j being equal to 1, 2, 3 or 4 depending on the part of the fluid domain.

3.1.2 Potential expression, $\underline{\phi}_1$, in zone 1

In zone 1, the boundary conditions are the same as in Section 2.1.1. Hence, the expression of $\underline{\phi}_1$ is similar and is written as:

$$\underline{\phi}_1 = -\frac{igA}{\omega}Z_0(z)e^{ik_0(x+a)} + \sum_{n=0}^{\infty}\underline{R}_n e^{-i\underline{k}_n(x+a)}Z_n(z) \tag{3.1.6}$$

with A being the incident wave amplitude, $\underline{k}_n$ the wave-number, g gravity, ω the angular frequency, and Z_n fluid vertical eigenmodes. As the boundary conditions are the same as in Section 2.1.1, Z_n are defined for $n \in \mathbb{N}$ with a similar expression:

$$Z_n(z) = \frac{\cosh(\underline{k}_n(z+h))}{\cosh(\underline{k}_n h)}. \tag{3.1.7}$$

In Equation (3.1.6), the first term corresponds to the incident wave. The second term is an infinite sum corresponding to the reflected waves. As in 2.1.1, incident waves are assumed to come from a source infinitely far. Hence, no evanescent waves, *i.e.* modes of imaginary wave-number, have to be considered. On the contrary, reflected waves are generated at the plate location, and evanescent waves have to be examined. In addition, those modes will ensure continuity at the interface between the different fluid domains.

Potential expressions, $\underline{\phi}_2$ and $\underline{\phi}_3$, in zones 2 and 3

As $\underline{\phi}_2$ and $\underline{\phi}_3$ are related through boundary conditions on the plate, the two potential expressions are related. The process to obtain potential expressions is the same as in the case of Section 2.1.1. Considering, for the sake of simplicity, that $\underline{\phi}_2$ and $\underline{\phi}_3$ are only composed of one mode, separation of variables is performed so that:

$$\underline{\phi}_{(2,3)} = \underline{G}^{(2,3)}(z)\underline{F}^{(2,3)}(x), \tag{3.1.8}$$

where notation $(2,3)$ stands for 2 or 3 and $\underline{G}$ and $\underline{F}$ are functions of z and x respectively. Injecting Equation (3.1.8) into Laplace's equation:

$$\frac{\underline{G}''^{(2,3)}}{\underline{G}^{(2,3)}}(z) = -\frac{\underline{F}''^{(2,3)}}{\underline{F}^{(2,3)}}(x) = \underline{\sigma}^2, \tag{3.1.9}$$

$\underline{\sigma}$ is a constant independent of x and z. $\underline{\sigma}$ is calculated in the following section. It is found to be independent of the zone and depends on plate parameters and wave frequency. Therefore, $\underline{G}$ and $\underline{F}$ are solutions of second order differential equations, so that:

$$\underline{F}^{(2,3)} = \underline{A}^{(2,3)}e^{i\underline{\sigma}x} + \underline{B}^{(2,3)}e^{-i\underline{\sigma}x}, \tag{3.1.10}$$

with $\underline{A}^{(2,3)}$ and $\underline{B}^{(2,3)}$ being the amplitudes of the waves propagating forward and backward, respectively. Furthermore, the boundary condition on the plate imposes that:

$$\partial_z\underline{\phi}_2 = -i\omega\underline{\xi} \text{ and } \partial_z\underline{\phi}_3 = -i\omega\underline{\xi},\ \forall x \in [-a,a] \text{ and } z = -d, \tag{3.1.11}$$

which implies that:

$$\partial_z\underline{\phi}_2 = \partial_z\underline{\phi}_3,\ \forall x \in [-a,a] \text{ and } z = -d. \tag{3.1.12}$$

As this condition is valid for all x between $-a$ and a but at an imposed depth, $z = -d$, it becomes necessary that $\underline{F}_2$ and $\underline{F}_3$ are equal. It imposes that the wave-number, $\underline{\sigma}$, in zones 2 and 3 is the same.

Concerning the expression of $\underline{G}_{(2,3)}$ zones 2 and 3 have to be treated separately, before utilizing Equation 3.1.12 to close the problem. In zone 2, Equation (3.1.9) stated that G_2 can be written as:

$$\underline{G}^{(2)}(z) = \underline{\alpha}_2\cosh(\underline{\sigma}z) + \underline{\beta}_2\sinh(\underline{\sigma}z), \tag{3.1.13}$$

with $\underline{\alpha}_2$ and $\underline{\beta}_2$ being two constants to be determined. $\underline{\alpha}_2$ and $\underline{\beta}_2$ are related using the free surface boundary condition:

$$g\underline{\sigma}\underline{\beta}_2 = \omega^2\underline{\alpha}_2, \tag{3.1.14}$$

so that:

$$\underline{G}^{(2)}(z) = \underline{\alpha}_2[\cosh(\underline{\sigma}z) + \frac{\omega^2}{g\underline{\sigma}}\sinh(\underline{\sigma}z)]. \tag{3.1.15}$$

In zone 3,

$$\underline{G}^{(3)}(z) = \underline{\alpha}_3\cosh(\underline{\sigma}_n(z+h)) + \underline{\beta}_3\sinh(\underline{\sigma}_n(z+h)), \tag{3.1.16}$$

with $\underline{\alpha}_3$ and $\underline{\beta}_3$ being constants to be determined. The condition at the bottom (Equation (3.1.2)) imposes that:

$$\underline{\beta}_3 = 0, \tag{3.1.17}$$

so that:

$$\underline{G}^{(3)} = \underline{\alpha}_3\cosh(\underline{\sigma}_n(z+h)). \tag{3.1.18}$$

$\underline{\alpha}_2$ and $\underline{\alpha}_3$ are related using Equation (3.1.12), which gives:

$$\underline{\alpha}_3\sinh(\underline{\sigma}(h-d)) = \underline{\alpha}_2(-\sinh(\underline{\sigma}d) + \frac{\omega^2}{g\underline{\sigma}}\cosh(\underline{\sigma}d)). \tag{3.1.19}$$

which is satisfied for:

$$\begin{cases} \underline{\alpha}_2 = \sinh(\underline{\sigma}(h-d)), \\ \underline{\alpha}_3 = -\sinh(\underline{\sigma}d) + \frac{\omega^2}{g\underline{\sigma}}\cosh(\underline{\sigma}d), \end{cases} \tag{3.1.20}$$

As described in next subsection multiple values of σ are allowed. Consequently, the potentials in zones 2 and 3 are the sum of modes, where each modes corresponds to a possible value of $\underline{\sigma}$. Thus, ϕ_2 and ϕ_3 write as:

$$\underline{\phi}_2 = \sum_{n=-2}^{\infty}(\underline{A}_n e^{i\underline{\sigma}_n(x+a)} + \underline{B}_n e^{-i\underline{\sigma}_n(x-a)}))\underline{G}_n^{(2)}(z), \tag{3.1.21}$$

and:

$$\underline{\phi}_3 = \sum_{n=-2}^{\infty}(\underline{A}_n e^{i\underline{\sigma}_n(x+a)} + \underline{B}_n e^{-i\underline{\sigma}_n(x-a)})\underline{G}_n^{(3)}(z). \tag{3.1.22}$$

Exponential functions are written as a function of $x+a$ and $x-a$ in order to simplify expressions in the remainder of the Section. The index n is the index of the mode number and $\underline{G}_n^{(2)}$ and $\underline{G}_n^{(3)}$ are defined as:

$$\begin{cases} \underline{G}_n^{(2)}(z) = [\frac{\omega^2}{g\underline{\sigma}_n}\sinh(\underline{\sigma}_n z) + \cosh(\underline{\sigma}_n z)]\sinh(\underline{\sigma}_n(h-d)), \\ \underline{G}_n^{(3)}(z) = [\frac{\omega^2}{g\underline{\sigma}_n}\cosh(\underline{\sigma}_n d) - \sinh(\underline{\sigma}_n d)]\cosh(\underline{\sigma}_n(z+h)), \end{cases} \tag{3.1.23}$$

As made by Renzi [2016], the summation begins at $n=-2$ to add degrees of freedom. It is a practical choice that allows to introduce easily the plate boundary conditions in the equation system to be solved in the end.

Wave-number in zones 2 and 3, $\underline{\sigma}_n$

As in Section 2.2.1, the plate equation of motion is given by:

$$EI\partial_x^4\Xi(x) + \rho_p S\partial_t^2\Xi(x) = F_p(x), \tag{3.1.24}$$

where F_p is the pressure force acting on the plate, E is Young's modulus, I the moment of inertia, Ξ the plate displacement, ρ_p plate density and S plate cross section. As buoyancy is neglected, considering that the forcing is harmonic, and since the problem is linear, Ξ and F_p can be separated into the product of a function of space and a function of time so that:

$$\Xi(x,t) = \mathrm{Re}\left\{\underline{\xi}(x)e^{-i\omega t}\right\} \text{ and } F_p = \mathrm{Re}\left\{\underline{f}_p(x)e^{-i\omega t}\right\}. \tag{3.1.25}$$

In the complex space, it leads to:

$$EI\partial_x^4\underline{\xi} - \rho_p\omega^2 S\underline{\xi} = \underline{f}_p. \tag{3.1.26}$$

Both $\underline{\xi}$ and $\underline{f}_p$ can be expressed in terms of the flow potential using plate boundary condition (3.1.3) and pressure forces expressions. On the one hand, over the plate length:

$$\underline{\xi}(x) = \frac{i}{\omega}\partial_z\underline{\phi}(x,-d),\ \forall x \in [-a,a]. \tag{3.1.27}$$

On the other hand, the pressure applied on the plate, $\mathbf{f_p}$, is the sum of the pressure force applied by the flow in zone 2 and the flow in zone 3:

$$\mathbf{f_p} = \mathbf{f_{p2}} + \mathbf{f_{p3}}, \tag{3.1.28}$$

with $\mathbf{f_{p(2,3)}}$ pressure forces applied by the flow in zone 2 and 3 respectively. $\mathbf{f_{(2,3)}}$ can be expressed as:

$$\begin{cases} \mathbf{f_{p2}} = -P_2\mathbf{dS_2}, \\ \mathbf{f_{p3}} = -P_3\mathbf{dS_3}, \end{cases} \tag{3.1.29}$$

with $\mathbf{dS_{(2,3)}}$ oriented surfaces along the plate width. Using the fact that the dynamic pressure can be related to the potential (see Equation (2.1.33)). Note that static pressure does not intervene in this problem as all the plate is at the same depth. Coming back to the complex space, it is obtained that:

$$\begin{cases} \underline{\boldsymbol{f_{p2}}} = -i\omega\rho\phi_2 b\mathbf{e_z}, \\ \underline{\boldsymbol{f_{p3}}} = i\omega\rho\phi_3 b\mathbf{e_z}, \end{cases} \tag{3.1.30}$$

where $\mathbf{e_z}$ is a unit vector along the axis z and b is the plate width. In the end:

$$\underline{f_p} = ib\omega\rho(\underline{\phi_3} - \underline{\phi_2}). \tag{3.1.31}$$

Finally, Equation (3.1.26) can be rewritten solely in terms of the complex potentials:

$$EI\frac{i}{\omega}\partial_x^4\partial_z\underline{\phi}_{2,3}(x,-d) - \rho_p\omega^2 S\frac{i}{\omega}\partial_z\underline{\phi}_{2,3}(x,-d) = ib\omega\rho(\underline{\phi_3}(x,-d) - \underline{\phi_2}(x,-d)),\ \forall x \in [-a,a] \tag{3.1.32}$$

Injecting potentials expressions in the Equation (3.1.32), the dispersion relation in zones 2 and 3 is obtained:

$$\begin{aligned}&[\frac{EI\underline{\sigma}_n^4}{\omega} - \rho_p S\omega](\frac{\omega^2}{g\underline{\sigma}_n}\cosh(\underline{\sigma}_n d) - \sinh(\underline{\sigma}_n d))\underline{\sigma}_n \tanh(\underline{\sigma}_n(h-d)) \\ &= b\omega\rho[\frac{\omega^2}{g\underline{\sigma}_n}\cosh(\underline{\sigma}_n d) - \sinh(\underline{\sigma}_n d) - (\cosh(\underline{\sigma}_n d) - \frac{\omega^2}{g\underline{\sigma}_n}\sinh(\underline{\sigma}_n d))\tanh(\underline{\sigma}_n(h-d))].\end{aligned} \tag{3.1.33}$$

From that expression, it appears that wave-numbers are imposed by plate properties. More

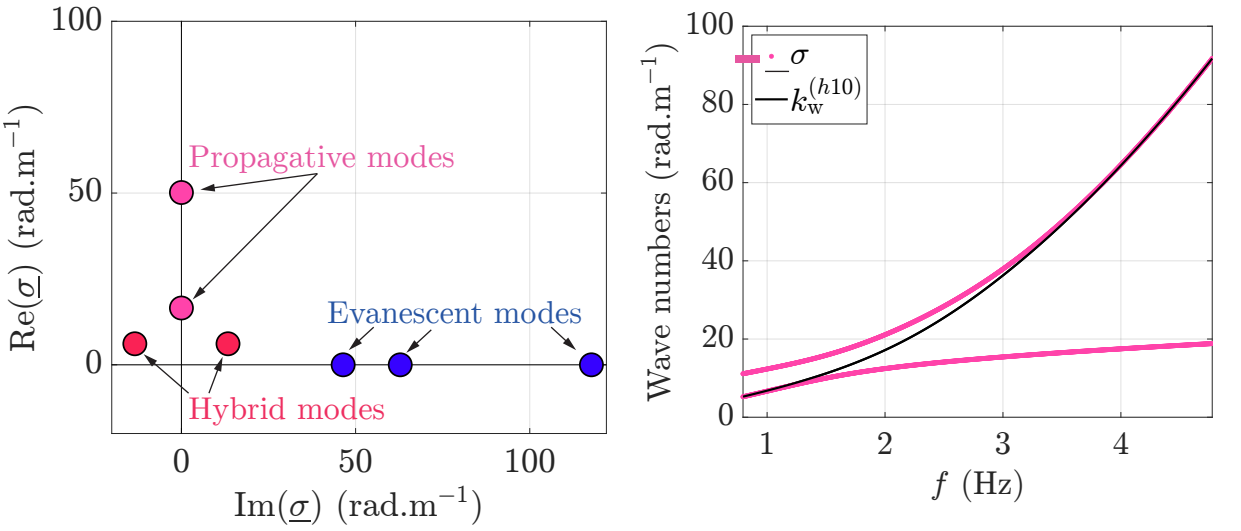

Figure 3.2: **A** Roots of Equation 3.1.33 in the complex space. Wave frequency, f, is taken equal to 3.5 Hz, total depth, h=10 cm, plate stiffness, EI=0.08 N.m^2, plate depth, $d = 5$ cm, plate thickness, $l = 1$ mm, plate density, ρ_p=1200 kg.m^{-3} and, plate width, b=10 cm. Those parameters are the same in Section 3.3.1. As in [Hassan et al., 2009], [Renzi, 2016] or [Behera, 2021] two roots are found to be real, two to be in the complex plane and others are imaginary. **B** Curves in pink represent the two real roots evolution as a function imposed frequency f. Black curve shows, ($k_{\mathrm{w}}^{(h10)}$), gravity waves wave number for a 10 cm total depth. At low frequencies, the smaller real root matches with waves dispersion relation over a 10 cm, while at higher frequencies it is the larger real value of σ that matches $k_{\mathrm{w}}^{(h10)}$.

specifically, it depends on the plate stiffness EI, the plate density, ρ_p, thickness, l, submer-

gence depth, d. It also depends on water depth, h and on the wave frequency. In the end, the only parameter of which $\underline{\sigma}_n$ are independent is the plate length. The roots of this equation can be found numerically in the complex space. As the dispersion relation is even in terms of $\underline{\sigma}_n$, each mode is associated with two possible values of $\underline{\sigma}_n$. As done by Hassan et al. [2009], Renzi [2016] or Behera [2021], only values in the first and fourth quadrants of the complex plane are considered to avoid repetitions. Dispersion relation root values are illustrated in Figure 3.2 **A** for a plate at a 5 cm depth, for a 10 cm total depth and 2 Hz waves. The dispersion relation results in two purely propagative modes, corresponding to the two real-valued roots of the equation, an infinity of evanescent (or non-propagative) modes corresponding to purely imaginary solutions, and two hybrid modes corresponding to $\underline{\sigma}$ being in the complex plane. The evolution of the two $\underline{\sigma}$ values associated with propagative modes is presented in Figure 3.2 **B** as a function of the frequency f. Their evolution is compared to $k_{\mathrm{w}}^{(h10)}$, the wave number associated with gravity waves propagating over a flat bottom at a 10 cm depth. It appears that at lower frequencies ($f < 1.5$ Hz), the smaller real-valued $\underline{\sigma}$ value matches with k while at higher frequencies ($f > 3.5$ Hz), k matches with larger real-valued $\underline{\sigma}$ value. This observation gives information on the plate deformation. Indeed, $\underline{\sigma}$ are also the wave number of plate modes because of Equation (3.1.12). Its states that for certain range of frequencies, one of the wave number propagating through the plate is the same as that of the incident wave. The exact range of frequencies where it is the case depends on the plate characteristics and configuration, but this effect occurs for most of the parameter sets tested.

Potential expression, $\underline{\phi}_4$, in zone 4

In zone 4, only transmitted waves propagate and evanescent waves have to be taken into account near the plate. The boundary conditions are the same as in zone 1 and ϕ_4 can be written as:

$$\underline{\phi}_4 = \sum_{n=0}^{\infty} \underline{T}_n e^{i\underline{k}_n(x-a)} Z_n(z), \tag{3.1.34}$$

with $\underline{T}_n$ being the complex amplitude of the mode n in zone 4.

Boundary condition of the plate

Plate boundary conditions are the same as in Chapter 2, Section 2.2.1:

$$\begin{cases} \underline{\xi}(-a) = 0 \\ \underline{\xi}'(-a) = 0 \\ \underline{\xi}''(a) = 0 \\ \underline{\xi}'''(a) = 0 \end{cases}, \tag{3.1.35}$$

As previous works focus either on semi-infinite plates or on plates held at both edges, computing the boundary conditions of Equation (3.1.35) constitutes the main difference with respect to previous studies. Utilizing Equation (3.1.27), Equation (3.1.35) can be expressed in terms of potentials, so that:

$$\begin{cases} \sum_{n=-2}^{\infty}(\underline{A}_n + \underline{B}_n e^{2i\underline{\sigma}_n a})\underline{G}_n'^{(2,3)}(-d) = 0 \\ \sum_{n=-2}^{\infty} i\underline{\sigma}_n(\underline{A}_n - \underline{B}_n e^{2i\underline{\sigma}_n a})\underline{G}_n'^{(2,3)}(-d) = 0 \\ \sum_{n=-2}^{\infty} -\underline{\sigma}_n^2(\underline{A}_n e^{2i\underline{\sigma}_n a} + \underline{B}_n \underline{G}_n'^{(2,3)}(-d) = 0 \\ \sum_{n=-2}^{\infty} -i\underline{\sigma}_n^3(\underline{A}_n e^{2i\underline{\sigma}_n a} - \underline{B}_n \underline{G}_n'^{(2,3)}(-d) = 0 \end{cases}, \tag{3.1.36}$$

with $\underline{G}_n'^{(2,3)}$ the derivative of $\underline{G}_n^{(2)}$ or $\underline{G}_n^{(3)}$ according to z. As for $z = -d$ derivatives of $\underline{G}_n^{(2)}$ and $\underline{G}_n^{(3)}$ are equal, either $\underline{G}_n'^{(2)}$ or $\underline{G}_n'^{(3)}$ can be used interchangeably.

System solution

At this point, four families of unknown variables remain, $(\underline{R}_n)_{n\in\mathbb{N}}$, $(\underline{T}_n)_{n\in\mathbb{N}}$, $(\underline{A}_n)_{n\in\mathbb{N}}$ and $(\underline{B}_n)_{n\in\mathbb{N}}$. The system of equations (3.1.36) gives the first four relations between these amplitudes. Other relations come from the continuity equations between zones 1 and 2-3 and zones 2-3 and 4. The pressure being continuous, it is imposed that:

$$\underline{\phi}_1(-a,z) = \begin{cases} \underline{\phi}_2(-a,z), & \forall\ z \in [-d,0]. \\ \underline{\phi}_3(-a,z), & \forall\ z \in [-h,-d]. \end{cases} \tag{3.1.37}$$

$$\underline{\phi}_4(a,z) = \begin{cases} \underline{\phi}_2(a,z), & \forall\ z \in [-d,0]. \\ \underline{\phi}_3(a,z), & \forall\ z \in [-h,-d]. \end{cases} \tag{3.1.38}$$

As the fluid velocity in the x direction, u_x, must also be continuous between zone 1 and 2-3 and zone 2-3 and 4, the following equations are obtained:

$$\partial_x\underline{\phi}_1(-a,z) = \begin{cases} \partial_x\underline{\phi}_2(-a,z), & \forall\ z \in [-d,0]. \\ \partial_x\underline{\phi}_3(-a,z), & \forall\ z \in [-h,-d]. \end{cases} \tag{3.1.39}$$

$$\partial_x\underline{\phi}_4(a,z) = \begin{cases} \partial_x\underline{\phi}_2(a,z), & \forall\ z \in [-d,0]. \\ \partial_x\underline{\phi}_3(a,z), & \forall\ z \in [-h,-d]. \end{cases} \tag{3.1.40}$$

Upon integrating previous equations over the fluid depth and using orthogonality of $(Z_n)_{n\in\mathbb{N}}$, it can be found that, $\forall\ m \in \mathbb{N}$:

$$0 = \frac{2igA}{\omega}\delta_{m0} + \frac{1}{N_m}\sum_{n=-2}^{\infty}[(1+\frac{\underline{\sigma}_n}{\underline{k}_m})\underline{A}_n + (1-\frac{\underline{\sigma}_n}{\underline{k}_m})\underline{B}_n \mathrm{e}^{2i\underline{\sigma}_n a}]\underline{b}_{nm}, \tag{3.1.41}$$

$$0 = \sum_{n=-2}^{\infty}((1-\frac{\underline{\sigma}_n}{\underline{k}_m})\underline{A}_n \mathrm{e}^{2i\underline{\sigma}_n a} + (1+\frac{\underline{\sigma}_n}{\underline{k}_m})\underline{B}_n)\underline{b}_{nm}, \tag{3.1.42}$$

$$\underline{T}_m = \frac{1}{N_m}\sum_{n=-2}^{\infty}(\underline{A}_n \mathrm{e}^{2i\underline{\sigma}_n a} + \underline{B}_n)\underline{b}_{nm}, \tag{3.1.43}$$

and

$$\underline{R}_m = \frac{igA}{\omega}\delta_{m0} + \frac{1}{N_m}\sum_{n=-2}^{\infty}(\underline{A}_n + \underline{B}_n \mathrm{e}^{2i\underline{\sigma}_n a})\underline{b}_{nm}. \tag{3.1.44}$$

$$\begin{cases} a_m = \int_{-h}^{0} \frac{\cosh(k_0(z+h))}{\cosh(k_0 h)} Z_m(z)\mathrm{d}z, \\ \underline{b}_{nm} = \int_{-d}^{0} \underline{G}_n^{(2)}(z) Z_m(z)\mathrm{d}z + \int_{-h}^{-d} \underline{G}_n^{(3)}(z) Z_m(z)\mathrm{d}z, \\ N_m = \int_{-h}^{0} Z_m^2(z)\mathrm{d}z. \end{cases} \tag{3.1.45}$$

In summary, $(\underline{R}_n)_{n\in\mathbb{N}}$, $(\underline{T}_n)_{n\in\mathbb{N}}$ are expressed as a function of $(\underline{A}_n)_{n\in\mathbb{N}}$, $(\underline{B}_n)_{n\in\mathbb{N}}$. The last two family of unknowns, $(\underline{A}_n)_{n\in\mathbb{N}}$ and $(\underline{B}_n)_{n\in\mathbb{N}}$, are found numerically by solving the system of equations given by Equation (3.1.41) and Equation (3.1.42).

3.2 Numerical procedures

The problem exposed in Section 3.1 has to be solved numerically since no analytical solution can be easily found. Particular numerical procedures are utilized for two calculations. Firstly, in order to solve the dispersion relation in zones (2,3), $(\underline{\sigma}_n)_{n\in\mathbb{N}}$ values are determined. Secondly, in order to calculate $(\underline{A}_n)_{n\in\mathbb{N}}$ and $(\underline{B}_n)_{n\in\mathbb{N}}$ values, the system formed by Equations (3.1.41) and (3.1.42) is solved.

3.2.1 Relation dispersion root calculation

$(\underline{\sigma}_n)_{n\in\mathbb{N}}$ are complex values. Consequently, the dispersion relation in zones 2 and 3 has to be solved in the complex space. The Matlab[1] built-in tool, $fsolve$, is utilized to that aim. $fsolve$ is a function which comprises several root-finding algorithms. It only returns one solution per call, which may depend on the (user-defined) initial guess, on the chosen root-finding algorithm, and on the existence, or otherwise, of multiple zeros. However, multiple roots have to be found in the complex plane, which requires multiple calls to $fsolve$, with appropriate initial guesses. In practice, the calls are performed with initialization values,

[1] www.mathworks.com

homogeneously distributed following a regular grid in the complex space. The chosen grid for initialization values is refined enough to ensure that no root is missed in the intervals between neighbouring solutions. Redundant values are obtained and have to be deleted, providing the final set of $\underline{\sigma}_n$. Note that the number of roots depend on the size of the domain of initialization values.

3.2.2 $(\underline{A}_n)_{n\in\mathbb{N}}$ and $(\underline{B}_n)_{n\in\mathbb{N}}$ calculation

To solve the system formed by Equations (3.1.41) and (3.1.42), infinite sums have to be truncated to a certain number, N_{trunc}. The influence of N_{trunc} on the final result is discussed in Section 3.3.1. The truncated system is then written as a matrix equation:

$$Y = DX, \tag{3.2.1}$$

where X contains the two families of unknowns, $(\underline{A}_n)_{n\in\mathbb{N}}$ and $(\underline{B}_n)_{n\in\mathbb{N}}$ and Y is a column matrix corresponding to the second member of the system given by Equation (3.1.41) and Equation (3.1.42). X and Y can be written:

$$X = \begin{pmatrix} A_{-2} \\ A_{-1} \\ A_0 \\ \vdots \\ A_{N_{\text{trunc}}} \\ B_{-2} \\ B_{-1} \\ B_0 \\ B_1 \\ \vdots \\ B_{N_{\text{trunc}}} \end{pmatrix} \quad \text{and} \quad Y = \begin{pmatrix} 0 \\ 0 \\ 0 \\ \vdots \\ 0 \\ 0 \\ 0 \\ 0 \\ \frac{-2igA}{\omega} \\ 0 \\ \vdots \\ 0 \end{pmatrix}.$$

D contains the prefactors of boundary conditions on its first four lines and the prefactors of Equations (3.1.41) and (3.1.42). D is given in Appendix for $N_{\text{trunc}} = 1$.
Expressions of $(\underline{A}_n)_{n\in\mathbb{N}}$ and $(\underline{B}_n)_{n\in\mathbb{N}}$ are then simply obtained by numerically inverting Equation (3.2.1).

3.3 Study of a baseline case

3.3.1 Baseline case: reflection and transmission

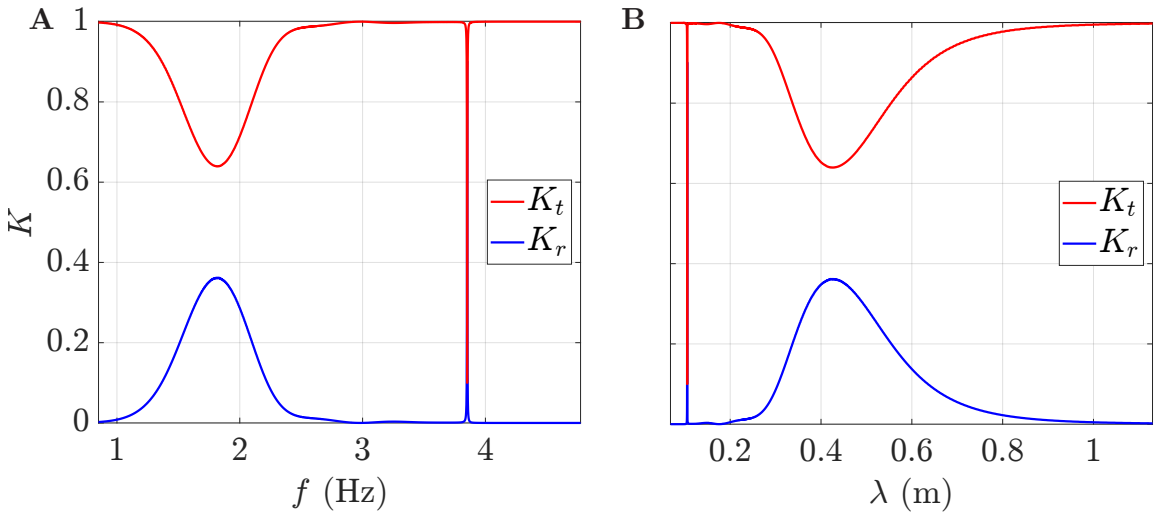

Figure 3.3: **A** Reflection and transmission coefficients, K_r and K_t as a function of wave frequency, f, for a plate of stiffness EI=9.10^{-2} N.m^2, density, ρ_p=1200 kg.m^{-3}, length L = 28 cm, thickness l = 1 mm and a plate depth of 5 cm over a 10 cm total depth. Two reflection peaks can be observed a wide one at 1.8 Hz and a sharper one at 3.85 Hz. **B** Reflection and transmission coefficients, K_r and K_t as a function of wave wavelength, λ. The same reflection peaks can be observed at respectively the associated wavelengths.

$\underline{R_1}$ and $\underline{T_1}$ are associated with propagative modes up-wave and down-wave. In other terms, $\underline{R_1}$ stands for the complex amplitude of the reflected wave and $\underline{T_1}$ is the transmitted wave complex amplitude. Thus, $\underline{R_1}$ and $\underline{T_1}$ calculations allows to obtain reflection and transmission coefficients, K_r and K_t as defined in Chapter 2, Section 2.1. K_r and K_t are defined as:

$$\begin{cases} K_r = (\frac{\omega}{gA})^2 \underline{R_1}\underline{R_1^*}, \\ K_t = (\frac{\omega}{gA})^2 \underline{T_1}\underline{T_1^*}, \end{cases} \tag{3.3.1}$$

with the superscript, *, designating the complex conjugate.

This section presents the K_r and K_t calculation for a specific plate. The physical parameters chosen for this section are representative of the experimental setup (see Chapter 4). As for the experiments, the water depth, h, is fixed at 10 cm. The plate characteristics are given in Table 3.1.

A well characterized behavior is observed with this parameters choice. K_r and K_t are shown

Plate depth, d	Plate length, L	Plate thickness, l	Plate width, b	Density, ρ_p	Stiffness, EI
5 cm	28 cm	1 m	10 cm	1200 kg.m^{-3}	8.10^{-2} N.m^2

Table 3.1: Plate characteristics.

for such a plate in Figure 3.3 as a function of wave frequency, f, (**A**) and of the incident wave wavelength, λ (**B**) for $N_{\text{trunc}} = 20$. It appears that in such a configuration, a submerged elastic plate reflects waves for a certain range of frequencies or wavelengths. More precisely, two different reflection zones can be observed. A wide one, between f =1.2 Hz and f =2.3 Hz or λ = 0.3 m and λ =0.75 m and a sharp reflection peak located around f=3.85 Hz or $\lambda = 0.105$ m.

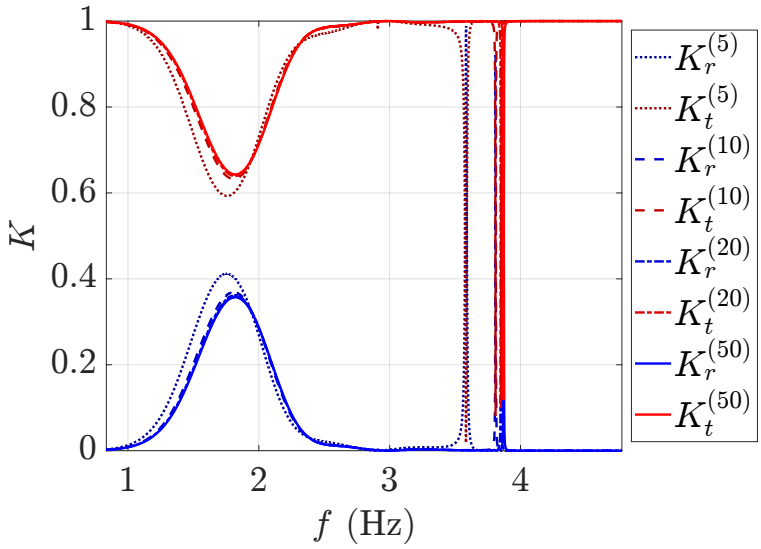

Figure 3.4: Coefficients of reflection and transmission, K_r and K_t as a function of wave frequency for different values of N_{trunc} for the same parameters as in Figure 3.3. Dotted curve corresponds to $N_{\text{trunc}} = 5$, dashed curve to $N_{\text{trunc}} = 10$, alternation of dash and points to $N_{\text{trunc}} = 20$ and plain curve to $N_{\text{trunc}} = 50$. For $N_{\text{trunc}} \geq 20$, curves are coherent with each other.

Convergence test

Figure 3.3 is obtained by solving the system given by Equation (3.1.41) and Equation (3.1.42) truncated at $N_{\text{trunc}} = 20$. Evaluating the truncation impact is primordial in order to confirm calculation accuracy. Figure 3.4 shows K_r and K_t calculations for N_{trunc} equal to 5, 10, 20 and 50 as a function of wave frequency. For $N_{\text{trunc}} \geq 10$, it appears that K_r and K_t show negligible variations. In the remainder of this thesis, N_{trunc} is taken equal to 20. It is chosen

as an appropriate compromise between accuracy and computational cost.

K_r and K_t as a function of normalized quantities

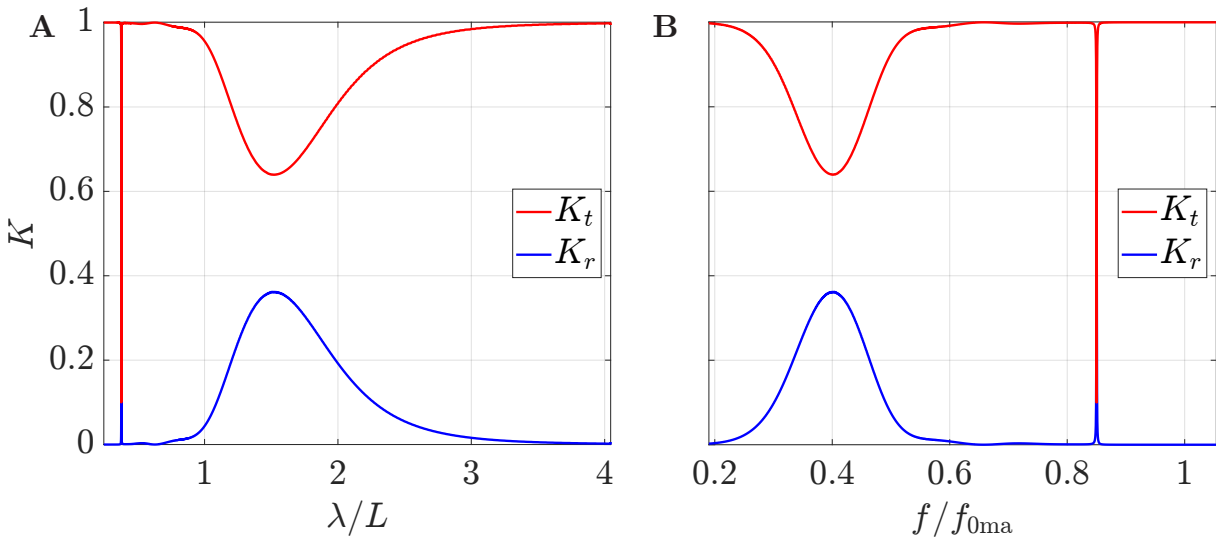

Figure 3.5: **A** Reflection and transmission coefficients, K_r and K_t as a function of wave wavelength, λ, normalized by plate length, L. **B** Reflection and transmission coefficients, K_r and K_t as a function of wave frequency, f, normalized by plate resonance frequency, $f_{0\mathrm{ma}}$, for which added mass is taken into account. The same reflection peaks can be observed at the associated wavelengths.

Reflection can be caused primarily by geometrical effects (**i.e.** diffraction by the plate), by the plate motion (radiation effect) or a combination of both. To investigate a possible link between reflection and plate dimensions, Figure 3.5 **A** presents K_r and K_t as a function of wavelength normalized by plate length, L. A sharp reflection peak occurs at $\lambda/L = 0.37$, and wide peak for $1 \leq \lambda/L \leq 3$ the effect of plate length on reflection is not obvious.
To discuss a possible radiation effect, K_r and K_t are plotted in Figure 3.5 **B** as a function of wave frequency, f, normalized by $f_{0\mathrm{ma}}$, the plate resonance frequency in a still fluid. $f_{0\mathrm{ma}}$ is evaluated using Equation (2.2.20) with a typical plate amplitude of 1 mm. It appears that none of the two reflection peaks is located at $f/f_{0\mathrm{ma}}$=1. It means that reflection is not due to the excitation of the plate at its resonance frequency in a still fluid. However, this observation does not exclude radiation effects to be responsible for reflection. It is just stated here that reflections are not due to a simple resonance at the plate natural frequency.
The latter two observations allows to appreciate the complexity of the system studied here. To gain insight on this complex behavior, some of the simulation parameters are changed and the plate motion is analyzed.

3.3.2 Submerged elastic plate motion in the baseline case

Section 3.3.1 has shown reflection and transmission coefficients for a given plate configuration. Those calculations have shown that a submerged elastic plate is able to reflect waves. Two types of reflection were highlighted, a wide reflection peak and sharper ones. This section focuses on plate motion and aims at investigating the connection between reflection and transmission coefficients calculation and plate motion amplitude.

Plate motion observation in the baseline case at given frequencies

The plate deformation can be calculated from the potential, ϕ, using Equation (3.1.27). It allows to compute the plate deflection profile at every time. This section shows motion of the first plate presented in Section 3.3.1 at four different frequencies. As a reminder, r=1019.2, d=5 cm and $L = 28$ cm for this plate. Figure 3.6 **A** shows three captions of the elastic plate in a wave field corresponding to three different times over a wave period T. The x axis extends from -2a to 2a or equivalently, -L to L and the z axis from 0 to -h the total depth. In Figure 3.6 **A**, the wave frequency is 1 Hz and wave incoming amplitude, A is taken equal to 2 mm. The plate is represented in black and colors from blue to red correspond to the dynamical pressure, p. At 1 Hz the elastic plate transmits waves almost completely, with $K_t \simeq 1$. This can be seen looking at dynamical pressure in the domain where maximum intensity down-wave is the same as maximum intensity up-wave. Figure 3.6 **B** shows a superposition of the plate position over one wave period for the same parameters as Figure 3.7 **A**. The plate amplitude, ξ, is similar to that of A. Furthermore, the inset in the top left of the Figure shows the decomposition of the plate motion on the deformation modes of a cantilevered beam of identical dimensions. To obtain the amplitude of each mode, ξ can be decomposed, so that:

$$\xi(x) = \sum_n \xi_n f_n(x), \tag{3.3.2}$$

with ξ_n being the n^{th} mode amplitude and f_n the n^{th} eigenfunction, as defined in Chapter 2, Section 2.2.1. For a given n, the modes amplitudes, ξ_n, can be computed as:

$$\xi_n = \frac{1}{2a}\int_{-a}^{a} \xi(x) f_n(x) \mathrm{d}x, \quad \forall n \in \mathbb{N}. \tag{3.3.3}$$

In the inset, the mode amplitudes are normalized by $\hat{\xi}$, the normalized plate amplitude defined as:

$$\hat{\xi} = \sqrt{\frac{1}{L}\int_0^L \frac{\xi(x)^2}{A^2}\mathrm{d}x}. \tag{3.3.4}$$

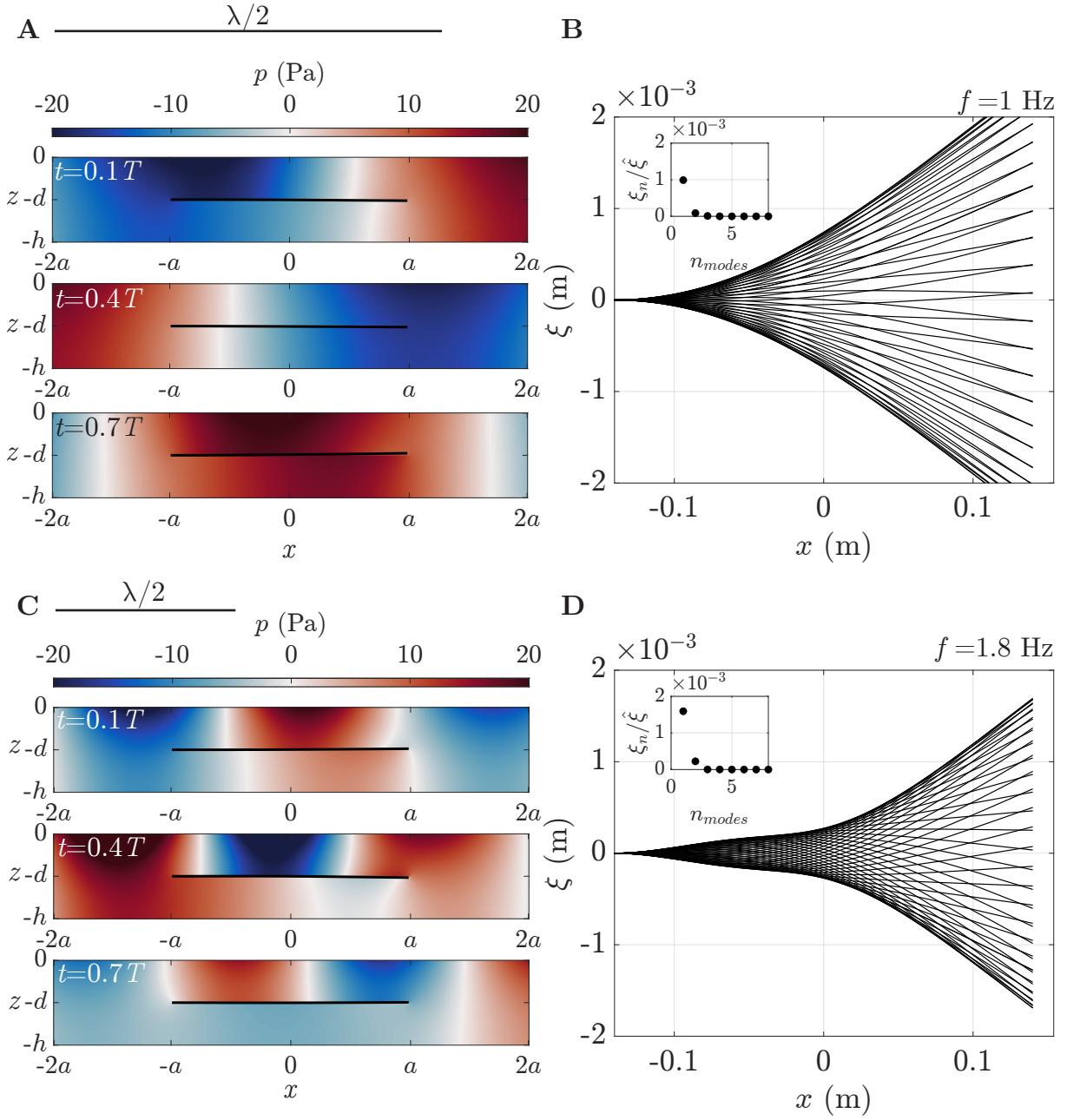

Figure 3.6: **A** Caption showing the plate forced by waves of 1 Hz frequency and 2 mm amplitude. The representation domain goes from the free surface to bottom depth, $z = -h$ and $-2a$ to $2a$ at three different times, t, during a wave period, T. Colors represent the dynamic pressure, p. **B** Superposition of plate positions over one wave period. The inset presents plates modes amplitude. **C** and **D** same as **A** and **B** but for 1.8 Hz wave frequency.

This definition of $\hat{\xi}$ allows to quantify the plate motion amplitude independently of the plates modes and wave amplitude. Here, the plate motion corresponds mostly to the first mode of a cantilever beam.

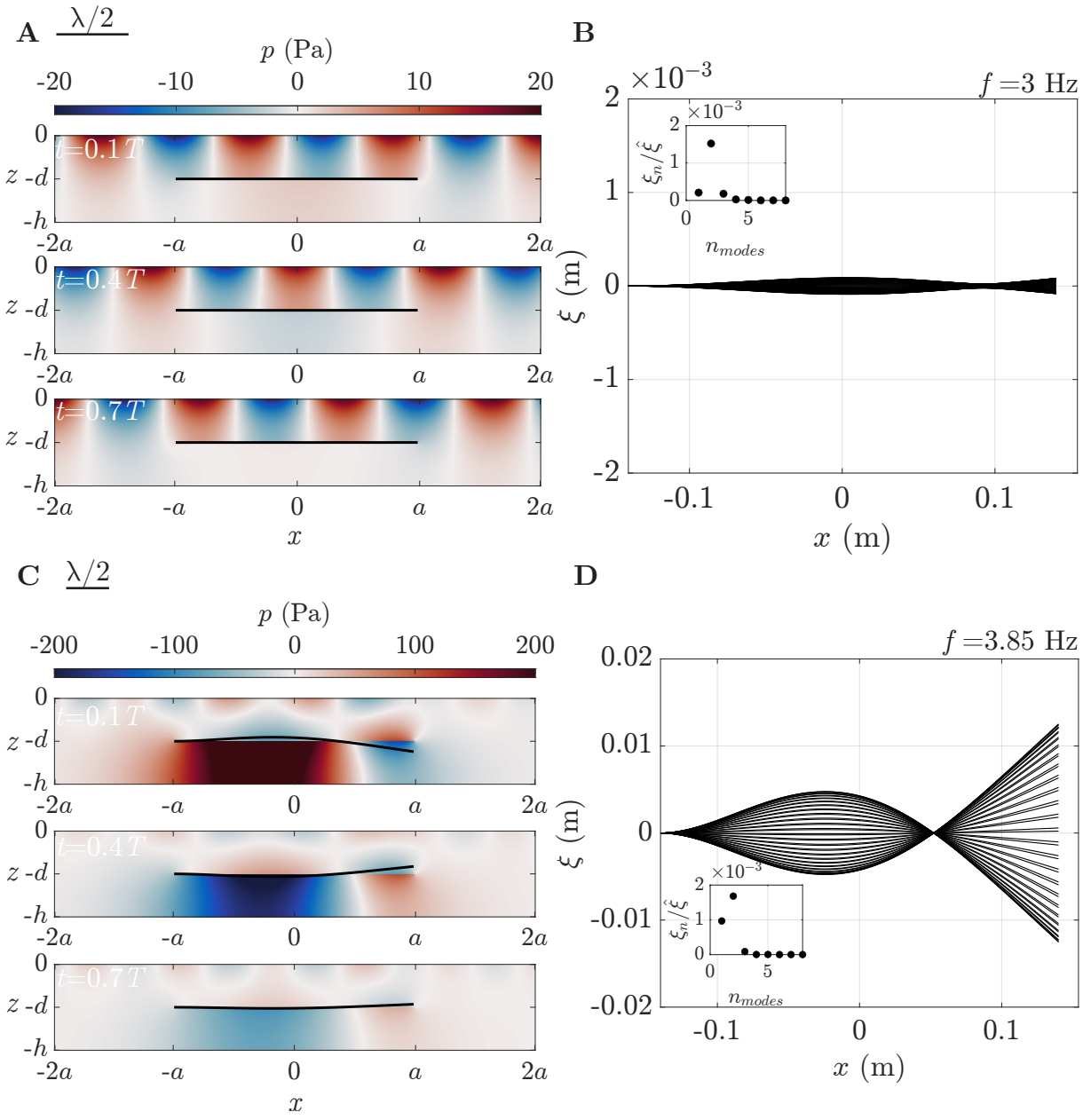

Figure 3.7: Same as Figure 3.6 but for f=3 Hz (**A** and **B**) and f=3.85 Hz (**C** and **D**).

Figure 3.6 **C** shows the plate at 1.8 Hz. This frequency corresponds to the wide peak maximum where $K_r \simeq 0.38$. The plate seems to have a more significant effect on the flow than at 1 Hz. Particularly, at $t = 0.4T$ a small depression ($p < 0$) can be observed at the tip of the plate. Figure 3.6 **D** shows ξ for different time over one wave period. Plate amplitude appears to be slightly lower than at 1 Hz but the excited modes remain qualitatively similar as $n_{\text{modes}} = 1$ is still predominant.

Figure 3.7 **A** shows the plate at 3 Hz, a frequency for which K_t=1 and $K_r = 0$. As in

Figure 3.6 **A** the plate does not perturb much the wave field. Figure 3.7 **B** shows ξ over one wave period. At this frequency, the plate behavior changes drastically as the principal mode of the deformation is mode 2 and the plate amplitude of deformation is significantly smaller. The decrease in ξ maximum value can be explained because of the potential decrease with frequency at a given depth. Indeed, as shown in Chapter 2, Section 2.1.1, ϕ, scales as $\frac{\cosh(k(z+h))}{\cosh(kh)}$ with depth z. Consequently, it is also the case of dynamical pressure and fluid velocity. As k increases with frequency, it implies that forcing on the plate decreases with frequency.

Finally, Figure 3.7 **C** and **D** show plate behavior for a wave frequency of 3.85 Hz, corresponding to the plate sharp peak. Note that compared to previous Figures, scales in Figures **C** and **D** have been multiplied by 10. The plate amplitude is drastically larger than at other frequencies as well as dynamic pressure. In Figure **C**, the plate undergoes considerable deformations, which results in the small plate amplitude assumption being violated. It results that the small plate amplitude assumption is broken in this situation. It is particularly visible in the first two captions, where the junction between zones 2 and 3 is visible, approximately 1 cm away from the plate tip. Maximum and minimum of pressure occurs under plate at the plate antinode. This behavior corresponds to a plate resonance. As shown in the inset, the resonance is not due to the excitation of a plate mode defined by an Euler-Bernoulli beam theory. Indeed, modes 1 and 2 coexist. A plausible explanation is the effect of radiation damping. Indeed, as the plate radiates waves, it experiences a force proportional to its speed. This force is not taken into account when calculating f_n and would modify the eigenfunction.

The normalized plate motion amplitude in the baseline case

In order to have a better view across all the frequencies, Figure 3.8 shows $\hat{\xi}$ normalized wave amplitude as a function of wave frequencies. Observation from snapshots are confirmed by this Figure. First, plate amplitude decreases from 0.8 Hz to 3 Hz to be almost equal to zero at 3 Hz. A minor elevation can be seen near the wide reflection peak exhibiting a small plate amplitude increase in that range of frequencies. At 3.85 Hz, $\hat{\xi}$ increases sharply exhibiting a clear resonance of the plate.

Consequently, reflection peaks appear to be associated with an increase in wave amplitude. The increase is more significant in the case of sharp reflection peaks.

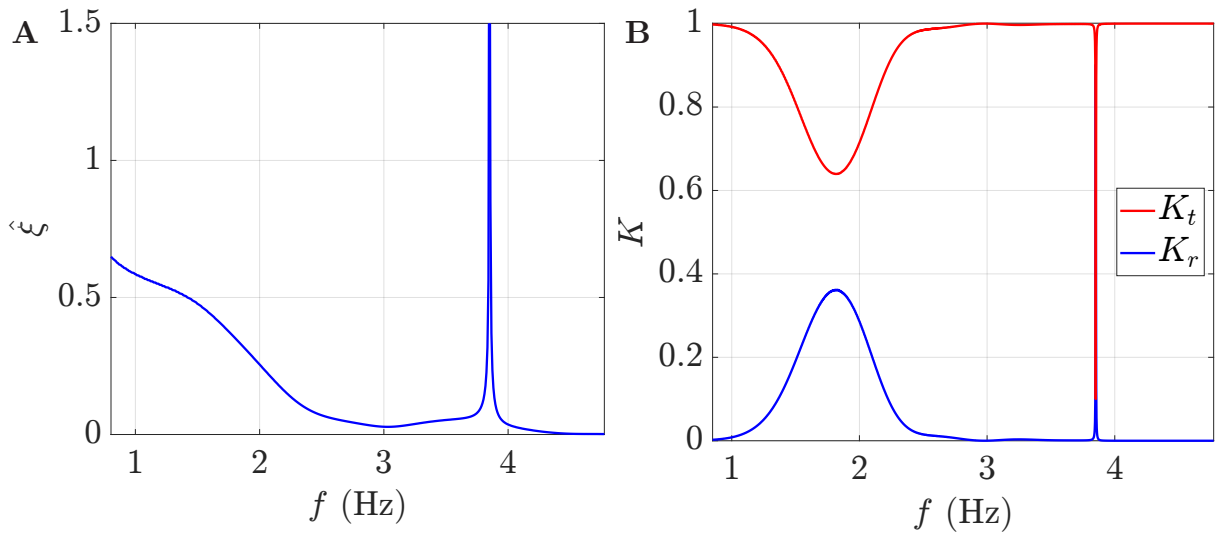

Figure 3.8: **A** Normalized wave amplitude, $\hat{\xi}$, as a function of wave frequency, f. For frequencies where waves are reflected, an increase in plate amplitude can be observed. **B** Same as Figure 3.3

3.4 Parametric analysis

3.4.1 Effect of plate depth

The effect of depth variation on the plate used in Section 3.3.1 is investigated in Figure 3.9. Figure 3.9 shows reflection and transmission as a function of wave frequency for eight different submergence depths ranging from 1 cm to 9 cm. As a reminder, results in Section 3.3.1 correspond to a 5 cm depth. In Figure 3.9 **A**, one can observe a much more complex transmission and reflection pattern for a 1 cm plate depth. Multiple wide peaks exist. For a 2 cm plate depth (Figure 3.9 **C**), a wide reflection peak is present between 1 and 1.8 Hz where K_r reaches values over 0.9. A second, relatively wide, peak can be seen between 2.5 and 3 Hz. Finally, a sharp reflection peak can be seen around 4.6 Hz. From comparison between **A** and Figure 3.9 **B**, it seems that most of wide peak intensities decreased at the exception of the reflections at lower frequencies.

Figure 3.9 **E** shows that reflection peaks observed in Figure 3.9 **A** and Figure 3.9 **C** are simply a growth of simple wide peaks that exist at a larger submergence depth. Indeed, it presents K_r and K_t for a plate located at a 3 cm depth. A first wide peak can be observed around 1.7 Hz with a maximum value close to 1. A smaller peak exist at 3 Hz, it can be seen as the initialization of the peak between 2.5 and 3 Hz at a 2 cm depth. Finally, a sharp peak can be seen close to 4.3 Hz.

Figures 3.9 **G**, **B**, **D**, **F**, and **H** show K_r and K_t for plate larger submergence depths ranging

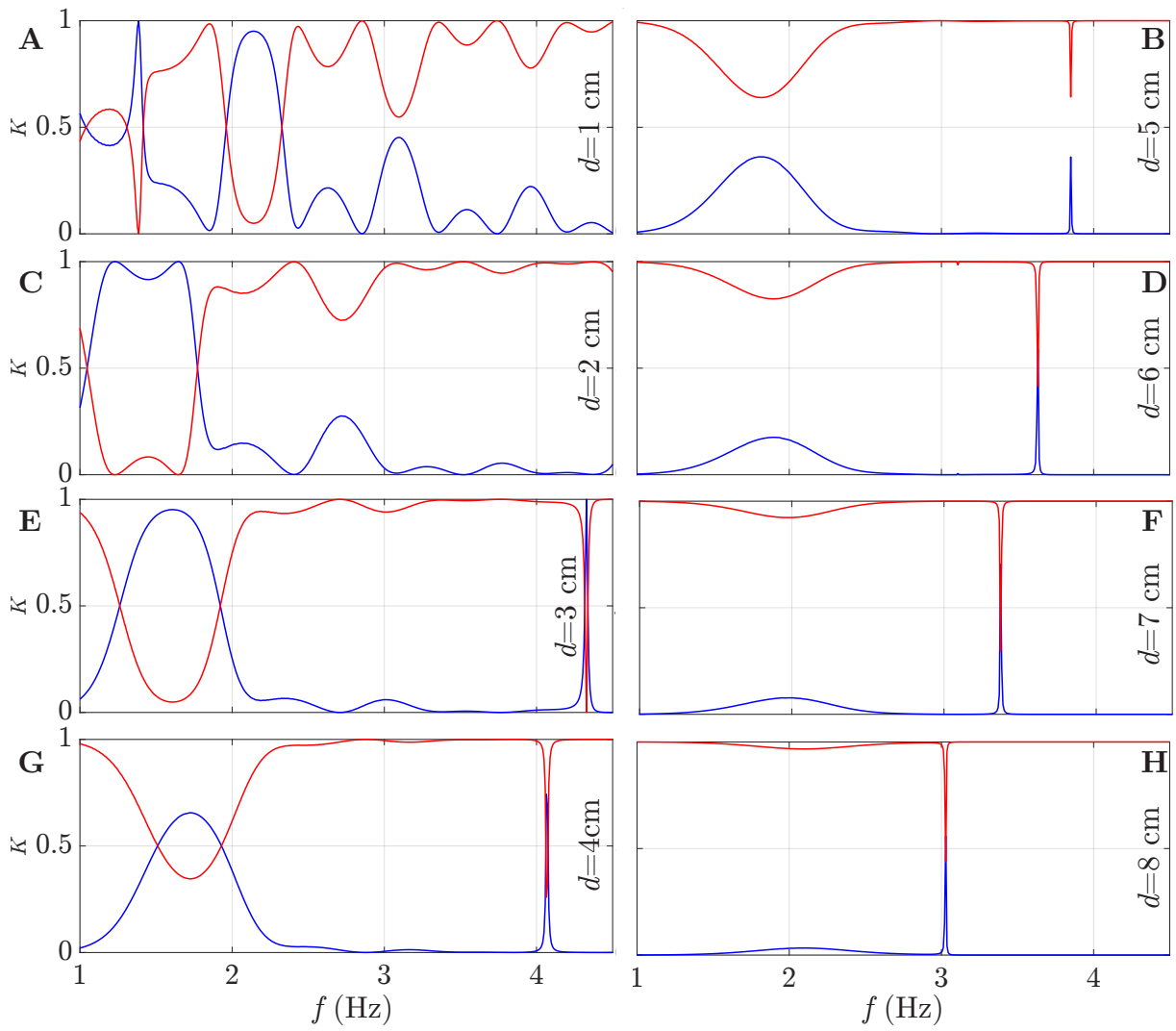

Figure 3.9: Effect of depth variation on wave transmission and reflection by a flexible plate of stiffness EI=9.10^{-2} N.m^2, density, ρ_p=1200 kg.m^{-3}, length, L = 28 cm and thickness, l = 1 mm, over a 10 cm total depth. **A** 1 cm depth, **B** 5 cm depth, **C** 2 cm depth, **D** 6 cm depth, **E** 3 cm depth, **F** 7 cm depth, **G** 4 cm depth and **H** 8 cm depth.

from 4 cm to 8 cm. Results in those figures confirm the trend highlighted in the aforementioned comments. Indeed, at lower frequencies a wide peak can be observed, and a sharper one is present at higher frequencies. The wide peak intensity decreases with depth and the frequency of its maximum is shifted towards higher frequencies when depth increases.
The comparison between all those figures gives a hint on mechanisms that lead to the apparition of complex reflection patterns at small submergence depth. The wide peak observed at a 2 cm submergence depth is shifted towards higher frequencies and its intensity decreases with depth. Wide peak shape at a 1 cm and 2 cm depths, with local minima at the center of the reflection zone, results from the increase in the reflection. As depth decreases, the peak

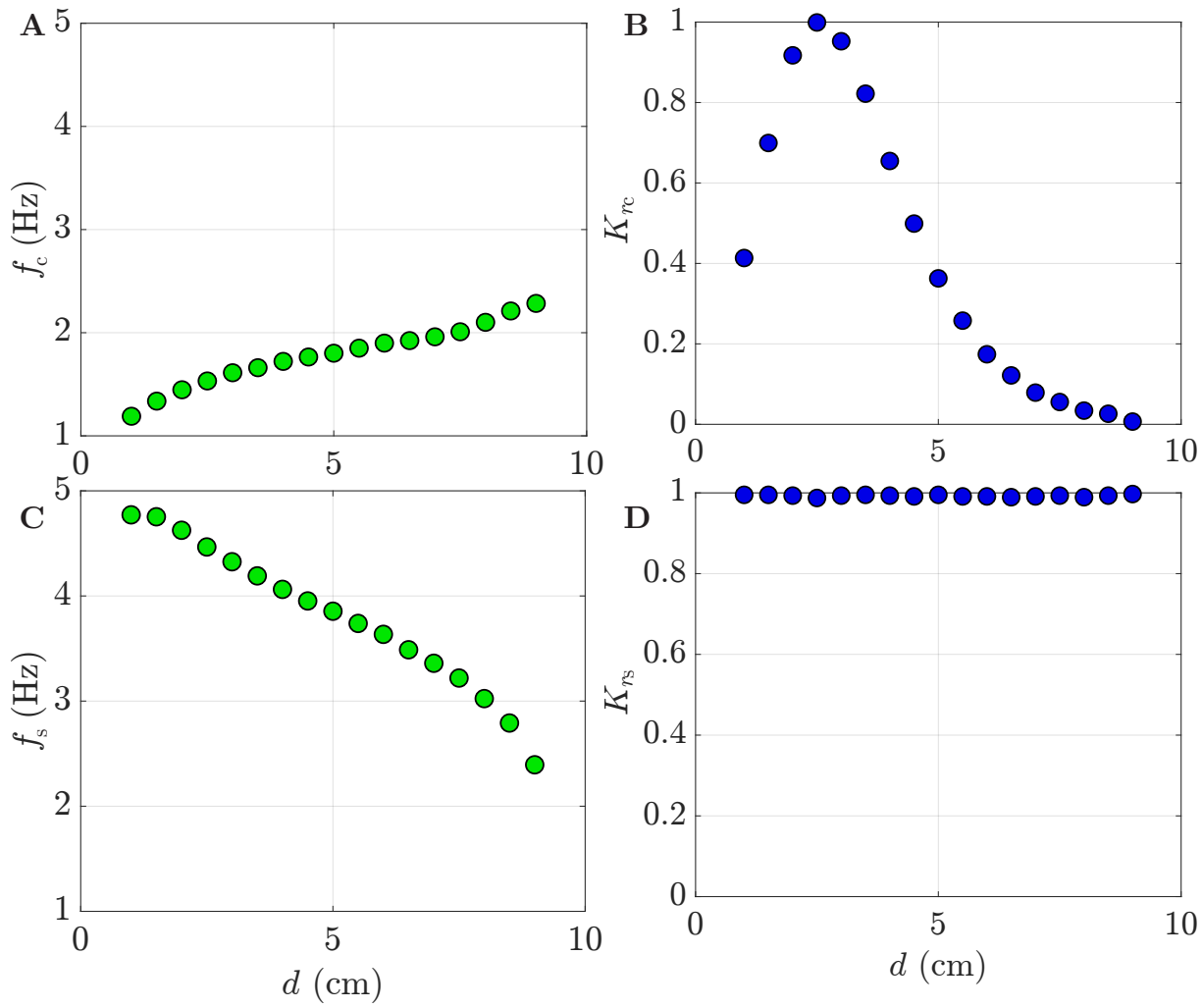

Figure 3.10: **A** Central frequency of the wide peak, f_c, as a function of plate submergence depth, d. **B** Reflection coefficient value at the central frequency, K_{rc} as a function of plate depth, d. **C** Sharp peak frequency as a function of plate depth. **D** Sharp peak maximum value.

grows and splits after K_r reaches 1 for a certain critical depth. Contrary to the wide peak, the sharp peak frequency decreases with depth.

To confirm the latter observations, the central frequency, f_c and the corresponding reflection value, K_{rc}, of the wide peaks are measured. Central frequency and value refer to the frequency and value at the center of the reflection zone. For instance, in the case of a 2 cm depth, the measured frequency and reflection values measured correspond to the local minimum at approximately 1.4 Hz. In the 2 cm case, the frequency measured is therefore 1.4 Hz and the reflection value is $\simeq$0.9. Similar measurements are performed to measure the frequency of sharp reflection peak, f_s and the associated reflection value. The definitions of K_{rc} and f_c are illustrated in Figure 3.9.

Measurement results are plotted in Figure 3.10. Figure 3.10 **A** shows the wide peak center

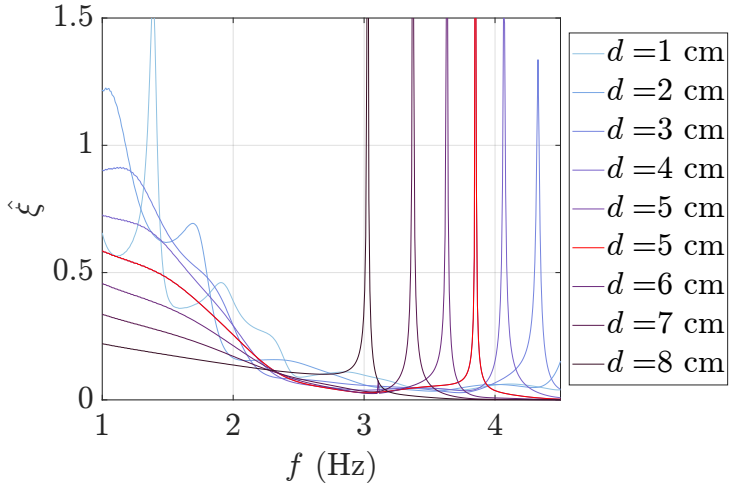

Figure 3.11: Plate normalized motion amplitude, $\hat{\xi}$ as a function of wave frequency for submergence depth ranging from 8 cm (darker curves) to 1 cm (lighter curves). The baseline case (d=5 cm) is represented in red.

location as a function of the plate submergence depth, d. It appears that the peak frequency increases with depth going from 1.1 Hz at 1 cm depth to 2.1 Hz at 9 cm. Central reflection value as a function of depth is represented in Figure 3.10 **B**. It can be observed that this value, first, increases with plate depth to reach 1 for a 2.5 cm depth. Then, K_r decreases to reach almost 0 for a 9 cm depth. The first increase in the reflection is a consequence of the dynamic described in Figure 3.9. For plate depth larger than 2.5 cm, reflection peaks have a fairly simple shape similar to a cardinal sinus. However, for plate depth smaller than 2.5 cm, peaks splits and a local minimum can be observed at their center. Results in Figure 3.10 **B** show that this local minimum decreases as the plate is closer to the surface. However, for plate depth smaller than 2.5 cm, total reflection, *i.e.* $K_r = 1$, happens for frequencies close to the one presented in Figure 3.10 **A**.

Figure 3.10 **C** shows sharp reflection peak frequency as a function of depth. Contrary to the wider peak, sharp reflection peak frequency decreases with depth. This behavior underlines that the two observed peaks are of different nature. Since no sharp peak can be observed for depth smaller than 2 cm in the considered frequency range, measurements in Figure 3.10 **C** start for a 2 cm submergence depth. However, given the observed trend, the sharp peak probably exists at larger frequencies, but it is located outside the measurement window.

Figure 3.10 **D** shows sharp reflection peak intensity for different values of plate depth d. Sharp peaks reach $K_r = 1$ for all configurations.

In summary, this section on depth influence shows that the two reflection peaks observed are of different nature. Indeed, the wide peak frequency increases with depth, contrary to sharp

peak frequency. In addition, the observation of the effect of depth variation indicates that reflection behavior is not only due to intrinsic plate properties such as stiffness, density or length, and is more probably due to a combination of all parameters.

Figure 3.11 shows normalized plate amplitude, $\hat{\xi}$, as a function of wave frequency, f, for depths ranging from 1 to 8 cm. For all depths, $\hat{\xi}$ decreases with wave frequency similarly to observations made for the baseline case. In addition, plate resonance is observed at sharp peaks frequencies. The sharp peak frequency dependence on plate submergence depth, described in Figure 3.10 **C** and **D**, is illustrated here as the plate resonance are located at higher frequencies for small submergence depths. At lower frequencies, $\hat{\xi}$ decreases with depth. Similarly to the case of reflection and transmission coefficients, complex patterns can be observed close to the free surface.

3.4.2 Effect of length

Similarly to depth, the plate length can be changed to investigate its effect on wave reflection and transmission. K_r and K_t are calculated for plate length, L, going from 4 cm to 120 cm. Other physical parameters are taken equal to their value in Section 3.3.1, $EI = 8.10^{-2}$ N.m^2, $d = 5$ cm, $h = 10$ cm, $e = 1$ mm, $b = 10$ cm and $\rho_{\mathrm{m}} = 1200$ kg.m^{-3}.

Figure 3.12 shows the results of eight K_r and K_t calculations for wave frequencies going from 1 Hz to 4.5 Hz and eight different plate lengths, L, ranging from 4 cm to 100 cm. As a reminder, $L = 28$ cm in Section 3.3.1. For a 4 cm long plate, $K_t \simeq 1$ and $K_r \simeq 0$ over all the frequencies studied. Two phenomena could be at stake here. First, as the plate is small compare to water wave wavelength, reflection due to diffraction effects are unlikely to happen. Second, large plate motion amplitude could be more inhibited by small plate lengths.

As the plate length increases, a behavior similar to the one depicted for a change of depth can be observed. A wide reflection peak can be observed near to 2 Hz. Its maximal value seems to increase with L. Sharp peaks can be observed but appear to be extremely sensitive to plate length. For instance, for L=32 cm a sharp peak can be observed for $f = 2.9$ Hz but it does not exist for the 20 or 44 cm long plates.

Finally, for much larger plates, reflection and transmission patterns turn out to be much more complex. As illustrated in Figure 3.12 **H** multiple sharp peaks can be observed for $L = 100$ cm as well as a wider reflection zone close to 1.8 Hz.

Figure 3.13 **A** presents the wide reflection peak central frequency. Similarly to Section 3.4.1, the central frequency, f_{c}, refers to the frequency in the middle of the peak and is not necessarily the frequency of the maximum reflection. This can be observed that central frequency decreases with plate length, L. This results does not say anything fundamental except that

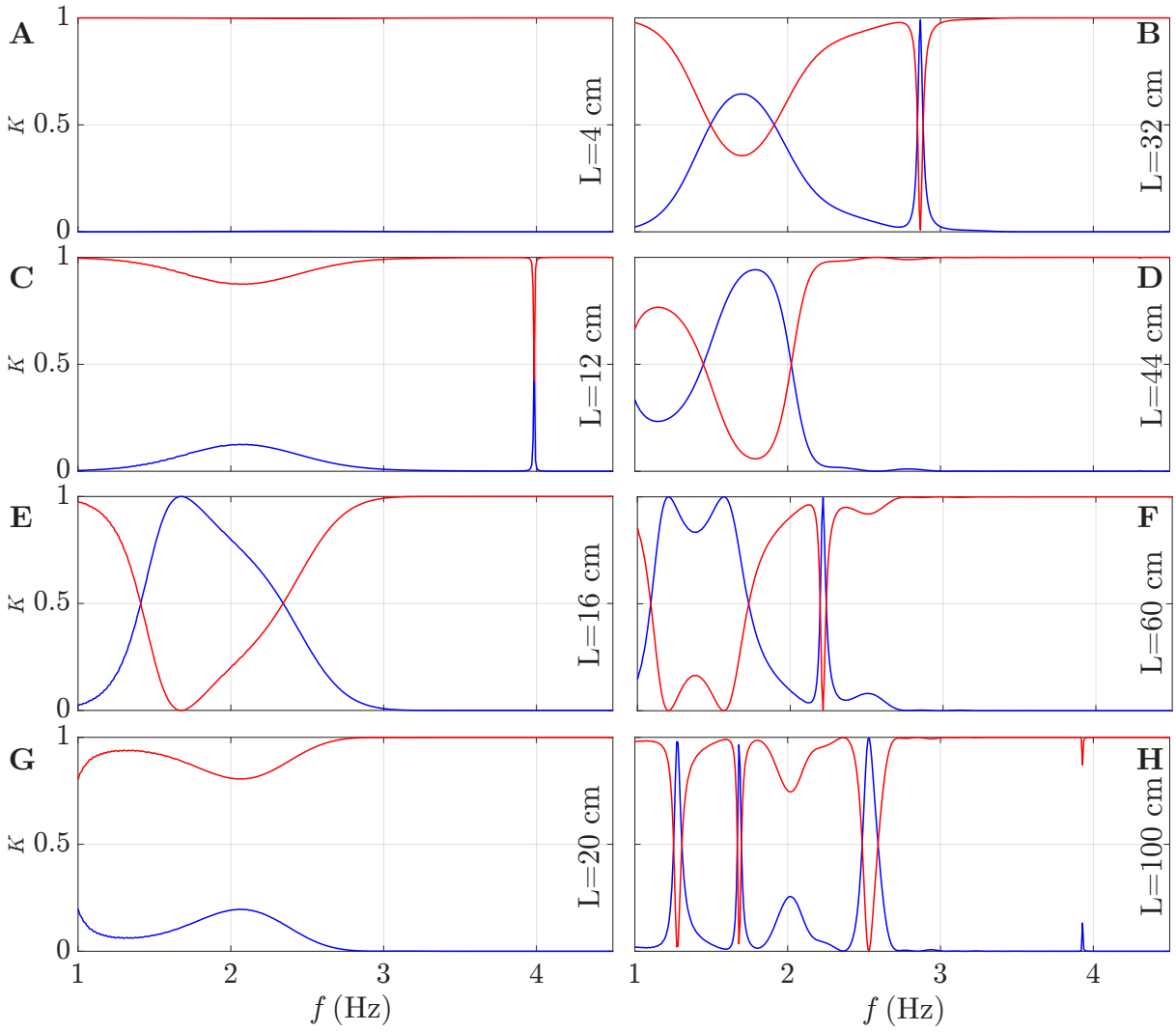

Figure 3.12: Effect of length variation on wave transmission and reflection by a flexible plate of stiffness EI=9.10^{-2} N.m^2, density, ρ_p=1200 kg.m^{-3}, depth d = 5 cm, width b=10 cm and thickness l over a 10 cm total depth. **A** 4 cm length, **B** 32 cm length, **C** 12 cm length, **D** 44 cm length, **E** 16 cm length, **F** 60 cm length, **G** 20 cm length, and **D** 100 cm length.

plate length, L, plays a role in wave reflection. Results obtained here appear more noisy than for the effect of depth. It can be explained because sharp peaks are sometimes located near the wide reflection peak making it difficult to measure f_c. Figure 3.13 **B** shows K_{rc}, the reflection value at the central frequency as a function of plate length, L. For plate length smaller than 58 cm, K_{rc} increases with plate length with one exception being L = 16 cm. K_{rc} reaches 1 for L = 60 cm. For superior lengths, the wide peak splits in the same manner as for a decrease in depth. It results in a decreases in K_{rc} with plate length. K_{rc} reaches 0 for L = 80 cm. For plates longer than 80 cm, the wider peak splits again leading to an extremely complex behavior similar to the one observed for a 120 cm. Consequently, it is not

possible to measure f_c and K_{rc} for plates longer than 80 cm.
To sum up, an increase in plate length leads to the increase in the wide peak intensity and the decrease of its central frequency. Another notable fact is the apparition of multiple sharp peaks, particularly for longer plates.
Figures 3.14 **A** and **B** show, respectively, K_t and K_r in plate length-frequency diagrams. In this representation, sharp peaks evolution is particularly striking. Wide peak central frequency is represented by a green line. As observed in Figure 3.13 **B**, its intensity is small compared to sharp peaks for plate lengths smaller than 30 cm. For $L > 30$ cm, wide peak central value reaches one. Finally, for plates longer than 60 cm the peak splits in two.
Figure 3.14 **C**, presents plate length frequency diagram. For short plates, $\hat{\xi}$ is close to zero. Total transmission observed in Figure 3.12 **A** is associated with no plate motion. As plate length increases, more complex patterns appear. Comparing, Figures **A**, **B** and **C**, it is observed that $\hat{\xi}$ increases are associated with sharp peaks. It seems to confirm that sharp peaks are associated to plate resonances.

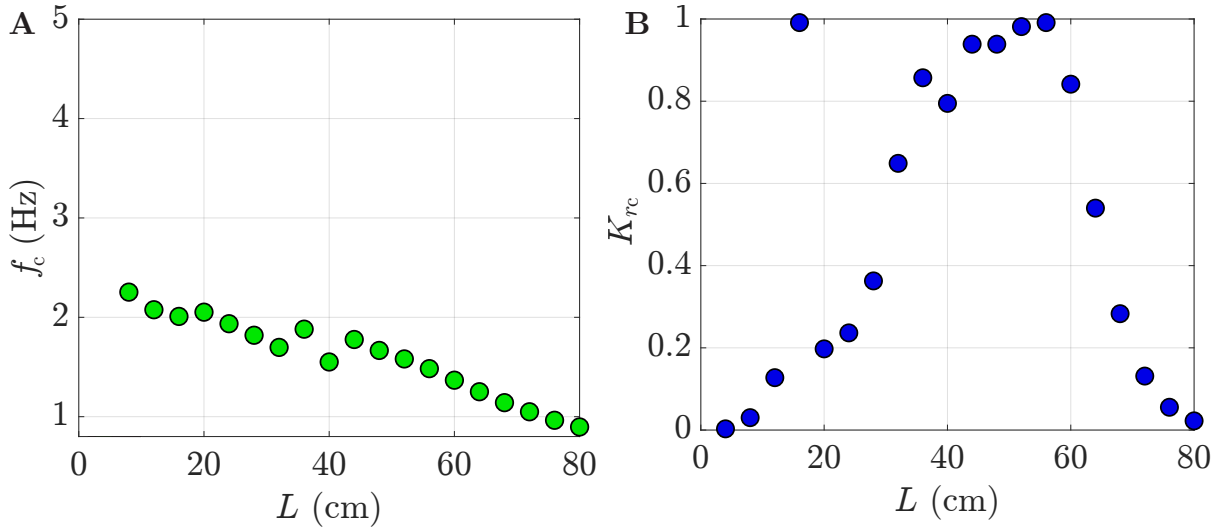

Figure 3.13: **A** Central frequency of the wide peak, f_c, as a function of plate length. **B** Reflection coefficient value at the central frequency of the wide peak as a function of plate length.

3.4.3 Effect of plate stiffness and density

The three last physical parameters that can impact reflection and transmission patterns are plate stiffness, EI, plate cross section, S and plate density, ρ_p. EI, S and ρ_p only appear in the left hand of the dispersion relation in zones 2 and 3 and not in continuity equations as d and L. Furthermore, they appear in two separates terms that can be compared with each

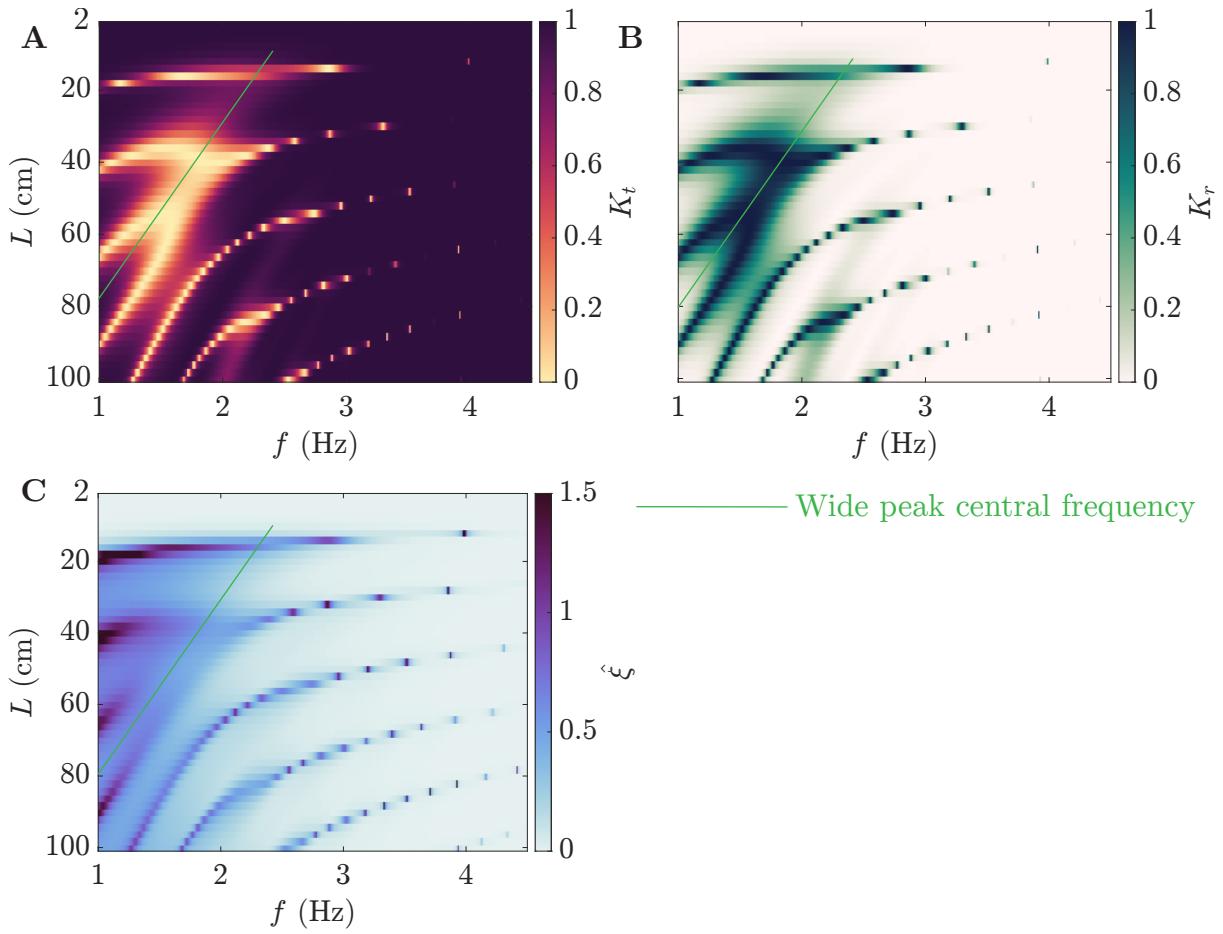

Figure 3.14: Plate length frequency diagram showing **A** reflection coefficient, K_r, **B** transmission coefficient, K_t, and **C** normalized plate motion amplitude, $\hat{\xi}$.

other. Consequently, to observe the effect of EI, S and ρ_p on reflection and transmission patterns, the dispersion relation is written as:

$$[r^* - 1]\rho_p S\omega\left(\frac{\omega^2}{g\underline{\sigma}_n}\cosh(\underline{\sigma}_n d) - \sinh(\underline{\sigma}_n d)\right)\underline{\sigma}_n \tanh(\underline{\sigma}_n(h-d)) \tag{3.4.1}$$
$$= b\omega\rho\left[\frac{\omega^2}{g\underline{\sigma}_n}\cosh(\underline{\sigma}_n d) - \sinh(\underline{\sigma}_n d) - \left(\cosh(\underline{\sigma}_n d) - \frac{\omega^2}{g\underline{\sigma}_n}\sinh(\underline{\sigma}_n d)\right)\tanh(\underline{\sigma}_n(h-d))\right].$$

with r^* being defined as:

$$r^* = \frac{EI\underline{\sigma}_n^4}{\rho_p S\omega^2}. \tag{3.4.2}$$

In the case where $r^* \gg 1$, stiffness will control the plate dynamics and on the other hand, if $r^* \ll 1$, inertia will rule plate motion. r^* varies with wave frequency and plate wave number. It means that for a given set of parameters r^* can vary. More strikingly, stiffness and inertia importance will differ among plate modes at a given frequency.

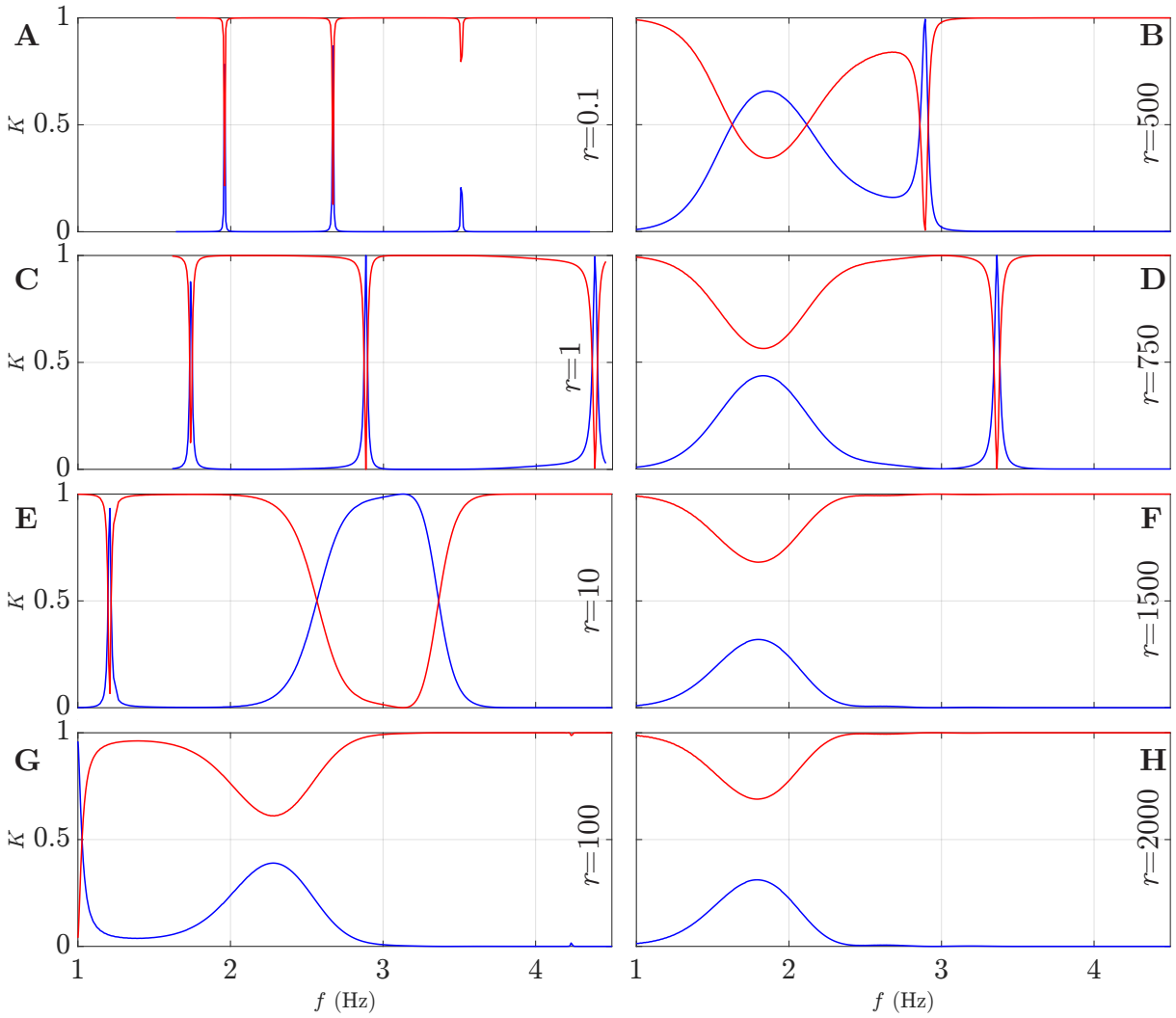

Figure 3.15: Effect of the stiffness and interia parameter, r, variations on wave transmission and reflection by a flexible 28 cm long plate at a 5 cm depth, b=10 cm and thickness l of 1 mm over a 10 cm total depth. **A** r=0.1, **C** r=1 due to numerical convergence difficulties the frequency domain has to be restricted for those two r values. **B** r=500, **D** r=750, **E** r=10, **F** r=1500, **G** r=100, and **H** r=2000.

To probe the effect of stiffness and inertia, a parameter r is varied. r corresponds to the value of r^* for $f = 2$ Hz and a wave number, $\underline{\sigma}_n^4$, of $\frac{2\pi}{L}$. Resulting in:

$$r = \frac{4\pi^2 EI}{\rho_p S[4\text{ Hz}^2]L^4}. \tag{3.4.3}$$

These choices are made in order to evaluate the importance of stiffness against inertia for a given set of EI, S and ρ_p. Note that with Section 3.3.1 parameters, r is equal to 1019.2 which is approximately 1000. It means that in previous Sections, the plate dynamics is mostly

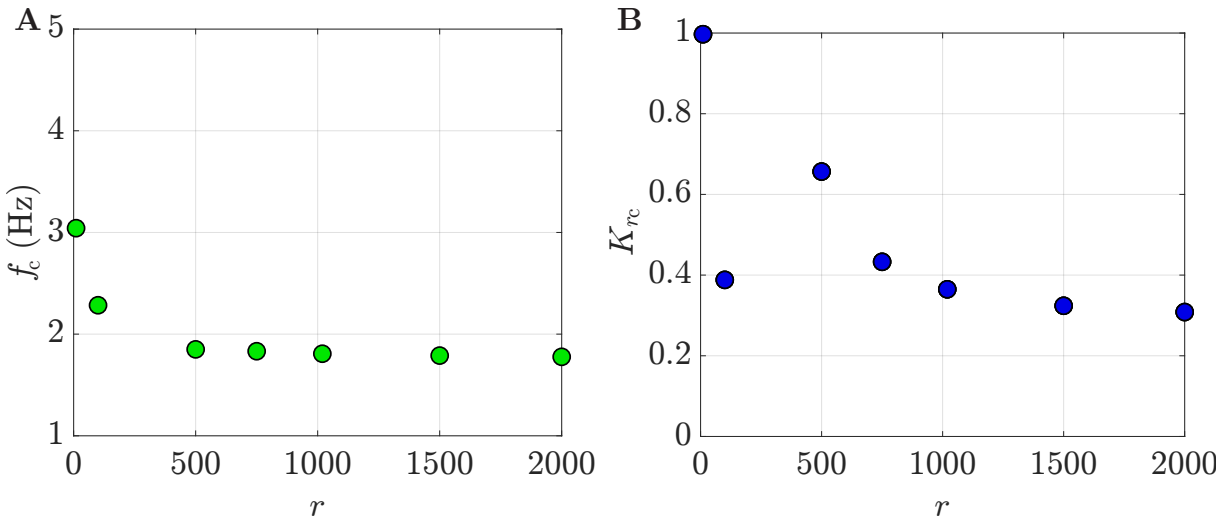

Figure 3.16: **A** Central frequency, f_c, as a function of r, for a range of r where it is present *i.e.* from r=10 to r=2000. **B** Reflection coefficient at the central frequency for the same values of r as **A**.

ruled by stiffness. Since plate parameters were close to the plates used in the experiments this value of r is unsurprising given the considerations of Section 4.4.1. Indeed, to ensure the plate horizontality experimentally, the plate must be rigid enough to compensate the effect of gravity. In practice, the tip of a plate with low r and a small density difference with water would either sink or float.

That being said, the model used here allows to vary r without being limited with those considerations. Therefore, K_r and K_t are calculated for r going from 0.1 to 2000. The different values of r are changed by changing the Young's Molulus, E. Figure 3.15 **A** presents K_r and K_t as a function of wave frequency for $r = 0.1$. First of all, the frequency domain is narrower than for other situations calculated before, which is due to numerical limitations. Taking r=0.1, (as well as 1) leads to particularly high values of wave vectors in zones 2 and 3 so that matrix, D, can be ill-conditioned, thus making its inversion prone to numerical errors. Over the frequency interval where results are consistent, numerous sharp reflection peaks can be observed as reflection increases drastically around 2 Hz, 2.7 Hz, 3.5 Hz and 4.3 Hz. In contrast to stiffness-dominated cases, no wide reflection peaks can be observed. The multiplicity of sharp reflection peaks reminds of the behavior of long plates. As r is inversely proportional to L, $r \simeq 3$ for a 100 cm long plate. Small values of r, therefore, seem associated with a higher number of sharp peaks. Indeed, when increasing r, the number of sharp reflection peaks becomes similar to the one observed for short plates.

Similar observations can be made for $r = 1$ in Figure 3.15 **C**.

In Figure 3.15 **E** K_r and K_t are shown as a function of wave frequency for r=10. A wide

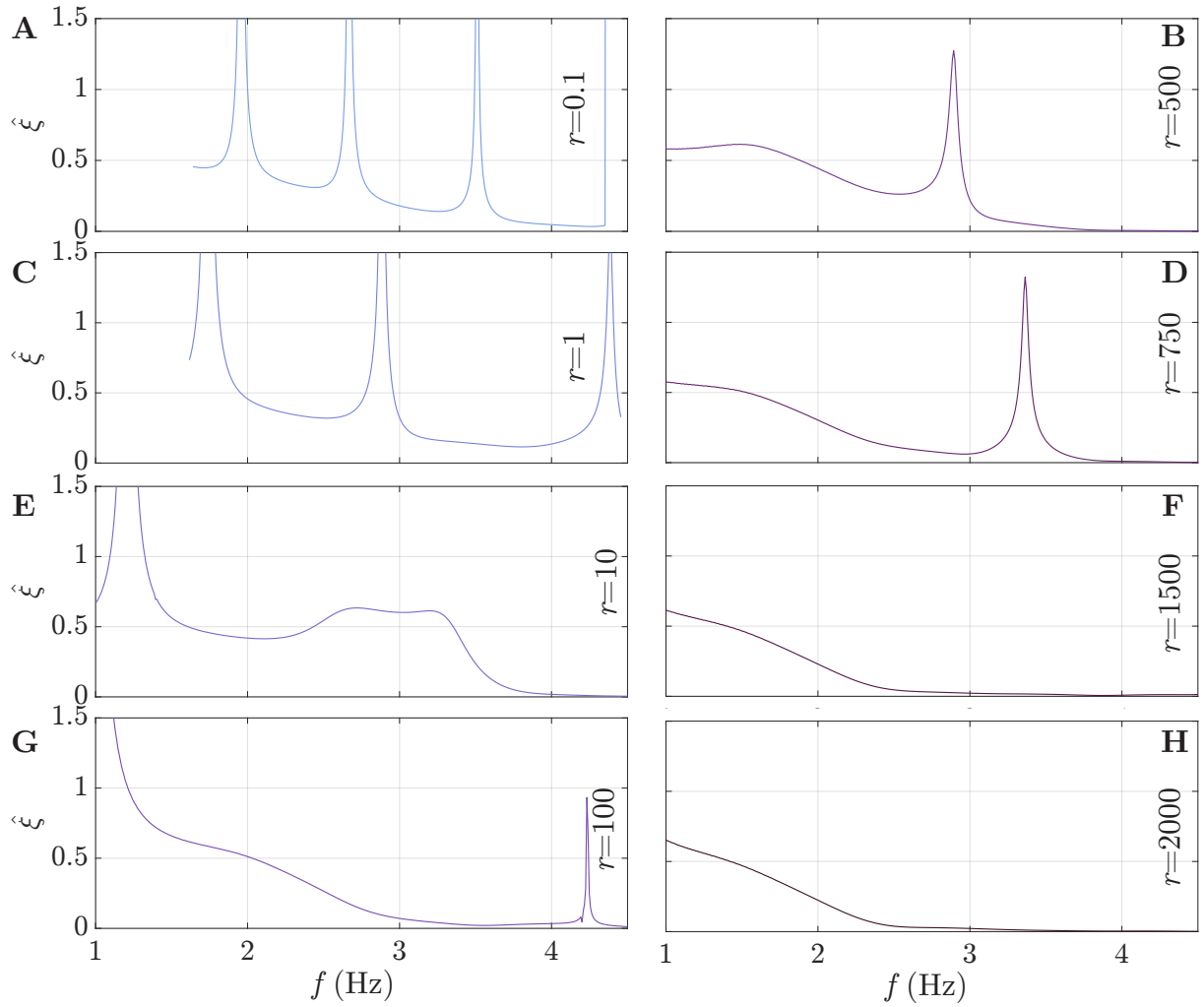

Figure 3.17: Plate normalized motion amplitude, $\hat{\xi}$, as a function of frequency for increasing values of r going from 0.1 to 2000.

reflection peak can be observed around 3 Hz. It shows that increasing r allows to observe a wide reflection peak in the domain. Similar results can be seen in the other cases, which presents K_r and K_t as a function of wave frequency for r ranging from 100 to 2000. On the five Figures, wide reflection peaks can be observed as well as a sharp ones for $r = 500$ and $r = 750$.

Figure 3.16 **A** presents the central frequency of the wide peak, f_c, as a function of r. In this Figure, r goes from 10, first value of r where a wide peak can be observed, to 2000, highest r value for which K_r and K_t have been calculated. It appears that f_c decreases drastically from 10 to 500 and is relatively constant then. Figure 3.16 **B** shows, K_{rc} as a function of r. As in Figure 3.16 **B**, r goes from 10 to 2000. A non monotonic behavior can be observed. Indeed, between 10 and 100, K_{rc} is divided by more than 2, going from 1 to 0.4. For r going

from 100 to 500, r increases to reach approximately 0.65. Finally, from $r = 500$ to 2000, K_{rc} decreases monotonously.

In summary, the quantity $r = \frac{4\pi^2 EI}{\rho_p S[4\ \mathrm{Hz}^2]L^4}$ has been introduced to compare the effect of stiffness and inertia. At low r, *i.e.* when inertia dominates, no wide reflection peak can observed and multiple sharp peaks can be observed. However,for r larger than one, the number of sharp peaks seems to decrease and a wide peak is visible. Finally, measuring K_{rc} and f_c shows that as r increases, its influence on the wide reflection peak decreases. More importantly, in those calculations, all dimensions remain identical. In the case where diffraction would be the only source of reflection, changing r would not have any influence on the reflection and transmission patterns. Varying r allows to conclude that wave reflection is mostly due to radiation.

Finally, $\hat{\xi}$ can be computed for values of r. Results are shown in Figure 3.17. $\hat{\xi}$ behaves similarly to previous observations. Resonance peaks are observed at frequencies corresponding to sharp reflection peaks and plate motion amplitude decreases with frequency. However, stiffness seems to impact $\hat{\xi}$. Indeed, $\hat{\xi}$ reaches higher values at low frequencies for the more flexible plates.

3.5 Conclusion

This Chapter gave first elements of understanding concerning the elastic plate behavior in a wave field using wave linear theory. First, plate modeling underlines that dynamic pressure effects force the plate, generating oscillations. Plate reaction depends on multiple parameters, geometrical ones, such as plate length or submergence depth and intrinsic ones such as plate stiffness or density. The study of a baseline case exhibits a complex behavior, where submerged elastic plates being able to reflect waves. Reflections are associated with an increase in plate motion amplitude corresponding to plate resonance. Two types of resonance can be distinguished , wide and sharp ones. Both resonance types vary differently when varying plate parameters. However, the exact mechanism leading to those resonances is not clear yet.

Chapter 4
Experimental methods

Chapter 3 proposed a description of the plate-wave interaction using potential flow theory to gain insight into the physics of the problem.
In parallel, an experimental setup is utilized to characterize the interaction using a different approach. A special feature of the setup is its small size. This feature allows the use of methods such as Particle Image Velocimetry (PIV) to measure the flow velocity field or Fast Checkerboard Demodulation (FCD) to reconstruct the free surface height. This section gives a general description of the experimental setup designed to study the interaction between water waves and a flexible plate clamped at one edge. The setup is briefly described in Section 4.1.1 and more details on each component are given in the following sections.

4.1 Wave tank

4.1.1 Set up general description

The experimental setup employed in all this study is pictured in Figure 4.1. As represented in Figure 4.1, waves are generated by a flap-type wave-maker. The plate is placed approximately halfway through the tank length. An absorption beach is located at the tank end to mitigate wave reflection.
Experiments are recorded by means of two cameras. The first one pointing downward, from above the tank, allows to measure surface elevation in the whole tank by means of Schlieren imaging (see [Wildeman, 2018]), as detailed in Section 4.2. A second camera, which films a side view of the tank, can have two different objectives. Depending on the experiment, it can either record and track the plate motion (see Section 4.4) or record particles motion when conducting Particle Image Velocimetry (PIV) experiments (see Section 4.5). The cameras utilized in the different configurations are presented in the Table below.

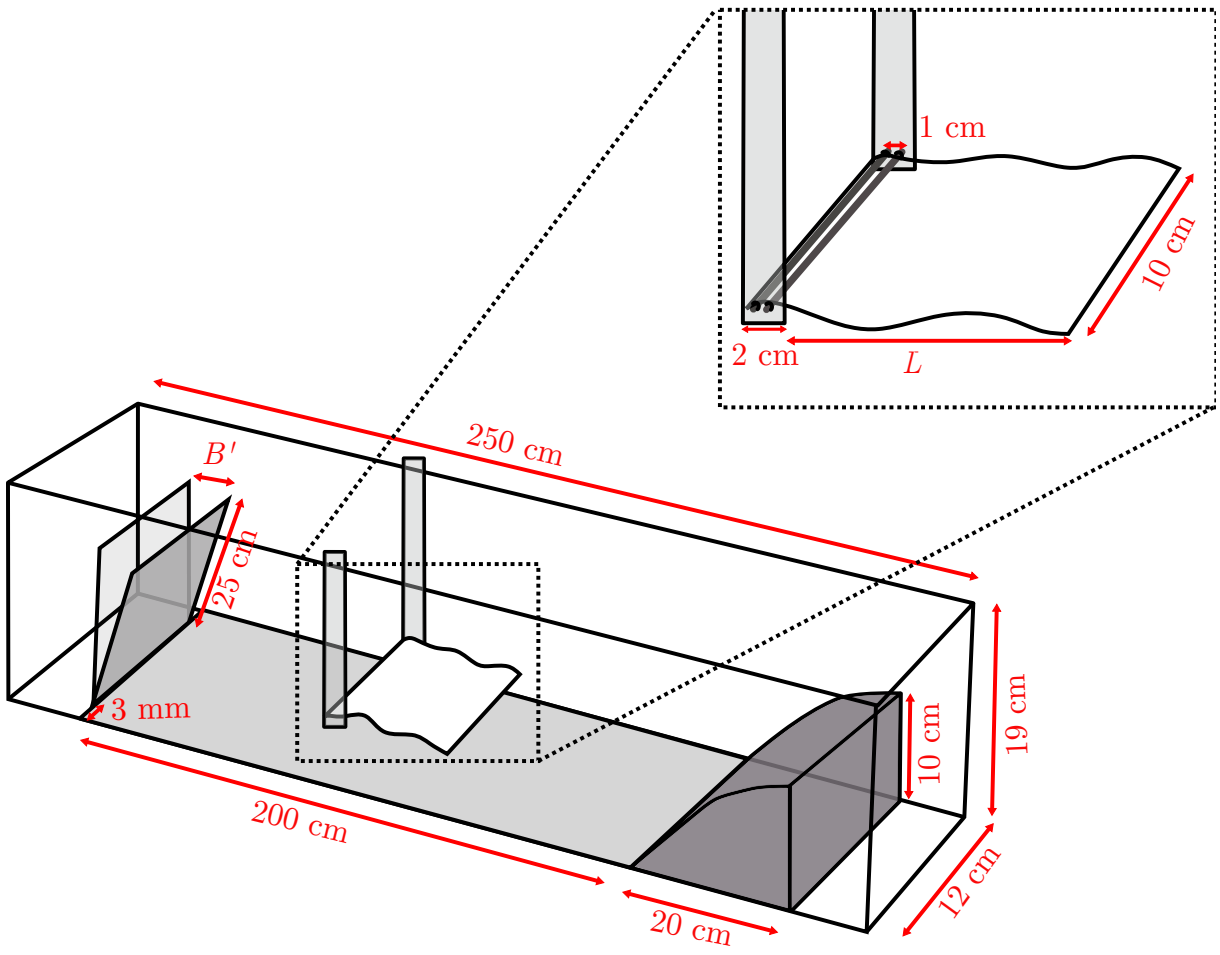

Figure 4.1: Schematic of the experimental setup. The total tank length is 2.5 m and the part that can actually be used for the experiments is 2 m long. The width of the wave-tank is 12 cm. The flap-type wave-maker is represented on the left. It is made of 25 cm plate hinged at the bottom. The plate is separated from tank side walls by a 3 mm space. It can oscillate at a frequency, f, and with an amplitude, B', to generate waves, both f and B' can be chosen for a given experiment. The plate is placed close to the middle of the tank. It is fixed by using two poles that are maintained on a fixed structure out of the tank. As pictured in the caption in the zoomed-in view, the plate is linked to the poles using to carbon rods that are glued to the plate and inserted into poles holes. A breaking beach is placed at the end of the tank to avoid wave reflection on the end wall. As the height of the beach is 10 cm, water depth must also be equal to 10 cm to ensure beach efficiency.

4.1.2 Wave-maker

Wave-maker design

As mentioned in Section 4.1.1, a flap-type wave-maker is employed. Waves are produced by the oscillations of a plate hinged to the tank bottom. The plate displacement is imposed using

Camera	Model	Resolution	Typical frame rate (Hz)
Top view	Basler acA2000-165um	150×1930 1 pxl.mm^{-1}	50
Side view PIV	Phantom Miro M120	1080×1920 4 pxl.mm^{-1}	40×wave frequency (*i.e.* [1.5,4] Hz)
Side view Plate traking	Basler acA3088-57um	564×2088 15 pxl.mm^{-1}	40

Table 4.1: Specification of the different cameras employed in this thesis as well as their typical settings.

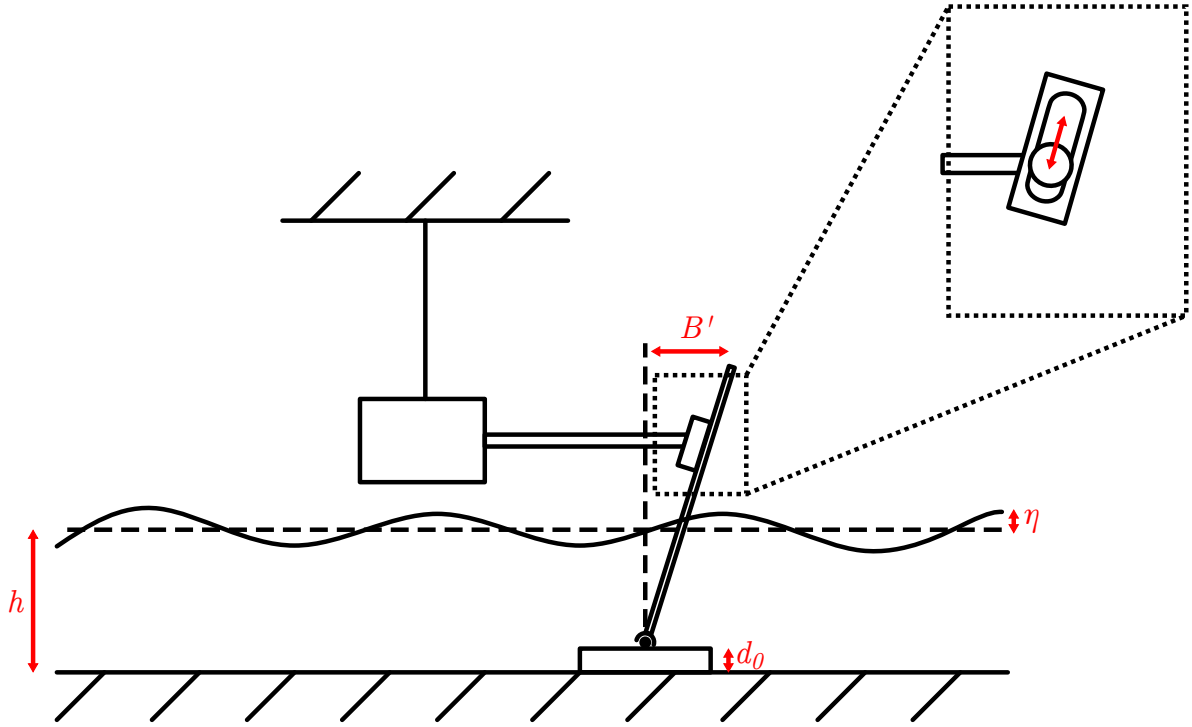

Figure 4.2: Sketch representing the wave-maker. The plate rotates around its hinge axis at a depth $(h - d_0)$, where h stands for the water depth. The plate has a total length l_w. Here, $l_w = 20.6$ cm and $d_0 = 1$ cm. The motor acts onto the plate by imposing a sinusoidal motion of amplitude b' which results in a sinusoidal motion of amplitude b at the free surface.

a linear motor, which allows to control both its frequency and its amplitude when generating monochromatic waves. In order to generate waves of frequencies between 1.5 and 4 Hz and of amplitudes between 0.5 and 6 mm, a DM01-23x80F-HP-R-60_MS11 from Linmot®[1] is utilized. In order to make the plate oscillate between a vertical position and a tilted one,

[1] https://linmot.com/fr/

plate position, B', is imposed using the linear motor:

$$B'(t) = \mathrm{Re}\left\{\underline{b}'(e^{-\mathrm{i}\omega t} + 1)\right\}, \tag{4.1.1}$$

where b' is the motion amplitude and Re stands for the real part. As stated in Equation 4.1.1, plate motion is the sum of a sinusoidal motion and an offset to ensure plate verticality at rest. The junction between the plate and the motor axis is a key element. Indeed, the motor cannot simply be attached to the plate. Indeed, the plate rotation around an axis implies that the contact point height changes with the displacement, b'. To address this issue, PMMH's workshop designed a junction which allows the motor tip axis to slide along the plate while pushing it. The junction is sketched in Figure 4.2 zoomed-in view.

Relation between wave-maker motion and wave amplitude

Wave amplitude, η, is related to the plate amplitude at the free surface, $\underline{b}'$. This relationship has been largely studied (see [Schäffer, 1996], [Flick and Guza, 1980] or [Ursell et al., 1960] for instance) and, using the notations presented in Figure 4.2, the following equations can be obtained:

$$\frac{\underline{b}'}{\underline{\eta}} = -\frac{ikl_w}{4\ \sinh(kh)} \frac{\sinh(2kh) + 2kh}{k(h-d_0)\ \sinh(kh) - \cosh(kh) + \cosh(kd_0)} \tag{4.1.2}$$

where k is the wave-number associated to the wave-maker frequency through water wave dispersion relation (see Equation 2.1.35) and l_w is the wave-maker plate total length. Writing the complex free surface deformation $\underline{\eta}$ as:

$$\underline{\eta} = Ae^{-\mathrm{i}\omega t + \mathrm{phase}}, \tag{4.1.3}$$

it is possible to relate wave amplitude, A, to wave-maker amplitude. Note that this relation is valid at the first order only and that the second order might differ from works by Schäffer [1996], Flick and Guza [1980] or Ursell et al. [1960]. Indeed, in the three articles, the wave-maker performs oscillations centered on the vertical, whereas vertical is the maximum strokes of the wave-maker used here. The theoretical amplitude given by the Equation (4.1.2) is presented Figure 4.3 **A** for a range of typical (b', f) pairs.

The main interest of such a result is to have an estimate of waves amplitude, when imposing a given displacement amplitude to the wave-maker. For instance, it is shown here that, in order to obtain a constant wave amplitude across all frequencies, one would have to decrease the wave-maker amplitude. To that aim different wave-maker amplitudes are imposed and rep-

resented using black empty squares in Figure 4.3 **A**. The points are chosen so as to follow, as close as possible, contour lines of Equation 4.1.2. A comparison between the measured amplitude and the theoretical amplitude from Equation 4.1.2 is presented Figure 4.3 **B**. The points correspond to the experimental values measured using Schlieren imaging (see Section 4.2), while lines represent the predicted wave amplitudes. At low frequencies, the measured and predicted values match while, at larger frequencies, the wave amplitude obtained is systematically smaller than that expected from theory, discrepancy can be observed elsewhere. This influence of frequency can be understood from the fact that at higher frequencies, waves are steeper, which leads to more non-linearities and dissipation. Another source of discrepancy comes from the fact that Equation 4.1.2 is written for a wave-maker oscillating with no offset (*i.e.* $B'(t) = \mathrm{Re}\left\{b'e^{-\mathrm{i}\omega t}\right\}$). Equation 4.1.2 remains true at the first order for both plate motions but adding an offset might enhance non-linearities.

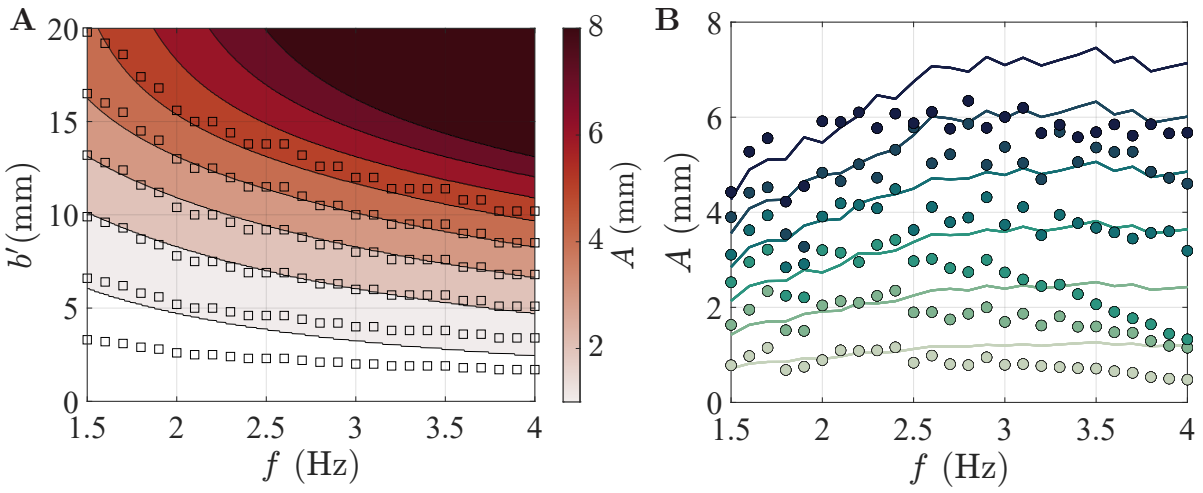

Figure 4.3: **A** Motor amplitude-frequency diagram showing the theoretical water wave amplitude. The black squares corresponds to experimental points that were chosen to produce the Figure **B**. **B** Measured wave amplitude as a function of the frequency for various wave-maker amplitudes. The lines corresponds to the waves theoretical amplitudes for similar (b',f) couples.

In the rest of the thesis, when conducting experiments, a Target Wave Amplitude, TWA, is chosen and wave amplitude is then measured to know the exact wave amplitude at object location. For instance, in Figure 4.3, TWA=1 mm to TWA=6 mm.

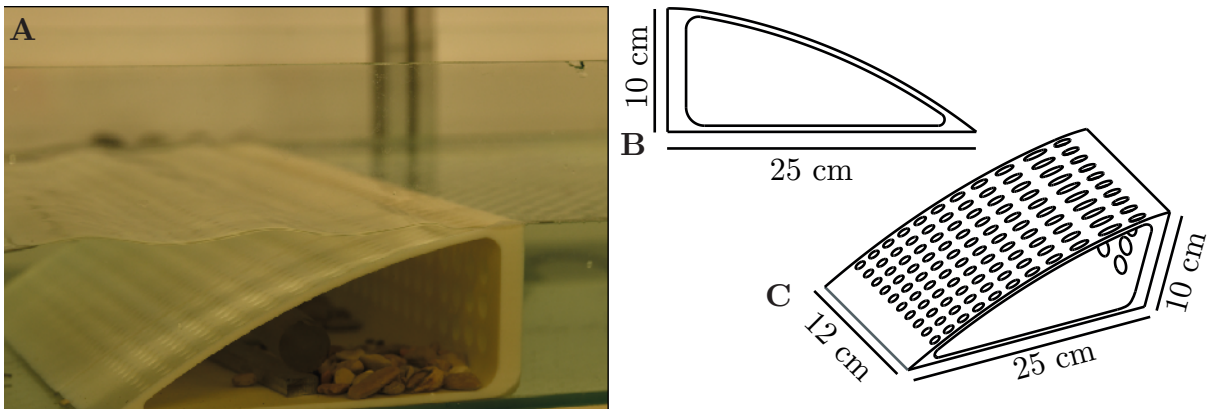

Figure 4.4: **A** Picture of the beach while sending 3 Hz waves. After the beach the free surface is undeformed. It underlines the beach ability to not transmit incoming waves. **B** Scheme of a beach side view. **C** Isometric view of the beach.

4.1.3 Absorption beach

General considerations on beach design

A beach is placed at the end of the tank to ensure that waves are not reflected by the end wall, which would disrupt experiments. As underlined in Ouellet and Datta [1986], a wide variety of beach types can be installed, ranging from a simple, straight inclined plate, to an array of object. One could even think of using a controlled plate as an efficient active wave absorber Schäffer and Klopman [2000]. For the sake of practicability in such a small-scale set-up, a passive beach is employed. The physical principle of a passive beach consists in breaking the waves in order to damp them. To do so, a common strategy is to progressively decrease the water depth. As the bottom becomes increasingly shallow, waves steepness increases and waves eventually break. In addition, an efficient beach is characterized by a small amount of wave reflection. The main reason why a beach would reflect waves is because the object creates a discontinuity in the water waves propagation. An ideal beach would therefore be an infinitely long plate that would go from the tank bottom to the free surface, achieving the water depth decrease with almost no discontinuity. However, as the tank has a finite size, a beach with a parabolic shape is preferred to achieve that aim approximately. Indeed, as underlined in the conclusion of the survey conducted by Ouellet and Datta [1986] a parabolic shape offers the most satisfactory wave damping capabilities, among a variety of beach profiles. The beach is also pierced with holes with the idea that many small orifices might enhanced damping through viscous dissipation, but the real impact of the holes has not been quantified here.

Absorption beach shape and performance

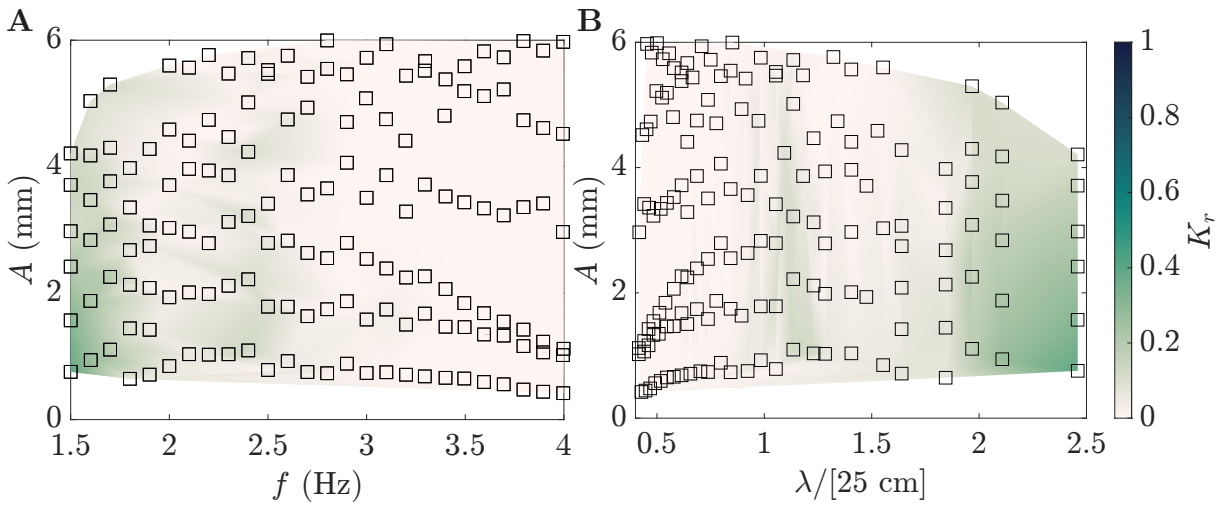

Figure 4.5: **A** Reflection coefficient, K_r, as defined in Chapter 2, as a function of waves amplitude and frequency. At lower frequencies the beach is less efficient and reflects energy. **B** Reflection coefficient as a function of wave amplitude and of the wavelength normalized by the beach length. When λ is twice the beach length reflection becomes significant. Interestingly, a small amount reflection is also observed when $\lambda \approxeq$25 cm, the beach length.

The beach is a 3D printed structure presented in Figure 4.4. Figure 4.4 **A** shows a picture taken while performing experiments. A 3 Hz wave comes from the left and propagates to the beach. This picture illustrates the beach efficiency to avoid wave transmission, as the free surface on the right appears perfectly still. Avoiding wave transmission is crucial for an absorption beach, as transmitted waves are eventually reflected on the tank end wall. The beach dimensions are shown in Figure 4.4 **B** and **C**. It is 12 cm wide to cover all the tank width. Its height is a key factor as the beach is only efficient for a water depth equal to its height. The water depth is therefore fixed at 10 cm to maximize the beach efficiency. Finally, the beach length is a crucial parameter when considering its efficiency at dissipating water waves. As mentioned before, depth variations must be as smooth as possible to avoid reflections due to a sharp change in the bathymetry. Thus, the chosen beach length (25 cm) results from a compromise between achieving satisfactory wave absorption, on the one hand, and keeping a reasonably long wave measurement zone in the rest of the tank, on the other hand.

In order to evaluate the beach efficiency, its reflection is measured for various incoming wave amplitudes and frequencies. The results are presented Figure 4.5. It appears that for high frequencies, *i.e.* when the wavelength is smaller, the beach shows no reflection. However, at lower frequencies, the beach reflects up to 20 % of water waves energy. This reflection

appears to be a consequence of the beach finite size and increases when λ is larger than twice the beach length.

4.1.4 Tank dimensions

The tank length has been mostly chosen to fit in the experiment room, on a table top. On the contrary, the tank width can be modified using a mobile wall. The tank width is a key parameter when conceiving a wave tank. Main reason why is the apparition of three dimensional modes in the tank. Those modes are waves that propagate along the x and y axis (as defined in Figure 4.1), as opposed to the x axis only. As stated by Ursell [1952], the norm, k_o, of the wave vector of these modes is given by the dispersion relation for gravity waves. Furthermore, as they propagate in the direction x and y, it is also imposed that, in the direction y:

$$k_o = \sqrt{(k_x^2 + k_y^2)}, \tag{4.1.4}$$

where k_x and k_y are the wave vector components in the x and y direction respectively. k_y is imposed by the tank width as:

$$k_y = \frac{n\pi}{b_t}, \quad n \in \mathbb{N}, \tag{4.1.5}$$

with b_t the tank width. On the other hand, due to the beach absorption and wave dissipation along the tank, waves can be considered to propagate to infinity in the x direction. Since from Equation 4.1.4, k_y cannot exceed k_0, there exists a maximum value of n. The maximum value of n, $n_{\max}$ is given by:

$$n_{\max} = \lfloor \frac{k_o b_t}{\pi} \rfloor = \lfloor 2\frac{b_t}{\lambda} \rfloor \tag{4.1.6}$$

with $\lfloor . \rfloor$ standing for the floor function and λ for the water wave's wavelength given by the dispersion relation. Thus, when $\lambda > 2b_t$, $n_{\max}$=0 and no oblique mode can exist.

To illustrate those considerations, experiments with b_t=0.48 m and b_t=0.12 m are conducted, generating 2 and 3 Hz waves. Using Schlieren imaging (see Section 4.2), the free surface height is reconstructed. Applying a 2D Fourier transform, one can obtain the energy distribution in the (k_x, k_y) space, as presented in Figure 4.6. It appears that most of the energy is located around the mode $n = 0$, *i.e.* the propagative mode with $k_x = k_0$ and k_y. However, for the wider tank energy is also distributed along the circles of norm k_0 (in red on the figures). This distribution reveals the creation of transverse modes in the case of the wider tank. In addition, bigger circles can be observed experimentally in the wider tank. They correspond to the apparition of non-linear modes of double and triple frequency.

Since transverse waves will interfere with the experiments the tank is taken as narrow as reasonably possible. As pictured in Figure 4.1 the tank width is taken equal to 12 cm. For

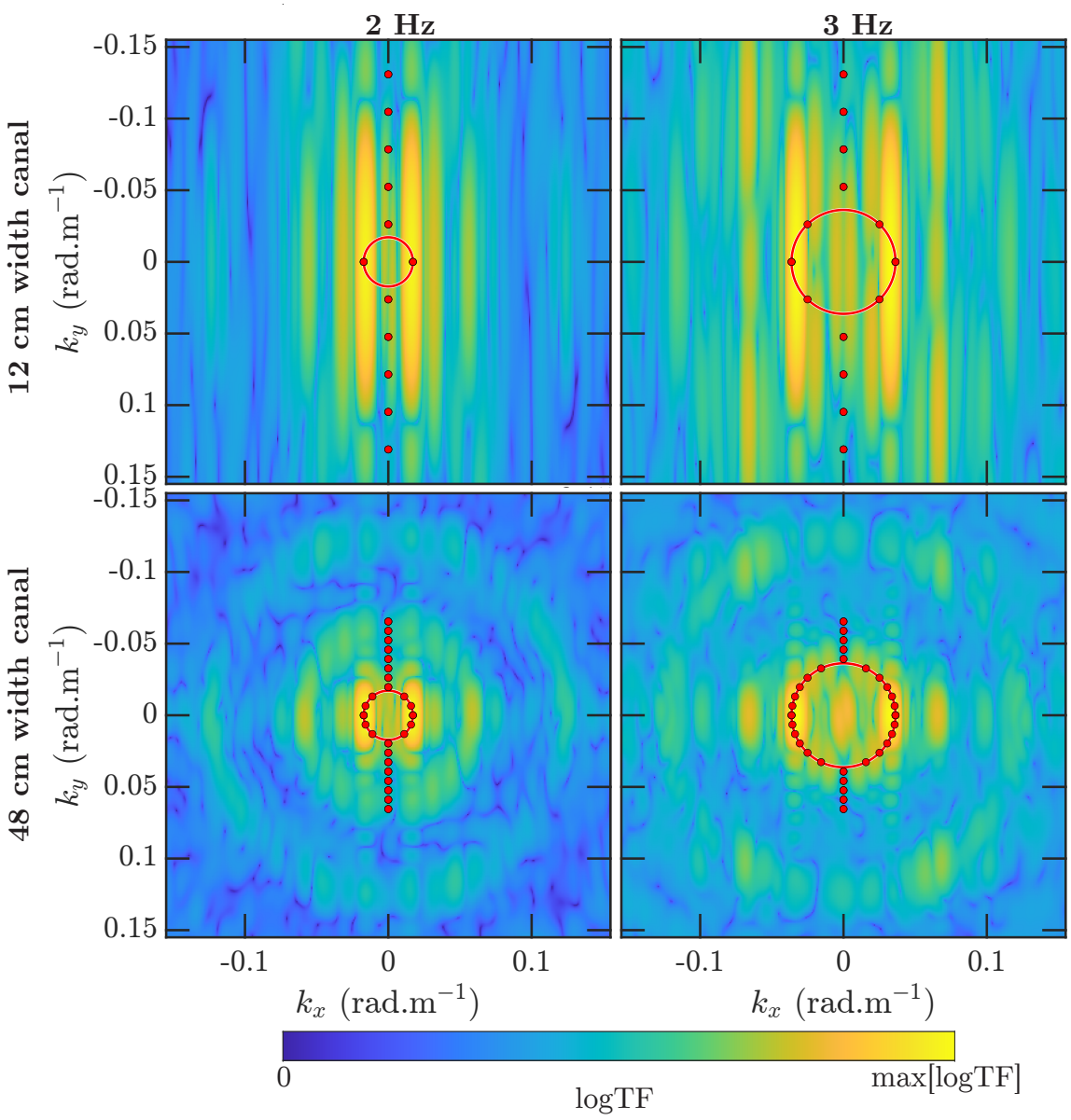

Figure 4.6: Fourier transforms of free surface height at a given time in the k-space. To facilitate visualization, a logarithm has been applied as well as Hann windowing and zero padding. Rows correspond to different tank sizes with respectively a 12 and 48 cm width. Right column show the result for 2 Hz waves and the left one for 3 Hz waves. On all the figures, the red circle has a radius k_0, the wave vector norm associated with the wave frequency. Each point corresponds to possible values of k_x and k_y for transverse modes. It appears that most of the energy is located near the mode $n = 0$ (*i.e.* $k_x = k_0$ and $k_y = 0$). However, for the wider tank, the energy is more distributed along the circle. It underlines that transverse modes can appear for a wider tank. Also, bigger circles can be observed for the 48 cm width tank. They correspond to emitted waves harmonics.

typical wavelength observed in this thesis, it leads to $n_{\max}$=2 for minimal wavelengths. More precisely, for frequencies between 1 and 2 Hz, $n_{\max} = 0$, between 2 and 3 Hz, $n_{\max} = 1$, and $n_{\max} = 2$ for frequencies above 3 Hz. However, the mode $n = 1$ corresponds to an antisymmetric mode, which has no particular reason to become excited if the problem remains symmetric.

4.2 Schlieren Method

4.2.1 General considerations

Various methods can be utilized to measure the deformation of a free surface. For most laboratory study using gravity waves, point based method are employed, using wave probes placed at specific locations. Wave probes are usually made of one or two metallic cylinders that are placed in the water. While the free surface gets deformed and the water height changes at the probe location, its resistivity or capacitance changes. Measuring resistivity or capacitance allow to measure locally water height after calibration. In essence, this method only gives access to local measurements at discrete locations. Since cylinders are plunged into water, it can also be disruptive, especially at shorter wavelengths. As a consequence, for small-scale experiments (few meters long) with a free-surface, optical methods are commonplace to measure the free-surface deformation, with the two benefit of allowing a non disruptive measurement and giving access to measurements all over the tank.
As highlighted by various reviews as Slavchov et al. [2021] Falcon and Mordant [2022] or Gomit et al. [2022] a large variety of techniques can be utilized to measure wave heights in the whole tank. One idea is to use the deformation of a known pattern to compute the free surface height. For instance, it is possible to project a known pattern onto the surface after adding a dye in the liquid so that it becomes reflective and record its deformation by filming. However, to achieve this technique one needs to use a chemical dye such as Titanium Dioxyde (TiO_2) to taint water, thus making it impossible to record the motion of submerged objects (see [Kucher et al., 2023] for instance). Due to this constraint Synthetic Schlieren Imaging is prefered for this study. Synthetic Schlieren imaging is also based on the deformation of a pattern but in contrast to the method described previously, the pattern is placed at the bottom of the tank. A camera is placed over the tank and films the pattern. As the free surface is deformed by the waves, the pattern also appears deformed on the camera images. As it thoroughly described in Moisy et al. [2009] this deformation is related to water height. In the specific study of Moisy et al. [2009] a random dot pattern is employed and the image deformation is measured using Particle Image Velocimetry (PIV) technique. The relation

between surface gradient of elevation and the deformation is also calculated by Moisy et al. [2009] using optical geometry. In the end, for small deformations, it is obtained that:

$$\boldsymbol{\nabla}\eta = -\frac{\mathbf{u}}{h^*}, \tag{4.2.1}$$

where η is the free surface height, $\mathbf{u}$ is the pattern deformation observed by the camera and h^* is a coefficient linked to water depth and measuring conditions. In the specific case of this thesis, the pattern is placed directly in contact to the bottom of the tank and the camera high compared to water depth:

$$h^* = (1 - \frac{n_a}{n_w})(h + \frac{n_w}{n_g}h_g), \tag{4.2.2}$$

where n_a, n_w and n_g are the optic index of air, water and glass, respectively. h is the water depth in the tank and h_g is the thickness of glass between the pattern and the tank (equal to 0.7 cm here). This method is known for giving accurate results but running PIV algorithm can be relatively slow. Consequently, a periodic pattern is preferred which allows to obtain the deformation using the protocol proposed in Wildeman [2018]. Thus, the main interest of using a periodic pattern is to obtain the deformation using Fast Fourier Transform (FFT) algorithms, decreasing dramatically the computation time and increasing slightly the precision [Vinnichenko et al., 2023].
The intensity of a periodic image undeformed (as presented Figure 4.7 **A**) at a given location $\mathbf{r}$ in the (x,y) plan, $\mathrm{I}_{\mathrm{ref}}(\mathbf{r})$, can be decomposed as:

$$\mathrm{I}_{\mathrm{ref}}(\mathbf{r}) = \sum_{m,n} a_{mn} \exp(\mathrm{i}\mathbf{k}_{mn}\mathbf{r}) = \sum_{m,n} g_{mn-\mathrm{ref}}(\mathbf{r}), \tag{4.2.3}$$

with $\mathbf{k}_{mn}$ being the wave vectors of the periodic pattern. In the case of a horizontal checkerboard, it can be obtained for instance that:

$$\mathbf{k}_{mn} = m\frac{2\pi}{\lambda_{check}}\mathbf{e_x} + n\frac{2\pi}{\lambda_{check}}\mathbf{e_y}, \tag{4.2.4}$$

] with $\mathbf{e_x}$ and $\mathbf{e_y}$ being unit vectors in the x and y direction and λ_{check} the checkerboard spatial period. a_{mn} the coefficients associated with each of this wave numbers in the Fourier space and $g_{mn-\mathrm{ref}}$ the carrier peaks of the reference image defined as:

$$g_{mn-\mathrm{ref}}(\mathbf{r}) = a_{mn} \exp(\mathrm{i}\mathbf{k}_{mn}\mathbf{r}). \tag{4.2.5}$$

Similarly, the intensity of the distorted image, $\mathrm{I}_{\mathrm{def}}(\mathbf{r}')$, can be written as:

$$\mathrm{I}_{\mathrm{def}}(\mathbf{r}') = \sum_{m,n} a_{mn} \exp(\mathrm{i}\mathbf{k}_{mn}\mathbf{r}') = \sum_{m,n} a_{mn} \exp(\mathrm{i}\mathbf{k}_{mn}(\mathbf{r}-\mathbf{u})) = \sum_{m,n} g_{\mathrm{mn-def}}(\mathbf{r}+\mathbf{u}), \quad (4.2.6)$$

with its carrier peak in the Fourier space:

$$g_{mn-\mathrm{def}}(\mathbf{r}+\mathbf{u}) = a_{mn} \exp(\mathrm{i}\mathbf{k}_{mn}(\mathbf{r}-\mathbf{u})) \quad (4.2.7)$$

Filtering in the Fourier space both the reference and distorted image allows to extract only two of the carrier peaks.
Then, to obtain $\mathbf{u}$, Wildeman introduces the phase φ_0 defined as:

$$\varphi(\mathbf{u}) = \mathrm{Im}[\ln(g^*_{\mathrm{ref}} g_{\mathrm{def}})] = \mathrm{Im}[\ln(|a_{mn}|^2 \exp(-\mathrm{i}\mathbf{k}_{mn}\mathbf{u}))], \quad (4.2.8)$$

Because $|a_{mn}|^2$ is real, the latter expression leads to:

$$\varphi(\mathbf{u}) = -\mathbf{k}_{mn}\mathbf{u} \quad (4.2.9)$$

Since $\mathbf{u}$ has two components x-wise and y-wise, two equations are needed to obtain the deformation in the two dimensions of space. To do so, a second filter around a second wave vector, $\mathbf{k}_{m'n'}$, linearly independent from the first one is applied. It allows to write a second equation:

$$\varphi'(\mathbf{u}) = -\mathbf{k}_{m'n'}\mathbf{u} \quad (4.2.10)$$

For the sake of illustration if $\mathbf{k}_{mn}$ is purely along x and $\mathbf{k}_{m'n'}$ is purely along y, one would obtain the simple system giving $\mathbf{u}$ on both dimensions:

$$\begin{cases} u_x &= -\varphi_0(\mathbf{u})/k_{m'n'} \\ u_y &= -\varphi_1(\mathbf{u})/k_{m'n'} \end{cases} \quad (4.2.11)$$

where u_x stands for the deformation along x and u_y the deformation along y. Once the deformation is obtained, the wave height can be computed by a gradient inversion, *i.e.*:

$$\eta = h^* \boldsymbol{\nabla}^{-1}\mathbf{u}. \quad (4.2.12)$$

The complete code to perform Schlieren imaging by fast checkerboard demodulation can be found on Sander Wildeman Github and has been employed throughout this thesis. Figure 4.7 presents a typical application example of this method. Figure 4.7 **A** presents the undisturbed image taken from the top view of the tank with 10 cm. A checkerboard with 1 cm squares

is placed under the tank. The object at the center is a Lego plate that can be employed to fix different objects. The undisturbed imaged serves as a reference, I_{ref}. Figure 4.7 **B** shows a snapshot taken while 3.5 Hz waves of 2.5 mm amplitude are generated. The deformed checkerboard image is I_{def}. Finally, Figure 4.7 **C** shows post-processed data of the snapshot. The numerical procedure to perform the treatment is also described through a flowchart diagram in Figure 4.8 **A**.

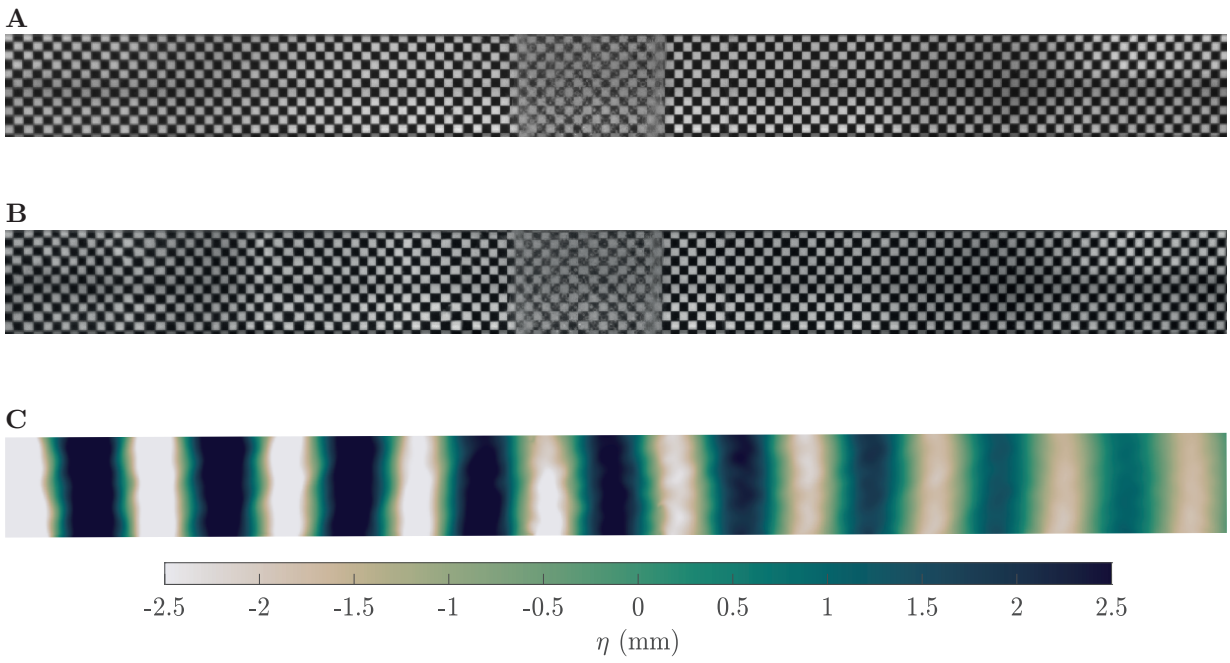

Figure 4.7: Illustration of the use of the Schlieren imaging method to reconstruct the surface height. **A** Top view of the tank. The tank is filled with water, so that water height is 10 cm. Since no waves are propagating, the checkerboard is not deformed. This image corresponds to I_{ref}. **B** Top view of the tank while 3.5 Hz waves are propagating. Waves deform the checkerboard. This image corresponds to I_{def}. **C** Water waves height calculated after applying Schlieren imaging processing for waves with 3.5 Hz and an amplitude of 2.5 mm.

4.2.2 Schlieren Imaging testing

In order to examine the accuracy of such a technique, a virtual environment is created. A reference image taken from the top view of the up-wave region is deformed numerically. To do so, a sinusoidal deformation with damping, $\mathbf{u}_{th}$, is applied on the image. So that:

$$\mathbf{u}_{th} = u_0 \cos(\omega t - kx) \exp(-\nu x)\mathbf{n}_x \tag{4.2.13}$$

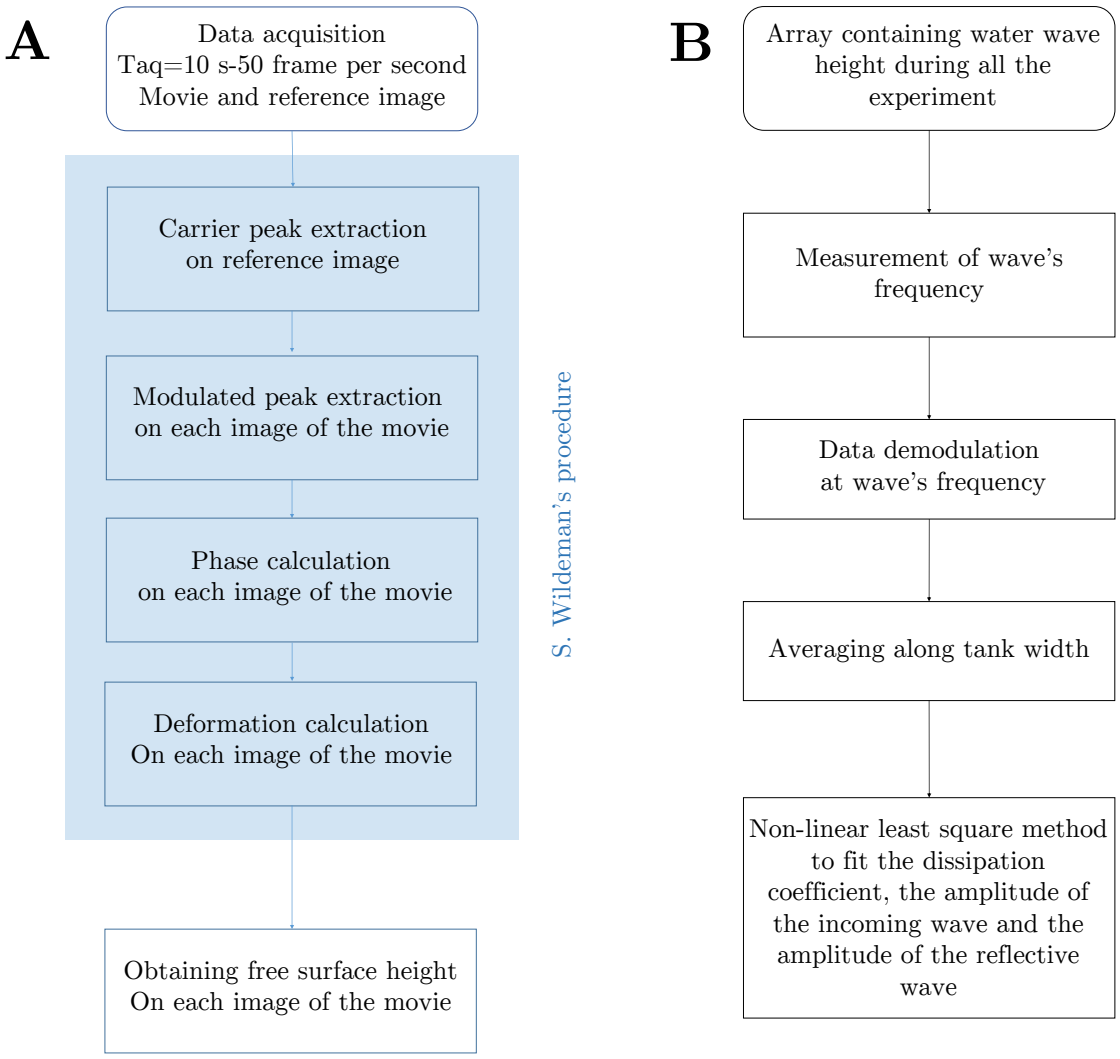

Figure 4.8: **A**: Flow chart describing the numerical treatment performed to obtain deformation and water height from a deformed checkerboard. **B**: Flow chart describing the numerical treatment performed to separate the amplitude of water waves propagating in opposite direction with the same frequency.

where u_0 is the deformation amplitude, ω the angular frequency, k the wave number and ν the wave damping. This deformation is representative of propagating waves with longitudinal attenuation, which are typically observed in the experiments of this thesis as detailed in Section 4.6.2. Also, ω and k are related to the dispersion relation for gravity waves, $\omega^2 = gk\tanh(kh)$ (see Equation 2.1.35). The treatment described in Figure 4.8 is then applied to compare the calculated deformation with the applied one. The passage from the image deformation to the free surface deformation is also examined.

A single set of parameters is illustrated here, taking $\lambda = 500$ mm, u_0=1 pxl and ν=0 mm^{-1}.

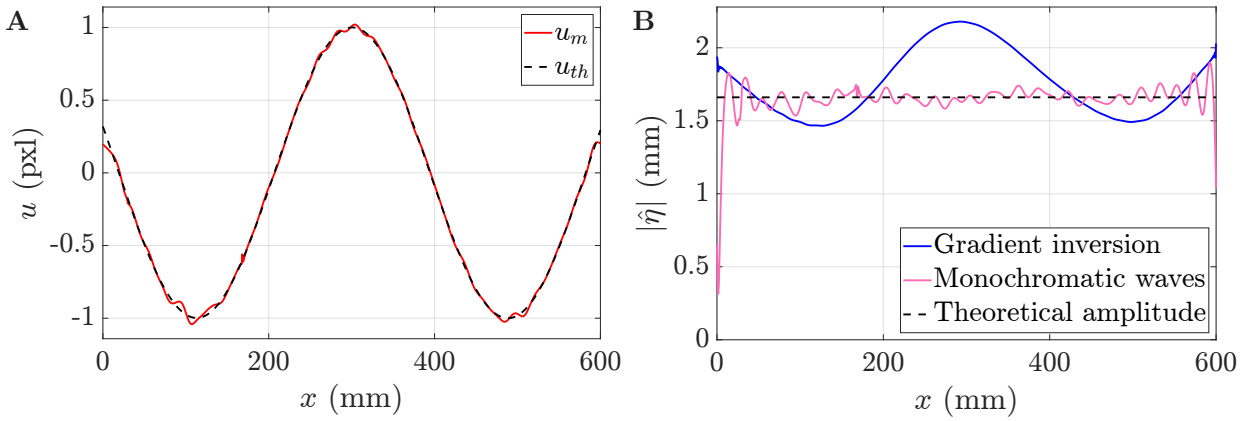

Figure 4.9: Results of the use of the fast checkerboard demodulation method for an image artificially deformed. **A** Comparison of the measured deformation, u_m and the imposed deformation u_{th} at a given time. Data is averaged along the tank width. **B** Elevation's envelope averaged along the width measured using gradient inversion (blue) or considering monochromatic waves (pink) compared to the amplitude imposed theoretically (dashed black).

Figure 4.9 **A** shows a direct comparison between the deformation imposed artificially and the deformation measured using fast checkerboard demodulation. It appears that the measured deformation (in red) fits accurately the imposed deformation (in dashed black). Measuring the deformation is the first step into measuring the wavy water surface elevation. A second one needs to be made to obtain water wave height from deformation. As shown by Moisy et al. [2009] and reminded in Section 4.2.1, the deformation scales as the water height gradient. The general method to solve this problem consists logically in inverting the gradient. As explained by Moisy et al. [2009], several methods can be used to that aim, using Fourier transforms or least-squares method. However, as illustrated in Figure 4.9 **B**, those methods can lead to substantial errors when the measurement domain isn't much greater than the wavelength. Indeed, inverting a gradient implies to have access to a constant. In the case where waves don't reach the measurement window edges, this constant can be taken equal to zero by volume conservation. However, in the case of waves propagating along the tank, water waves height is, in general, non zero on the edges and the calculation of this constant becomes an additional unknown which cannot be measured. An approximation can be made in the specific case of monochromatic waves to avoid this issue. Indeed, waves can be described as:

$$\eta = \mathrm{Re}(\underline{A}\exp(-i(\omega t - kx) - \nu x)), \tag{4.2.14}$$

Injecting this expression into Equation (4.2.1), it is obtained, in the complex space and x

direction, that:

$$(ik-\nu)\underline{A}\exp(-i(\omega t-kx)-\nu x)=\frac{\underline{u}_x}{h^*}. \tag{4.2.15}$$

It comes that u_x has the same wave-number, k, and the same damping coefficient, ν, as η. As illustrated Figure 4.9 **A**, the deformation estimate is accurate. Consequently, k and ν can be calculated using only the deformation, u_x. In addition, noticing that η can be written as in Equation (4.2.14) allows to write:

$$\underline{A}\exp(-i(\omega t-kx)-\nu x)=\frac{\underline{u}_x}{h^*(ik-\nu)}, \tag{4.2.16}$$

i.e.

$$\eta=\mathrm{Re}(\frac{\underline{u}_x}{h^*(ik-\nu)}). \tag{4.2.17}$$

It means that for monochromatic waves, η can be simply computed using the local measurement of the deformation. In addition, k and ν can be calculated from deformation measurements. Hence, the monochromatic wave approximation avoids inverting a gradient. As presented in Figure 4.9 **B**, it allows to reduce the maximal error made reconstructing the free surface.

4.3 Measurement of wave reflection and transmission near an obstacle

4.3.1 General considerations

Looking at wave reflection and transmission past an obstacle, gives key information in order to characterize its behavior in a wave field. In order to evaluate the significance of transmission or reflection, coefficients of reflection, K_r and transmission, K_t, are evaluated. To do so, the up-wave free-surface height must be separated between an incident wave propagating from the wave-maker to the plate and a reflected wave propagating in the opposite direction. Different methods have been developed to separate the incident and reflected wave depending on the experiment setup. In large facilities, free surface height is measured using point based methods. Therefore, a large variety of techniques utilizing point based measurements has been developed to separate incident and reflected waves. For instance, Stamos and Hajj [2001] employed a one point method based on wavelet analysis while Mansard and Funke [1980] proposed a method based on linear least-squares method and point measurements at multiple locations in the tank. As shown by Abdolali et al. [2012] and Kolahdoozan et al. [2014] point based measurements can be sensitive to the probe location and number.

In this thesis, in contrast with most wave flumes, the free surface height is known at every location, which is equivalent to having as many probes as there are pixels on the image, increasing measurement precision. However, in a small wave-tank, waves are noticeably damped. Damping can be taken into account when separating incident and reflected waves, as in [Mérigaud et al., 2021]. Similarly to [Mansard and Funke, 1980], a linear least square method is employed and, a dissipation coefficient, ν, is added as an imaginary part of the wave-number to account for dissipation. To scale ν, an experiment without object has to be performed before any measurements with the object. However, as emphasized in Section 4.6.2, ν can vary drastically over a day leading to more uncertainty in the result.
To improve measurements accuracy and easiness, a new method based on non-linear least squares method has been developed to evaluate simultaneously dissipation, ν, and the reflected and incident wave amplitudes.
As depicted in Figure 4.8 **B**, the numerical treatment starts from water elevation measurements using Schlieren imaging. Wave frequency and wavelength are extracted using a 2D Fourier transform in the x direction and in the time space. The maximum of energy in that space gives both wave frequency and wave number, k. This measurement is utilized to filter the signal at wave frequency and remove noise. This operation allows to sum up the 15 seconds experiment into a single array that has the same size as a single picture of the tank. In order to obtain only the information related to the excitation frequency, a time-wise Fourier transform is performed at every place of the tank, as:

$$\underline{u}_{\text{demod}} = \frac{2}{N_{\text{frames}}} \sum_{n=1}^{N_{\text{frames}}} u_x(x, y, n/f_{acq}) \exp(2ni\pi f/f_{acq}), \tag{4.3.1}$$

where f is the wave frequency of a given experiment and f_{acq} the frame rate at which the movie was recorded.
This operation results in a 2D signal that can be averaged along the y direction to obtain a simple 1 D signal describing the water height in the tank as:

$$\underline{u}_{\text{demod}} = \underline{u}_+ \exp(ikx - \nu x) + \underline{u}_- \exp(-ikx + \nu x), \tag{4.3.2}$$

where u_+ and u_- are respectively the amplitudes of the incoming and reflected wave and ν being a dissipation coefficient characterizing wave amplitude decrease along the tank. The values of u_+, u_- and ν are obtained by averaging the signal along the tank width (y-axis) and fitting a function of the form described in 4.3.2. Fitting is performed using Matlab built-in tool to solve non-linear least-squares curve fitting problems. The concept of this operation consists in finding the optimal values of the three parameters fitted, u_+, u_- and ν so that

the system of equations 4.3.3 is correct.

$$\begin{cases} \underline{u}_{\text{demod}}(x_1) = \underline{u}_+ \exp(ikx_1 - \nu x_1) + \underline{u}_- \exp(-ikx_1 + \nu x_1) \\ \vdots \\ \underline{u}_{\text{demod}}(x_{\max}) = \underline{u}_+ \exp(ikx_{\max} - \nu x_{\max}) + \underline{u}_- \exp(-ikx_{\max} + \nu x_{\max}). \end{cases} \tag{4.3.3}$$

In this system, x_1 denotes the position of the first probe, *i.e.* the first pixel, and $x_{\max}$ of the last.
Finally, obtaining the incident and reflected wave amplitude allows to estimate the coefficients of reflection and transmission, K_r and K_t. Performing this treatment both up-wave and down-wave, K_r and K_t can be defined as:

$$K_r = \left(\frac{u_-^{(\text{up})}}{u_+^{(\text{up})}}\right)^2 \quad K_t = \left(\frac{u_+^{(\text{down})}}{u_+^{(\text{up})}}\right)^2 \tag{4.3.4}$$

To give more details on practical considerations, values of x are taken so that the origin is located at the center of the obstacle. That way, amplitudes in the up and down regions refer to the same locations in the tank. This trick allows to avoid using corrective coefficients based on the dissipation when calculating the coefficients of transmission and reflection.

4.3.2 Testing the measurement of reflection and transmission coefficients

To evaluate the method efficiency, a numerical environment is used. As it has been made in section 4.2.2 an undisturbed tank image is taken and is deformed artificially. To mimic the presence of an object, the tank is divided into two regions. The upper region, where the incident and reflected waves propagate and the down region, where the transmitted wave propagates. A perfect beach is assumed so that there is no reflected wave in the down-wave region. When deforming the image, K_r, K_t, wave dissipation, ν, wave frequency, f, and incident wave amplitude, A, are imposed. The deformation amplitude relative to the incident wave, $u_+^{(\text{up})}$, is calculated using the relationship between the free surface deformation and the image distortion (4.2.1) in the case of monochromatic waves, leading to:

$$u_+^{(\text{up})} = Akh^*, \tag{4.3.5}$$

where k is the wave-vector calculated using the dispersion relation:

$$\omega^2 = gk \tanh(kh) \tag{4.3.6}$$

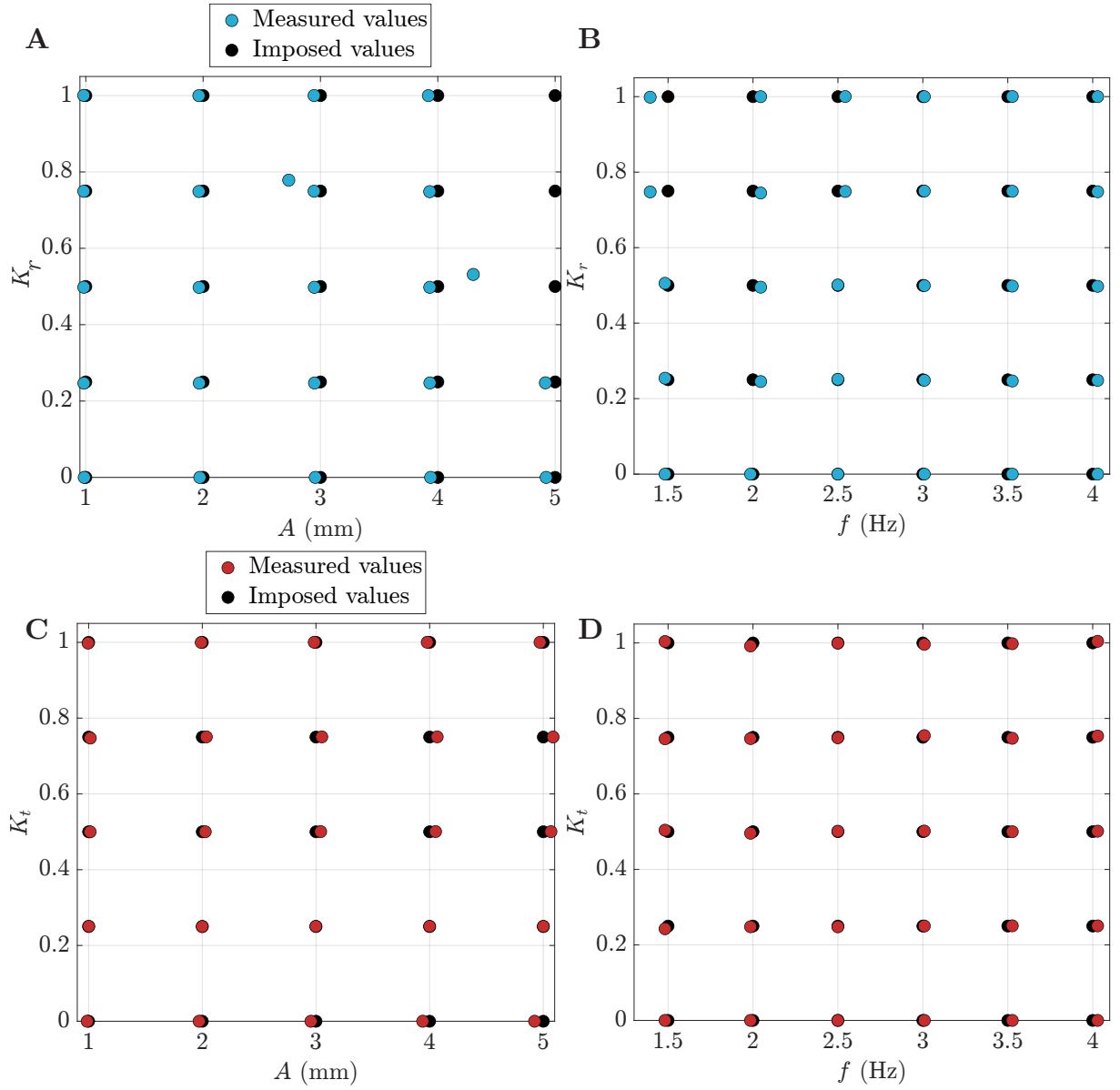

Figure 4.10: **A** Reflection coefficients, K_r, as a function of wave frequency, f, for imposed values in black and measured values in light blue. K_t is taken equal to 0, ν=0 mm^{-1} and $f = 1.5$ Hz. **B** Reflection coefficients, K_r, as a function of wave frequency, f, for imposed values in black and measured values in light blue. Other parameters are: K_t is taken equal to 0, ν=0 mm^{-1} and $A = 1$ mm. **C** Reflection coefficients, K_t, as a function of wave amplitude, A, for imposed values in black and measured values in light blue. Other parameters are: K_r is taken equal to 0, ν=0 mm^{-1} and $f = 1.5$ Hz. **D** Reflection coefficients, K_t, as a function of wave frequency, f, for imposed values in black and measured values in light blue. Other parameters are: K_r is taken equal to 0, ν=0 mm^{-1} and $A = 4$ mm.

The reflected and transmitted waves amplitude are calculated respectively as:

$$u_-^{(\text{up})} = \sqrt{K_r} u_+^{(\text{up})} \text{ and } u_+^{(\text{down})} = \sqrt{K_t} u_+^{(\text{up})} \tag{4.3.7}$$

The different parameters values, presented 4.2, are chosen to be representative of the experiments conducted in the wave tank.

Parameters	Values					
A (mm)	1	2	3	4	5	
f (Hz)	1.5	2	2.5	3	3.5	4
K_r	0	0.25	0.5	0.75	1	
K_t	0	0.25	0.5	0.75	1	
ν (10^{-4}mm^{-1})	0	1	5	10	20	

Table 4.2: Set of parameters tested to validate the separation procedure accuracy.

The numerical treatment described in the last section is then applied on the numerically distorted image. The numerical treatment measures a reflection coefficient $K_r^{(\text{mes})}$, a transmission coefficient, $K_t^{(\text{mes})}$, a dissipation coefficient, $\nu^{(\text{mes})}$, a wave frequency, $f^{(\text{mes})}$, and a wave amplitude, $A^{(\text{mes})}$.
Some measurements examples are presented in Figure 4.10 and compared with the imposed value. Figure 4.10 **A** shows K_r as a function of wave amplitude A. Light blue points corresponds to measured values, *i.e.* $A^{(\text{mes})}$ and $K_r^{(\text{mes})}$ and black points to parameters used to distort the image. In Figure 4.10 **A**, ν=0, K_t=0 and f=1.5 Hz. The comparison between black and blue points gives information on the precision of the method developed for a given set of parameters. From the observation of Figure 4.10 **A**, the method gives relatively accurate results for imposed amplitudes below 5 mm and imposed reflection coefficient below 0.5.
Figure 4.10 **B** shows K_r as a function of wave frequency, f for ν=0, K_t=0 and A=1 mm. In this case, the results are accurate for all K_r and f imposed values.
Similarly, Figure 4.10 **C** shows a comparison between K_t measured and imposed values as a function of wave amplitude, A for ν=0, K_r=0 and f=1.5 Hz. In this case, the results seems accurate over all the diagram.
Finally, Figure 4.10 **D** shows K_t as a function of wave frequency, f for ν=0, K_r=0 and A=1 mm. In this case, results appears accurate for all values tested.

In summary, the method developed for this thesis seems to be relatively precise for some sets of parameters but very inaccurate for others. In order to get a more general view on the method efficiency and on parameters influencing the measurement accuracy, the success of virtual experiments is measured. A measurement is called successful when the measured value corresponds to more or less 10 % of the imposed value. The number of successful experiments over the total number of experiments is called, success rate, R. It is presented Figure 4.12, in amplitude frequency diagram, taking various imposed parameters fixed.

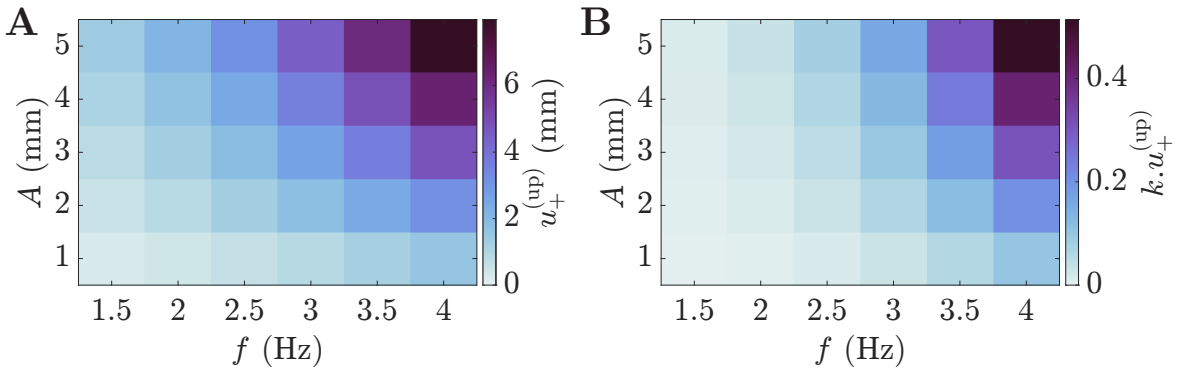

Figure 4.11: **A** Amplitude-frequency diagram showing the amplitude of image deformation for typical pair $(A,\ f)$. As the wave slope increases, the deformation becomes higher . **B** Amplitude-frequency diagram showing $k.u_+^{(\mathrm{up})}$. As mentioned in Wildeman [2018], this product must be smaller than $\frac{1}{\sqrt{2}}$ *i.e.* ≈ 0.7.

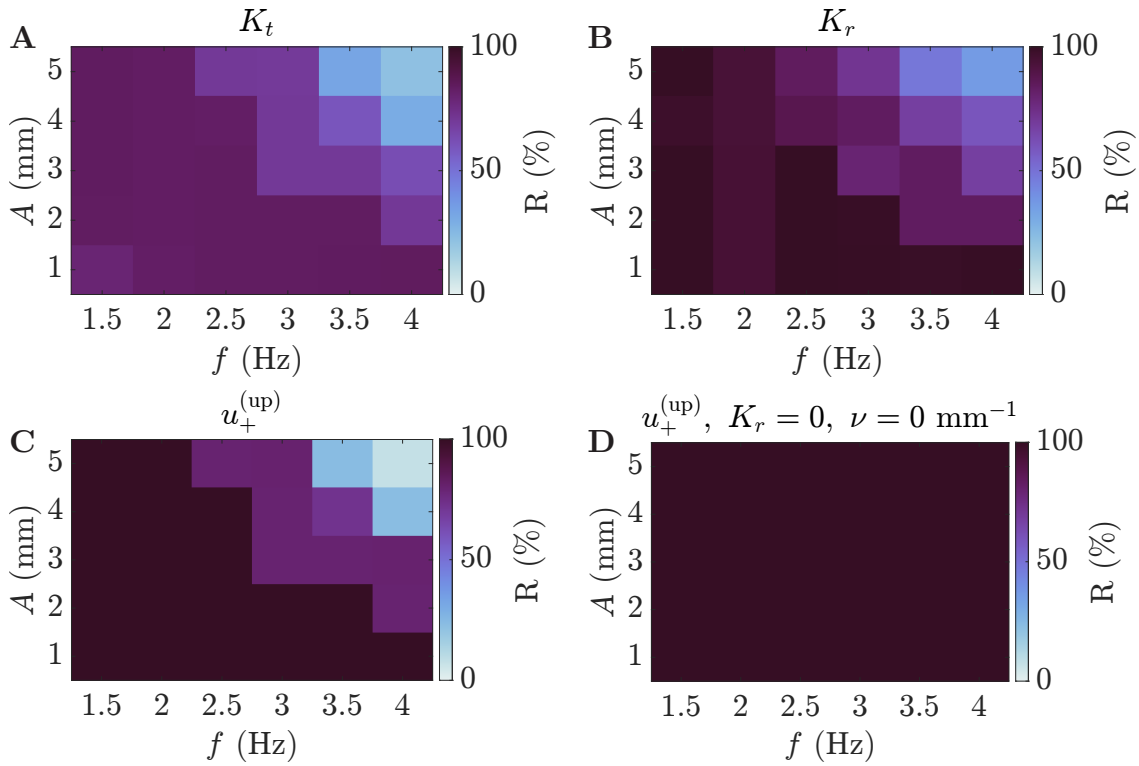

Figure 4.12: **A** Amplitude-frequency diagram showing success rate R for K_t measurements. **B** Amplitude-frequency diagram showing success rate R for K_r measurements. **C** Amplitude-frequency diagram showing success rate R for $u_+^{(\mathrm{up})}$ measurements. **D** Amplitude-frequency diagram showing success rate R for $u_+^{(\mathrm{up})}$ measurements for $\nu = 0\ \mathrm{mm}^{-1}$ and $K_r = 0$. In those conditions the measurements match exactly the imposed values showing that errors are mostly caused by a high reflection coefficient and high dissipation.

The results show that at low amplitude and low frequencies the method is efficient to obtain reflection and transmission coefficients. However, when A and f are maximum this efficiency decreases drastically. As illustrated Figure 4.12 **D**, this decreases is due to mostly two factors, an increase in the dissipation, ν and in the reflection coefficient, K_r. The impact of K_r can be easily understood as it will default the accuracy condition stating that for a checkerboard:

$$|\mathbf{k}|.|\mathbf{u}| < \frac{1}{\sqrt{2}}, \tag{4.3.8}$$

as stated in Wildeman [2018]. As it is illustrated in Figure 4.11, this criteria is met in all the space of parameters tested when there is no reflection. It is therefore not enough to explain the discrepancy observed. However, for high reflections, the deformation at the antinode will be the sum of the two deformations breaking the condition (4.3.8). As it will appear in the Chapter 5, showing results of reflection and transmission measurements, the zone of the amplitude-frequency diagram where high reflection can be critical are zones with no reflection. The impact of high values of ν can also be understood when reminding that the deformation amplitude is defined here as the amplitude at the center of the obstacle. Since the up-wave region has a typical length of half a meter, the deformation amplitude at the beginning of the tank is $\exp(2.10^{-3}.500)u_+^{(\mathrm{up})} \approx 2.7u_+^{(\mathrm{up})}$. As for the high reflection case, it leads to deformations that break the criterion (4.3.8). In the following, two criteria are chosen to validate the measurements:

- $k(u_+^{(\mathrm{up/down})} + u_-^{(\mathrm{up/down})}) < \frac{1}{\sqrt{2}}$
- $ku_+^{(\mathrm{up/down})} \exp(\nu L_{\mathrm{up}}) < \frac{1}{\sqrt{2}}$

with L_{up} being the up-wave length region.

Figure 4.13 shows the success rate in the different tests when applying these two criteria. For most of (A, f) pair the success rate, R, is always above 80% for K_t and 65% for K_r. It illustrates the efficiency of these criteria as a large increase in R for highers amplitudes and frequencies is observed. In practice to ensure the measurements validity, each experiment is performed three times.

To sum up, this study in a virtual environment shows rigorously the numerical procedure efficiency to measure reflection and transmission coefficients by extending the limits of the detection method to two waves propagating in opposite directions, and considering wave damping.

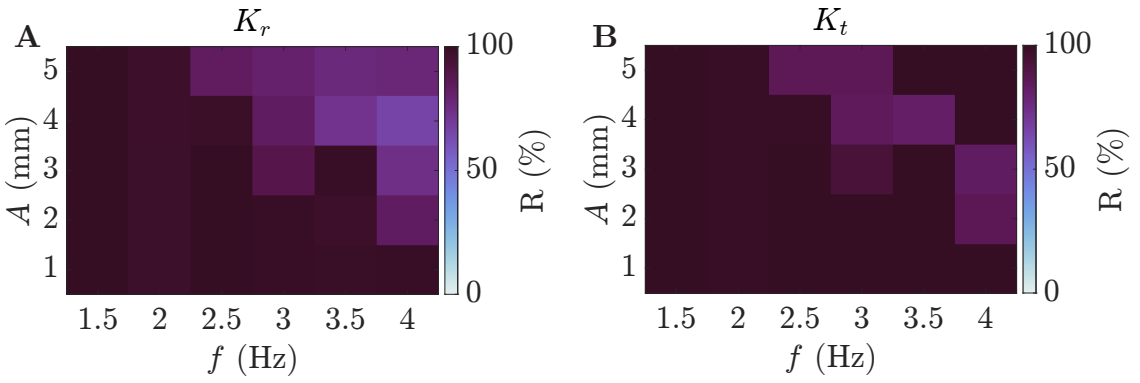

Figure 4.13: **A** Amplitude-frequency diagram showing success rate R for K_r measurements when applying the two more restrictive criteria. **B** Amplitude-frequency diagram showing the success rate R for K_t measurements when applying the two more restrictive criteria.

4.3.3 Protocol to measure wave reflection and transmission

In all this document, the protocol to measure reflection and transmission coefficients is the same. First the reference image is captured. Then, waves of a given frequency are generated using the wave-maker. The wave amplitude wanted is estimated using the relationship given in 4.1.1 but is always measured afterward to obtain the precise wave amplitude. The waves are sent for one minute and fifteen seconds. Recording is only made in the last fifteen seconds to ensure that a steady state has been reached in the tank.
Then, the treatment described in the previous subsections is applied to measure K_r, K_t, the wave amplitudes and frequencies or other parameters depending on the situation.

4.4 Plate's properties

4.4.1 Materials and dimension

General considerations on plate design

As presented in Chapter 3, parameters that will impact plate's motion and interaction with the waves are its length, density, rigidity and its submersion depth. However, the exploration of those parameters is limited in real life. The main limiting criterion that limits these explorations is that the plate should remain relatively horizontal, placed at a certain distance below water surface. However, in contrast to the case of a plate in a flow or in heaving and pitching, the forcing by the waves is not strong enough to keep the plate relatively horizontal, and the plate will sink or float depending on its density, changing drastically the system

behavior. Different strategies have been tried in order to make the plate neutrally buoyant. For instance, salt have been dissolved into the water or masses glued to the plate. If these idea provided temporary solutions to maintain a low rigidity plate horizontal, over the course of an hour the plate would sink or float again (maybe due to change in temperature, increase in salt concentration due to slow dilution...). More controlled and repeatable conditions have then be preferred. As no material matching water density has been found, rigidity is used to keep the plate horizontal. Tap water is simply chosen and density problems are avoided by taking a material with small density difference with water but rigid enough so that gravity effect becomes negligible or, at least, small.
As this study is restricted to a two dimensional case, the plate characteristics are also chosen so that three dimensional motion is small, to avoid flexion along the y direction and torsion about the x axis. To avoid flexion along y, the aspect ratio has to be chosen so that L, the plate length is bigger than b, its width. Furthermore, the competition between torsion and flexion is only set by material properties. For most materials, torsion is favored. Experimentally, longer plates do not exhibit torsion. One possible explanation can lie in the forcing that is symmetrical about the y direction and the clamping system which restrain plate motion.

Plates characteristics

To meet all those criteria, two materials have been selected and are utilized to design elastic plates. Polypropylene plates of density 1.03 and Polycarbonate plates of density 1.2. Simple names, composed of two characters, are given to the plates based on their length and rigidity. First, character is a letter, S or L, it designates the plate length. S stands for small and corresponds to 19 cm plates. The second character is a number ranging from 1 to 4. It quantifies plate stiffness, 1 being the least stiff plate and 4 the stiffest plate. Plate characteristics are given in Table 4.3.

Preparation of PP_L28_e450

The raw material is manufactured and sold in the form of 30.5 cm×20 cm sheets. Probably because of their fabrication process or storage, initially sheets have a curvature, leading to an asymmetric behavior in flexion. To reduce this curvature, after cutting the plate with a given length and aspect ratio, it is heated using a heat press, for 1 hour at 110 °C and cooled down to ambient temperature under the press for at least 5 hours. The resulting plates have no noticeable curvature at rest.

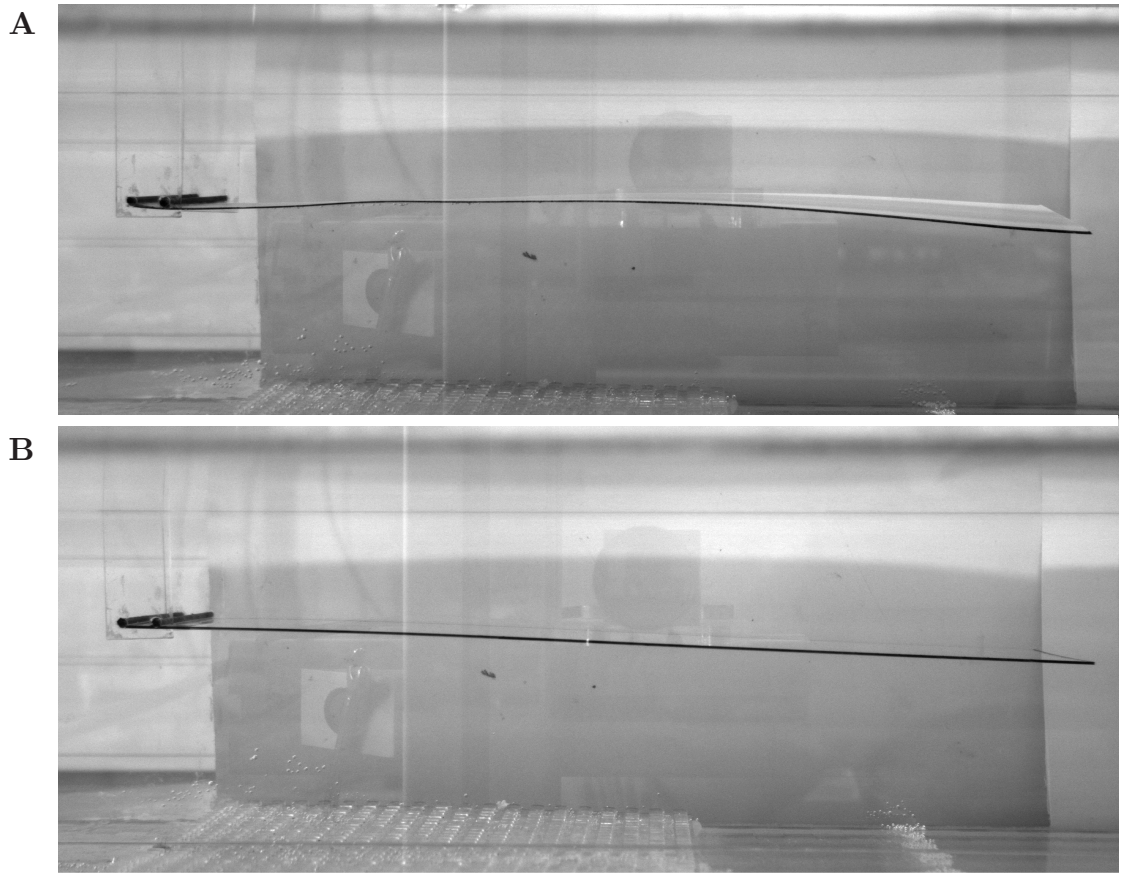

Figure 4.14: Pictures of two plates of 28 cm long at rest taken from the side view. The plates side is colored in black to track its motion. On picture **A**, the plate is made of Polypropylene. On picture **B**, the plate is made of Polycarbonate.

Rigid plate

To highlight even more the role played by flexibility in the reflection, experiments with a rigid plate are performed. The rigid plate has a 10 cm width and a 28 cm length as L1, L2 and L3. It is made of Aluminum of 750 μm thickness. As for the flexible plates, it is maintained by sticking carbon rods to the plate. Carbon rods are then inserted in thin Plexiglass poles that go out of the water. However, contrary to the elastic plates, the rigid aluminum plate is maintained at its tip and at its tail. In the rest of the thesis the rigid Aluminum plate is referred as L4 since it has the same length as other long plate and is the most rigid.

4.4.2 Young's modulus measurements

To estimate the plate Young's modulus, a free-decay test in the air is performed. The plate is clamped from the top and its tip is moved from its equilibrium position. Releasing the tip, the plate starts to oscillate. The plate Young's modulus can simply be estimated by measuring the plate oscillation frequency in a free oscillation test and using Equation (2.2.14). As shown in the Appendix, in order to obtain the oscillation frequency, a movie of the plate is recorded. Then, a Fourier transform is applied to measure the frequency.
Those measurements are performed for the two materials, Polypropylene and Polycarbonate, using L1 for Polypropylene and L2 for Polycarbonate. The repetition of five measurements gives a Young's modulus, E, of respectively 2 GPa and 2.15 GPa.

Short name	Material	Length, L (cm)	Thickness, l (μm)	Density, ρ_p (kg.m^{-3})	Stiffness, EI (10^{-3}.N.m^2)
L1	Polypropylene	28	450	1035	1.7
S2	Polycarbonate	19	750	1200	7.6
L2	Polycarbonate	28	750	1200	7.6
L3	Polycarbonate	28	1000	1200	18
L4	Aluminum	28	1000	2700	Not measured

Table 4.3: Plate characteristics. Their short name is chosen to indicate their material (first two letters) their length in cm and their thickness in μm.

4.4.3 Plate tracking

To follow plate's motion while conducting experiments, it is filmed from the side. Its visible edge is colored in black to allow tracking. Due to differences in lightning and the relatively small thickness of the plates, methods based on binarization and contour are not efficient to achieve this purpose [Bovik, 2009]. Indeed, no threshold can be found so that all the plate is differentiated from the background. Therefore, a tracking algorithm is designed. The principle is fairly simple. For each movie, the user has to indicate the plate leading edge position, as a line and a column. To reconstruct the plate's position along all its length using an iterative process. It consists in tracking the darker squares column by column as depicted on the flow chart Figure 4.15 **A**. The Figures 4.15 **B** and **C** illustrate the accuracy of this method as Figure 4.15 **B** shows a reference image and Figure 4.15 **C** shows the same image, on which plate's tracking have been superposed in red. It can be seen that the detection follows accurately the plate's edge.

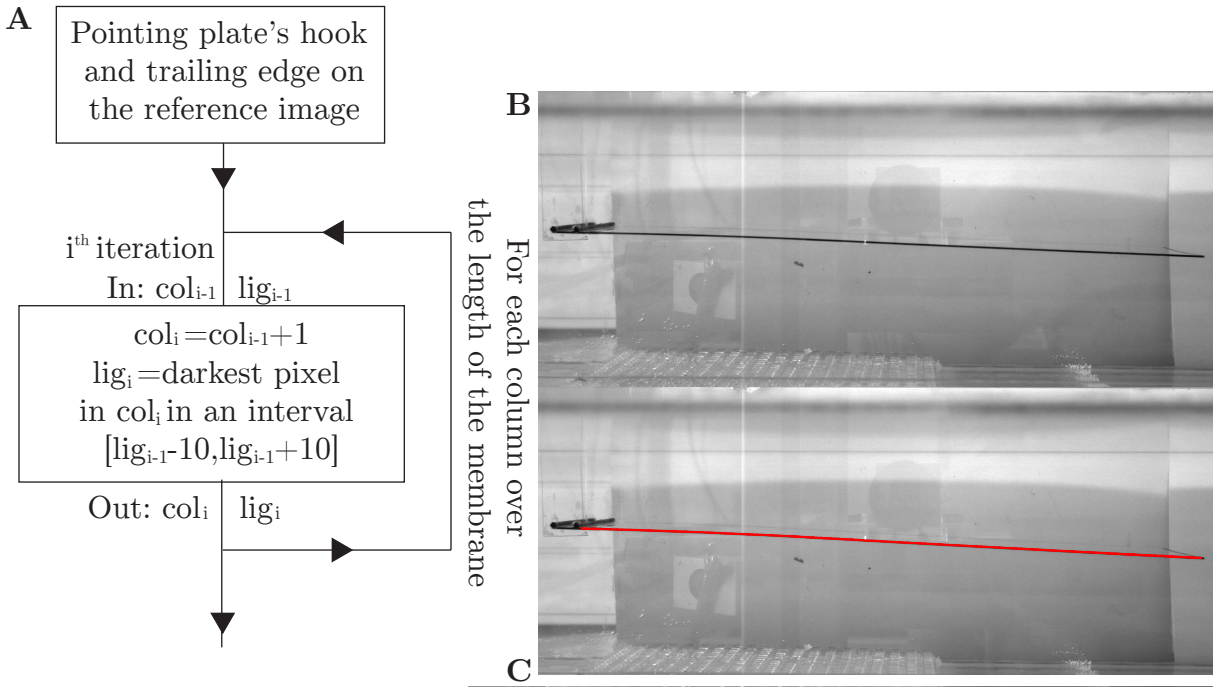

Figure 4.15: **A** Flowchart describing the treatment to extract plate's shape. **B** Side view of L2 without waves. **C** Same view as **B** but plate shape detected numerically is superposed and presented in red.

4.4.4 Clamping system

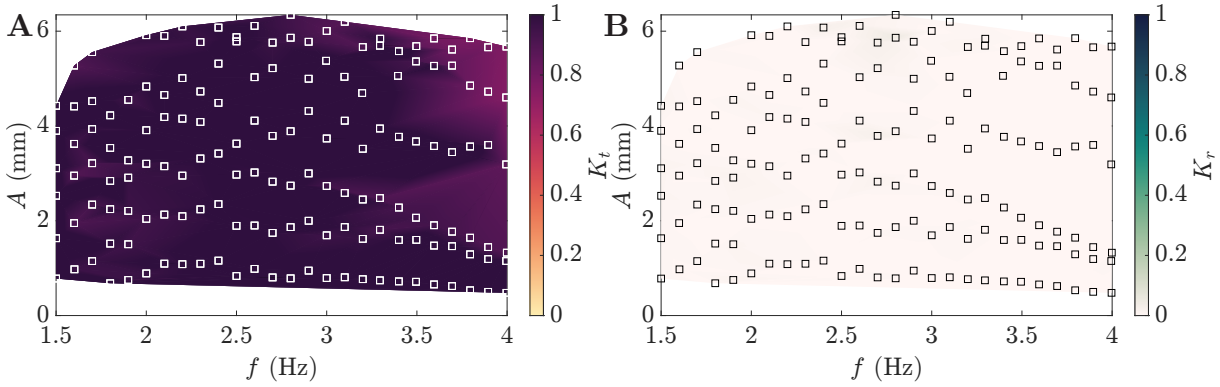

Figure 4.16: **A** Amplitude-frequency diagram presenting the measurements of transmission coefficients when there are only the attachment poles in the tank. **B** Same as **A** but for reflection coefficients. Kt is equal to 1 and K_r is equal to 0 for all couples, illustrating the fact that the poles do not disturb the wave field.

The plate clamping system is a primordial part of the experiment. Its main role is to maintain the plate fixed at its leading edge. The main difficulty when building such a system is that

it has to be rigid but also non intrusive to measure only the effects of the plate on the waves. The choice made here is to clamp the plate using a carbon rod of 1 mm radius that provides good rigidity for the system while taking very little space. Two parallel rods, separated by 1 cm, are then glued to the plate using epoxy adhesive. To maintain the two poles at a given depth two poles have been cut in PVC. They have a 2 mm thickness and pierced with holes of the same diameter as the carbon rods. The two poles are maintained out of water and rigidly fixed to the tank. Carbon rods are inserted into the holes at a given depth as sketched in the zoom view of Figure 4.1 or pictured in Figures 4.15 **B** and **C** or Figures 4.14 **A** and **B**.

As mentioned, it is crucial for the attachment to be as non-intrusive as possible. To test that, coefficients of reflection and transmission measurements are performed for different waves amplitudes and frequencies, with the clamping system alone, without the plate. The results are presented in Figure 4.16. It can be observed that for all (A, f) pairs, the coefficient of transmission is equal to one and the coefficient of reflection is equal to zero, showing that the poles do not disrupt the waves.

4.5 Particle Image Velocimetry

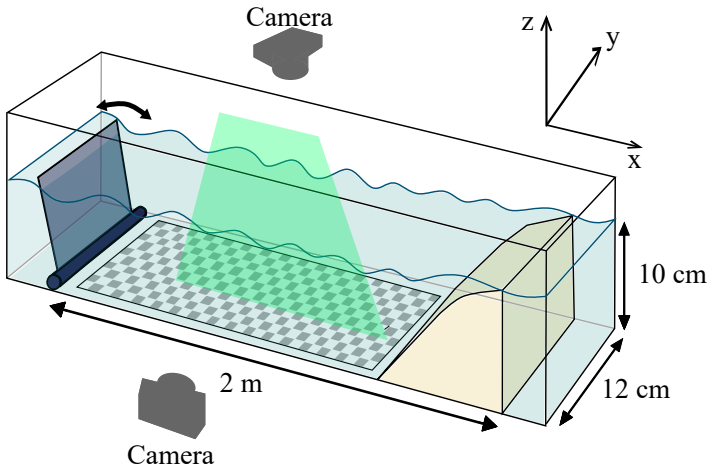

Figure 4.17: Scheme of the experiment when performing PIV experiment in an empty tank. Filming from the side gives access to particle and fluid motion. Filming from the top allows wave field reconstruction as presented in section 4.2. A laser sheet is sent from the top using a laser and a cylindrical lens.

General considerations on Particle Image Velocimetry (PIV)

To gain insights on the behavior of the elastic plate in a wave field, PIV is employed. PIV consists in seeding the fluid with particles and to track their motion. In order to observe only a given part of the flow, a laser sheet is sent and illuminates particles. Particles located in the laser sheet will diffract laser light and appear brighter. Particles appear clearly when filming or taking pictures of the experiment. Similarly to the use of dye, simple observation of particles trajectories, over a certain period of time, can offer qualitative information on fluid motion. In addition, PIV offers quantitative measurements as it allows to deduce the velocity fields from particles observations. To do so, cross correlation is calculated between two successive images. Typically, successive images are obtained by filming the experiment but taking two photos can be sufficient to obtain the speed at a given instant. When performing PIV experiment the choice of particles is crucial. The first constraint is that they act as tracers which means that their motion follows that of the flow. In practice, for sufficiently small particles and speeds, when the fluid accelerates particles undergo Stokes force. The particle will then reach the same velocity as the fluid but with a delay, τ_p. This delay is function of their density ρ_{pa} and, for spherical particles, their diameter d_p. According to Raffel et al. [1998] for a constant acceleration, τ_p scales as:

$$\tau_p = \frac{d_p^2 \rho_{\text{pa}}}{18 \mu_d}, \tag{4.5.1}$$

with μ_d water dynamical viscosity.
Delay, tau_p, gives a good approximation of the maximal frame rate that can be chosen to obtain particles moving at the same speed as the flow on every frame. As it will be shown in Section 4.5, this criteria will not be restrictive. However, sedimentation also plays a key role when performing PIV in a wave field as there is no mean flow opposing gravity effects. As particles are not exactly density-matched with water, they tend to sediment. This effect is more significant for larger particles, so that the use of smaller particles is also encouraged. Looking at these considerations it seems that particles as small as possible should be employed. However, particle size also plays a role to scatter light and bigger particles will appear more clearly. The setup designed to record data is then particularly crucial and parameters such as shutter speed must be chosen so that particles appear clearly visible.

Setup configuration to perform PIV measurements in the wave tank

Polyamid seeding particles of 20 μm diameter and a density of 1.03 are used. According to Equation (4.5.1), the relaxation time, τ_p, is equal to 10^{-5} s meaning that particles will be

good tracers if the frame rate remains inferior to 10000 s^{-1}. This criteria is not very restrictive so one could think of using larger particles given the typical fluid velocity values, which are observed in capillary and gravity water waves. However, because bigger particles are more sensitive to sedimentation, particles of and 20 μm appeared to be a good compromise that could be employed without having to add more particles during the course of several hours. To prepare the mixture, 10 g of particles are mixed with 10 g of soap. Water is then added to obtain a volume of 500 mL. Typically before beginning experiments, 100 mL of suspension are poured into the tank where they are mixed by hand and by sending waves.
The laser used here is a Genesis MX532-8000 from Coherent®[2]. It is continuous and has a 532 nm wavelength. As its power can be tuned, experiments will be performed using power values between 0.8 W and 1 W depending on the size of the laser sheet or on the camera position. The laser sheet is formed and oriented using a cylindrical lens and a mirror. The laser sheet obtained is similar to the one sketched in Figure 4.17.
As presented in Figure 4.17, two cameras are utilized. The one at the top films the checkerboard for wave measurements and the one at the side records particles motion and plate's motion. As Fast Checkerboard Demodulation would not work in the dark, a filter is placed on the side view camera, removing all wavelengths except the laser's one. It allows to work with the room light turned on and to measure water waves height with Schlieren imaging and fluid velocity with PIV simultaneously. The top view camera frame rate is imposed at 50 frames per seconds. The side view frame rate is tuned depending on wave frequency with the relation $f_{acq} = 40.f$, with f being the wave frequency and f_{acq}, the frame rate. This choice allows to perform phase averaging with enough image for each period. The exposure time is then fixed at $1/f_{acq}$.
Velocity fields are then extracted using the Davis software developed by LaVision®[3]. For most experiments, correlation windows have a 12 × 12 or 16 × 16 pixels with a 5 pixels maximum displacement.

4.6 Verification of experimental methods

4.6.1 PIV in a wave field

As emphasized in Section 4.5, the use of a filter on the camera allows achieving water wave height measurements and PIV measurements simultaneously. The coherence between these two measurements is a good proof that all the tools chosen for this study are well scaled.

[2] https://www.coherent.com/
[3] http://www.lavision.de/en/

This section focuses on the comparison between measurements obtained using PIV and water wave height evaluation using synthetic Schlieren imaging by looking at particles trajectories and velocity in a wave field without obstacle.

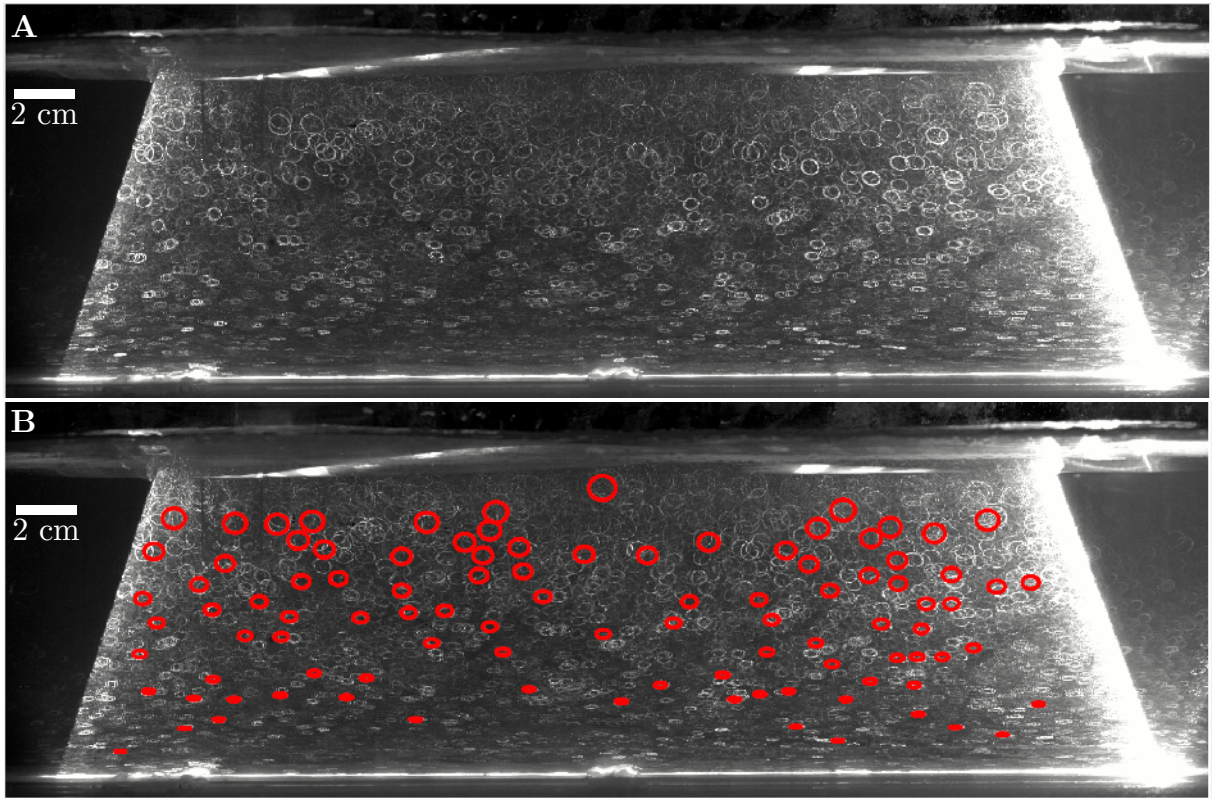

Figure 4.18: **A** Particle trajectories in 2 Hz waves with an amplitude of 4.7 mm. **B** Same as **A** but particles trajectories predicted theoretically are added in red. A good matching between theoretical and experimental particles trajectories.

Particle trajectories

Particle trajectories in a wave field is given by linear theory (see Equation 2.1.45) and particles follow ellipses of radius proportional to wave amplitudes. Particle trajectories over a given time interval can be evaluated using the measured particle trajectory. To do so, the maximum intensity at each pixel over that time interval is taken. As particles appear brighter on each image, the result of that operation displays their trajectories, as shown in Figure 4.18 **A**. To ensure a good visibility of particles trajectories and avoid overlap, it is useful to decrease particles concentration.

The trajectory of particles as it is given by linear theory can also be computed, using the wave amplitude measured by means of Schlieren imaging. The comparison between trajectories observed and those predicted theoretically is presented in Figure (4.18) **B**. It can be

observed that the predicted trajectories fit with the observed ones. As this result has high sensitivity to the wave amplitude measurement, which confirms the consistency between the two measurements.

Velocity measurements

The flow velocity at a given position and time can be evaluated using PIV experiments. In order to compare the velocities measured using PIV with the theoretical values from linear theory, the maximum flow speed along x or z measured at a given position is computed. By averaging this data along x, the speed profile along z is obtained. The comparison between the speed profile obtained experimentally and the theoretical one is presented in Figure 4.19. A good agreement can be observed except close to the free surface. Interestingly, a constant $\approxeq 5$ mm.s^{-1} a shift can be observed looking at u_z.

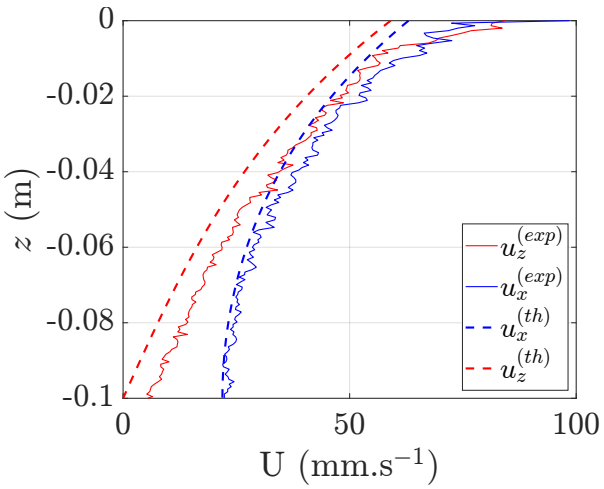

Figure 4.19: Maximum flow speed in the x and z direction for different depths for theoretical and experimental values for 2 Hz. A 4.7 mm amplitude wave amplitude is measured using Schlieren imaging during the same experiment. The experimental values are averaged along all the observation window. Except close to the free surface, theory and experiments show good agreements.

4.6.2 Wave dissipation measurements

As emphasized in Section 4.3, the dissipation coefficient ν makes measuring reflection and transmission coefficients challenging. Wave damping represents one of the main challenges when performing small-scale experiments, partly because it adds a non-linear term in the shape of wave envelope. A specific method to measure reflection and transmission coefficients, K_r and K_r (see Section 4.3) is thus needed. Also, this dissipation coefficient varies largely

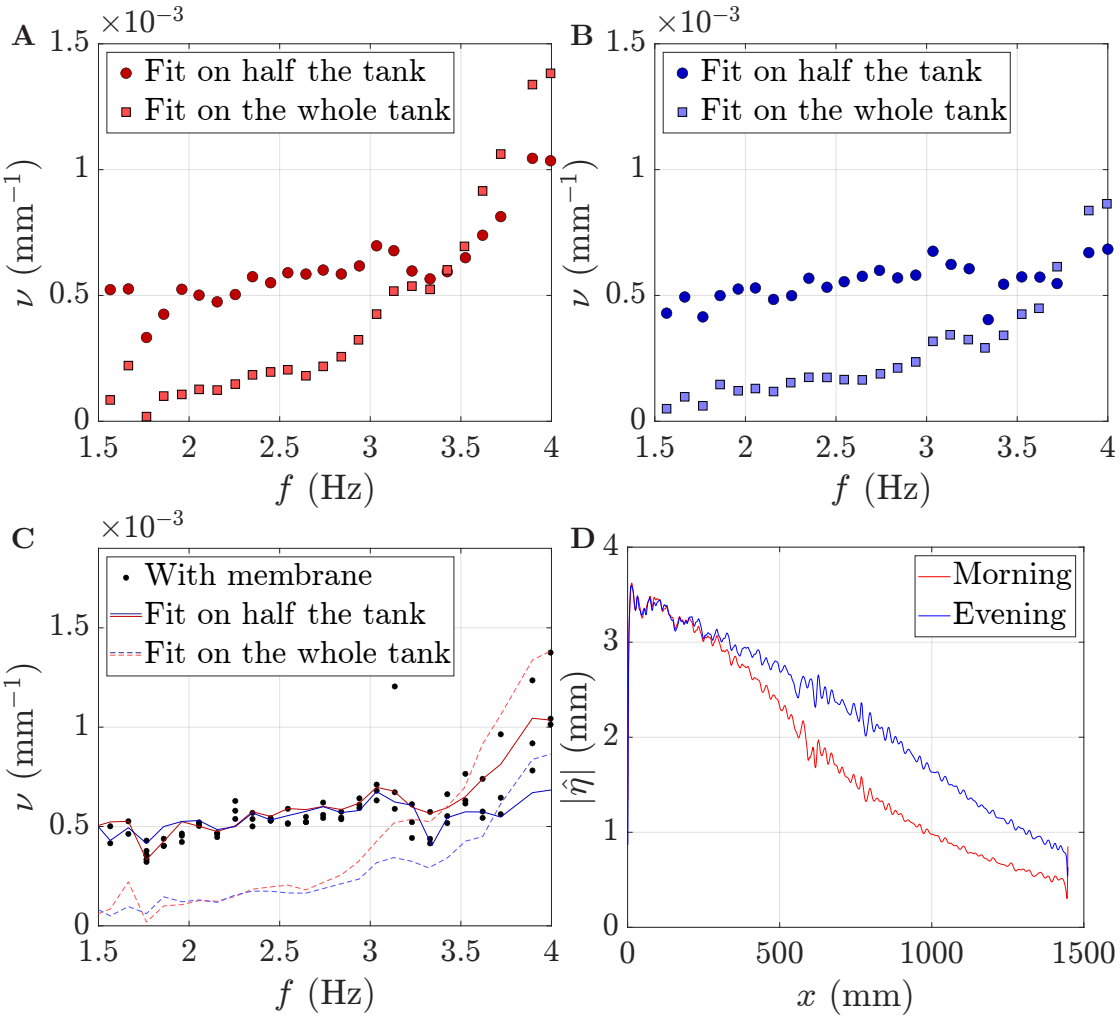

Figure 4.20: (**A-B**) ν measurements in an empty tank for various frequencies. Measurements in **A** were performed in the morning before conducting experiments with an object and measurements in **B** in the evening of the same day, after conducting experiments with the plate. For both figures, darker circles correspond to measurements performed using only half the tank and light-colored squares to ν measurements using all the tank. At low frequencies the dissipation appears to be largely overestimated when using only half the tank.
C Dissipation coefficient, ν as a function of wave frequency. Data presented in Figure **A** and **B** are superposed using the same colors but using lines. Black dots represent data obtained while performing experiments with an obstacle. At low frequencies results are similar to what is obtained by taking fitting ν by using half the tank without obstacles. At higher frequencies measurements are coherent with what was obtained without obstacles, showing good agreement when dissipation is particularly significant.
D Wave amplitude, $|\hat{\eta}|$, as a function of the position in the tank for waves of 4 Hz frequency *i.e.* the maximum dissipation. As for the other figures, red corresponds to the experiment without plate in the morning and blue to the experiment performed in the evening.

due to water cleanliness or the type of surfactant polluting the free surface (see Alpers and Hühnerfuss [1989] or Sergievskaya et al. [2019] for instance), leading to non negligible variations even on the scale of a single day as illustrated in Figure 4.20 **D**. The precise understanding of wave damping mechanisms is out of scope of this thesis but the fact that the dissipation coefficient cannot be calibrated once and for all, even for a single day experiments, motivates the need to evaluate the dissipation simultaneously with the coefficients of reflection and transmission. The precision of this measurement is affected by both the measurement window size and by the presence of reflection. To ensure the validity of this measurements, experiments comparing values measured in the empty tank and in the presence of an object are performed.

To do so, measurements with waves going from 1.5 Hz to 4 Hz are performed in the tank without obstacles. Then, three repetitions of experiments with a plate are performed. Finally, the first set of experiment is repeated at the end of the day. It took a day to perform those experiments, so that the two experiments without plate were made respectively with a six hours delay.

This study has two aims, first, to examine the impact of using only half of the tank length (x direction in Figure 4.1) to measure the dissipation, ν. Indeed, it is expected that when using only half the tank, the estimation of ν will be less accurate as the wave amplitude decay is less significant on shorter distances. Secondly, these measurements are utilized to investigate the object influence when measuring the dissipation.

Results for the comparison between dissipation measurements in the tank without plate but using either the complete tank length or only half of it to estimate dissipation are presented in Figure 4.20. Figure **A** corresponds to measurements performed at the beginning of the day and Figure **B** to measurements performed at the end of the day. The comparison between the two Figures emphasizes the significant variations of dissipation that can be observed through the day, particularly at higher frequencies. Looking at each figure, it appears that using only half of the tank tends to overestimate dissipation at low frequencies but offer relatively accurate results at higher frequencies when wave damping is significant. This difference makes the method employed here inefficient to conduct a precise study on the evolution of wave damping at the same time as measuring reflection and transmission. However, for our purpose overestimating ν at low frequency does not represent a real issue as wave amplitude decay remains small.

Figure 4.20 **C** presents the comparison between values of ν measured with the object and without object. The results are coherent with measurements made with the empty tank. Dissipation appears higher than the one measured using all the tank length. However, when dissipation is significant *i.e.* for wave frequencies above 3 Hz, the measurement has the same

order of magnitude as the dissipation measured in the morning and in the evening. Note that the measure at 3.1 Hz led to an abnormally high value of ν but it is kept on the figure as nothing disturbed the experiment.

4.7 Conclusion

In summary, this Chapter lists the various methods and procedures that can be used in the small scale setup as well and the advantages and disadvantages of such a setup.
To study wave behavior, Schlieren imaging is employed and specific treatments have been developed to measure reflection and transmission coefficients while taking wave dissipation into account. PIV can be performed from the tank side view. Study of the velocity field is coherent with wave height measurements obtained with Schlieren imaging. In addition, a complete description of plates used in the Chapter 5 is given, underlining the experimental challenge of maintaining a plate horizontal in a wave field.

Chapter 5

Experimental investigation of the interaction between water waves and a submerged elastic plate

The experimental procedures described in Chapter 4 are used to characterize experimentally the interaction between water waves and a submerged elastic plate clamped at one end. This Chapter, first, focuses on small wave amplitudes where the results are expected to be closer to the linear theory. The reflection and transmission coefficients and plate motion amplitudes are measured and compared with numerical results, showing relatively good agreement. The experimental investigation also highlights the key role of flexibility in wave reflection.
Secondly, the impact of higher wave amplitudes is evaluated looking at the reflection and transmission coefficients, plate motion, and dissipation of wave energy for increasing wave amplitudes. It is shown that for sufficiently high waves, the more flexible plate, L1, can act like a perfect wave terminator. Finally, the causes of dissipation in the fluid are investigated using Particle Image Velocimetry (PIV) from the side view. As a reminder, the plates used here are described in Chapter 4. The first letter, S or L, for small or long, indicates their length, 19 cm for S plates and 28 cm for L plates. The number following indicates their rigidity from 1 to 4, 1 being the more flexible one, made of Polypropylene, and 4 being the completely rigid plate made of Aluminum (see Table 5.1).

Short name	Material	Length, L (cm)	Stiffness, EI (10^{-3}.N.m^2)
S2	Polycarbonate	19	7.6
L1	Polypropylene	28	1.7
L2	Polycarbonate	28	7.6
L3	Polycarbonate	28	18
L4	Polycarbonate	28	Not evaluated

Table 5.1: Compact version of Table 4.3 in Chapter 4. It reminds the different plates characteristics and their designation.

5.1 Wave-plate interaction for low amplitude waves

In order to characterize the interaction between water waves and a submerged elastic plates, coefficients of reflection, K_r, and of transmission, K_t are measured for different plate lengths, stiffness or depths. K_r and K_t are defined as in Section 2.1.2 of Chapter 2. In all this Section, the experimental procedure followed is the same, waves are generated for one minute before starting data acquisition from top and side view during 15 s. At each frequency, three measurements are made. The wave-maker amplitudes used are the same as in Chapter 4, Section 4.1.2 over frequencies ranging from 1.5 Hz to 4 Hz. In this Section focusing on small wave amplitudes, the Target Wave Amplitude, TWA, is fixed at 1 cm

5.1.1 A baseline case: study of wave interaction with L2 at a 3 cm depth

Reflection and transmission coefficients measurements for L2 at a 3 cm depth

Figure 5.1 **A** presents K_r and K_t as a function of wave frequency for L2 at a 3 cm depth. It appears that at low frequencies the plate mostly transmits wave energy. However, as the frequency increases, K_t decreases and, K_r increases showing a wide reflection peak centered at 2.2 Hz. At this frequency, the plate reflects almost 75 % of wave energy. Finally, for frequencies higher than 2.5 Hz, almost all the wave energy is transmitted by the plate. The standard deviation of the three measurements is shown with black errobars. Even though overall data appear relatively noisy, reflection and transmission coefficients calculations are very repeatable.

Figures 5.1 **B**, **C** and **D** present the same data but as a function of normalized quantities. In Figure 5.1 **B**, K_r and K_t are presented as a function of wave frequency divided by the plate resonance frequency in the air, f_0. As explained in Chapter 4 plate resonance frequency is estimated performing a free-oscillation test. The reflection peak central value is located at $f/f_0 \sim 1$, suggesting that wave reflection could be fully driven by the specific excitation of the plate first mode. However, study of reflection and transmission for other plates will show that this result is more of a coincidence. To anticipate on the rest of this Chapter, L3 at 3 cm exhibits a wide peak for the same wave frequency, even thought f_0 is higher for L3.

Similarly, Figure 5.1 **C** shows K_r and K_t as a function of wave frequency, f, normalized by plate natural frequency measured in a still fluid, $f_{0\text{ma}}$. $f_{0\text{ma}} = 1.7$ Hz for L2. The reflection peak frequency appears for f=1.2-1.3 $f_{0\text{ma}}$.

Finally, **D** explores possible diffraction effect using the plate length, L, to normalize, respec-

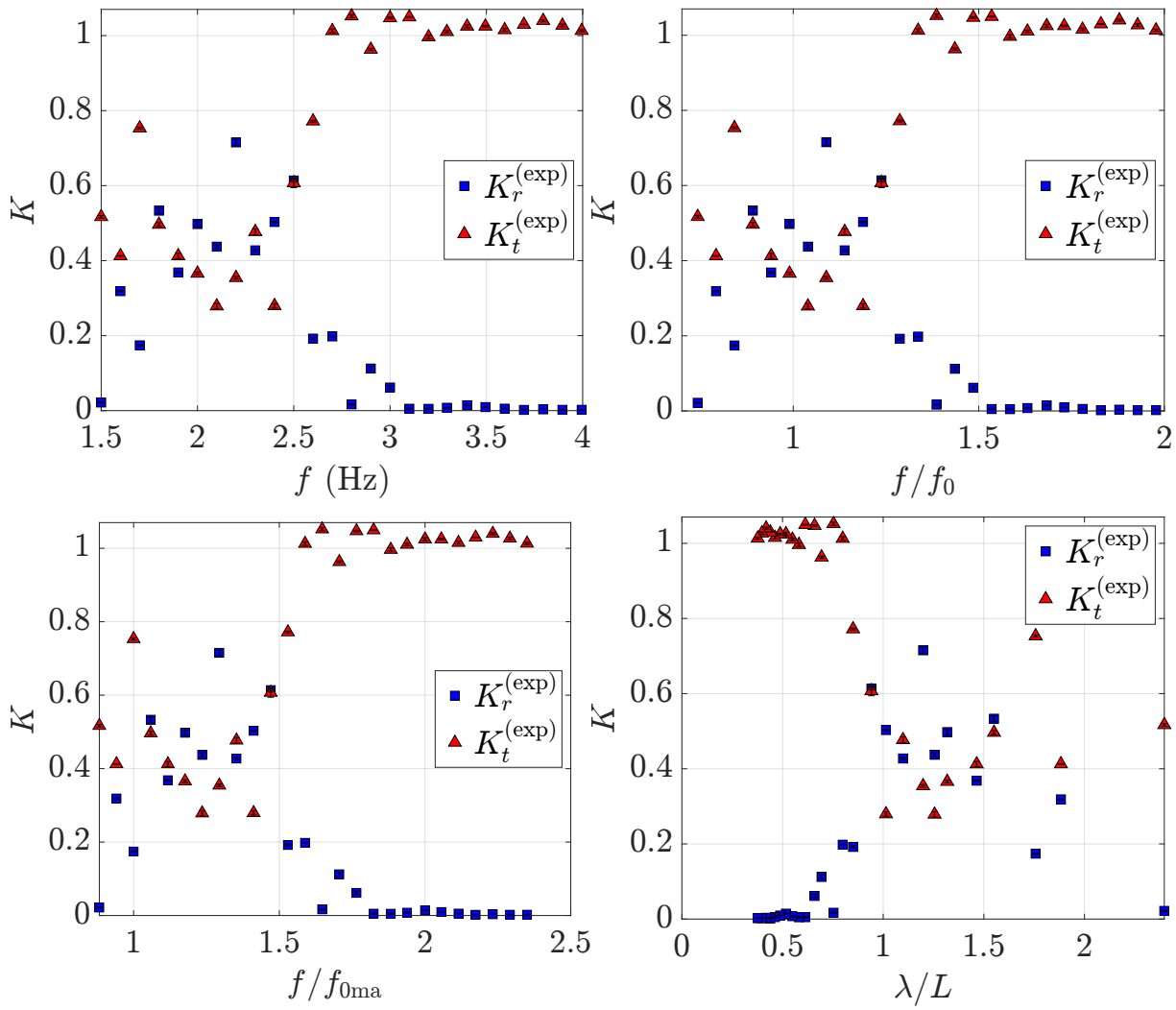

Figure 5.1: Reflection and transmission coefficients measurements for L2 at a 3 cm depth. Experimental reflection and transmission coefficients, $K_r^{(\mathrm{exp})}$ and $K_t^{(\mathrm{exp})}$ as a function of wave frequency, f, (**A**), wave frequency normalized by the resonant plate frequency in air, f_0, (**C**), wave frequency normalized by the resonant plate frequency in still water, $f_{0\mathrm{ma}}$, (**C**), and the wavelength, λ, normalized by the plate length, L, (**D**). In all the Figures errorbars show standard deviation.

tively, λ, the wavelength. As the reflection peak frequency is observed for λ=1.2-1.3 L , plate length, L does not seems to be the crucial parameter to account for reflection.
From the different normalization it seems that reflection happens when wave parameters are close to plate characteristics. However, no clear explanation arise from those observations.

K_r and K_t measurements can be compared with calculations performed in Chapter 3. Figures 5.2 show the comparison between reflection and transmission coefficients for L2 at a 3 cm depth. The theoretical and experimental values show a similar behavior. Indeed, linear theory predicts a wide reflection peak centered at 2.2 Hz that matches with the wide reflection

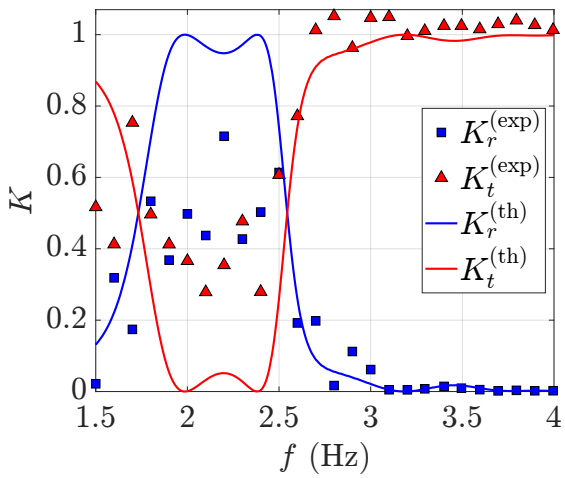

Figure 5.2: Reflection and transmission coefficients measurements for L2 at a 3 cm depth as a function of wave frequency, f. $K_r^{(exp)}$ and $K_t^{(exp)}$ are the experimental reflection and transmission coefficients and $K_r^{(th)}$ and $K_t^{(th)}$ coefficients calculated using wave linear theory for an equivalent plate. The experimental points correspond to mean over three experiments.

peak observed experimentally. However, the K_r and K_t values differ between experiments and linear theory. Indeed, $K_t^{(exp)}$ drops to 0.3. The theoretical minimum transmission coefficient $K_t^{(th)}$ reaches 0 at 2 Hz and at 2.4 Hz. On the other hand, reflection coefficients are overestimated theoretically.

The frequencies where a full transmission is predicted by linear wave theory match very well with experimental measurements. For $f \geq 2.7$ Hz, $K_t = 1$ for both theoretical results and experimental measurements. In addition, contrary to theoretical values, $K_t^{(exp)}$ and $K_r^{(exp)}$ underline the fact that waves loose energy due to the interaction with the plate as their sum can be slightly less than one. Wave energy dissipation suggests fundamental differences between experiments and linear wave theory. Those differences are discussed in Section 5.1.3.

Plate motion analysis

In Chapter 3, dedicated to the investigation of a submerged plate behavior in the frame of linear theory, it has been observed that wave reflection is associated with higher plate motion amplitudes. This section focuses on L2 motion. As a reminder the plate is filmed from the side of the tank and its movement is reconstructed using the procedure described in Chapter 4 and Section 4.3.

Figure 5.3 shows the plate position with respect to the horizontal, w, during a wave period for a Target Wave Amplitudes, TWA, of 1 mm and 4 different frequencies (1.5 Hz, 2 Hz, 2.5 Hz and 3 Hz). $w = 0$ if the plate is at the same depth than its hinged point. In other cases, w is less than 0 if the plate is above its hinged point and, w is more than 0 if the plate

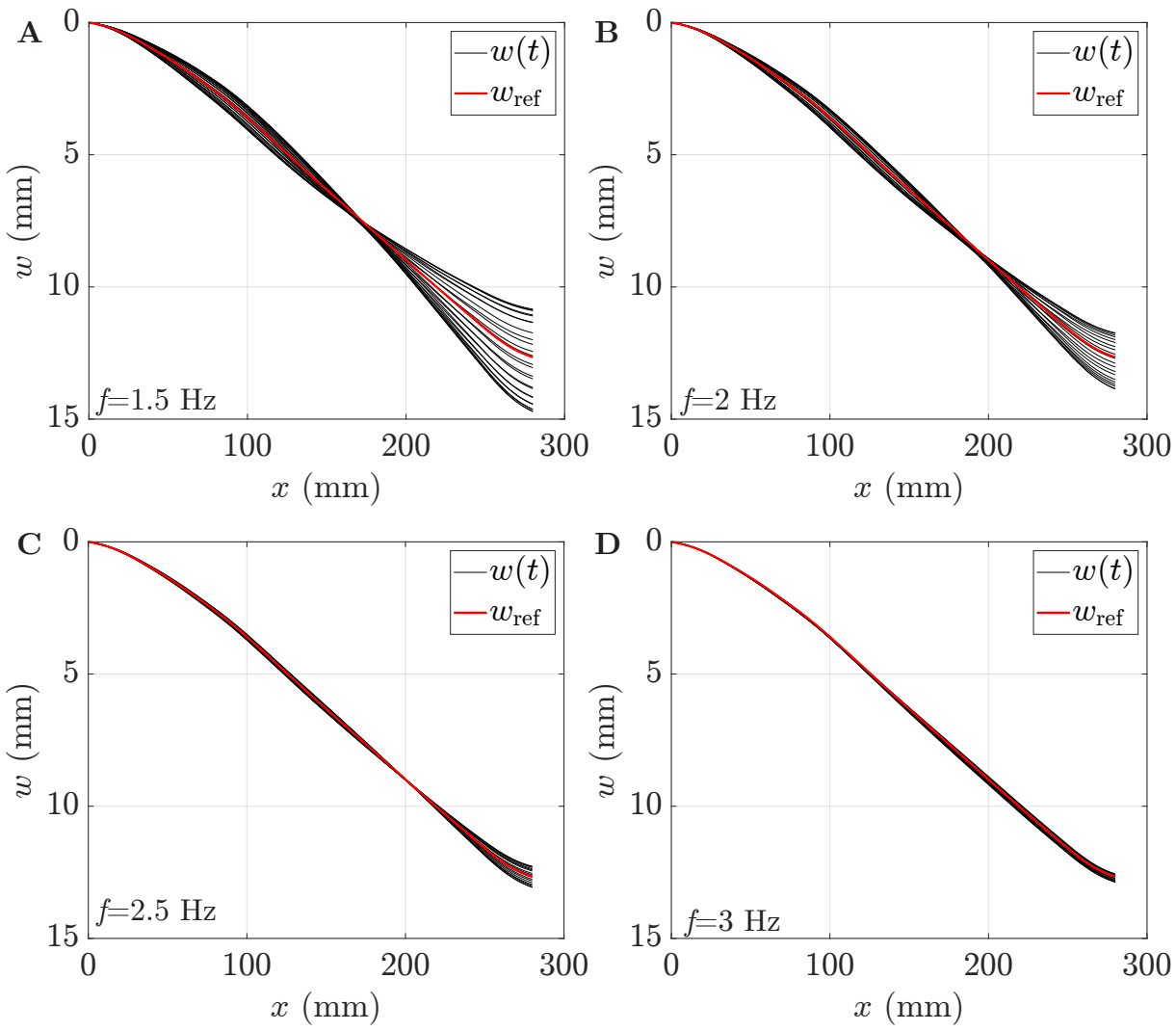

Figure 5.3: Plate displacement, w, for TWA=1 mm in black. Plate reference position, $w_{(\text{ref})}$, corresponding to plate position when no waves are sent is plotted in red. **A** 1.5 Hz, **B** 2 Hz, **C** 2.5 Hz, and **D** 3 Hz.

is below its hinged point. The red curve, w_{ref}, corresponds to the plate reference position, *i.e.* plate position when no waves are generated. It appears that the plate oscillates around its reference position and plate motion amplitude seems to decrease with frequency.
In order to compare the plate behavior with previous numerical results (see Chapter 3, Section 3.3.2), w is written as:

$$w(x,t) = \xi(x)\cos(\omega t) + w_{\text{mean}}(x), \tag{5.1.1}$$

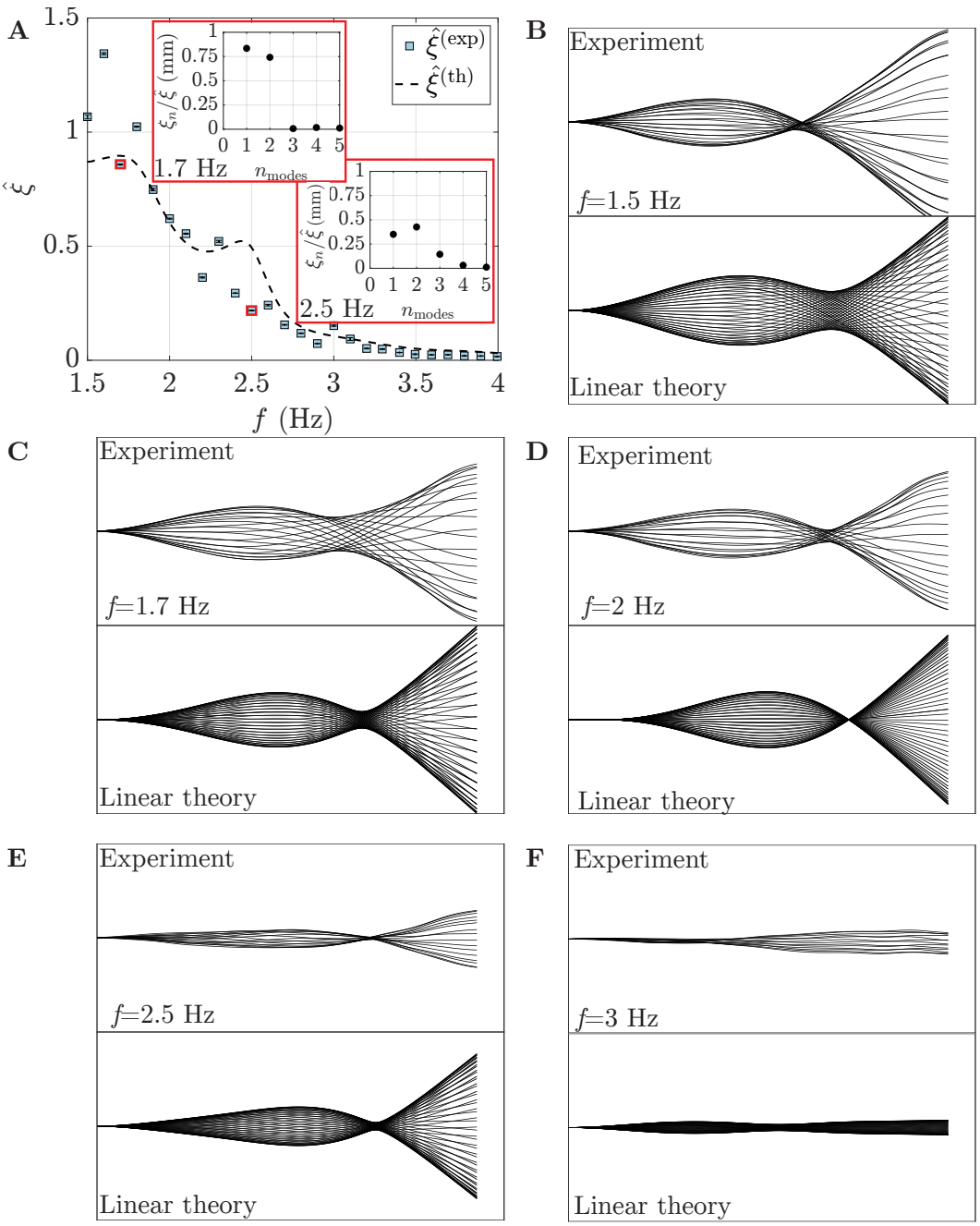

Figure 5.4: **A** Plate normalized amplitude, $\hat{\xi}$, as a function of wave frequency for L2 at a 3 cm submergence depth and TWA=1 mm. Experimental values are shown as light blue squares and theoretical predictions in a black dashed curve. Inserts show mode amplitude distribution among the first five modes of a cantilevered beam at 1.7 Hz and 2.5 Hz. **B-C-D-E-F** show comparisons between the experimental observations for the deformation around the equilibrium position, and linear theory predictions for $\xi(x)\cos(\omega t)$ over one wave period for, respectively, 1.5, 1.7, 2, 2.5 and 3 Hz waves.

with ξ being plate motion envelope with respect to the plate mean position during the experiment, w_{mean}. For small wave amplitudes, $w_{\text{mean}} = w_{\text{ref}}$ but those two quantities can differ for larger wave amplitudes. From this expression, the normalized plate motion amplitude, $\hat{\xi}$, can be computed. Similarly to Chapter 3, it is evaluated by considering the plate motion envelope ξ, so that:

$$\hat{\xi} = \sqrt{\frac{1}{L}\int_0^L \frac{\xi(x)^2}{A^2}\mathrm{d}x}. \tag{5.1.2}$$

$\hat{\xi}$ values are presented in Figure 5.4 **A** as a function of the wave frequencies for TWA=1 mm and compared with the theoretical predictions.

Experimental values of $\hat{\xi}$ decrease with the wave frequency. Both theoretical and experimental values follow a similar trend. It seems that linear theory predicts relatively well the the downward trend of experimental data. However, experimental data do not show any resonance, contrary to theoretical values for which an increase in plate motion amplitude is visible at 2.4 Hz. For better visualization, and to gain insight on the differences between plate behavior in linear theory and in experiments, the plate motion at different frequencies can be computed. Figure 5.4 **B**, **C**, **D**, **E** and **F** show the plate normalized relative displacement, $\frac{\xi}{A}\cos(\omega t)$, with A being the incident wave amplitude for five wave frequencies, 1.5, 1.7, 2, 2.5, and 3 Hz, respectively.

Experimental values show a node and one half anti-node at all frequencies below 3 Hz. The node position changes with frequency and seems to get closer to the plate tip when frequency increases. As shown in Chapter 2, this behavior is typical of a cantilevered beam first and second modes, with the node position changing as a function energy distribution between the modes. To illustrate this affirmation, similarly to Chapter 3, ξ can be written:

$$\xi(x) = \sum_n \xi_n f_n(x), \tag{5.1.3}$$

with ξ_n being the n^{th} mode amplitude and f_n the n^{th} cantilevered beam mode eigenfunction, as defined in Chapter 2. For a given n, the mode amplitude, ξ_n, can be computed as:

$$\xi_n = \frac{1}{L}\int_0^L \xi(x) f_n(x)\mathrm{d}x., \tag{5.1.4}$$

Inserts in Figure 5.4 **A**, show the mode amplitude distribution among the first five modes of a cantilevered beam at 1.7 Hz and 2.5 Hz, respectively. The fact that both plate modes 1 and 2 exist when the plate reflects the waves confirms that reflection is not associated to the excitation of unique plate mode. Additionally, the plate amplitude decrease with wave

frequency can also be observed. At 3 Hz, the plate is found to remain almost still.
For each frequency, the plate motion predicted theoretically is plotted below experimental results. It appears that theoretical plate motion has the same shape and amplitude as in the experiments. However, node position slightly differ. As underlined by Ramananarivo et al. [2014], changes in the node position could be attributed to fluid damping effects. The plate tip appears much more straight in linear theory predictions. This could also suggests the presence of non-linear flow effects that would slightly resist plate tip motion, resulting in a small bending.

5.1.2 Sensitivity analysis: varying plate stiffness, length and submergence depth

The case of L2 at a 3 cm submergence depth suggests a relatively good agreement between linear theory and experiments. To confirm this good agreement, a sensitivity analysis is carried out by the changing the plate stiffness, length and submergence depth. The trends followed by the wide reflection peak will be observed and compared with theoretical trends of Chapter 3.

K_r and K_t measurements

First, the effect of plate length change is observed. To that aim, experiments with S2, the 19 cm plate with the same stiffness as L2, are conducted. Results are presented in Figure 5.5 **A**. It presents K_r and K_t measured experimentally and calculated for S2. As for L2, experimental values exhibit a wide resonance peak centered around 2 Hz and full transmission for frequencies above 2.7 Hz. In comparison with L2, K_r reaches much smaller values as the maximum in reflection is measured equal to 0.35 versus 0.7 for L2. However, reflection frequency remains roughly the same.
The theoretical calculations from Chapter 3 are coherent with observations, since they show a similar trend as experimental work as peak amplitude decreased compared to L2. However, maximum reflection value is still poorly estimated in linear theory. A sharp reflection peak can be observed at 3.7 Hz. This reflection peak is not visible in experimental results. As observed in Chapter 3, sharp reflection peaks are associated with extremely intense plate resonance. Such amplitude cannot exist in reality as they would be damped. However, one could expect to observe at least a small variation in K_r and K_t that is not observed experimentally.
The effect of submergence depth is investigated by examining the L2 plate at a 5 cm submer-

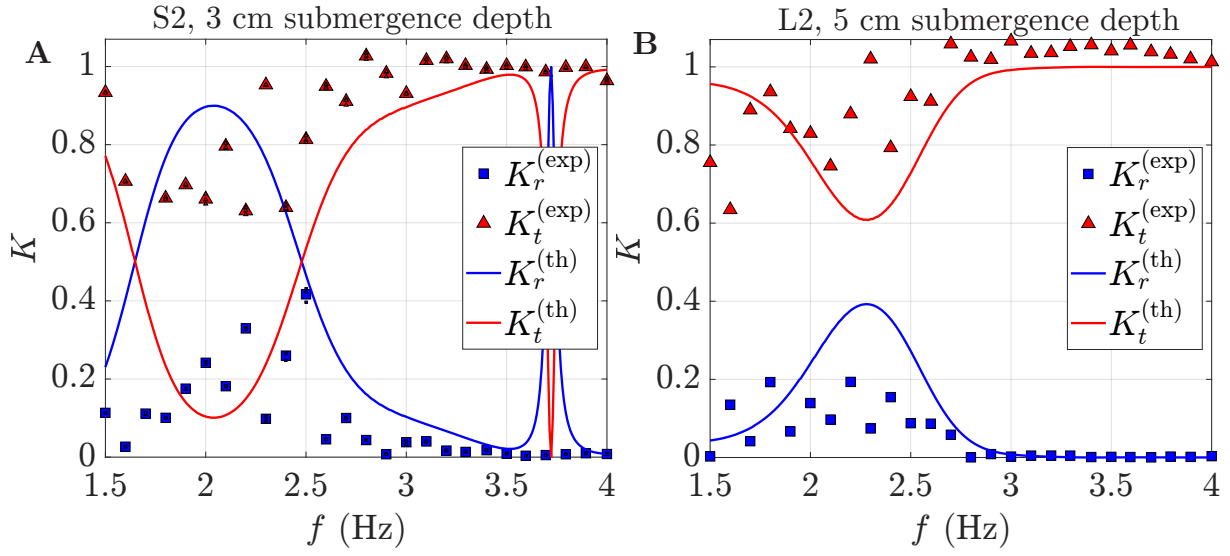

Figure 5.5: **A** K_r and K_t as a function of wave frequency for S2 at a 3 cm depth and TWA=1 mm. Experimental values $K_r^{(\text{exp})}$ and $K_t^{(\text{exp})}$ are represented with blue squares and red triangles respectively. Results from linear theory for the corresponding plate, $K_r^{(\text{th})}$ and $K_t^{(\text{th})}$ are represented in full lines of the same color as experimental values. **B** Same Figure but for K_r and K_t as a function of wave frequency for L2 at a 5 cm depth and TWA=1 mm.

gence depth. Figure 5.5 **B** shows K_r and K_t measurements for L2 at a 5 cm submergence depth. At low frequency, no reflection is observed while transmission is not equal to 1, showing wave energy dissipation. A wide reflection peak can be observed between 2 and 2.7 Hz and full transmission for larger frequencies. As for plate length, the change in submergence depth decreases reflection intensity but has no clear effect on frequency.

Similar behavior can be observed for linear theory where the reflection peak maximum decreases when increasing the submergence depth. Frequencies at which waves are fully transmitted by the plate are also correctly estimated.

Finally, the effect of plate stiffness is investigated by examining the L1, L3, and L4 plates at a 3 cm depth. Results are presented in Figures 5.6 **A**-**B**, **C**-**D** and **E** respectively. For L1, the more flexible plate, no reflection is observed experimentally at low frequencies. A wide reflection peak can be observed at higher frequencies. It reaches its maximum reflection at 2.8 Hz and zero transmission is even observed at 2.5 Hz. For frequencies above 3.2 Hz, waves are fully transmitted by the plate. In comparison with L2, the decrease in stiffness seems to shift the reflection peak towards higher frequencies.

The theoretical predictions for reflection and transmission exhibit a complex pattern that is far from the experimental reality, the only reasonnable agreement occurs for th lower frequencies at which waves are fully transmitted. For L1 plate in Figure 5.6 **A**, at low frequencies,

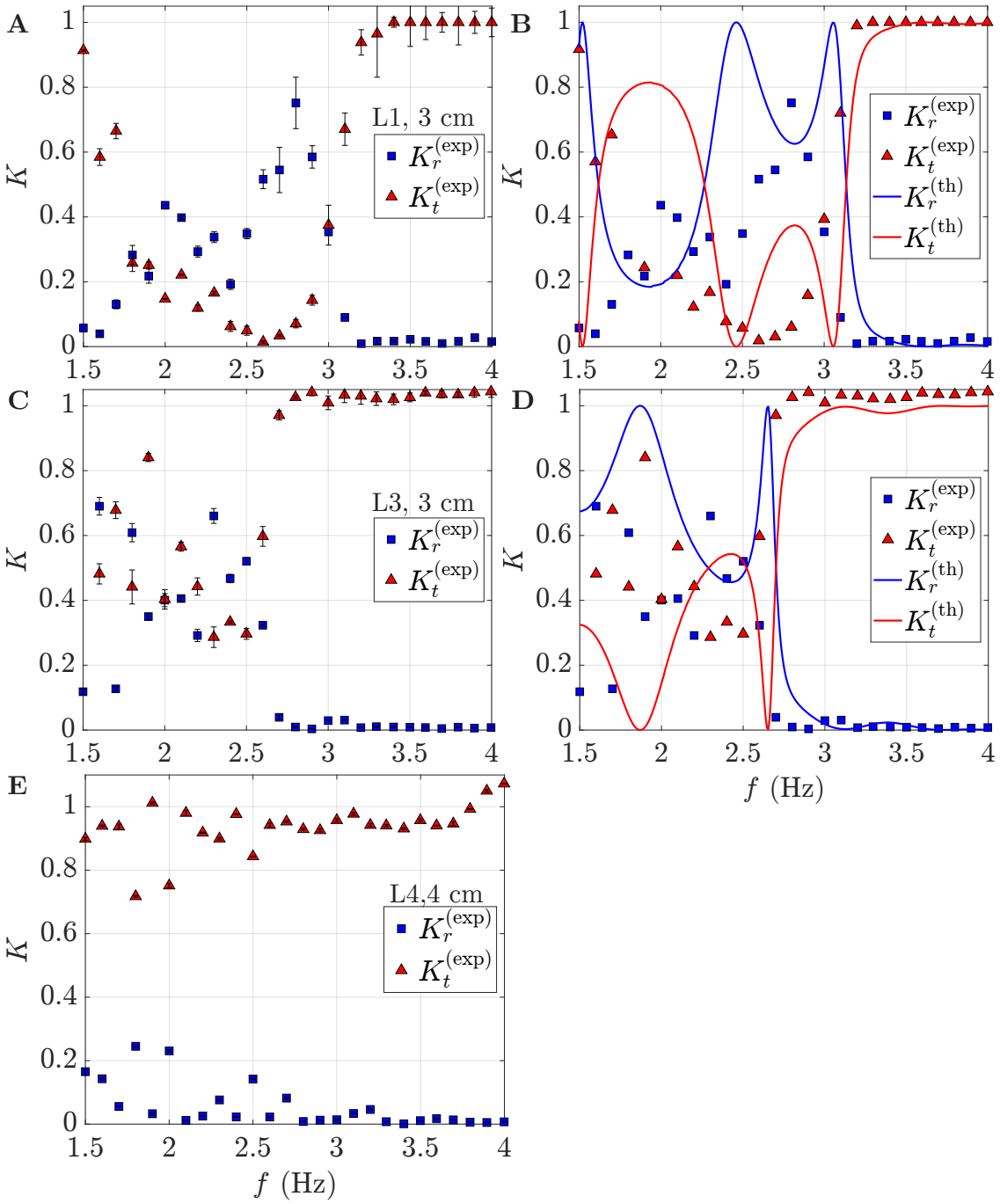

Figure 5.6: K_r and K_t as a function of wave frequency. Left column presents experimental results only and right column their comparison with corresponding theoretical values. Experimental values $K_r^{(\mathrm{exp})}$ and $K_t^{(\mathrm{exp})}$ are represented with blue squares and red triangles respectively. The Results from linear theory, $K_r^{(\mathrm{th})}$ and $K_t^{(\mathrm{th})}$ are represented in full lines of the same color as experimental values. **A-B** L1 at a 3 cm depth and TWA=1 mm. **C-D** L3 at a 3 cm depth and TWA=1 mm. **E** L4 at a 3 cm depth and TWA=1 mm.

a sharp peak can be observed. Between 2 and 3 Hz a splitted wide reflection peak is present and waves are fully transmitted by the plate at higher frequencies. Splitted wide reflection peaks have been described in Chapter 3 and results of a wide peak growth. Similarly to experimental observations, central frequency of this peak is shifted towards higher frequencies compared to L2.

K_r and K_t for L3 at a 3 cm submergence depth are shown in Figure 5.6 **B**. Experimental data is particularly noisy at low frequency but a reflection peak can also be observed experimentally. It does not appear to be shifted compared to L2. As for other experiments, frequencies at which reflection is observed correctly predicted but not the exact values of K_r and K_t. Linear theory predicts an important change in wide peak frequency at low stiffness and relatively constant value for higher stiffness. This behavior seems to be similar to what is observed experimentally. To give more comparison with Chapter 3 values of r, parameter that compares plate stiffness and density, are respectively of 58, 135 and 240 for L1, L2 and L3. Given those values, it is not surprising to observe a clear difference in f_c between L1 and the two other plates.

Finally, experiments are conducted with L4, the rigid plate. Results are presented in Figure 5.6 **C**. It appears that L4 mostly transmits wave energy across all frequencies. This observation is primordial in order to understand wave reflection by a flexible plate. As mentioned in Chapter 2, two effects can be responsible for reflection, diffraction, *i.e.* the plate shape, or radiation, *i.e.* the plate motion. Here, it is shown experimentally that, over this range of frequencies, a rigid plate does not reflect waves. It means that reflections observed are mostly due to radiation. In this system, flexibility enables wave reflection.

To sum up the parametric analysis results, trends followed experimentally and numerically are presented in Table 5.2.

	Theory	Experiments
Reflection frequency with depth	Increase	Not clear
Reflection intensity with depth	Decrease for $d > 2$ cm	Decrease
Reflection frequency with length	Increase	Not clear
Reflection intensity with length	Increase	Increase
Reflection frequency with stiffness	Decrease	Decrease
Reflection intensity with stiffness	Non monotonic	Not clear

Table 5.2: Evolution of the reflection frequency and its intensity, when varying plate depth, length or r.

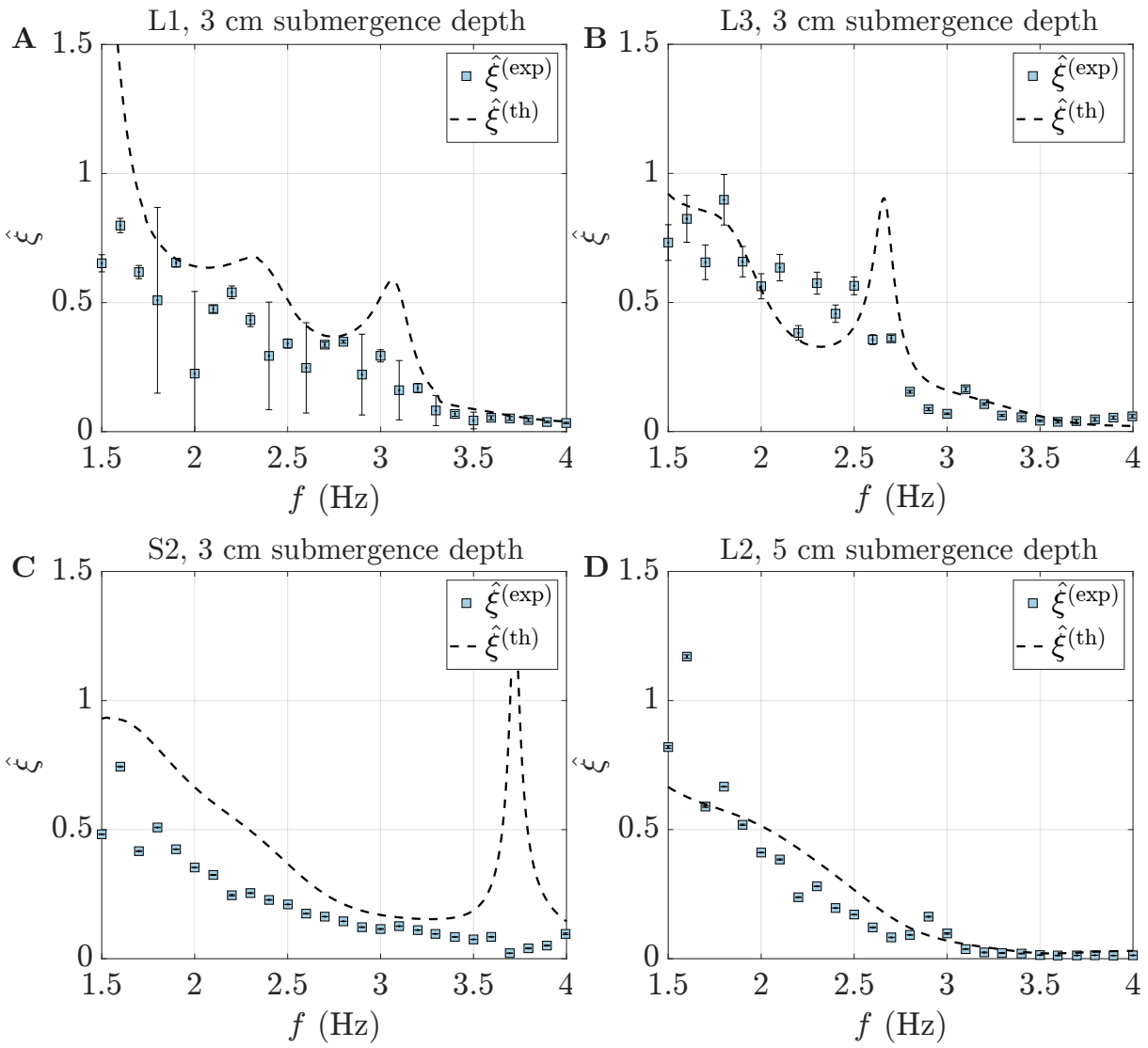

Figure 5.7: **A** Normalized plate motion amplitude, $\hat{\xi}$ as a function of wave frequency for L1 at a 3 cm submergence depth. Experimental values, $\hat{\xi}^{(\mathrm{exp})}$, are obtained with TWA=1 mm and are shown in light blue squares. Theoretical values, $\hat{\xi}^{(\mathrm{th})}$, are represented using a black dashed curve. **B-C-D** Same Figures but for other set of parameters, respectively: L3 at a 3 cm submergence depth, S2 at a 3 cm submergence depth and L3 at a 5 cm submergence depth.

Plate motion analysis

A parametric analysis can also be performed for normalized plate motion amplitude, $\hat{\xi}$. To that aim, the effect of submergence depth, length and stiffness on $\hat{\xi}$ is investigated. Figure 5.7 presents $\hat{\xi}$ as a function of wave frequency for L1 at a 3 cm depth, (**A**), L3 at a 3 cm depth, (**B**), S2 at a 3 cm depth, (**C**) and L3 at a 5 cm depth, (**D**). In all those Figures, $\hat{\xi}$ decreases with wave frequency and the theoretical model predicts relatively well

the experimental values. Similarly to the case of L2 at a 3 cm depth, resonance peaks are not observed experimentally. Finally, as in Chapter 3, varying plate rigidity does not exhibit a clear difference in $\hat{\xi}$ measurements.

5.1.3 Discussion on possible discrepancy sources

Linear theory is able to predict frequencies at which plates reflect wave energy and the plate motion amplitude trend with frequency. However, precise values of reflection and transmission in the reflection peaks do no match. Finally, the plate resonances predicted by linear theory are not observed experimentally. In the following the possible discrepancy sources are discussed. Some are due to linear theory intrinsic limitations and fundamental differences between experiments and the theoretical problem.

Fundamental differences between the experimental setup and the theoretical framework

Experiments and the theoretical model show good agreement concerning the wide peak location and the same trends when varying depth, plate length and plate rigidity. However, discrepancies appear looking at precise reflection and transmission coefficients values, when plates reflect wave energy. Experiments and theoretical model have some fundamental differences that could be responsible for discrepancy. First of all, the equations ruling linear theory are written for a 2D system. However, in the experiments, the plate has a finite extension in the y direction. The plate finite extension is a source of non-linearities, as it is discussed in Section 5.3, and could therefore lead to differences between experimental and theoretical results.

Plate mean position is another source of discrepancy. Indeed, 2D linear theory considers a perfectly horizontal plate. However, due to density difference between the plate material and water, plates tend to sink and are not at a constant depth over all their length.

Furthermore, in experiments, $K_r + K_t$ can be very different from one. Particularly at resonance frequency. It means that in the experiments, plate is able to remove energy from the waves. This effect is not taken into account in the linear theory and can be a source of error, particularly when trying to scale precise values of K_r and K_t.

Finally, in the experiments, the wave amplitude decreases along the tank. Wave dissipation is another factor not taken into account in the 2D linear theory developed here.

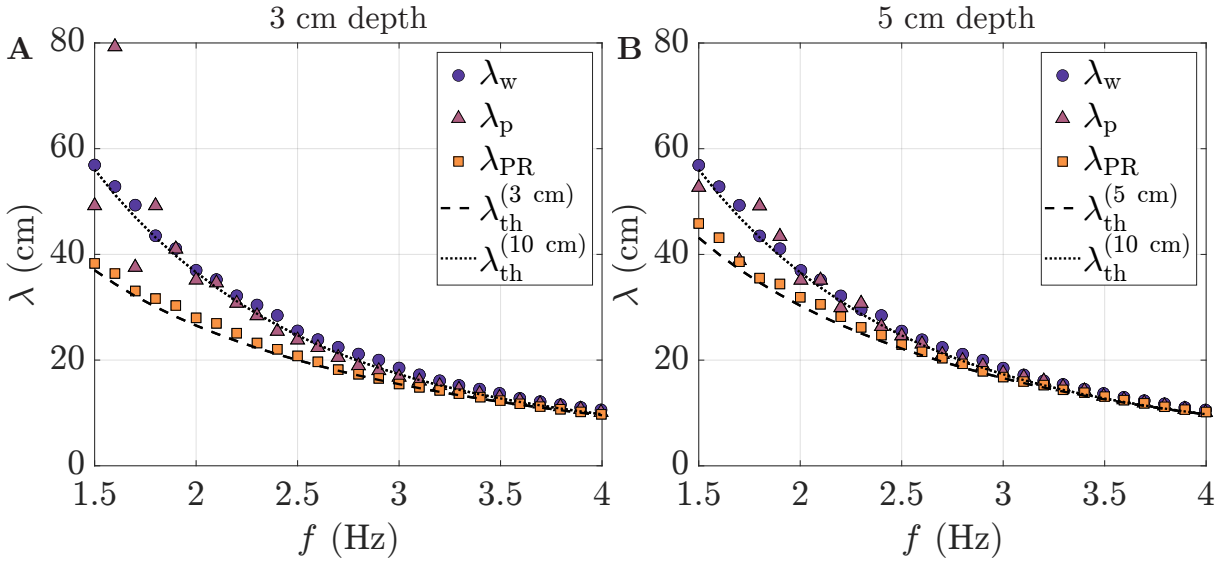

Figure 5.8: **A** Wavelength measured in different regions of the tank as a function of the frequency while conducting experiment with L2 or the rigid plate, L4, at a 3 cm depth. Dark blue circles show wavelengths in the up-wave region, λ_w, purple triangle wavelength over the elastic plate, λ_p, and orange squares wavelength over the rigid plate, λ_{PR}. **B** Same figure but for plates maintained at a 5 cm depth. For both depths, λ_w and λ_p follow $\lambda_{th}^{(10\text{ cm})}$ and λ_{PR} the theoretical value at their respective depth.

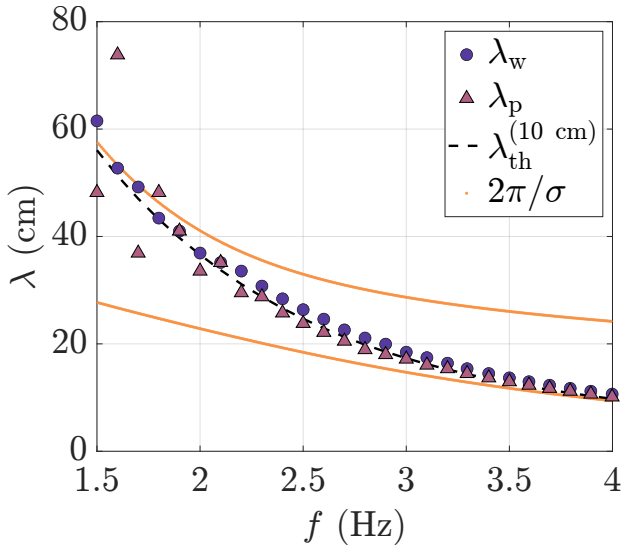

Figure 5.9: Wavelength measured in different tank regions as a function of the frequency while conducting experiment with L2 at a 3 cm depth. Dark blue circles show wavelengths in the up-wave region, λ_w. Purple triangle wavelength over the elastic plate, λ_p. Orange lines correspond to wavelengths associated with the two propagative modes in zone 2 and 3 in the linear theory, $2\pi/\sigma$.

Wavelengths over the plate do not match the values expected by linear theory

The dispersion relation above the plate, corresponding to regions 2 and 3 in the linear theory problem is supposed to be ruled by the plate characteristics, as explained in Section 3.2.1 of Chapter 3. However, it can be measured that waves propagating above the plate simply follow the dispersion relation for a 10 cm depth flat bottom. Those measurements are shown here.

First, dispersion relation measurements are performed over L2 and L4. The dispersion relation can be computed by estimating water wave frequency, f, and wavelength, λ, from surface elevation measurements. Dispersion relation measurements can be not only performed in the up-wave and down-wave region but also over the plate.

L2 is made of transparent Polycarbonate. The checkerboard placed at the bottom of the tank is visible from the top view camera and free surface deformation can be computed by measuring checkerboard deformation. However, as Polycarbonate refractive index, n_{pc}, differs from the water refractive index, n_{w}, the plate motion can also deform the checkerboard. The amplitude of checkerboard deformation due to the plate, δ, can be estimated in the limit of small deformation as:

$$\delta = \frac{n_{\mathrm{w}} i_{\mathrm{inc}}}{n_{\mathrm{pc}}} l, \tag{5.1.5}$$

with i_{inc} the plate angle with the horizontal. The side view measurements show that i_{inc} maximal values are of 10^{-1} rad. As thickness, l, is equal to 0.75 mm for L2, it comes that maximal checkerboard deformation due to plate motion, δ, scales as 0.05 mm. As δ is smaller than the smallest checkerboard deformation due to waves, that are approximately of 0.07 mm, it can be neglected when performing measurements over the transparent plate.

In the rigid plate case, the plate remains still in the wave field. A checkerboard is simply glued on the plate. In order to perform free surface reconstruction over the rigid plate, the deformation of the checkerboard glued on the plate is simply computed.

Figure 5.8 **A**, shows wavelength measurements, λ as a function of the measured frequency, f, while conducting experiments either with L2 at a 3 cm depth or the rigid plate, L4, placed at the same depth. Dark blue circles show wavelength measurements in the up-wave region while performing experiments with L2, λ_{w}. The measurements follow accurately the theoretical water wave dispersion relation for a bottom tank depth of 10 cm, $\lambda_{\mathrm{th}}^{10\ \mathrm{cm}}$, represented with a dotted line. More surprisingly, the measurements over L2 show similar results. Indeed, even if the plate is maintained at a 3 cm depth, water waves wavelength over the plate λ_{p} scales as $\lambda_{\mathrm{th}}^{(10\ \mathrm{cm})}$ for wave frequencies larger than 2 Hz. For smaller frequencies a certain discrepancy can be observed. It can be explained because the measurement window over the plate starts being small compared to water waves wavelength. Contrary to the elastic plate, the rigid

plate acts like a decrease in water depth as measured wavelength over the rigid plate, λ_{PR}, follows accurately the theoretical water wave dispersion relation for a bottom tank at a 3 cm depth, $\lambda_{th}^{(3\text{ cm})}$, represented with a dashed line.
Figure 5.8 **B** shows the same quantities as in Figure 5.8 **A** but for plates at a 5 cm depth. Similar observations can be made as λ_w and λ_p scale accurately with the theoretical dispersion relation for a 10 cm bottom, $\lambda_{th}^{(10\text{ cm})}$. Also, λ_{PR} scales as $\lambda_{th}^{(5\text{ cm})}$.
To sum up, elastic plates do not appear to change waves relation dispersion contrary to a rigid plate that acts like a bottom elevation.
The latter result is interesting by itself but it also gives keys to understand the discrepancies causes between experiments and linear theory. Figure 5.9 shows a comparison of experimental wavelengths before the plate (blue circles) over the L2 plate (purple triangles) and wavelengths predicted by linear theory for a similar plate (orange curve). Experimental wavelengths measured over the plate match with the theoretical value over a total depth of 10 cm. On the contrary, wavelengths associated with the two propagative modes in zones 2 and 3 in linear theory do not match with experimental data. This discrepancy between theoretical and experimental wavelengths over the plate is a first possibility to explain differences between theoretical and experimental values of K_r, K_t and $\hat{\xi}$. This experimental result is even more intriguing since writing equations of linear theory and force wave-numbers in zone 2 and 3 to be equal to $k_{th}^{(10\text{ cm})}$ does not seem to be an easy task.

Non-linearities are a major source of discrepancy

By definition, linear wave theory is linear. Consequently, non-linearities that exist in an experimental system are not taken into account. As mentioned in Chapter 2, non-linearities can arise from an elastic plate forced in a fluid (see Section 2.1.3 for instance) or simply by a rigid plate in a wave field. A first source of non-linearities come from waves. As wave amplitude increases, non-linear terms, proportional to wave steepness or the square steepness become more significant leading to Stokes' drift and eventually wave breaking (see Section 2.1.3 or [Mei et al., 2005] Part 2). However, as this Section focused only on the smaller wave amplitudes, wave non-linearities are not expected to be a major source of dissipation.
Drag created by the plate relative motion to the flow is a dissipation source and a symptom of non-linearities. Relative motion between waves and the plate leads to a force proportional to U_{ref}^2. Because of that, drag force cannot be included in the equation ruling plate motion in the linear theory. In practice, drag on the plate would appear through vortex creation at its edges for instance.
Indeed, vortices are expected to be produced because of the discontinuity at plate edge. For instance, Poupardin et al. [2012] observed mean flow creation associated to vortex formation

at a rigid plate tip. As mentioned in Chapter 3, vortex creation by a flexible plate is a problem that has been largely covered experimentally, theoretically and numerically, even using potential theory in the theoretical case (see [Michelin et al., 2008] for instance). However, in those works mean flow makes it possible to simplify the problem. Solutions have been proposed to incorporate vortex formation created at an object edge in the potential wave theory without the help of a mean flow, [Chang et al., 2015]. However, it has not been implemented in this thesis.
Furthermore, the drag force tends to decrease plate and wave amplitudes and dissipate wave energy. Consequently, the presence of drag will mitigate plate resonances by limiting its amplitude. For instance, it is not surprising that sharp reflections peaks cannot be observed experimentally as they correspond to critically high values of plate motion amplitude.

5.2 Wave plate interaction in the amplitude-frequency space

Section 5.1 showed that plate behavior in a wave field is relatively well predicted by linear theory for small amplitude waves. If experimental work is more limited than theoretical work in the parametric analysis, it makes it possible to probe the effect of wave amplitude variation on the wave-plate interaction and to go further in the observation of non-linear phenomena. To that aim, Target Wave Amplitudes, TWA, ranging from 1 mm to 6 mm were studied for frequencies ranging from 1.5 Hz to 4 Hz (see Section 4.1.2). Similarly to Section 5.1, K_r and K_t measurements are presented first before looking at plate motion amplitude. From those observations, wave energy dissipation will be measured. Finally, to investigate dissipation causes, PIV experiments are performed.

5.2.1 K_r and K_t measurements for different plate lengths and submergence depths and amplitude

As in Section 5.1, waves are imposed for one minute and fifteen seconds and recording of free-surface deformation and plate motion is done during the last fifteen seconds. Each wavemaker amplitude and frequency is repeated three times.
Figure 5.10 shows amplitude-frequency diagram obtained with this procedure for K_r and K_t for L2 at a 3 cm depth. Wave amplitude, A, corresponds to incident wave amplitude at the

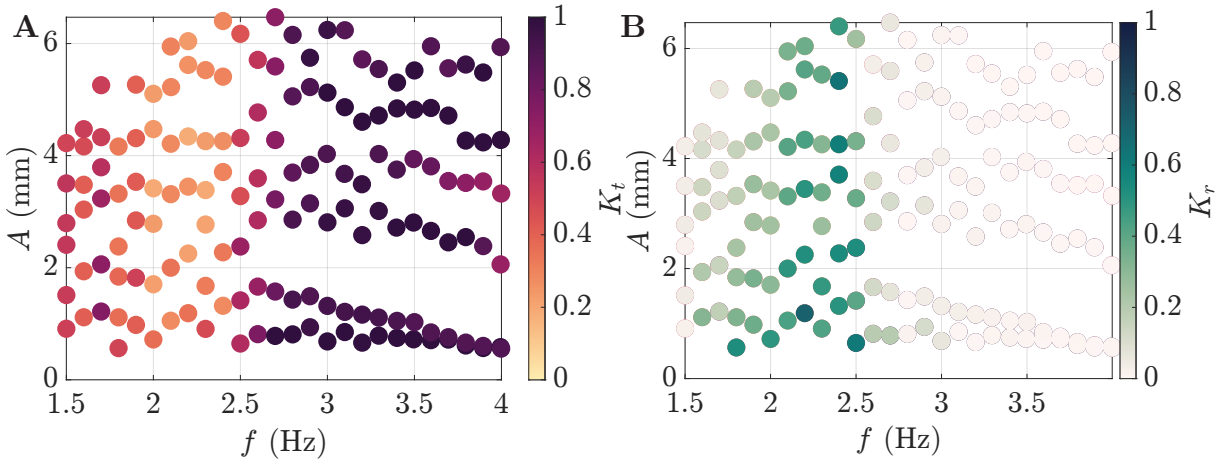

Figure 5.10: **A** Amplitude-frequency diagram showing transmission coefficient K_t for L2 at a 3 cm submergence depth. **B** Amplitude-frequency diagram showing reflection coefficient K_r for L2 at a 3 cm submergence depth. Across all incident wave amplitude, A, a wide reflection peak can be observed between 2 and 2.5 Hz.

middle of the plate. Each point corresponds to the average over three experiments and its color stands for the wanted quantity value, K_t in Figure 5.10 **A** or K_r in Figure 5.10 **B** **B** for instance. To avoid overloading of the diagram, the experimental deviations on A, f, K_r or K_t are not represented. The standard deviation for the different measurement is represented in Annexes.

Observation of the amplitude-frequency diagram for K_r and K_t for L2 at a 3 cm depth shows that the wave amplitude has little impact on the wave transmission and reflection coefficients. Indeed, the diagrams are relatively invariant along the y-axis and the transmission and reflection patterns are similar to what was observed for small amplitude waves. At low frequencies, L2 mostly transmits waves. A wide reflection peak is observed between 2 Hz and 2.5 Hz. For larger frequencies, waves are fully transmitted by the plate.

5.2.2 Impact of wave amplitude on plate motion

Contrary to reflection and transmission coefficients, the plate motion is modified as the wave amplitude, A, increases. Figure 5.11 **A** shows the plate displacement with respect to the horizontal, w, over one wave period for the Target Wave Amplitude TWA=6 mm in black. Similarly to the case of small amplitude waves, it shows one node and one and a half anti-node. Red curve corresponds to plate reference position, *i.e.* the plate position before sending waves and the blue curve corresponds to the mean plate position while sending waves. The blue and red curves are clearly distinct underlining a plate displacement from its reference position due to wave forcing. This displacement is quantified using the quantity Δ_i. As

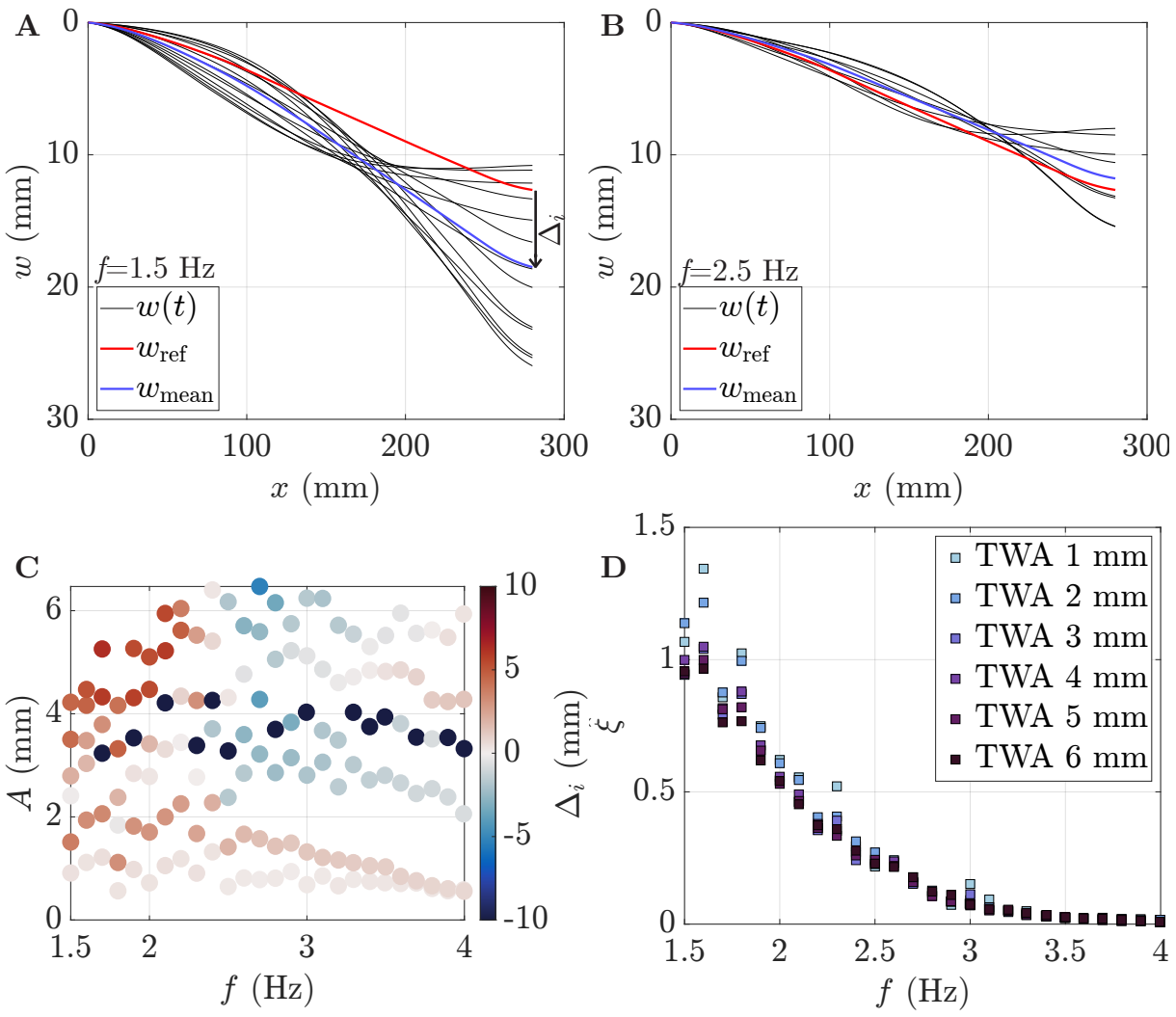

Figure 5.11: **A** In black, plate displacement with respect to the horizontal, w, during one wave period when sending 1.5 Hz waves at TWA=6 mm over L2. In red, plate reference position, w_{ref}, *i.e.* plate position when no waves are sent. In blue, w_{mean}, plate mean position when plate undergoes wave forcing. Δ_i definition as the difference plate tip reference position and plate tip mean position is also illustrated. **B** Same Figure but for 1.5 Hz waves at TWA=6 mm over L2. **C** Amplitude frequency diagram showing Δ_i for L2. **D** Normalized plate motion amplitude, $\hat{\xi}$ as a function of wave frequency for TWA ranging from 1 mm to 6 mm. In **C** and **D** each point corresponds to the mean over 3 experiments.

illustrated in Figure 5.11 **A**, Δ_i corresponds to the difference between the plate tip reference and positions.

Figure 5.11 **B** shows the same quantities with TWA=6 mm but for 2.5 Hz. A displacement from mean position can also be observed. However, contrary to $f = 1.5$ Hz, the plate tip moves toward the free-surface. This situation corresponds to a negative value of Δ_i.

Figure 5.11 **C** shows the amplitude-frequency diagram for Δ_i. Different regions of the plan

jump out from this graph. At low amplitudes, Δ_i is small, but as wave amplitude, A, increases Δ_i differs from 0. Two frequency domains can be distinguished. For frequencies lower than 2.5 Hz. Δ_i is higher than 0 meaning that the plate tip moves toward the tank bottom and for higher frequencies, Δ_i is less than zero, plate tip goes upward, to the free-surface. At sufficiently high amplitudes, waves exert a force on plate tip changing plate mean position. PIV experiments in Section 5.3 will show that the plate mean displacement can be correlated with the orientation of a jet created at plate tip and that could be the cause of the force.
Finally, the effect of wave amplitude, A, on normalized wave amplitude, $\hat{\xi}$ is observed in Figure 5.11 **D**. It shows $\hat{\xi}$ as a function of the wave frequencies for six different values of TWA. As the curves collapse, it appears that the plate motion amplitude is simply linear in wave amplitude despite the change in plate mean position.

5.2.3 K_r and K_t measurements for other plates

Wave amplitude effect on plate of different stiffness

The impact of wave amplitude on plates of different rigidity can be observed utilizing, L1, L3 and L4. Phase amplitude diagrams for L3 and L4 are plotted in Figure 5.12 (**A**-**B**) and (**C**-**D**), respectively. For those two plates K_r and K_t are independent of wave amplitude since, similarly to L2, their amplitude-frequency diagrams are relatively invariant along the y-axis. For L3, a wide reflection peak is located between 1.5 and 2.5 Hz across all the wave amplitudes. For L4, the rigid plate, no reflection is observed in all the diagram. It confirms the fact that the wave reflection are induced by flexibility in this system.
K_r and K_t invariance with A is in practice observed for all the other plates except for the most flexible, L1.
Figure 5.13 **A** shows the amplitude-frequency diagram for L1 at a 3 cm submergence depth. Contrary to stiffer plates, varying the wave amplitude for L1 induces a rich behavior. At low amplitudes (*i.e.* <2.5 mm), the behavior is similar to the one presented in Section 5.1 (regions (I), (II) and (III)). At frequencies smaller than 2 Hz, the plate mostly transmits waves. For frequencies between 2 and 3 Hz, the reflection increases and reaches a maximum around 2.7-2.8 Hz. For frequencies larger than 3 Hz, the plate transmits all the wave energy. However, at higher amplitudes (*i.e.* >2.5 mm) the system behavior changes drastically. For frequencies larger than ∼2 Hz (region (V)), transmission and reflection both go to zero. In this regime, the plate acts like a perfect wave terminator, it is able to remove all the energy from the waves.
As it is presented in Figure 5.14, this behavior is due to a displacement of the plate mean position. Figure 5.14 **A** shows the amplitude-frequency diagram for values of Diff for L1.

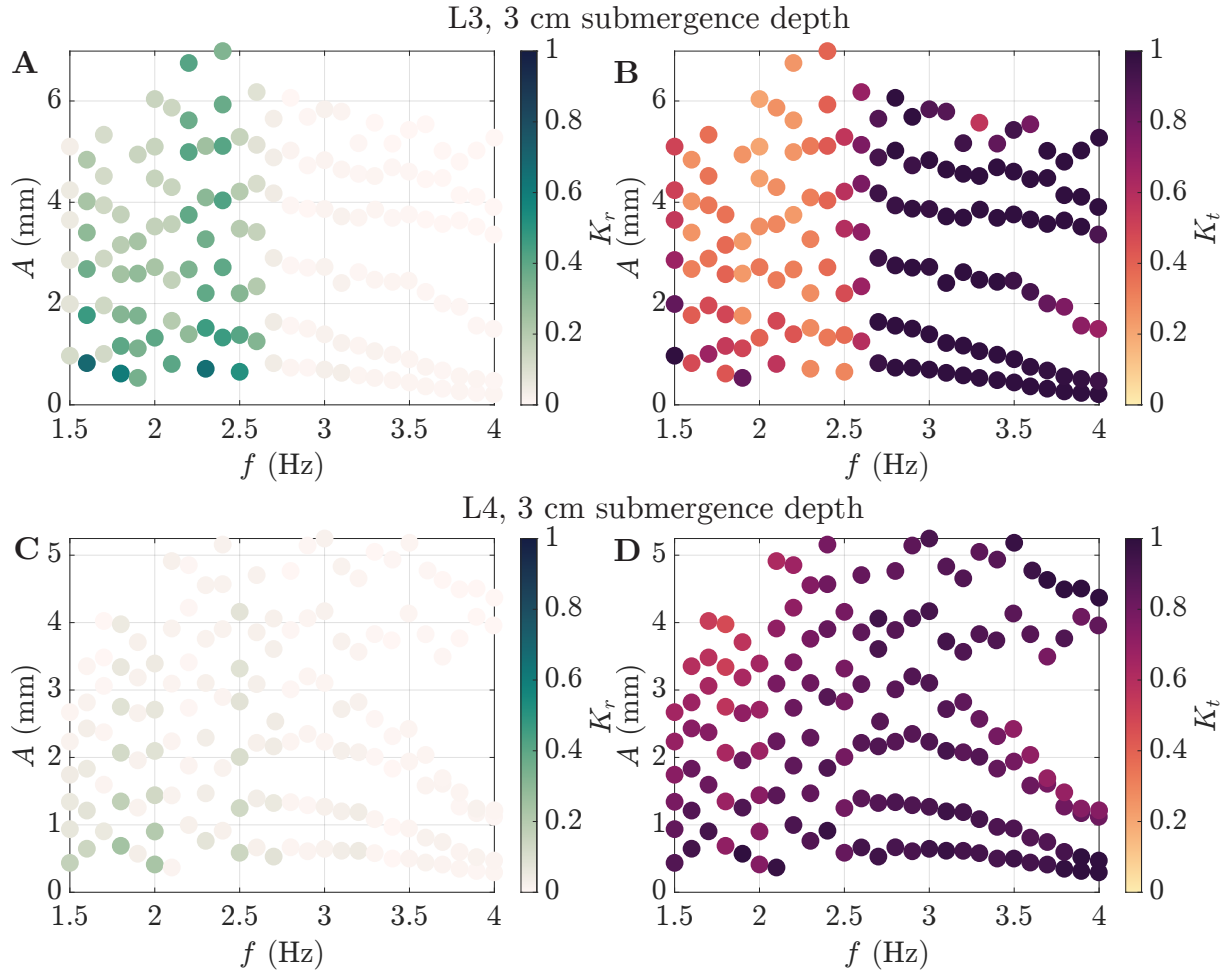

Figure 5.12: **A** Amplitude-frequency diagram presenting K_r for L3 at a 3 cm submergence depth. **B** Amplitude-frequency diagram presenting K_t for L4 at a 3 cm submergence depth. **C** Amplitude-frequency diagram presenting K_r for L3 at a 3 cm submergence depth. **D** Amplitude-frequency diagram presenting K_t for L4 at a 3 cm submergence depth.

Region (V) appears clearly in this diagram. Points in the amplitude-frequency diagrams of K_r and K_t where $K_r = 0$ and $K_t = 0$ are all located in region (V). Hence, the are associated with Δ_i being equal to -3 cm, meaning that plate tip reaches the free-surface. Figure 5.14 **A**. This phenomenon is illustrated in Figure 5.14 **B**, showing a snapshot from tank side when sending 3 Hz and 5 mm waves. The plate tip clearly reaches the free-surface. L1 tip reaching the free surface is due to the wave forcing. In this configuration, the plate is extremely efficient to break waves.

To sum it up, K_r and K_t for L1 shows, one, a dependence in frequency as the plate reflects wave of frequencies between 2 and 3 Hz and, two, a dependence in amplitude, in region (V) of the amplitude-frequency diagram, the plate breaks all incoming waves.

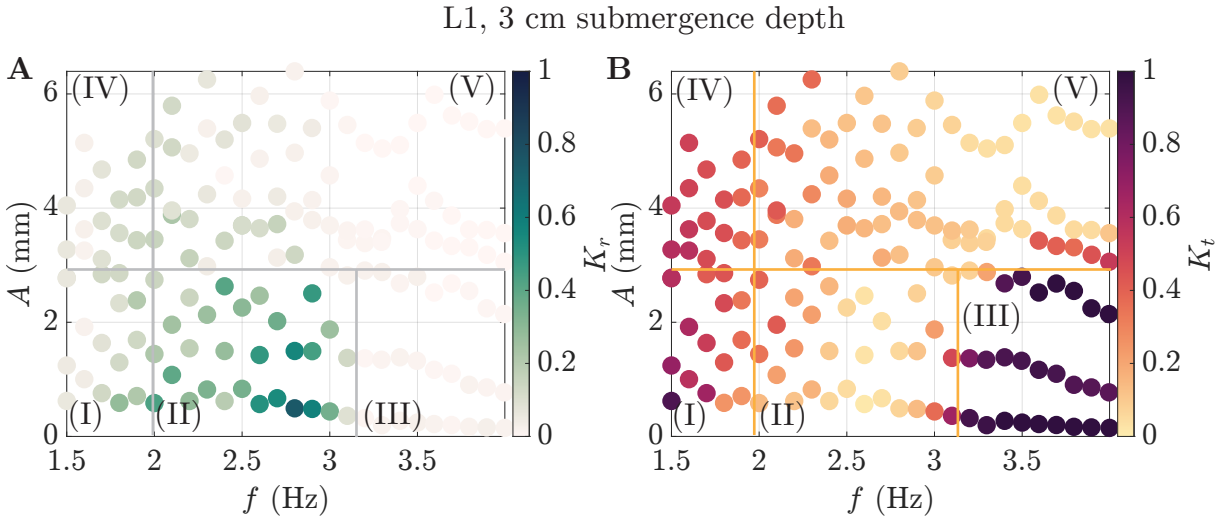

Figure 5.13: Amplitude-frequency diagram showing the reflection coefficient, K_r, in Figure (**A**) and the transmission coefficient, K_t, on Figure (**B**) for L1 at a 3 cm submergence depth. Points here correspond to the averaged value over three experiments. It exhibits a rich behavior and five different zones can be delimited on that diagram.
- (I) $A \in [0.5, 2.5]$ mm and $f \in [1.5, 2]$ Hz, K_r is less than 0.2 and K_t is more than 0.4 so waves are mostly transmitted.
- (II) $A \in [0.5, 2.5]$ mm and $f \in [2, 3]$ Hz, K_r is higher than K_t, so waves are mostly reflected.
- (III) $A \in [0.5, 2.5]$ mm and $f \in [3, 4]$ Hz, K_r drops to 0 and K_t reaches one. It corresponds to total transmission.
-(IV) $A \in [2.5, 6]$ mm and $f \in [1.5, 2]$ Hz, K_r is less than 0.2 and K_t is more than 0.4 so waves are mostly transmitted.
- (V) $A \in [2.5, 6]$ mm and $f \in [2, 4]$ Hz, K_r drops to 0 as well as K_t. The plate acts like a perfect wave breaker as wave energy is completely dissipated.

5.2.4 Wave energy dissipation by submerged elastic plates

Measuring K_r and K_t does not only provide information on reflection and transmission, but also on energy preservation. As $K_r + K_t$ is supposed to be equal to one if the energy in the waves is preserved in the wave-plate interaction. Looking at the sum tells if wave energy is dissipated ($K_r + K_t < 1$) or increased ($K_r + K_t > 1$) because of the interaction with the object. The latter case would only concern active objects that are able to produce waves, and are beyond the scope of this work. Consequently, the purpose of this Section is to characterize wave energy dissipation due to the presence of the plate.
To do so, the loss coefficient, K_l is defined as:

$$K_l = 1 - (K_r + K_t), \tag{5.2.1}$$

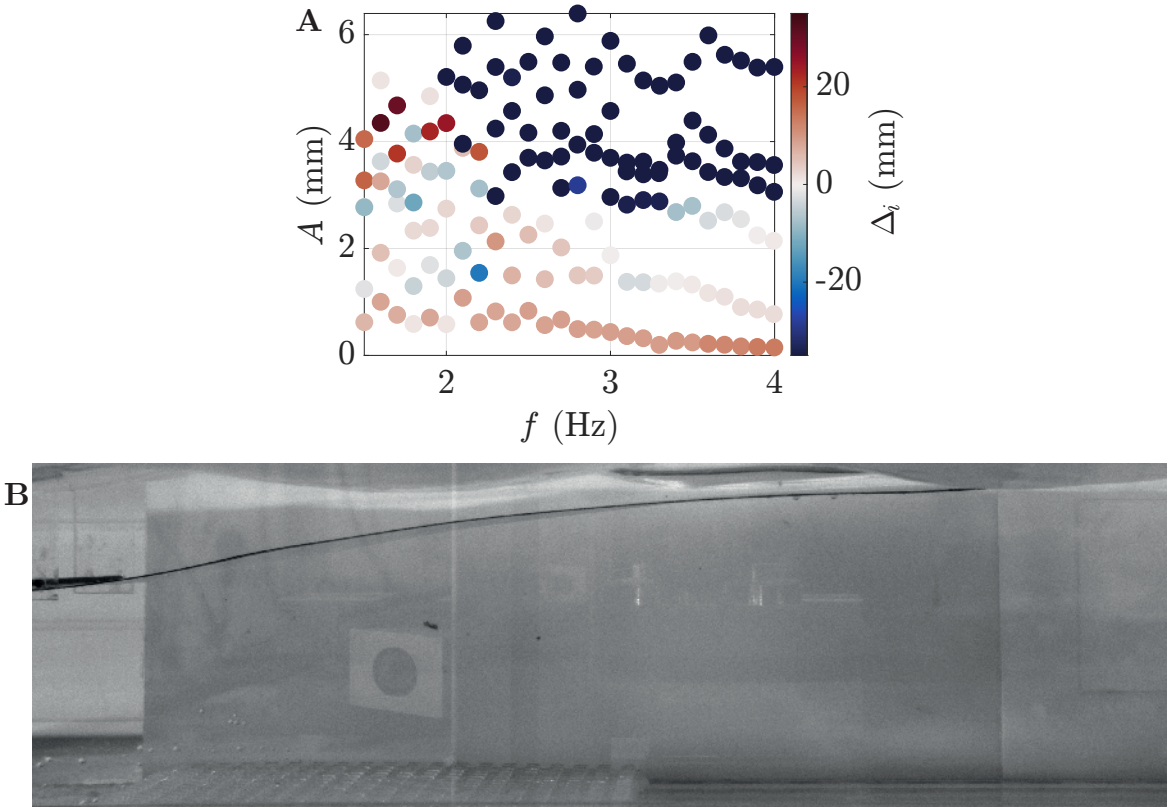

Figure 5.14: **A** Amplitude-frequency diagram showing Δ_i for L1 at a 3 cm depth. **B** Picture taken from tank side view while conducting experiments with L1 at a 3 cm depth sending 3 Hz waves of 5 mm amplitude. Waves come from the left. Plate edge is colored in black.

and quantifies the incoming wave energy fraction that is removed from the waves by the plate, having in mind that the incoming wave energy is calculated as in Equation (2.1.50) of Chapter 2.

Figure 5.15 presents the amplitude-phase diagrams for loss coefficients, K_l, for 28 cm plates at a 3 cm depth. It appears that the plate removes more energy from the waves at high amplitudes. Also, even if the rigid plate dissipates some wave energy, this dissipation is less significant than for elastic plates. Furthermore, among the flexible plates tested (L1, L2 and L3), the stiffer ones seems to dissipate less energy. It suggests that flexibility plays a key role in removing energy from the waves. It appears that dissipation is higher for frequencies where plates reflect waves (below 2.5 Hz for L2 and L3 and between 2 and 3 Hz for L1). At its maximum up to 60% of wave energy can be removed from the wave. Also, the fact that L1 is a perfect wave terminator at high amplitudes and frequencies can also be seen in Figure 5.15 **D**. Indeed, in this domain K_l reaches 1.

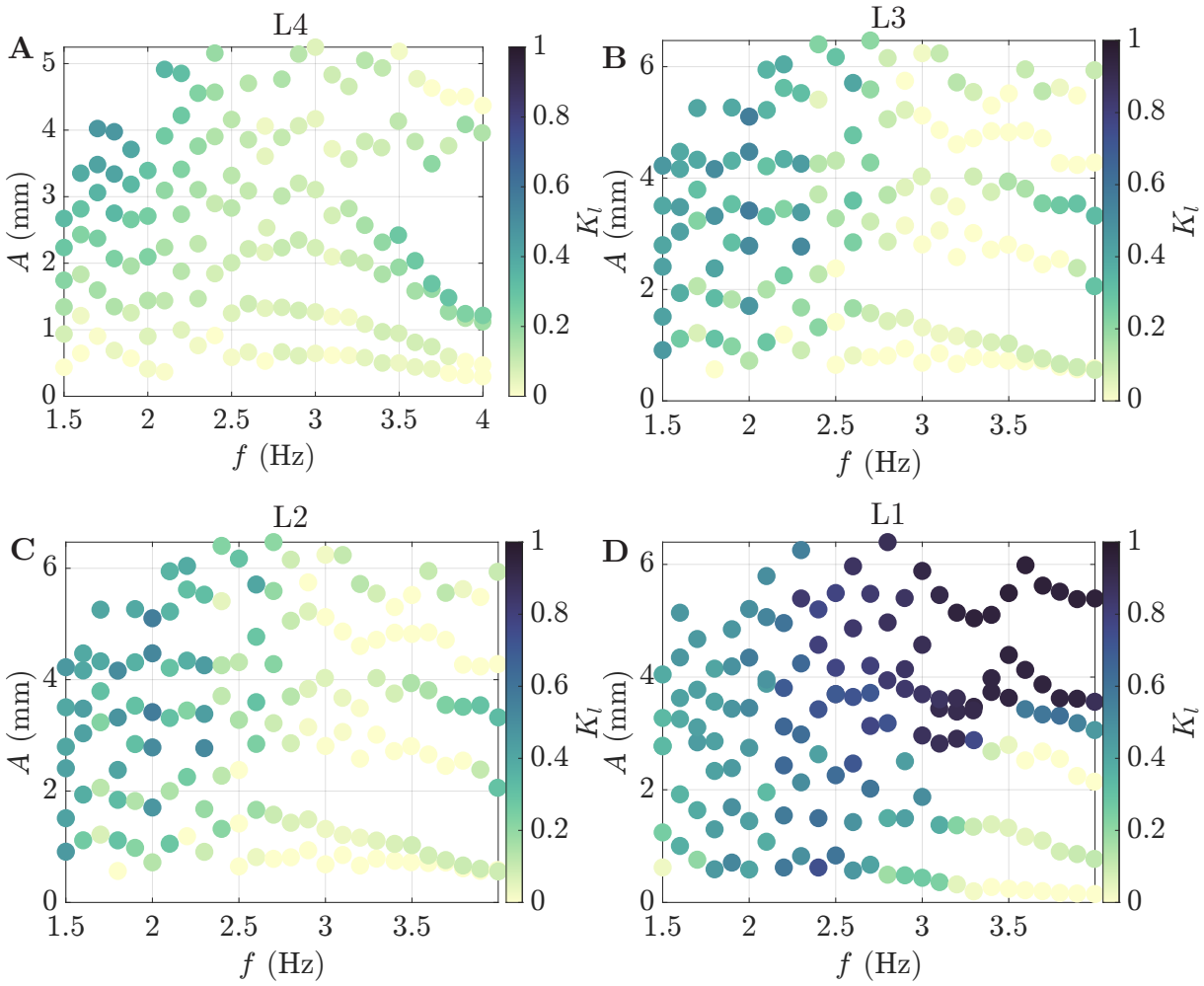

Figure 5.15: Amplitude-frequency diagram showing loss in wave energy, K_l, due to the interaction with plates of 28 cm length at a 3 cm depth and of different stiffness. **A** show the results for the rigid plate, L4, **B** for L3 **C** L2 and **D** L1. It can be observed that dissipation increases with amplitude and flexibility.

Examining potential sources of dissipation

Two mechanisms are plausible candidates to explain the ability of the plate to remove energy from waves, internal damping and drag dissipation. As mentioned in Section 2.2 of Chapter 2, internal damping can be caused by viscous effects within the material, which lead to energy dissipation. A value of this damping can be estimated when performing free oscillations tests. As pictured in Section 4.4.1 of Chapter 4, when performing a free oscillation test on a plate, oscillations amplitude decreases exponentially with a characteristic rate of dissipation, Γ, that can be fitted. For all plates, oscillations persist for around ten seconds, leading to values of Γ close to 0.2 s^{-1}. Considering that the decrease in amplitude is only due to internal damping, Γ can be used to estimate internal damping in wave-plate experiments. Note that such a

method necessarily overestimates internal damping. Indeed, during the free oscillations test other sources of dissipation due to fluid-structure interaction can account for the amplitude decrease.

Assuming a linear damping force, energy dissipated by internal damping over one wave period, $\mathcal{E}_{\text{in}}$, can then be estimated using the fact that it should scale as:

$$\mathcal{E}_{\text{in}} \sim 2\rho_p lb\Gamma f L\xi^2, \tag{5.2.2}$$

with ρ_p the plate density, l its thickness, b its width, L its length, f the wave frequency and ξ the plate motion amplitude (see [Nové-Josserand, 2018] Chapter 3, Section 2 or [Polly et al., 2021] for instance). To account for dissipation in the waves, this energy has to scale with incoming wave energy, $\mathcal{E}_{\text{w}}$:

$$\mathcal{E}_{\text{w}} \sim \frac{1}{2f}\rho_w gbA^2 c_g, \tag{5.2.3}$$

with ρ_w being the density of water, g the gravity, A its amplitude and c_g wave group velocity. Considering $\xi \sim A$ and $\rho_p \sim \rho_w$, it comes that:

$$\frac{\mathcal{E}_{\text{in}}}{\mathcal{E}_{\text{w}}} \sim 4\frac{l\Gamma L}{gc_g}f^2 \sim 10^{-3}. \tag{5.2.4}$$

Since, dissipation measured in practice can represent up to 50% of incoming wave energy, it shows that internal damping should not be responsible for the dissipation observed in the plate-wave interaction. Indeed, $\frac{\mathcal{E}_{\text{in}}}{\mathcal{E}_{\text{w}}}$ appears much smaller than 0.5 even with an estimate of internal damping that tends to overestimate $\mathcal{E}_{\text{in}}$.

Consequently, the second source of dissipation, namely, drag dissipation, must be considered to account for dissipation.

5.3 Non-linear effects: jet production by a submerged elastic plate in a wave field

The first part of this Chapter focused on results that could be obtained relatively simply, filming the experiment. However, probing all potential dissipation sources cannot be achieved in that manner. PIV experiments are performed following the procedure described in Chapter 4, while plates are forced by waves. This Section focuses on the main observations made while conducting PIV experiments, concentrating on only one plate, S2 at a 3 cm depth. Its behavior is representative of what was observed with other plates. Furthermore, its small size and the fact that it is transparent made experiments easier and gave clearer results. As

indicated in Chapter 4, the plates are filmed from the side of the tank. The camera frame rate is taken equal to $40f$, f being wave frequency and 20 wave periods are recorded.
Those experiments were performed with Diane Komaroff, who did an internship on the jet production by the plate.

5.3.1 Particle trajectories from tank side view for S2

Figure 5.16 **A B** show particle trajectories over one wave period while sending respectively, 1.5 and 3 Hz waves, for Target Wave Amplitude, TWA, of 1 mm. Particles trajectories are obtained as described in Chapter 4, Section 4.5, by taking the maximum at each pixel over one wave period. The plate clamping is located on the left of the images, at a 3 cm depth. The plate tip is located roughly at the center of the image. The second half of the image on the right enables us to observe the effect of the plate on the wave field. In the case of those two images, the plate has almost no effect on particles motions. Indeed, particle trajectories remain circular as predicted by the linear wave theory. Figure 5.16 **A** shows elliptical inclined trajectories typical of stationary waves. It illustrates beach imperfection at low frequency.
Figure 5.16 **C D** show particles trajectories at 1.5 Hz and 6 Hz but for TWA=6 mm, leading to higher wave amplitudes. More complex trajectories are observed. At 1.5 Hz (Figure **C**) circular trajectories can be observed over the plate and close to the tank bottom but elsewhere particles follow different trajectories. Below the plate vertical helicoidal motion can be observed, whereas at the plate tip particles also follow helicoidal motion but horizontal. Helicoidal motion at the plate tip is characteristic of the presence of a jet. Indeed, helicoidal trajectories result from the addition of the effects of waves and a mean velocity field that originates from the plate tip. This mean velocity field created at the plate tip will be referred to as the jet. A jet can also be observed in Figure 5.16 **D** for 3 Hz waves. However, contrary to the 1.5 Hz waves case, the jet is directed downward.
Mean flow creation is no surprise in the case of an horizontal plate in a wave field. First, because a forced elastic plate is expected to generate a mean current, see [D'Adamo et al., 2022], Figure 1 for instance. Second, because even in the case of a non moving rigid plate in a wave field, a mean current appears. Poupardin et al. [2012] observed, using PIV, the apparition of a mean flow, attributed to vortex creation at plate tip. In addition, Carter et al. [2006] have predicted numerically that a current could appear below a rigid plate or Carmigniani et al. [2017] even consider horizontal rigid plates as potential pumping devices. However, in the elastic plate case and to the author's knowledge no jet going upward has been reported. The interaction between the moving plate tip and the waves is probably causing that difference.

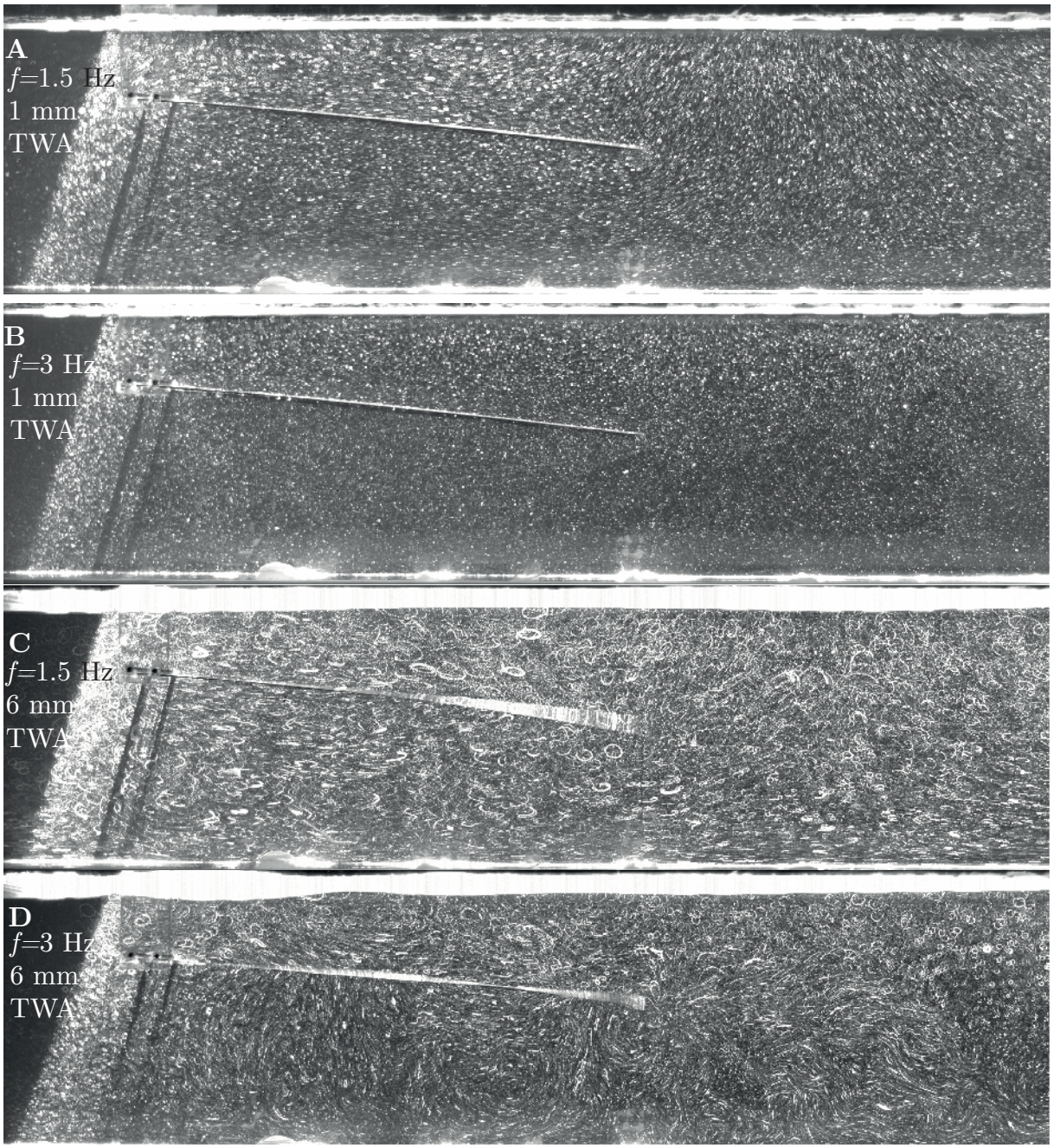

Figure 5.16: Particle trajectories while conducting PIV experiments. Trajectories are obtained by taking the maximum of intensity at a given point over one wave period. **A** Particles trajectories for 1.5 Hz waves and TWA=1 mm. **B** Particles trajectories for 3 Hz waves and TWA=1 mm. **C** Particles trajectories for 1.5 Hz waves and TWA=6 mm. **D** Particles trajectories for 3 Hz waves and TWA=6 mm

5.3.2 Velocity field

In order to confirm the presence of a jet at high wave-maker amplitudes, velocity fields are computed following the procedure described in Section 4.5. Figure 5.17 shows the mean ve-

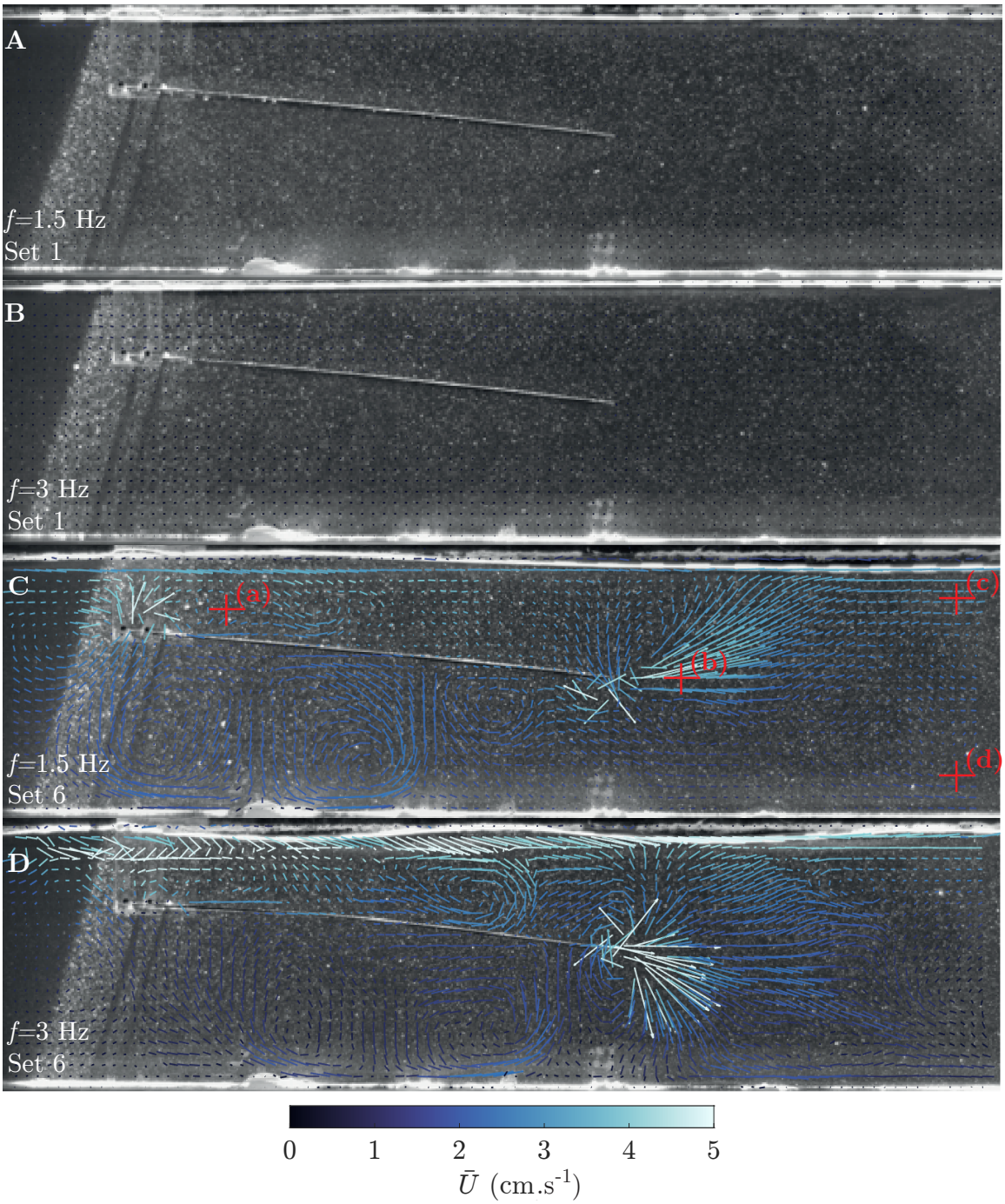

Figure 5.17: Mean velocity field obtained for the same experiments as in Figure 5.16. Arrows indicate mean fluid direction based on mean velocity along x and z axis. Arrow size depends on mean velocity along x and z values and their scales is chosen to ease visualization. Arrow colors corresponds to mean fluid velocity norm, $\bar{U}$. **A** $\bar{U}$ for 1.5 Hz waves and TWA=1 mm. **B** $\bar{U}$ for 3 Hz waves and TWA=1 mm. **C** $\bar{U}$ for 1.5 Hz waves and TWA=6 mm. **D** $\bar{U}$ for 3 Hz waves and TWA=6 mm.

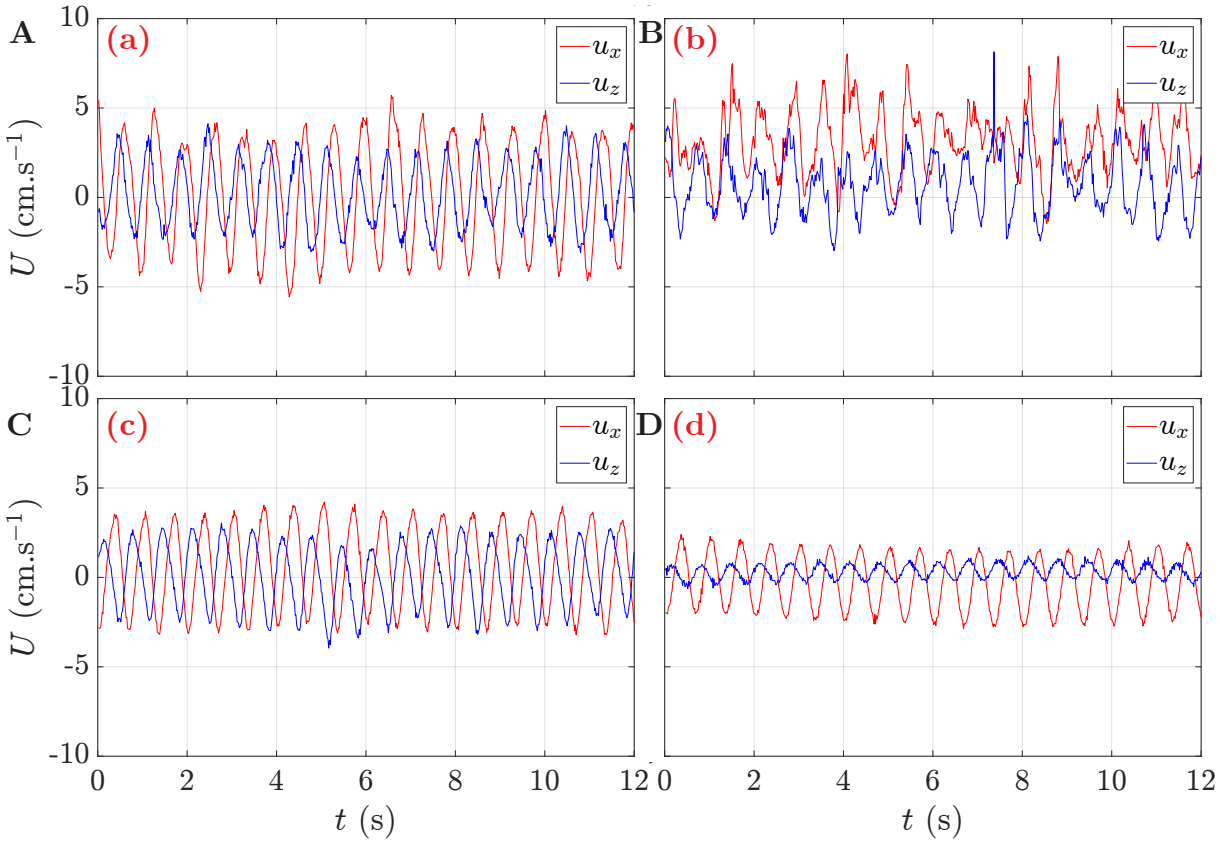

Figure 5.18: Instantaneous velocity measurements as a function of time for S2 at a 3 cm submergence depth for 1.5 Hz waves and TWA=6 mm at the four locations defined in Figure 5.17 **C**. **A** Instantaneous velocity at location (a). **B** Instantenous velocity at location (b). **C** Instantenous velocity at location (c). **D** Instantenous velocity at location (d).

locity fields for the same experiments as in Figure 5.16. Arrows indicate direction of the flow based on the ratio between mean velocity in the x direction, $\bar{U}_x$ and mean velocity in the z direction, $\bar{U}_z$. Arrow scale is chosen to ease visualization. The same arrow scale is used in the four Figures. Arrow color corresponds to the norm of mean flow speed, $\bar{U}$, as indicated in the colorbar at the bottom of the Figure. Figure 5.17 **A** and **B** correspond to TWA=1 mm at respectively 1.5 Hz and 3 Hz. Arrows in those two Figures are too small to be seen and black due to low value of $\bar{U}$. It confirms observations made in Figure 5.16. For the first set of wave-maker amplitudes particles follow circular trajectories with zero mean velocity.

Similarly, Figures 5.17 **C** and **D**, which correspond to TWA=6 mm, at respectively, 1.5 Hz and 3 Hz, confirms observations from particles trajectories visualization and show complex mean velocity patterns. At 1.5 Hz, a significant jet directed upward can be observed near point (b) in Figures 5.17 **C**. Far from the plate tip, the mean velocity is lower. Below the plate rolls can be observed, meaning that average speed form circles. At 3 Hz, (Figure **D**) a

similar behavior is observed. A jet exists at plate tip. It is mainly directed downward and is wider than the jet observed at 1.5 Hz. A roll can be observed above the plate and as for 1.5 Hz waves, two rolls exist under the plate.
In the rigid plate case, the mean velocity flows observed were associated with rolls, which does not seem to be the case for the jet created by an elastic plate.
In order, to get a better view on velocity fields at all times, Figure 5.18 presents instantaneous speed as a function of time at four different locations shown in Figure 5.17 **C** for 1.5 Hz waves and Target Wave Amplitude, TWA, of 6 mm. In all the figures, instantaneous velocity along x, u_x is represented in red and instantaneous velocity along z, u_z, is represented in blue. At location (a), mean velocity is close to zero and u_x and u_z oscillate between -5 and 5 cm.s^{-1}. At location (b), in the jet, the mean velocity differs clearly from zero, being close to 2 cm.s^{-1} for u_x. The signal appears also more noisy but oscillations due to the waves can still be observed. At (c) a behavior similar to location (a) is observed. Finally, at location (d), close to the bottom, both velocities have decreased and u_z is almost equal to 0 cm.s^{-1}, which is the expected mean velocity field for low amplitude waves.

5.3.3 Maximum velocity in the jet

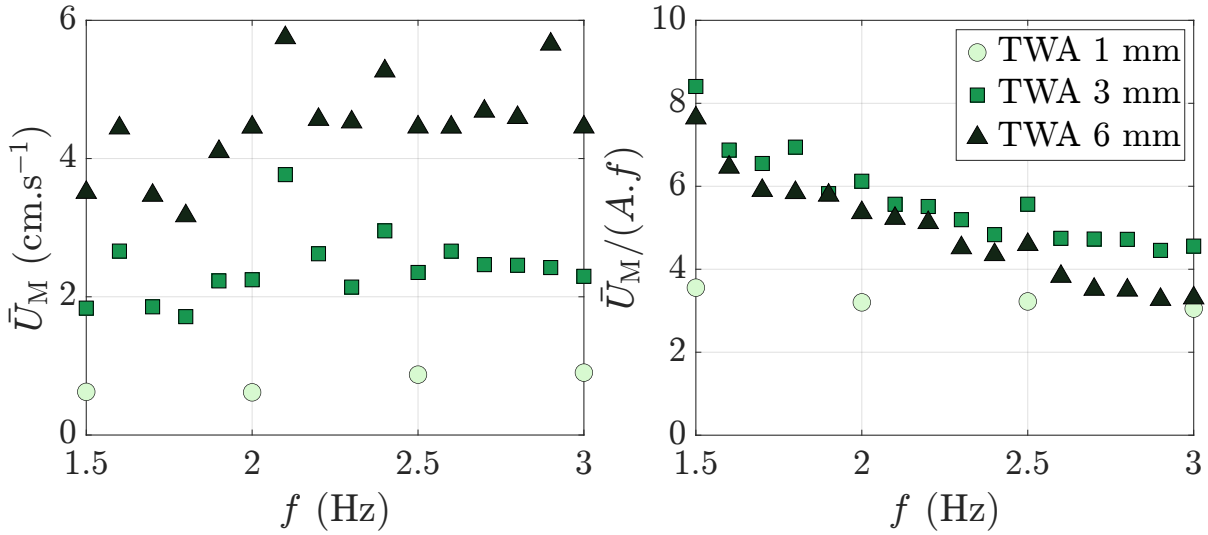

Figure 5.19: **A** $\bar{U}_M$ as a function of wave frequency, f, for three Target Wave Amplitudes. Light green circles corresponds to TWA=1 mm, green squares to TWA=3 mm and black triangles corresponds to TWA=6 mm. **B** $\bar{U}_M$ normalized by wave amplitude and frequency as a function of wave frequency, f, for three target wave amplitudes. Light green circles correspond to TWA=1 mm, green squares to TWA=3 mm and black triangles correspond to TWA=6 mm.

Observations of particular wave frequencies and amplitudes highlight the existence of a jet

at the plate tip. To obtain information on the jet at different frequencies and amplitudes, the 95% percentile of mean velocity field, $\bar{U}_{\mathrm{M}}$, is presented in Figure 5.19. In practice, 95% percentile of mean velocity field is preferred to $\bar{U}$ absolute maximum in order to eliminate incoherent values. Figure 5.19 **A**, shows $\bar{U}_{\mathrm{M}}$, as a function of wave frequency. Black triangles correspond TWA=6 mm, Green squares to TWA=3 mm and light green to TWA=1 mm. Unsurprisingly, maximum velocities observed are associated with higher wave amplitudes. It also appears that $\bar{U}_{\mathrm{M}}$ does not strongly depend on wave frequency, f. Figure 5.19 **B** shows $\bar{U}_{\mathrm{M}}$ normalized by wave amplitude and frequency. The relative data collapse of TWA 3 and 6 mm underlines the effect of wave amplitude, A, on the jet. At lower wave amplitudes (TWA 1 mm), when no jet is observed, $\bar{U}_{\mathrm{M}}/(Af)$ remains smaller than for the two other sets.

5.3.4 Jet orientation

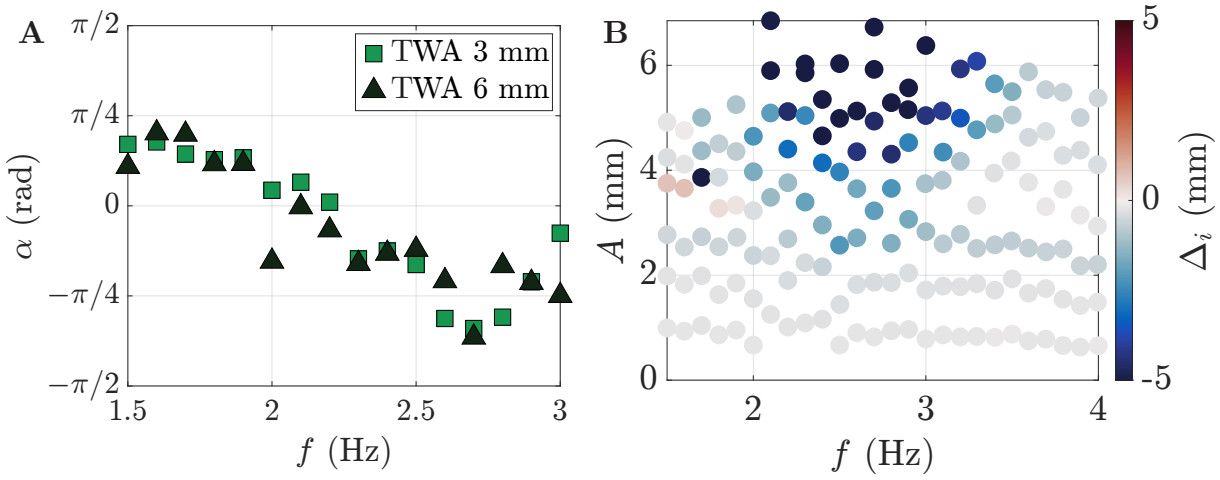

Figure 5.20: **A** Jet angle with respect to the horizontal, α as a function of wave frequency, f. Green squares correspond to TWA=3 mm and black triangles to TWA=6 mm. **B** Amplitude-frequency diagram of Δ_i measurements for S2.

As mentioned, looking at particle trajectories or mean flow velocity, the jet appears to change its orientation depending on wave frequency. To confirm this observation, the jet orientation, α, is shown in Figure 5.20 **A**. α corresponds to the angle between the jet direction and the horizontal. Negative values of α correspond to a jet directed downward and positive values to a jet directed upward. It appears that the jet follows the same direction for both TWA 3 mm and TWA 6 mm of wave-maker amplitudes. TWA 1 mm is not considered here as no jet can be observed. Jet orientation can be linked to plate mean position change for high wave amplitudes. Figure 5.20 **B** shows Δ_i the difference between the plate tip positions without waves and in the wave field. For low amplitude waves (below 2 mm), the plate tip remains

close to its initial position. However, for higher amplitudes, the plate tip mean position can change. For wave frequencies between 1.5 and 2 Hz plate Δ_i remains small but for frequencies between 2 Hz and 3.5 Hz the plate tip tends to go upward. The plate tip displacement is correlated with jet orientation. Indeed, the jet is directed downward for frequencies where the plate tip tends go upward. Even if it is difficult to measure directly, the jet could be producing a force on plate tip that changes its mean position.

5.3.5 Thrust production in the x direction by a submerged elastic plate in a wave field

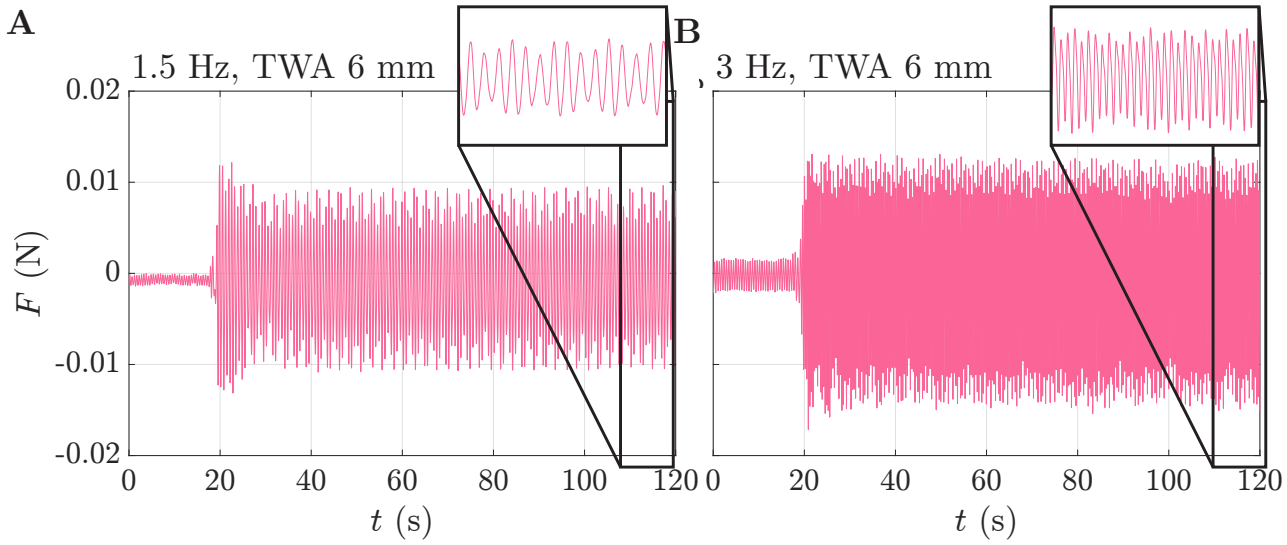

Figure 5.21: **A** Force exerted by waves on S2 at a 3 cm submergence depth, F, as a function of time for 1.5 Hz and TWA=6 mm. **B** Force exerted by waves on the plate, F, as a function of time for 3 Hz and TWA=6 mm.

The correlation between jet orientation and plate displacement from its position at rest suggests that the jet applies a force on the plate. As discussed in Chapter 2, it has been considered using submerged elastic plate as possible passive propulsion device for boats. To investigate the possible thrust created by the system, a uni-axial force sensor is placed to measure the force applied by the plate on the structure in the x direction. Recording is launched for 2 minutes and waves arrive approximately 20 seconds after the recording starts. Note that those measurements are performed simultaneously with PIV video recording.
Figure 5.21 **A** and **B** present the signal obtained for 1.5 and 3 Hz waves for the sixth set of wave-maker amplitudes. For the two wave frequencies, during the first 20 seconds, only noise

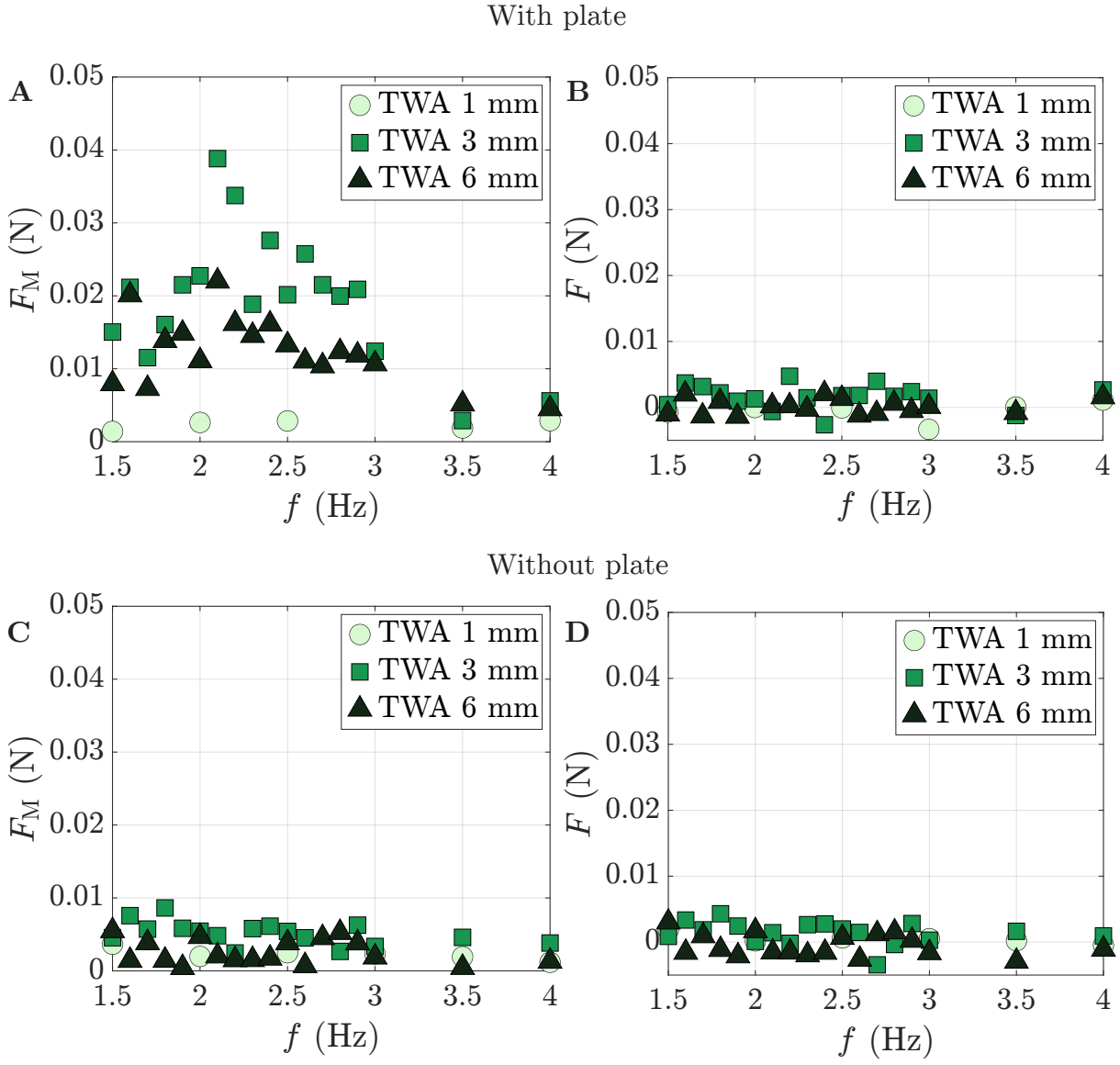

Figure 5.22: **A** F_M as a function of wave frequency, f, for S2 at a 3 cm depth, light green circles correspond to TWA=1 mm, green squares to TWA=3 mm and black triangles correspond to TWA=6 mm. **B** Mean force, $\bar{F}$, as a function of wave frequencies for Target Wave Amplitudes. Light green circles correspond to TWA=1 mm, green squares to TWA=3 mm and black triangles correspond to TWA=6 mm. **C-D** Same Figures but for measurements performed without waves. It makes it possible to quantify what part of the forces applied by the waves on the system can be attributed to the poles of the clamping system.

is observed and, when waves reach the plate, the measured force, F, increases drastically. As illustrated by the two insets, F oscillates at wave frequency.

For each experiment, the 95% percentile force, F_M, is measured as well as the mean force,

$\bar{F}$. Similarly to $\bar{U}_{\mathrm{M}}$, in practice the 95% is preferred to the absolute force maximum to avoid incoherent values caused by an exceptionally high punctual measures. Figure 5.22 **A** shows F_{M} for TWA=1,3 and 6 mm and frequencies ranging from 1.5 Hz to 4 Hz. It appears that F_{M} is higher for frequencies between 2 and 2.5 Hz. The highest force values are recorded for the TWA=3 mm, *i.e.* not the higher waves. Figure 5.22 **B** shows the mean force, $\bar{F}$. Mean force appears small as its maximum value is 0.004 N for 2.2 Hz waves and TWA=3 mm. This value is close to the force sensor resolution limit and can be consider to be zero, considering the dispersion of mean forces recorded mean force produced by the plate. Consequently, the system designed for this experiment is not able to produce thrust.
Finally, to ensure that forces recorded are not due to the poles maintaining the plate submerged, experiments are performed without plate. The poles are maintained plunging at a 3 cm depth. Force measurements in this situation are presented in Figure 5.22 **C** and **D**. It appears that waves does not apply force on the poles. The force observed in Figure 5.22 **A** and **B** is therefore due to the interaction between waves and the elastic plate.

5.3.6 Jet power

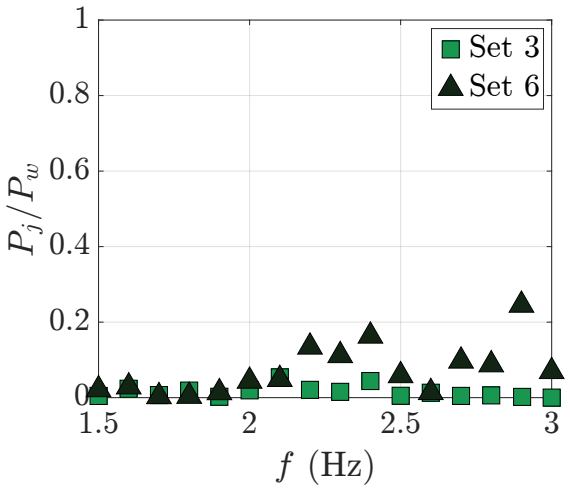

Figure 5.23: Ratio between jet power, P_{j}, and incoming wave power, P_{w} as a function of wave frequency for TWA=3 mm and TWA=6 mm.

Wave energy dissipation caused by the plate has been observed in Section 5.2.4. Dissipation is caused by the fact that plate motion does not only radiate waves but also creates drag. Energy lost in drag is actually transferred to the bulk and dissipated. The jet observed in this Section contains energy, initially in the waves, that is transferred to the fluid bulk by the plate oscillation. To measure what part of wave energy is transferred to the jet, power in the jet, P_{j}, can be compared to the incoming wave power, P_{w}.

Energy in the jet is in the form of kinetic energy. Consequently, P_j can be estimated as the kinetic energy flux across a surface in the jet. It leads to write:

$$P_\mathrm{j} = \frac{1}{2}\rho \int_\mathrm{S} \bar{U}^2 \bar{\mathbf{U}} \mathbf{dS}, \tag{5.3.1}$$

with $\mathbf{S}$ being a chosen oriented surface. In practice, $\mathbf{S}$, is taken as a rectangular surface of width b in the plan $y-z$. Doing so, the jet is assumed to be homogeneous in the y direction. Under this assumption P_j expression can be simplified to:

$$P_\mathrm{j} = \frac{1}{2}\rho b \int_{z_\mathrm{b}}^{z_u} \bar{U}^2 \bar{U}_x dz, \tag{5.3.2}$$

with z_b and z_u the jet limits in the z direction. The jet limits are defined as the frontier between regions where $\bar{U}_x > 0$, corresponding to the jet, and regions where $\bar{U}_x \leq 0$, outside the jet. The x value at which P_j is measured. In practice, x is chosen to maximize P_j.
The incoming wave power is estimated using the relation presented in Chapter 2, Equation 2.1.50, so that:

$$P_\mathrm{w} = \frac{1}{2}\rho b_\mathrm{t} c_g A^2, \tag{5.3.3}$$

with b_t the tank width. The ratio between P_j and P_w is presented in Figure 5.23 for the wave-maker amplitude TWA=3 mm and TWA=6 mm. Power in the jet represents a higher portion of incoming wave power for TWA=6 mm with $P_\mathrm{j}/P_\mathrm{w}$ reaching up to 0.25. Between 2 and 2.5 Hz the jet has more power, also corresponding to the region where S2 dissipates more energy. However, in that region, the plate dissipates approximately 60% of wave energy, significantly more than what is observed in the jet.

5.3.7 PIV experiment in the $y-z$ plan

To investigate other possible dissipation sources, PIV experiments are performed in the $y-z$ plan at 8 cm from the plate clamping points. To do so, a camera is placed at the end of the tank and the beach is replaced by a plastic plate so that plate can be seen from this view. As fluid particles are expected to have circular trajectories, in the $z-y$ plane. However, the laser sheet width makes it possible to maintain particles enlightened over enough frames to be able to apply PIV algorithms.
In Figure 5.24, the left column (Figures **A**, **C** and **E**) show particle trajectories while conducting experiments with TWA=6 mm at 1.5, 2 and 3 Hz. Contrary to PIV performed in the $x-z$ plan, trajectories are obtained by taking the maxima at each pixel over 20 waves periods. The small size of traits illustrates the fact that particles move out of the $y-z$.

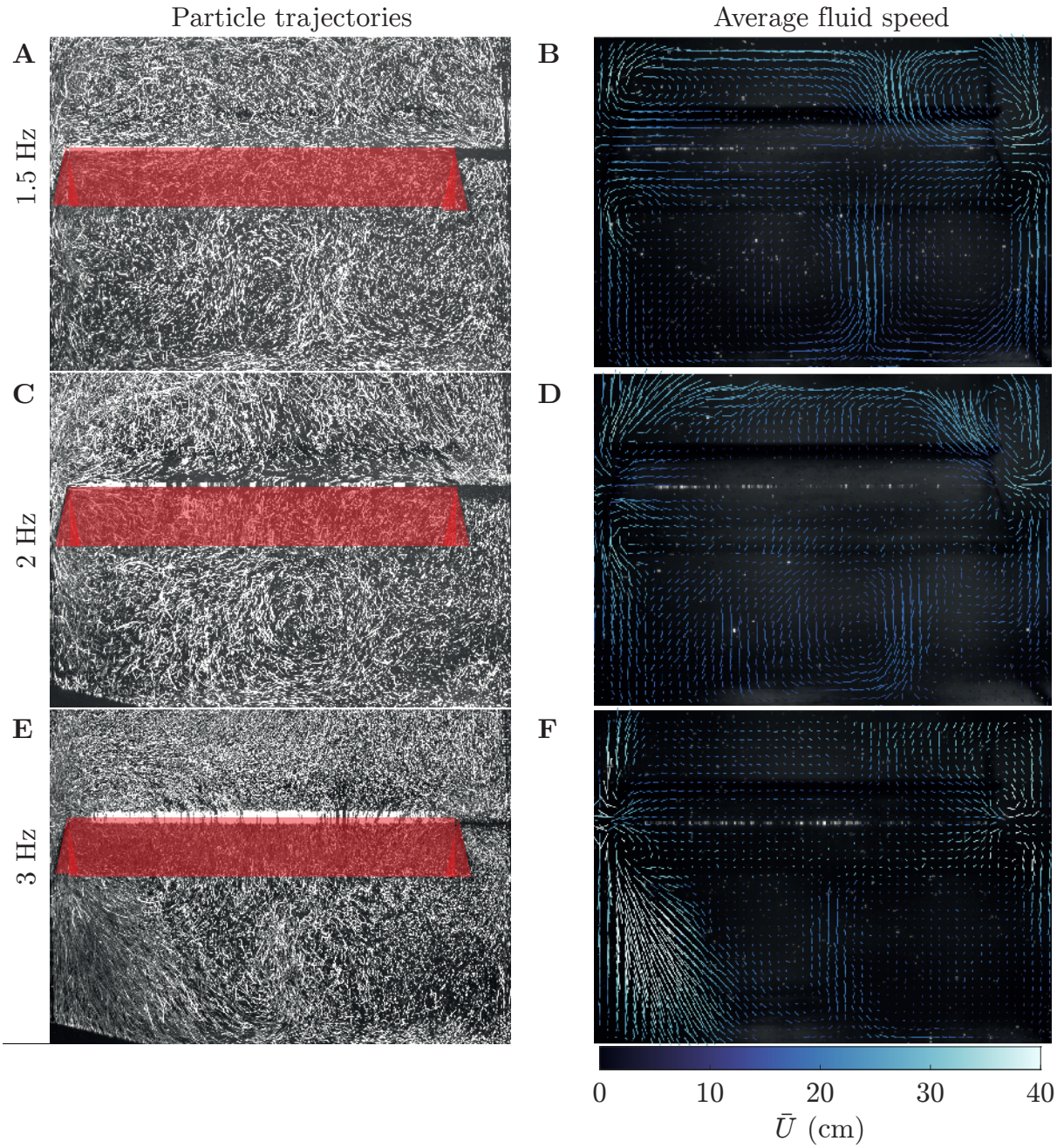

Figure 5.24: **A** Particle trajectories obtained during PIV experiment showing the $y-z$ plan *i.e.* the plane transverse to wave propagation for 1.5 Hz waves and TWA=6 mm. The red area corresponds to plate position. **B** Average fluid velocity in the the $y-z$ plan for 1.5 Hz waves and TWA=6 mm. **C-D-E-F** show the same quantities but for 2 and 3 Hz waves.

The tank walls are located just at the edge of the image and the plate is colored in red to underline its location. In these images, only the tip of the plate is visible as the clamped part is located at the other side of the laser sheet. Particle trajectories show that significant motion exists in the $y-z$ plan, particularly between the plate and the tank wall. Indeed,

in an unperturbed wave field particle trajectories should be vertical, which is not the case in those Figures.
The mean velocity for the same experiments is plotted in Figure 5.24, right column. Motion in the $y-z$ plan appears quite clearly, since rolls can be observed over and below the plate at all frequencies. Furthermore, significant velocities (up to 40 cm.s^{-1} at 3 Hz) can be observed at plate edge.
Raspa et al. [2014] performed PIV experiments around a heaving elastic plate in the same plan as in this wave experiment but in a still fluid. They show that complex flows appear at the edge of the plate in the yz plan. This effect, in addition to the relative motion due to the wave flow, might be responsible for the rest of wave energy dissipation measured in Section 5.2.4.

5.4 Conclusions

The experimental investigation of the interaction between a submerged elastic plate and a wave fields showed a rich and complex behavior. First, it has been shown that elastic plates can reflect energy in the range of frequencies studied. The fact that a rigid plate does not reflect wave energy shows that reflection is due to plate flexibility. The comparison between experimental and theoretical reflection and transmission coefficients is encouraging as linear theory is able to predict accurately frequencies at which reflection is observed. However, discrepancies remain in the reflection and transmission coefficients values. A possible explanation of the differences observed could be the presence of non-linearities that are not taken into account in the linear wave theory. To observe more clearly non-linearities sources, coefficients of transmission and reflection measurements are performed at higher wave amplitudes. From those measurements, wave energy dissipation and chang in mean plate position arise. Finally, PIV experiments show significant sources of nonlinearities in the wave-plate interaction as a jet is created at plate tip in the $x-z$ plan, formed by gravity and wave propagation direction and rolls in the $y-z$ plan, transverse to wave propagation direction.

Conclusion

This thesis described a wide variety of phenomena that can be observed when looking at the interaction between a submerged elastic plate and waves. First, the powerful tool of linear wave theory has been used to formalize the physical phenomena at stake and get first information about the plate response. From that study, a rich behavior arises. It is shown that the plate can reflect the waves. Two types of reflection patterns are observed, wide and sharp reflection peaks. If both reflection types are associated with an increase in the plate motion amplitude, sharp peaks exhibit particularly high motion amplitude. Reflection and transmission patterns vary with plate parameters, sharp and wide peaks having different dependencies in the various parameters.

At the same time, an experimental setup is used to study the interaction between the elastic plate and waves. Taking advantage ot the small size of the set-up, original experimental techniques can be utilized, such as Schlieren imaging to reconstruct the free surface height and Particle Image Velocimetry to analyze the flow field. Free surface height reconstruction allows to measure reflection and transmission coefficients. From those measurements, it appears that elastic plate are able to reflect waves. By comparing reflection and transmission coefficients for elastic and rigid plates, it emerges that reflection is due to elasticity. Experimental results are compared with theoretical predictions for small amplitude waves. Frequencies at which reflection occurs correspond to frequencies of predicted wide peaks. However, sharp peaks are not observed experimentally and reflection and transmission coefficients values are not well predicted. Non-linear effects could account for the observed discrepancy. Particularly, Particle Image Velocimetry experiments show that a jet is created at the plate tip and strong transverse effects can take place when the wave amplitude increases. For high amplitude waves, elastic plates can also act like perfect wave terminators.

Various effects were reported in this thesis, but questions remain open. The exact causes of plate resonance and reflection remain to be found. This work illustrated the complexity of such a problem as reflection depends on multiple parameters. In order to better understand

the discrepancies between experiments and simulation, the theoretical part could possibly be enhanced by the addition of vortices emission at the plate tip similarly to what was done by Shoele [2023] or Chang et al. [2015].
From a wave energy perspective, it could be interesting to perform experiments at larger scale to observe if the phenomena observed with the small scale set-up also exist at larger scale. However, the plate design might be particularly challenging. At smaller scales, similarly to what has been done by [Latif et al., 2021], adding internal damping mechanisms in the plate could be interesting to better mimic wave energy converters.

Appendix

Expression of matrix D

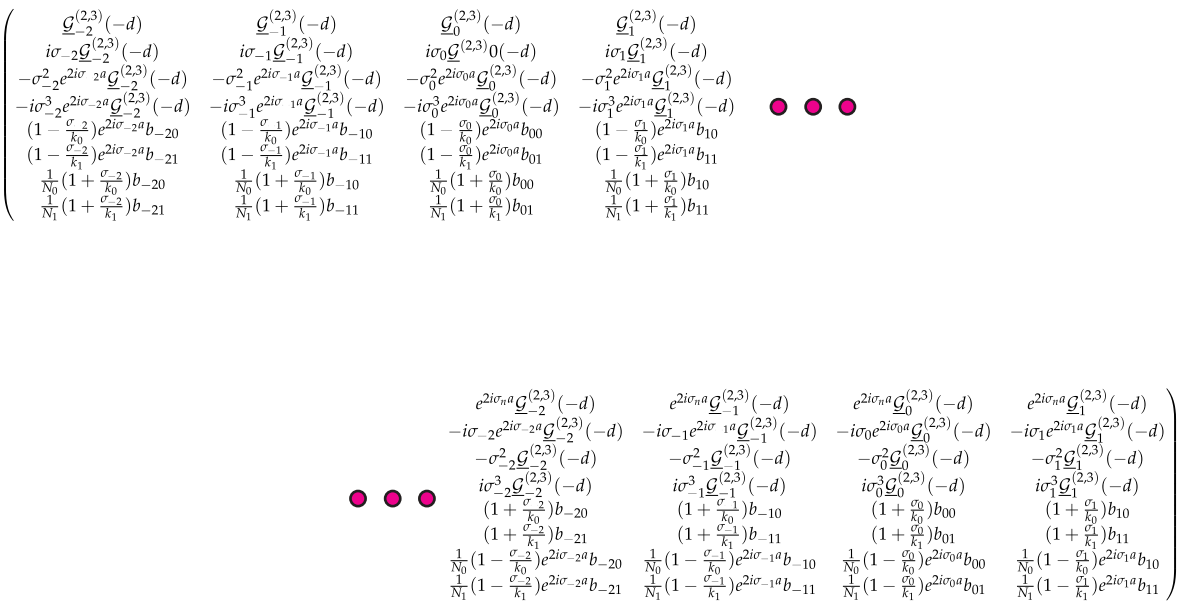

Figure 5.25: Expression of matrix D for $N_{\text{trunc}} = 1$. As the matrix is to big to fit on a line it is written on 2 lines with pink points symbolizing the junction between each part.

Relation between motor command and plate motion and complement information on the wave-maker.

Motor motion is imposed so that it does not reach its maximum stroke at each oscillation, avoiding noises and potential damages. This choice reduces the motor stroke to a 2.5 cm maximum amplitude and, will also impact the maximum wave amplitude produced by the wave-maker (see section 4.1.2).

The motion of the motor is imposed to a software. This section aims to investigate the relation between the motor command and its actual precision. Figure 5.26 presents an illustration of the motor use for a 9 mm amplitude and a 1.5 Hz frequency. Figure 5.26 **A** shows the motor tip position and the command position over ten seconds. In this case and for all the other pair of frequencies and amplitudes investigated, the two curves coincide. The motor accuracy is further confirm looking at the difference between the command and the actual motor position (see Figure 5.26 **B**). In the case presented here, the maximum difference observed is around 0.2 mm *i.e* ≈1% with respect to the command. The small difference between the command position and the actual position allows to approximate that the actual motor amplitude, b', is equal to the motor command position, b'_c.

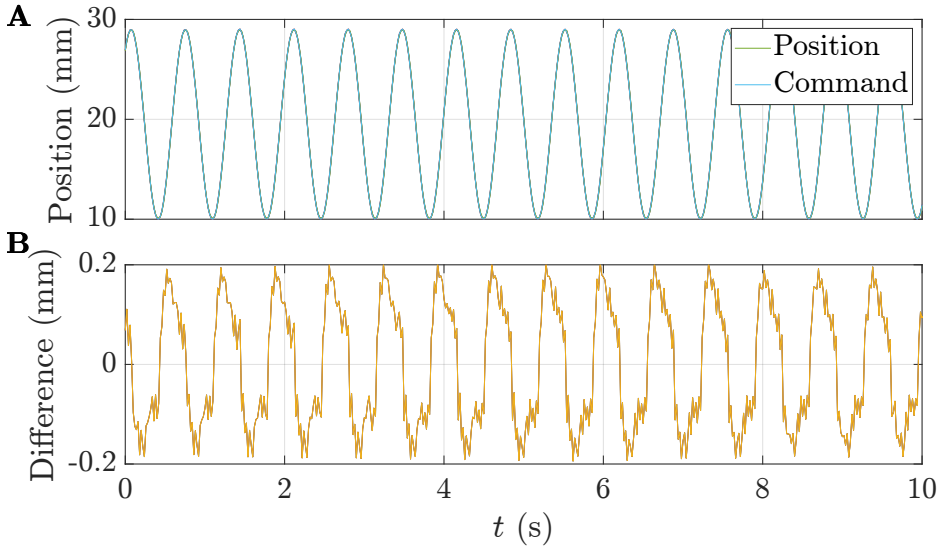

Figure 5.26: **A** Command position and actual motor position as a function of time for an amplitude of 9 mm at 1.5 Hz. The two curves coincide what underlines the good performance of the motor. **B** Difference between the command position and the actual position as a function of time. The difference has the same period as the one imposed by the motor, but does not exceed 1% of the imposed value. $\mathcal{G}$ stands for G'

Standard deviations

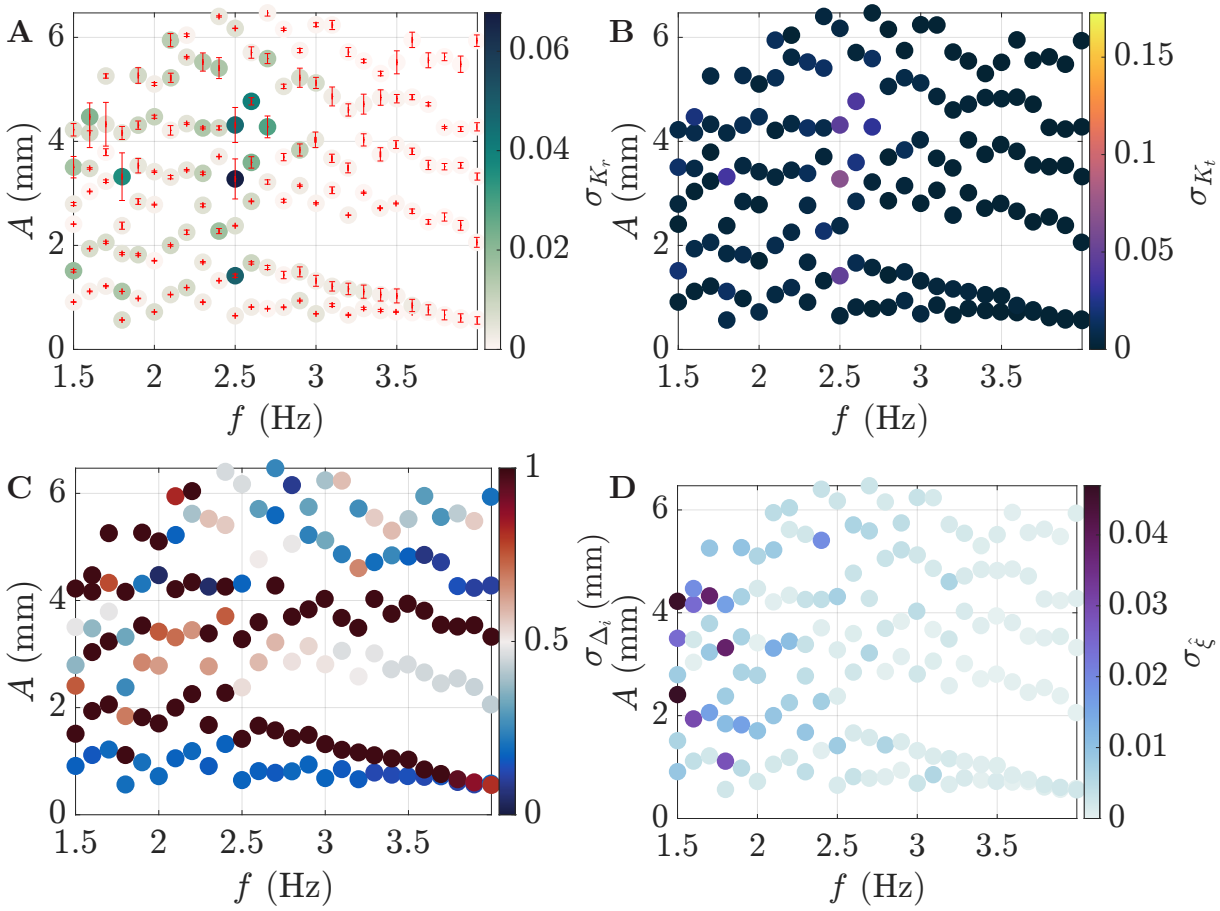

Figure 5.27: Amplitude-frequency diagram showing standard deviation over three repetitions for different parameters measured and for L2 at a 3 cm submergence depth. **A** Standard deviation of reflection coefficient, σ_{K_r}. Red errorbars show the standard deviation on the wave amplitude, A and on the wave frequency, f. **B** Standard deviation on transmission coefficient, σ_{K_t}. **C** Standard deviation on plate tip mean displacement, σ_{Δ_i}. **D** Standard deviation on the plate normalized motion amplitude, $\sigma_{\hat{\xi}}$.

Figure 5.27 show the standard deviation of the reflection coefficient, the transmission coefficient, the mean plate tip displacement, and the plate normalized motion amplitude. For all those quantities error appear to be small compared to measured values.

Natural frequency measurements

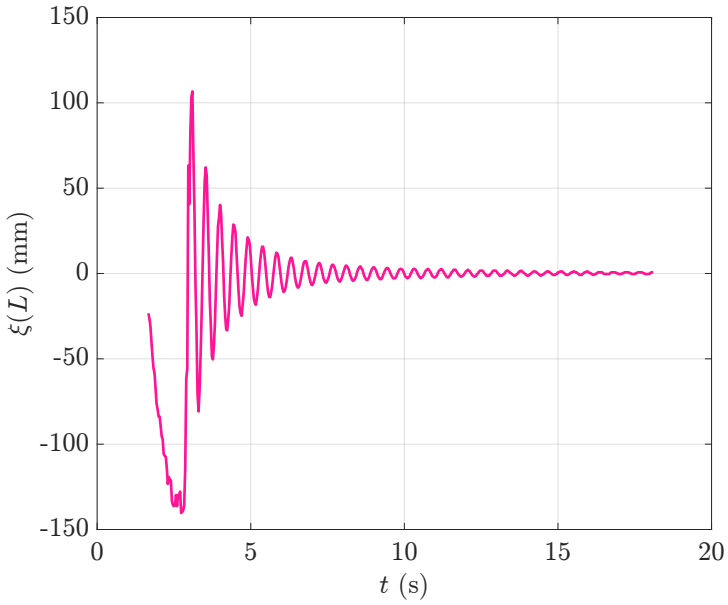

Figure 5.28: Plate displacement at its tip as a function of time conducting experiments with L2 in air.

Plate natural frequency is obtained by conducting free-oscillation tests. The plate is maintained in the plan $x - z$ to avoid gravity effects. The plate is excited by a small hit close to its clamping edge and starts to oscillate at its natural frequency. Oscillations are progressively damped. To measure this frequency, the plate is filmed and its edge is tracked. Figure 5.28 shows the result of this tracking while conducting experiment with L2 in the air. Experiments are conducted both in air and in water to measure respectively plate natural frequency and plate natural frequency with added mass. Results obtained are presented in the Table 5.3: As mentioned in Section 2.2.2, plate natural frequency with added mass can be estimated

Short name	f_0 (Hz)	$f_{0\text{ma}}^{(\text{th})}$ (Hz)	$f_{0\text{ma}}$ (Hz)
L1	1.33	0.86	0.8
L2	2.04	1.6	1.7
L3	2.80	2.2	Not measured

Table 5.3: Plate natural frequencies.

theoretically knowing the plate natural frequency in the air. The theoretical result is also presented in the Table 5.3. It appears that theoretical estimation of plate natural frequency is relatively well estimated.

Bibliography

A. Abdolali, M. Kolahdoozan, M. J. Alaee, and M. Allahyar. on the comparison of analytical methods using for the decomposition of wave characteristics. *Proceedings of COPEDEC*, 2012:20–24, 2012.

N. Achour, J. Mougel, D. Lo Jacono, and D. Fabre. Etude théorique de l'effet d'un faible courant sur les interactions houle/membrane flexible: application à la recuperation d'énergie. *Revue Paralia*, pages p. 495–504., 2020.

G. B. Airy. *Tides and waves*. B. Fellowes, 1845.

M.-R. Alam. Nonlinear analysis of an actuated seafloor-mounted carpet for a high-performance wave energy extraction. *Proceedings of the Royal Society A: Mathematical, Physical and Engineering Sciences*, 468(2146):3153–3171, 2012.

C. Algie, S. Ryan, and A. Fleming. Predicted power performance of a submerged membrane pressure-differential wave energy converter. *International journal of marine energy*, 20: 125–134, 2017.

J. Allen and A. Smits. Energy harvesting eel. *Journal of fluids and structures*, 15(3-4): 629–640, 2001.

W. Alpers and H. Hühnerfuss. The damping of ocean waves by surface films: A new look at an old problem. *Journal of Geophysical Research: Oceans*, 94(C5):6251–6265, 1989.

D. G. Andrews and M. McIntyre. An exact theory of nonlinear waves on a lagrangian-mean flow. *Journal of fluid Mechanics*, 89(4):609–646, 1978.

R. Antier. *Ailes battantes déformables inspirées de l'insecte et rigidifiées par un réseau de plis*. PhD thesis, Université Paris Cité, 2021.

A. Asaeian, M. Abedi, R.-A. Jafari-Talookolaei, and M. Attar. Wave propagation through a submerged horizontal plate at the bottom of a water channel. *Computational Engineering and Physical Modeling*, 3(4):1–19, 2020.

A. Babarit, J. Hals, M. J. Muliawan, A. Kurniawan, T. Moan, and J. Krokstad. Numerical benchmarking study of a selection of wave energy converters. *Renewable energy*, 41:44–63, 2012.

A. Babarit, F. Wendt, Y.-H. Yu, and J. Weber. Investigation on the energy absorption performance of a fixed-bottom pressure-differential wave energy converter. *Applied Ocean Research*, 65:90–101, 2017.

D. N. Beal, F. S. Hover, M. S. Triantafyllou, J. C. Liao, and G. V. Lauder. Passive propulsion in vortex wakes. *Journal of Fluid Mechanics*, 549:385–402, 2006.

H. Behera. Oblique wave scattering by a system of semi-infinite floating and submerged elastic plates. *Differential Equations and Dynamical Systems*, 29(1):157–173, 2021.

K. Belibassakis, E. Filippas, and G. Papadakis. Numerical and experimental investigation of the performance of dynamic wing for augmenting ship propulsion in head and quartering seas. *Journal of Marine Science and Engineering*, 10(1):24, 2021.

B. Boulier and M. Belorgey. Ecoulement tourbillonnaire et zone d'affouillement générés par la houle en présence d'une plaque immergée. *3èmes JNGCGC. Sète, France*, pages 39–45, 1994.

A. C. Bovik. *The essential guide to image processing*. Academic Press, 2009.

J. Burke. Scattering of surface waves on an infinitely deep fluid. *Journal of Mathematical Physics*, 5(6):805–819, 1964.

R. A. Carmigniani, M. Benoit, D. Violeau, and M. Gharib. Resonance wave pumping with surface waves. *Journal of Fluid Mechanics*, 811:1–36, 2017.

R. W. Carter, R. C. Ertekin, and P. Lin. On the reverse flow beneath a submerged plate due to wave action. In *International Conference on Offshore Mechanics and Arctic Engineering*, volume 47470, pages 595–602, 2006.

K.-H. Chang, M.-Y. Lin, and L.-H. Huang. Modified lagrangian vortex method with improved boundary conditions for water waves past a thin bottom-standing barrier. *International journal for numerical methods in fluids*, 77(4):183–205, 2015.

I. Cho and M. Kim. Interactions of a horizontal flexible membrane with oblique incident waves. *Journal of Fluid Mechanics*, 367:139–161, 1998.

I. Cho and M. Kim. Interactions of horizontal porous flexible membrane with waves. *Journal of waterway, port, coastal, and ocean engineering*, 126(5):245–253, 2000.

I. Collins, M. Hossain, W. Dettmer, and I. Masters. Flexible membrane structures for wave energy harvesting: A review of the developments, materials and computational modelling approaches. *Renewable and Sustainable Energy Reviews*, 151:111478, 2021.

C. Cummins and F. Dias. A new model of viscous dissipation for an oscillating wave surge converter. *Journal of Engineering Mathematics*, 103:195–216, 2017.

J. Davidson and R. Costello. Efficient nonlinear hydrodynamic models for wave energy converter design—a scoping study. *Journal of Marine Science and Engineering*, 8(1):35, 2020.

W. Dean. Onthe reflection of surface waves by a submerged plane barrier. *Grt. Brit. Ministry of Supply, Wave Report*, 8, 1945.

N. Desmars, J. Tchoufag, D. Younesian, and M.-R. Alam. Interaction of surface waves with an actuated submerged flexible plate: Optimization for wave energy extraction. *Journal of Fluids and Structures*, 81:673–692, 2018.

T. M. Dick and A. Brebner. Solid and permeable submerged breakwaters. In *Coastal Engineering 1968*, pages 1141–1158. 1968.

L. Domino, M. Fermigier, E. Fort, and A. Eddi. Dispersion-free control of hydroelastic waves down to sub-wavelength scale. *Europhysics Letters*, 121(1):14001, 2018.

J. D'Adamo, M. Collaud, R. Sosa, and R. Godoy-Diana. Wake and aeroelasticity of a flexible pitching foil. *Bioinspiration & Biomimetics*, 17(4):045002, 2022.

EIA. Electricity net production. https://www.eia.gov/international/data/world/electricity/electricity-consumption, 2019. [Online; accessed 29-August-2023].

E. Falcon and N. Mordant. Experiments in surface gravity–capillary wave turbulence. *Annual Review of Fluid Mechanics*, 54:1–25, 2022.

E. S. Filippas, G. P. Papadakis, and K. A. Belibassakis. Free-surface effects on the performance of flapping-foil thruster for augmenting ship propulsion in waves. *Journal of Marine Science and Engineering*, 8(5):357, 2020.

R. E. Flick and R. T. Guza. Paddle generated waves in laboratory channels. *Journal of the Waterway, Port, Coastal and Ocean Division*, 106(1):79–97, 1980.

M. Folley and P. Lamont-Kane. Optimum wave regime for lift-based wave energy converters. In *European Wave and Tidal Energy Conference: European Wave and Tidal Energy Conference*. European Wave & Tidal Energy (EWTEC), 2021.

R. Gayathri, C. Benny, and H. Behera. Wave attenuation by a submerged flexible permeable membrane. In *AIP Conference Proceedings*, volume 2277. AIP Publishing, 2020.

Y. Goda and A. T. Ippen. Theoretical and experimental investigation of wave energy dissipators composed of wire mesh screens. Technical report, Massaschusetts Intitute of Technology, Cambridge Hydrodynamic Laboratory, 1963.

R. Godoy-Diana and B. Thiria. On the diverse roles of fluid dynamic drag in animal swimming and flying. *Journal of The Royal Society Interface*, 15(139):20170715, 2018.

R. Godoy-Diana, C. Marais, J.-L. Aider, and J. E. Wesfreid. A model for the symmetry breaking of the reverse bénard–von kármán vortex street produced by a flapping foil. *Journal of Fluid Mechanics*, 622:23–32, 2009.

G. Gomit, L. Chatellier, and L. David. Free-surface flow measurements by non-intrusive methods: a survey. *Experiments in Fluids*, 63(6):1–25, 2022.

M. Göteman, R. Mayon, Y. Liu, S. Zheng, and R. Wang. Fluid dynamics and wave-structure interactions. 2022.

C. Gray and C. Greated. The application of particle image velocimetry to the study of water waves. *Optics and lasers in Engineering*, 9(3-4):265–276, 1988.

J. Grue. Nonlinear water waves at a submerged obstacle or bottom topography. *Journal of Fluid Mechanics*, 244:455–476, 1992.

Y. Guo, S. Mohapatra, and C. G. Soares. Wave energy dissipation of a submerged horizontal flexible porous membrane under oblique wave interaction. *Applied Ocean Research*, 94: 101948, 2020.

M.-u. Hassan, M. H. Meylan, and M. A. Peter. Water-wave scattering by submerged elastic plates. *The Quarterly Journal of Mechanics & Applied Mathematics*, 62(3):321–344, 2009.

L. H. Holthuijsen. *Waves in oceanic and coastal waters*. Cambridge university press, 2010.

M. Isaacson. Measurement of regular wave reflection. *Journal of Waterway, Port, Coastal, and Ocean Engineering*, 117(6):553–569, 1991.

C. Kalogeri, G. Galanis, C. Spyrou, D. Diamantis, F. Baladima, M. Koukoula, and G. Kallos. Assessing the european offshore wind and wave energy resource for combined exploitation. *Renewable energy*, 101:244–264, 2017.

J. B. Keller. Surface waves on water of non-uniform depth. *Journal of Fluid Mechanics*, 4 (6):607–614, 1958.

G. Knott and M. Mackley. On eddy motions near plates and ducts, induced by water waves and periodic flows. *Philosophical Transactions of the Royal Society of London. Series A, Mathematical and Physical Sciences*, 294(1412):599–623, 1980.

A. L. Kohout and M. H. Meylan. An elastic plate model for wave attenuation and ice floe breaking in the marginal ice zone. *Journal of Geophysical Research: Oceans*, 113(C9), 2008.

M. Kolahdoozan, M. J. Alizadeh, A. Tahershamsi, and A. Abdolali. Experimental study of the performance of floating breakwaters with heave motion. *Civil Engineering Infrastructures Journal*, 47(1):59–70, 2014.

S. Kucher, A. Koźluk, P. Petitjeans, A. Maurel, and V. Pagneux. Backscattering reduction in a twisted water wave channel. *arXiv preprint arXiv:2308.03783*, 2023.

R. Kumar and H. Shin. Thrust prediction of an active flapping foil in waves using cfd. *Journal of Marine Science and Engineering*, 7(11):396, 2019.

J. Lai and M. Platzer. Jet characteristics of a plunging airfoil. *AIAA journal*, 37(12):1529–1537, 1999.

P. Lamont-Kane, M. Folley, C. Frost, and T. Whittaker. Preliminary investigations into the hydrodynamic performance of lift-based wave energy converters. In *Proceedings of the 14th European Wave and Tidal Energy Conference, Plymouth, UK*, pages 5–9, 2021.

U. Latif, E. Ali, E. Uddin, Z. Ali, M. Sajid, S. R. Shah, and M. Y. Younis. Experimental investigation of energy harvesting eel in the wake of bluff body under ocean waves. *Proceedings of the Institution of Mechanical Engineers, Part M: Journal of Engineering for the Maritime Environment*, 235(1):81–92, 2021.

M. Lehmann, R. Elandt, H. Pham, R. Ghorbani, M. Shakeri, and M.-R. Alam. An artificial seabed carpet for multidirectional and broadband wave energy extraction: Theory and experiment. In *Proceedings of 10th European Wave and Tidal Energy Conference*, 2013.

M. Lehmann, F. Karimpour, C. A. Goudey, P. T. Jacobson, and M.-R. Alam. Ocean wave energy in the united states: Current status and future perspectives. *Renewable and Sustainable Energy Reviews*, 74:1300–1313, 2017.

M. Lighthill. Hydromechanics of aquatic animal propulsion. *Annual review of fluid mechanics*, 1(1):413–446, 1969.

C. M. Linton and P. McIver. *Handbook of mathematical techniques for wave/structure interactions*. CRC press, 2001.

M. Luhar, E. Infantes, and H. Nepf. Seagrass blade motion under waves and its impact on wave decay. *Journal of Geophysical Research: Oceans*, 122(5):3736–3752, 2017.

E. P. Mansard and E. Funke. The measurement of incident and reflected spectra using a least squares method. In *Coastal Engineering 1980*, pages 154–172. 1980.

C. C. Mei, M. A. Stiassnie, and D. K.-P. Yue. *Theory and applications of ocean surface waves: Part 1: linear aspects*. World Scientific, 2005.

P. Mercier. *Modélisation de la turbulence engendrée par la morphologie du fond dans le Raz Blanchard: approche locale avec la LBM-LES*. PhD thesis, Normandie, 2019.

A. Mérigaud, B. Thiria, and R. Godoy-Diana. A wide-spacing approximation model for the reflection and transmission of water waves over an array of vertical obstacles. *Journal of Fluid Mechanics*, 923:A2, 2021.

M. H. Meylan and M. A. Peter. Water-wave scattering by submerged elastic plates. *The Quarterly Journal of Mechanics & Applied Mathematics*, 62(3):321–344, 2009.

S. Michelin, S. G. L. Smith, and B. J. Glover. Vortex shedding model of a flapping flag. *Journal of Fluid Mechanics*, 617:1–10, 2008.

S. Mohapatra and T. Sahoo. Wave interaction with a floating and submerged elastic plate system. *Journal of Engineering Mathematics*, 87(1):47–71, 2014.

S. Mohapatra and C. G. Soares. Interaction of ocean waves with floating and submerged horizontal flexible structures in three-dimensions. *Applied Ocean Research*, 83:136–154, 2019.

S. C. Mohapatra and C. Guedes Soares. Hydroelastic response of a flexible submerged porous plate for wave energy absorption. *Journal of Marine Science and Engineering*, 8(9):698, 2020.

S. C. Mohapatra, T. Sahoo, and C. G. Soares. Interaction between surface gravity wave and submerged horizontal flexible structures. *Journal of Hydrodynamics*, 30:481–498, 2018.

F. Moisy, M. Rabaud, and K. Salsac. A synthetic schlieren method for the measurement of the topography of a liquid interface. *Experiments in Fluids*, 46(6):1021–1036, 2009.

J. Morison, J. W. Johnson, and S. A. Schaaf. The force exerted by surface waves on piles. *Journal of Petroleum Technology*, 2(05):149–154, 1950.

G. Mork, S. Barstow, A. Kabuth, and M. T. Pontes. Assessing the global wave energy potential. In *International Conference on Offshore Mechanics and Arctic Engineering*, volume 49118, pages 447–454, 2010.

D. Ning, X. Zhao, M. Göteman, and H. Kang. Hydrodynamic performance of a pile-restrained wec-type floating breakwater: An experimental study. *Renewable energy*, 95:531–541, 2016.

D.-z. Ning, R.-q. Wang, L.-f. Chen, and K. Sun. Experimental investigation of a land-based dual-chamber owc wave energy converter. *Renewable and sustainable energy reviews*, 105: 48–60, 2019.

C. Nové-Josserand. *Converting wave energy from fluid-elasticity interactions*. PhD thesis, Sorbonne Paris Cité, 2018.

C. Nové-Josserand, R. Godoy-Diana, and B. Thiria. Interference model for an array of wave-energy-absorbing flexible structures. *Physical Review Applied*, 11(3):034054, 2019.

G. Orer and A. Ozdamar. An experimental study on the efficiency of the submerged plate wave energy converter. *Renewable Energy*, 32(8):1317–1327, 2007.

Y. Ouellet and I. Datta. A survey of wave absorbers. *Journal of hydraulic research*, 24(4): 265–280, 1986.

F. Paraz, L. Schouveiler, and C. Eloy. Thrust generation by a heaving flexible foil: Resonance, nonlinearities, and optimality. *Physics of Fluids*, 28(1), 2016.

M. Patarapanich. Forces and moment on a horizontal plate due to wave scattering. *Coastal Engineering*, 8(3):279–301, 1984.

P. R. Payne. The virtual mass of a rectangular flat plate of finite aspect ratio. *Ocean Engineering*, 8(5):541–545, 1981.

M. Piñeirua, R. Godoy-Diana, and B. Thiria. Resistive thrust production can be as crucial as added mass mechanisms for inertial undulatory swimmers. *Physical Review E*, 92(2): 021001, 2015.

M. Piñeirua, B. Thiria, and R. Godoy-Diana. Modelling of an actuated elastic swimmer. *Journal of Fluid Mechanics*, 829:731–750, 2017.

G. Pinon, G. Perret, L. Cao, A. Poupardin, J. Brossard, and E. Rivoalen. Vortex kinematics around a submerged plate under water waves. part ii: Numerical computations. *European Journal of Mechanics-B/Fluids*, 65:368–383, 2017.

G. Polly, A. Mérigaud, R. Alhage, B. Thiria, and R. Godoy-Diana. On the interaction of surface water waves and fully-submerged elastic plates. *arXiv preprint arXiv:2111.03018*, 2021.

A. Poupardin, G. Perret, G. Pinon, N. Bourneton, E. Rivoalen, and J. Brossard. Vortex kinematic around a submerged plate under water waves. part i: Experimental analysis. *European journal of mechanics-B/fluids*, 34:47–55, 2012.

M. Raffel, C. E. Willert, J. Kompenhans, et al. *Particle image velocimetry: a practical guide*, volume 2. Springer, 1998.

S. Ramananarivo, R. Godoy-Diana, and B. Thiria. Propagating waves in bounded elastic media: Transition from standing waves to anguilliform kinematics. *EPL (Europhysics Letters)*, 105(5):54003, 2014.

E. Ransley, S. Yan, S. Brown, M. Hann, D. Graham, C. Windt, P. Schmitt, J. Davidson, J. Ringwood, P.-H. Musiedlak, et al. A blind comparative study of focused wave interactions with floating structures (ccp-wsi blind test series 3). *International Journal of Offshore and Polar Engineering*, 30(01):1–10, 2020.

V. Raspa, S. Ramananarivo, B. Thiria, and R. Godoy-Diana. Vortex-induced drag and the role of aspect ratio in undulatory swimmers. *Physics of Fluids*, 26(4), 2014.

E. Renzi. Hydroelectromechanical modelling of a piezoelectric wave energy converter. *Proceedings of the Royal Society A: Mathematical, Physical and Engineering Sciences*, 472 (2195):20160715, 2016.

E. Renzi, S. Michele, S. Zheng, S. Jin, and D. Greaves. Niche applications and flexible devices for wave energy conversion: A review. *Energies*, 14(20):6537, 2021.

M. Robbe-Saule, C. Morize, R. Henaff, Y. Bertho, A. Sauret, and P. Gondret. Experimental investigation of tsunami waves generated by granular collapse into water. *Journal of Fluid Mechanics*, 907:A11, 2021.

S. Roche, A. H. Clément, A. Babarit, and C. Bouneau. Transformer les vagues en énergie: utopie ou réalité? *Artefact. Techniques, histoire et sciences humaines*, (9):239–265, 2019.

K. V. Rozhdestvensky and V. A. Ryzhov. Aerohydrodynamics of flapping-wing propulsors. *Progress in aerospace sciences*, 39(8):585–633, 2003.

L. Rusu and F. Onea. The performance of some state-of-the-art wave energy converters in locations with the worldwide highest wave power. *Renewable and Sustainable Energy Reviews*, 75:1348–1362, 2017.

M. N. Sanz, F. Vandenbrouck, B. Salamito, and D. Chardon. Physique - tout en un - pc/pc* - collection j'intègre.

H. A. Schäffer. Second-order wavemaker theory for irregular waves. *Ocean engineering*, 23 (1):47–88, 1996.

H. A. Schäffer and G. Klopman. Review of multidirectional active wave absorption methods. *Journal of waterway, port, coastal, and ocean engineering*, 126(2):88–97, 2000.

I. Sergievskaya, S. Ermakov, T. Lazareva, and J. Guo. Damping of surface waves due to crude oil/oil emulsion films on water. *Marine pollution bulletin*, 146:206–214, 2019.

M. J. Shelley and J. Zhang. Flapping and bending bodies interacting with fluid flows. *Annual Review of Fluid Mechanics*, 43:449–465, 2011.

W. Sheng. Wave energy conversion and hydrodynamics modelling technologies: A review. *Renewable and Sustainable Energy Reviews*, 109:482–498, 2019.

S. Y. Shinde and J. H. Arakeri. Physics of unsteady thrust and flow generation by a flexible surface flapping in the absence of a free stream. *Proceedings of the Royal Society A: Mathematical, Physical and Engineering Sciences*, 474(2218):20180519, 2018.

K. Shoele. Hybrid wave/current energy harvesting with a flexible piezoelectric plate. *Journal of Fluid Mechanics*, 968:A31, 2023.

SIOcean. Wave and tidal energy market deployment strategy for europe. page 47, 2014.

R. I. Slavchov, B. Peychev, and A. S. Ismail. Characterization of capillary waves: A review and a new optical method. *Physics of Fluids*, 33(10):101303, 2021.

A. V. Slunyaev, D. E. Pelinovsky, E. N. Pelinovsky, et al. Rogue waves in the sea: observations, physics, and mathematics. *Uspekhi Fizicheskikh Nauk*, 193(2):155–181, 2023.

D. G. Stamos and M. R. Hajj. Reflection and transmission of waves over submerged breakwaters. *Journal of Engineering Mechanics*, 127(2):99–105, 2001.

M. Stiassnie, E. Naheer, and I. Boguslavsky. Energy losses due to vortex shedding from the lower edge of a vertical plate attacked by surface waves. *Proceedings of the Royal Society of London. A. Mathematical and Physical Sciences*, 396(1810):131–142, 1984.

S. Taneda. Waving motions of flags. *Journal of the Physical Society of Japan*, 24(2):392–401, 1968.

G. W. Taylor, J. R. Burns, S. Kammann, W. B. Powers, and T. R. Welsh. The energy harvesting eel: a small subsurface ocean/river power generator. *IEEE journal of oceanic engineering*, 26(4):539–547, 2001.

J. Tedd, J. P. Kofoed, W. Knapp, E. Friis-Madsen, and H. Sørensen. Wave dragon: prototype wave power production. In *Proceedings of the 9th World Renewable Energy Congress: WREC IX, Florence, Italy, August 2006*. Pergamon Press, 2006.

F. C. Ting and Y.-K. Kim. Vortex generation in water waves propagating over a submerged obstacle. *Coastal Engineering*, 24(1-2):23–49, 1994.

F. Ursell. Edge waves on a sloping beach. *Proceedings of the royal society of London. Series A. Mathematical and Physical Sciences*, 214(1116):79–97, 1952.

F. Ursell, R. G. Dean, and Y. Yu. Forced small-amplitude water waves: a comparison of theory and experiment. *Journal of fluid mechanics*, 7(1):33–52, 1960.

W. Van Horssen and M. Zarubinskaya. On an elastic dissipation model for a cantilevered beam. *Quarterly of Applied Mathematics*, 61(3):565–573, 2003.

N. Vandenberghe, J. Zhang, and S. Childress. Symmetry breaking leads to forward flapping flight. *Journal of Fluid Mechanics*, 506:147–155, 2004.

N. Vandenberghe, S. Childress, and J. Zhang. On unidirectional flight of a free flapping wing. *Physics of Fluids*, 18(1), 2006.

N. A. Vinnichenko, A. V. Pushtaev, Y. Y. Plaksina, and A. V. Uvarov. Performance of background oriented schlieren with different background patterns and image processing techniques. *Experimental Thermal and Fluid Science*, 147:110934, 2023.

wikipedia.org. wikipedia.org. https://en.wikipedia.org/wiki/CETO, 2023. [Online; accessed 29-August-2023].

S. Wildeman. Real-time quantitative schlieren imaging by fast fourier demodulation of a checkered backdrop. *Experiments in Fluids*, 59(6):1–13, 2018.

A. Williams and K. Wang. Flexible porous wave barrier for enhanced wetlands habitat restoration. *Journal of engineering mechanics*, 129(1):1–8, 2003.

J. Zhang, S. Childress, A. Libchaber, and M. Shelley. Flexible filaments in a flowing soap film as a model for one-dimensional flags in a two-dimensional wind. *Nature*, 408(6814): 835–839, 2000.

S. Zheng, M. Meylan, X. Zhang, G. Iglesias, and D. Greaves. Wave power extraction from a piezoelectric wave energy converter integrated in a pile-supported breakwater. In *14th European Wave and Tidal Energy Conference (EWTEC)*, page 2385, 2021.

Mot clés

Interaction vague-structure, théorie de la houle linéaire, bassin à houle à petite échelle, réflexion et transmission, jet.

Résumé

L'interaction vague-structure est un domaine riche et aux intérêts applicatifs cruciaux tels que la protection côtière ou la production d'électricité par conversion d'énergie des vagues. Cette thèse s'inscrit dans ce contexte et s'intéresse au cas spécifique d'une plaque élastique submergée, maintenue à son bord d'attaque, et excitée par des vagues. Ce dispositif, qui est envisagé comme un potentiel convertisseur d'énergie des vagues, a été longuement étudiée dans le cas d'un écoulement uniforme ou pour un fluide au repos. En revanche, l'effet de l'excitation, par des vagues, d'une plaque élastique submergée reste mal connu.
Pour pallier à ce manque, cette thèse a pour but de décrire l'interaction entre une plaque élastique submergée, tenue à son bord d'attaque et des vagues. Pour ce faire, un premier travail théorique est menée en s'appuyant sur la théorie de la houle linéaire. Le but de cette approche est d'obtenir une première compréhension du système, c'est-à-dire de formaliser le problème physique et d'obtenir des informations sur la réponse des plaques excitées par les vagues. Pour cela, la réflection et la transmission des vagues sont évaluées et mises en perspective grâce à l'observation des déplacements de la plaque. De cette étude, il ressort que les plaques élastiques possèdent des motifs de résonnance complexes, qui varient en fonction de la profondeur, longueur ou rigidité des plaques.
Cette approche théorique linéaire, limitée au cas idéal de petites amplitudes de vagues et des petits déplacements de la plaque, est enrichie par une étude expérimentale de l'interaction plaque-vagues. Une des originalités de cette thèse réside dans les dimensions du dispositif expérimental. Le bassin utilisé mesure 2 mètres par 50 centimètres et est beaucoup plus petit que pour la majorité des travaux d'interaction vague-structure. Cette petite taille permet d'utiliser des méthodes expérimentales différentes et d'obtenir des informations supplémentaires. Ainsi, la hauteur du champ de vagues peut être estimée en tout point par imagerie Schlieren, ce qui permet la mesure de coefficients de réflexion et de transmission. Les champs de vitesse du fluide peuvent être évalués par Vélocimétrie par Image de Particules. Plusieurs faits marquant ressortent de ces mesures. Tout d'abord, à petites amplitudes de vagues, les fréquences des pics de réflexions mesurés expérimentalement coincident avec les prévisions numériques de pics dits "larges". Ensuite, en comparant la réflexion engendrée par des plaques flexibles avec le cas d'une plaque rigide de même dimension, il apparaît que les réflexions sont dues à la flexibilité. Finalement, à grandes amplitudes de vagues, un jet est créé par la plaque. Le jet pourrait être responsable d'un changement de position moyenne de la plaque, pour la plaque la moins rigide, entraînant une dissipation totale de l'énergie des vagues.

Key words

Wave-structure interaction, linear wave theory, small scale wave tank, reflection and transmission, jet.

Abstract

Wave-structure interaction is a rich field with crucial application interests, such as coastal protection or electricity production through wave energy conversion. This thesis is part of that context and focuses on the specific case of a submerged elastic plate, attached at its leading edge, and forced by water waves. This device, considered as a potential wave energy converter, has been extensively studied for uniform flows or in a still fluid. However, the effect of wave-induced forcing on a submerged elastic plate remains little studied.

To address this gap, the purpose of this thesis is to describe the interaction between a submerged elastic plate, held at its leading edge, and a monochromatic surface wave field. For that purpose, an initial theoretical work is carried out based on linear wave theory. The objective of this approach is to gain a preliminary understanding of the system, namely, to formalize the physical problem and obtain information about the plate response to wave excitation. Thus, waves reflection and transmission are evaluated and contextualized through the plate's displacements observation. From this study, the elastic plates exhibit complex resonance patterns that vary based on the submergence depth, length, and rigidity of the plates.

This linear theoretical approach, limited to the ideal case of small wave amplitudes and small plate displacements, is complemented by an experimental study of plate-wave interaction. An original aspects of the thesis lies in the dimensions of the experimental setup. The utilized wave tank measures 2 meters by 50 centimeters, and is considerably smaller than the experimental facilities used in the majority of wave-structure interaction studies. This reduced size allows for the use of different experimental methods and the acquisition of additional information. Consequently, the wave field height measurements can be performed on the whole surface of the tank, using Schlieren imaging, leading to a robust estimation of wave reflection and transmission coefficient. Additionally, the fluid velocity field in the bulk can be assessed using Particle Image Velocimetry.

Several notable points emerge from those measurements. First, at small wave amplitudes, experimentally measured reflection peaks coincide with numerical predictions of so-called "wide" peaks. Furthermore, by comparing the reflection generated by flexible plates to the case of a rigid plate of the same dimensions, it becomes apparent that the reflections are due to flexibility. Finally, at large wave amplitudes, a jet is generated by the plate. This jet, could be responsible for a change in the average position of the plate, leading to total wave energy dissipation for the least rigid plate.